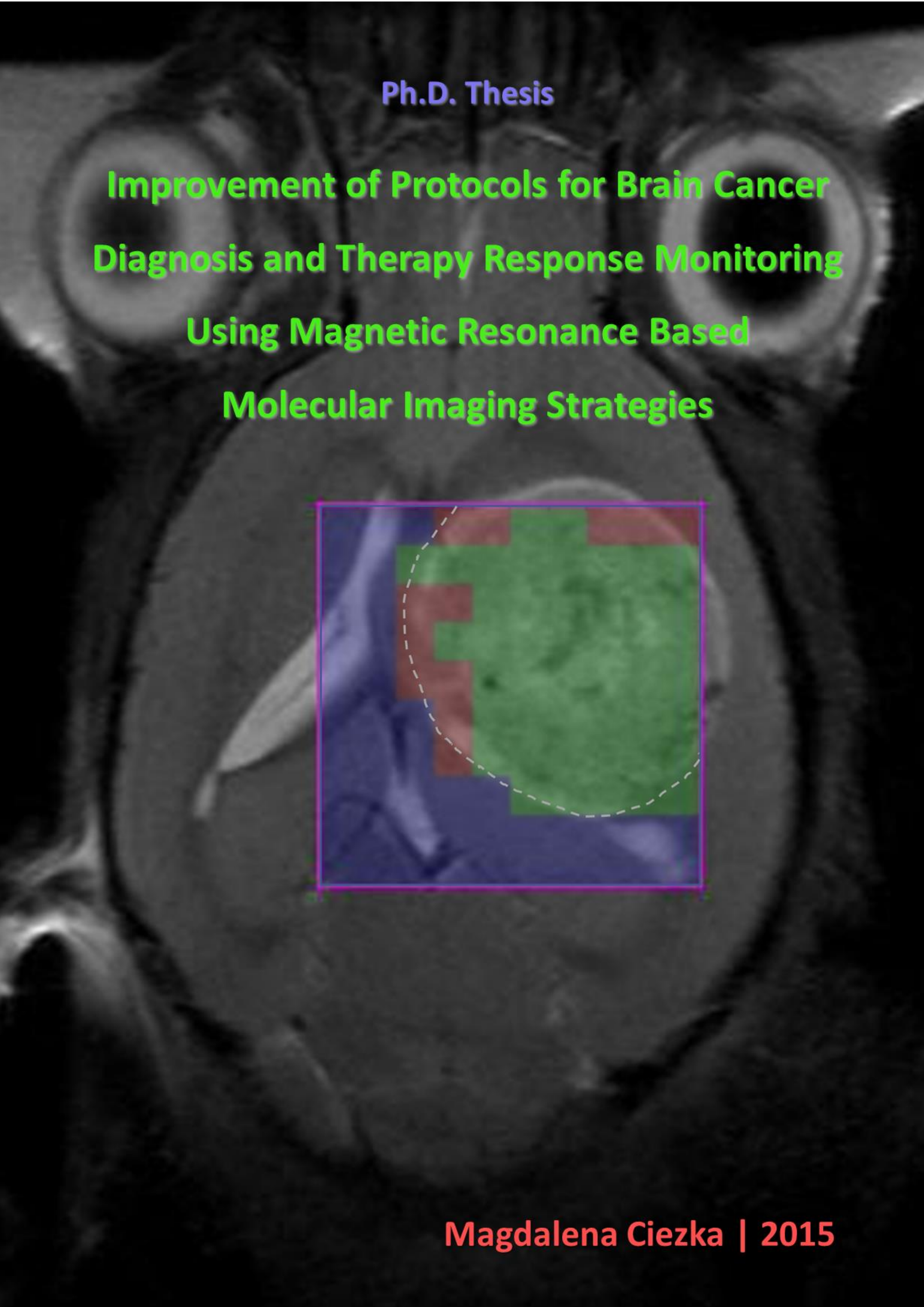

Ph.D. Thesis

# Improvement of Protocols for Brain Cancer Diagnosis and Therapy Response Monitoring Using Magnetic Resonance Based Molecular Imaging Strategies

Magdalena Ciezka | 2015

Universitat Autònoma de Barcelona

Departament de Bioquímica i Biologia Molecular

# Improvement of Protocols for Brain Cancer Diagnosis and Therapy Response Monitoring Using Magnetic Resonance Based Molecular Imaging Strategies

**Magdalena Ciezka**

**Ph.D. Thesis**

April, 2015

Dissertation presented by

**Magdalena Ciezka**

submitted for the Degree of Doctor of Philosophy at the

**Universitat Autònoma de Barcelona**

of the doctoral program in

**Biochemistry, Molecular Biology and Biomedicine**

of the department of

**Biochemistry and Molecular Biology**

surpervised by

**Dr. Carles Arús Caraltó** and **Dr. Ana Paula Candiota**

**Signatures of the supervisors**

Dr. Carles Arús Caraltó

Dr. Ana Paula Candiota

**Signature of the Ph.D. thesis author**

Magdalena Ciezka

*Cerdanyola del Vallès, 30th of April, 2015*

## Table of contents

**Index of Figure** ........ v

**Index of Tables** ........ x

**Abbreviations** ........ xi

**1. Introduction** ........ 1

- 1.1. Brain tumours ........ 3
  - 1.1.1. Epidemiology and classification ........ 3
  - 1.1.2. Genetic pathways in the evolution of gliomas ........ 7
  - 1.1.3. Cancer stem cells hypothesis ........ 10
  - 1.1.4. Detection ........ 16
  - 1.1.5. Therapy ........ 16
  - Surgical resection ........ 16
  - Radiotherapy ........ 17
  - Chemotherapy ........ 19
- 1.2. Preclinical models of human glioma ........ 21
  - 1.2.1. GL261 murine model ........ 21
  - 1.2.2. Genetically engineered mice (GEM) models ........ 22
- 1.3. Nuclear Magnetic Resonance (NMR) ........ 24
  - 1.3.1. Overview of basic MR principles ........ 24
  - *Physical properties of nucleus* ........ 24
  - Relaxation times ........ 28
  - 1.3.2. Applications of NMR in biomedical research of brain cancer ........ 32
  - 1.3.2.1. Magnetic Resonance Imaging ........ 32
  - 1.3.2.2. Magnetic Resonance Spectroscopy ........ 33
  - *Chemical shift* ........ 34
  - *Relaxation times and use of different Echo Times* ........ 36
  - *Resonances and biological significance of the major compounds of brain tissue* ........ 37
  - 1.3.2.3 Magnetic Resonance Spectroscopic Imaging ........ 39
  - 1.3.2.4. Pattern recognition analysis of NMR data ........ 41
  - Supervised PR ........ 42
  - Unsupervised PR ........ 42
  - Semi-supervised PR ........ 43

**2. General objectives** ........ 45

**3. General materials and methods ........................................................................................ 49**

3.1. GL261 cells.......................................................................................................................... 50

3.2. Gliospheres.......................................................................................................................... 51

3.3. Cell count.............................................................................................................................. 51

3.4. Animal models...................................................................................................................... 52

Wild type C57BL/6 mice ........................................................................................................ 52

Genetically engineered mice .................................................................................................. 53

*S colony: S100B-v-erbB/INK4A-ARF(+/-)*.................................................................................. 53

*R colony: GFAP-$V^{12}$HA-ras*............................................................................................... 53

3.5. Genotyping for GEM............................................................................................................. 55

*S colony*................................................................................................................................ 55

*R colony* ................................................................................................................................ 55

Gel electrophoresis of PCR products........................................................................................ 55

3.6. Generation of tumours by stereotactic injection of cells........................................................ 56

3.7. Tissue preservation for post-mortem procedures .................................................................. 57

3.8. Histopathological analysis .................................................................................................... 58

3.8.1. Analysis of brain/tumour tissue ......................................................................................... 58

3.8.2. Analysis of gliospheres ...................................................................................................... 59

3.9. Therapy protocol for GL261 GBM .......................................................................................... 59

3.10. In vivo MRI/MRS/MRSI......................................................................................................... 60

3.10.1. MRI acquisition................................................................................................................ 60

Contrast Enhanced MRI (CE MRI)............................................................................................. 61

Dynamic Contrast Enhancement (DCE)...................................................................................... 61

3.10.2. SV-MRS acquisition........................................................................................................... 61

3.10.3. PE-MRSI ........................................................................................................................... 62

3.10.4. MR data processing and post-processing........................................................................... 63

*Tumour volume calculation from MRI acquisitions*.................................................................. 63

*Calculation of tumour doubling time*....................................................................................... 64

*MRS in vivo data processing*................................................................................................... 64

*MRSI and PE-MRSI data processing* ........................................................................................ 64

3.11. Pattern recognition analysis.................................................................................................. 65

3.11.1. Voxel data selection and labelling for MRSI data grids....................................................... 66

3.11.2. Semi-supervised methodology for source extraction.......................................................... 66

3.11.2.1. Non-negative Matrix Factorization .................................................................................. 66

3.11.2.2. Semi-supervised extraction of source signals ............ 67

3.11.2.3. Nosological imaging of the response to therapy ............ 68

3.12. Statistical analysis ............ 69

**4. Pilot study and characterisation of GEM ............ 71**

4.1. Specific objectives ............ 73

4.2. Specific Materials and Methods ............ 73

4.3. Results and Discussion ............ 74

4.3.1. Genotypic characterisation ............ 74

4.3.2. MR screening and tumour incidence ............ 76

4.3.3. MRI/MRS/MRSI/PE-MRSI/DCE-MRI characterisation ............ 79

R colony ............ 81

S colony ............ 88

4.3.4. Histopathology of tumours ............ 95

4.4. General discussion for this section ............ 96

4.4. Conclusions ............ 97

**5. Developing a transplantable murine tumour model of low/intermediate grade ............ 99**

5.1 Rational and Objective ............ 101

5.2 Specific Materials and Methods ............ 101

5.3 Results and discussion ............ 102

5.3.1. Disaggregated tumour model using GL261 derived gliospheres ............ 102

5.3.2. Disaggregated tumour model from a GEM anaplastic ODG: the S912 tumour ............ 105

5.3.2.1. MRI assessment of tumour growth and estimation of penetrance ............ 106

5.3.2.2. MRS/CE MRI/ PE-MRSI ............ 110

5.3.2.3. Genotyping ............ 118

5.3.2.4. Histopathological diagnosis ............ 118

5.3.3. Survival ............ 122

5.4. Conclusions ............ 124

**6. Sequencing of selected genes in different tumour models ............ 125**

6.1. Specific objectives ............ 127

6.2. Specific Materials and Methods ............ 127

6.2.1 Selection of samples ............ 127

6.2.2 Sample obtention and DNA extraction ............ 127

6.3. Results and discussion ............ 129

6.4. Conclusions ............ 130

**7. Longitudinal studies of the GL261 GBM model response to temozolomide (TMZ) therapy .......131**
7.1. Specific Objectives ........ 133
7.2. Specific Materials and Methods ........ 133
7.3 Results and Discussion ........ 134
7.3.1. Growth kinetics of GL261 tumours subjected to therapy ........ 134
7.3.2. Evaluation of tumour response to TMZ according to RECIST criteria ........ 138
7.3.3. Survival ........ 140
7.3.4. MRI ........ 142
7.3.5. PE-MRSI and DMSO maps ........ 143
7.3.6. Source extraction in the training data set ........ 145
7.3.7. Nosological maps ........ 147
7.3.8. Histopathological studies and correlation between calculated nosologic maps ........ 158
7.4. Conclusions ........ 166
**8. General Discussion ........169**
**9. General Conclusions ........175**
**References ........179**
**ANNEXES ........191**

## Index of Figure

**Figure 1.1.** Age-standardised incidence and mortality rates in women and men worldwide estimated by GLOBOCAN ........ 3

**Figure 1.2.** Incidence age-standardised rate (ASR) per 100,000 of brain and central nervous system tumours in female and male worldwide estimated by GLOBOCAN........ 4

**Figure 1.3.** Distribution of primary brain and CNS gliomas by histology subtypes (CBTRUS Statistical Report 2006–2010........ 6

**Figure 1.4.** Genetic pathways in the evolution of gliomas........ 7

**Figure 1.5.** *INK4A* gene products pathways ........ 9

**Figure 1.6.** Schematic diagram of the proposed molecular consequences of IDH1 mutation ........ 10

**Figure 1.7.** Two models for tumour heterogeneity and propagation in solid cancer cells........ 11

**Figure 1.8.** The anatomy and functioning of the subventricular zone and subgranular zone in humans and rodents ........ 13

**Figure 1.9.** Hierarchical organization of the functional compartments in renewing tissues........ 15

**Figure 1.10.** Direct and indirect action of radiation therapy ........ 17

**Figure 1.11.** Temozolomide site of action and targets for regulation with other agents........ 20

**Figure 1.12.** Diagram representing a magnetic moment of a nucleus........ 25

**Figure 1.13.** Effect of an external magnetic field (B0) on the spins ........ 26

**Figure 1.14.** Graphical representation of the Larmor frequency........ 26

**Figure 1.15.** Graphical representation of the spins in thermal equilibrium in the presence of an external magnetic field B0........ 27

**Figure 1.16.** Representation of the perturbation of the macroscopic magnetization of a sample in a coordinate system (rotating at the resonance frequency) ........ 28

**Figure 1.17.** FID transformation (time domain) recorded in an NMR experiment, to a spectrum (frequency domain), after application of the TF ........ 29

**Figure 1.18.** T1 relaxation process after a 90° RF pulse is applied at equilibrium ........ 30

**Figure 1.19.** T2 and T2* relaxation processes after a 90° RF pulse is applied at equilibrium........ 32

**Figure 1.20.** Mean and SD spectra of normal white matter and 5 different human brain tumour types ........ 36

**Figure 1.21.** Spectral pattern and SD of GL261 tumours at two TE (12 ms and 136 ms) obtained from MRS explorations of C57BL/6 tumour bearing mice........ 38

**Figure 1.22.** CSI obtained from a mouse brain bearing GL261 tumour in vivo at 7T........ 42

**Figure 3.1.** Scheme for marking mice by ear punching........ 56

**Figure 3.2.** Gel electrophoresis of PCR products for genotyping of S and R colonies........ 58

**Figure 3.3.** A C57BL/6 mouse with a scull incision immobilized in a stereotactic holder........ 59

**Figure 3.4.** General scheme of the pre-established TMZ therapy protocol........ 61

**Figure 3.5.** Scheme of the volume measurement carried out in mice........ 65

**Figure 3.6.** Voxel selection and labelling .......... 68

**Figure 3.7.** Scheme of Non-negative Matrix Factorization method .......... 69

**Figure 3.8.** Diagram showing the main steps followed in the semi-supervised source extraction methodology, from the collection of MRSI data grids to the generation of the three main sources describing the metabolic profile of the tumours analysed .......... 70

**Figure 3.9.** Nosological imaging of response to therapy .......... 71

**Figure 4.1.** Total number of animals from the colony S genotyped (n = 130) during the pilot study of this PhD work and their genotype distribution .......... 77

**Figure 4.2.** Total number of animals from the colony S genotyped (n = 781) prior to the pilot study of this PhD work since the establishment of the colony, and their genotype distribution .......... 77

**Figure 4.3.** Total number of animals from the colony R genotyped (n = 139) during the pilot studies within this PhD work, and their genotype distribution .......... 78

**Figure 4.4.** Distribution of abnormality symptoms developed by mice among S and R colonies prior to abnormal brain mass detection by MRI .......... 79

**Figure 4.5**. $T_{2W}$ images of cases S851 and S857 with tumour location, respectively in the olfactory bulb and the brainstem, compromising possible MRS/MRSI explorations .......... 82

**Figure 4.6.** $T_{2W}$ MRI of R279 mouse brain at coronal orientation acquired on the day of detection and at 6 days post-detection (p.d.), and at axial orientation acquired at 6 days p.d. .......... 83

**Figure 4.7.** R279 tumour mass growth from the day of detection until the sacrifice of the animal, and type of explorations performed on each day .......... 84

**Figure 4.8.** $T_{1W}$ coronal images of R279 **A)** pre- intraperitoneal contrast administration and **B)** post-intraperitoneal contrast administration acquired one day p.d. **C)** Difference image between A) and B) showing the zone of contrast intake as hipointense region .......... 85

**Figure 4.9.** Comparison of the R279 tumour MR spectra on the day of the abnormal brain mass detection and on the day 6 p.d. at **A)** SET (12 ms) and **B)** LET (136 ms). .......... 85

**Figure 4.10.** PE-MRSI with DMSO of the R279 mass .......... 88

**Figure 4.11.** PE-MRSI: hyperglycaemia under mild hypothermia of R279 .......... 89

**Figure 4.12.** PR analysis for R279 mouse at day 6 p.d. .......... 89

**Figure 4.13.** S871 tumour volume growth profile measured from $T_{2W}$ images from the day of the abnormal mass detection until the sacrifice of the animal and the additional type of explorations performed on each day .......... 90

**Figure 4.14.** $T_{2W}$ HR MRI of S871 mouse brain at acquired on **A)** the day 2 p.d. and **B)** 51 p.d. .......... 91

**Figure 4.15.** $T_{1W}$ coronal images of S871 **A)** pre-intraperitoneal contrast administration and **B)** post-intraperitoneal contrast administration acquired on the day 2 p.d. of the abnormal mass. **C)** Difference image between A) and B) showing the zone of contrast intake .......... 91

**Figure 4.16.** Comparison of the S871 tumour spectra on the day 18 p.d. and on the day 51 p.d. at **A)** SET (12 ms) and **B)** LET (136 ms) .......... 92

**Figure 4.17.** PE-MRSI with DMSO of the abnormal mass of the S871 mouse at the day 27 p.d. .......... 93

**Figure 4.18.** PE-MRSI: hyperglycemia under mild hypothermia of the S871 case .......... 94

**Figure 4.19.** PR analysis for one representative animal from the S colony, S871 at day 51 p.d. .......... 95

**Figure 4.20.** Entire FOV view for $T_{2W}$ images and DCE-T1 data of the S910 mouse .......... 95

**Figure 4.21.** Time-course curve for the S910 case, showing the average signal enhancement in the tumour region, from the 3 slices studied, after bolus injection of the CA...................................... 96

**Figure 4.22.** Distribution of histopathological diagnosis found for abnormal brain lesions of the R GEM colony ........................................................................................................................ 98

**Figure 4.23.** Distribution of histopathological diagnosis found for brain masses of the S GEM colony (n =70)........................................................................................................................................ 98

**Figure 5.1.** Image from confocal microscopy (100X) of gliospheres generated from **A)** GL261 tumour and **B)** S912 GEM tumour............................................................................................... 105

**Figure 5.2.** Average growth curves representing the mean ± SD of tumour volumes ($mm^3$) grown from implanted: **A)** GL261 cells (n = 6); **B)** cells from gliospheres obtained from fresh GL261 tumour (n = 6), **C)** cells from gliospheres obtained from frozen GL261 tumour (n = 7) ................................... 106

**Figure 5.3.** Coronal $T_{1W}$ MRI of the S912 mouse brain **A)** pre- and **B)** post- pre-intraperitoneal contrast administration, as well as **C)** subtraction of the two previous images, acquired at 7T 32 days after initial tumour detection ........................................................................................... 108

**Figure 5.4.** Coronal $T_{2W}$ MRI of mice brains with different appearance of tumours, depending on type of cells implanted ................................................................................................... 110

**Figure 5.5.** Average SV MR spectra at SET(12 ms) and LET (136 ms) obtained from $(1.5 - 3.0\ mm)^3$ voxels of tumours generated from GEM S912 fresh gliospheres ................................................. 113

**Figure 5.6.** Average SV MR spectra at SET (12 ms) and LET (136 ms) obtained from tumours generated from frozen GEM S912 gliospheres and tumours generated from gliospheres obtained from a frozen piece of GEM S912 tumour ...................................................................... 114

**Figure 5.7.** Box-plots representing Cho/Cr ratios at SET for normal brain parenchyma (NB) of C57BL/6 mice, tumours generated from fresh S912 gliospheres: 'short latency' (SL) group at day 18, 21 and 40 p.i. and 'intermediate latency' (IL) group at 35-42 days p.i.; tumours generated from frozen S912 gliospheres: 'short latency' (SL) group, 'intermediate latency' (IL) group and 'long latency' (LL); tumours generated from S912 gliospheres obtained from frozen tumour (FT) and standard GL261 tumours.......................................................................................................... 116

**Figure 5.8.** Box-plots representing ML/Cr ratios at SET for normal brain parenchyma (NB) of C57BL/6 mice, tumours generated from fresh S912 gliospheres: 'short latency' (SL) group at day 18, 21 and 40 p.i. and 'intermediate latency' (IL) group at 35-42 days p.i.; tumours generated from frozen S912 gliospheres: 'short latency' (SL) group, 'intermediate latency' (IL) group and 'long latency' (LL); tumours generated from S912 gliospheres obtained from frozen tumour (FT) and standard GL261 tumours.......................................................................................................... 116

**Figure 5.9.** Changes in contrast intake and spectral pattern of G5-S912 tumour during its growth curve .......................................................................................................................... 118

**Figure 5.10.** PR analysis for representative mice from groups D and E of animals, implanted with fresh gliospheres, G1-S912 at day 39 p.i., and frozen gliospheres, Gc26-S912 at day 35 p.i.................. 119

**Figure 5.11.** $T_{2W}$ coronal MRI of G2-S912 tumour 43 days p.i and images of histological immuno-preparations of the tumour tissue done after the animal was sacrificed on day 62 p.i. with comparable orientation with respect to the reference MRI image .............................................. 122

**Figure 5.12.** Kaplan-Meier survival curves of C57BL/6 mice implanted with cells/gliospheres of different origin or different preparation protocol ....................................................................... 125

**Figure 6.1.** PCR amplification of the regions of interest of IDH1, IDH2 and p53 of murine DNA ....... 130

**Figure 6.2.** Comparison of IDH1 sequences at the region of expected mutation site (R132) for normal brain parenchyma of wt C57BL/6 mouse and a GL261 tumour showing no mutation detected in the tumour ........ 131

**Figure 7.1.** Volume growth dynamics of GL261 tumours treated with TMZ (n = 12) ........ 138

**Figure 7.2.** Mean growth rate (±SD) of GL261 tumours treated with TMZ in this thesis (n = 11) in comparison to the standard growth kinetics of untreated GL261 tumours (n = 6) ........ 139

**Figure 7.3.** Tumour growth rate (average values ± SD) of control (untreated) GL261 tumours (n = 6) and tumours treated with three TMZ cycles (n = 12) ........ 139

**Figure 7.4.** Mean growth rate ±SD of GL261 tumours treated with TMZ in comparison to both, previous results of the group and the standard growth kinetics of untreated GL261 tumours ..... 140

**Figure 7.5.** Average growth curves of each group of response defined by RECIST criteria ........ 142

**Figure 7.6.** Kaplan-Meier survival curves of animals harbouring GL261 tumours subjected to TMZ therapy classified as partially responding, stable disease, progressive disease, non-evaluable group and control GL261 group ........ 143

**Figure 7.7.** Kaplan-Meier survival curves of animals harbouring GL261 tumours subjected to TMZ and also control mice, from the current work and from previous group work, classified as partially responding, stable disease, progressive disease, non-evaluable group and control GL261 group 144

**Figure 7.8.** $T_{2W}$ coronal MRI of C819 tumour (classified as partially responding to the therapy) at selected time points along the tumour evolution ........ 145

**Figure 7.9.** Representative $T_{2W}$MRI and MRSI colour-coded maps of DMSO accumulation acquired at different time points p.i. for mouse C817 ........ 147

**Figure 7.10.** The three sources calculated with the semi-supervised methodology ........ 148

**Figure 7.11.** Nosologic imaging for three mice from the training set for source extraction: C418 and C586 at day 22 p.i. – treated with TMZ (T) and C583 at day 18 p.i. – untreated GL261 tumour control (C) ........ 150

**Figure 7.12.** Nosologic colour-coded maps corresponding to the partially responding case C819.... 154

**Figure 7.13.** Nosologic colour-coded maps corresponding to the partially responding case C817.... 155

**Figure 7.14.** Nosologic colour-coded maps corresponding to stable disease case C776 and C808 ... 156

**Figure 7.15.** Nosologic colour-coded maps corresponding to stable disease case C809 ........ 157

**Figure 7.16.** Nosologic colour-coded maps corresponding to stable disease case C821 ........ 158

**Figure 7.17.** Nosologic colour-coded maps corresponding to progressive disease case C797........ 159

**Figure 7.18.** Nosologic colour-coded maps corresponding to the non-evaluable group, considering the overall response, namely cases C774, C775, C794 and C795 ........ 160

**Figure 7.19.** Box-plots representing the reference ranges for proliferation, apoptosis and mitotic indexes calculated for control and treated tumours previously described in literature ........ 163

**Figure 7.20.** Nosologic maps and representative histopathological samples stained with Ki67 and caspase 3 of the longitudinal study cases selected for histopathology ........ 164

**Figure 7.21.** Digitalized histopathological image of the case C808, in which proliferation was counted in the thin layer (about 100 µm) of the periphery (in black), superimposed with the nosological image at the time of death (day 33 p.i.) ........ 166

**Figure 7.22.** Volume growth dynamics of GL261 tumours treated with TMZ from the longitudinal studies of this thesis that underwent histopathological analysis ........ 166

**Figure 7.23. A)** Contingency tables calculated with the cases from the test set considering the response detected by the semi-supervised methodology and the proliferation and apoptotic indexes from the corresponding histopathological slides. **B)** Proliferation and apoptotic indexes comparison between cases classified as responders or non-responders using the sources analysis ........................................................................................................................................ 167

## Index of Tables

**Table 3.1.** Possible expected genotypes of the progeny of the S and R colony crossings ................... 56

**Table 4.1**. Number of GEM genotyped and found to be transgenic by PCR genotyping and transgenic rate in each colony ........................................................................................................ 76

**Table 4.2.** Number of animals screened and tumour incidence rate among transgenic animals in each colony during the period of this work, as well as during the whole pilot studies ........................... 80

**Table 4.3.** Number and type of MR studies performed additional to $T_{2W}$ MRI.................................... 81

**Table 4.4.** Comparison of main ratios at SET between day 18 and day 51 p.d. for S871 case ............. 92

**Table 5.1.** Distribution of experimental animals depending on the source of cells used for the tumour generation protocol and identifiers of animals in each group...................................................... 103

**Table 5.2.** Number of animals assigned into each group, time of tumour detection, average final volume and doubling time of masses.............................................................................. 109

**Table 5.3.** Average metabolite peak height ratios at both short and long TE normalized spectra for tumours generated from fresh S912 gliospheres ......................................................................... 115

**Table 5.4.** Average metabolite peak height ratios at both short and long TE normalized spectra for tumours generated with frozen S912 gliospheres and from S912 gliospheres obtained from frozen tumour.......................................................................................................................... 115

**Table 5.5.** Histopathological diagnosis by HE staining for 12 tumours derived from implantation of gliospheres obtained from a fresh piece of S912 GEM tumour and IHC analysis obtained for selected tumours................................................................................................................. 121

**Table 5.6.** Histopathological diagnosis by HE staining for 27 tumours derived from implantation of frozen gliospheres obtained from a fresh piece of S912 GEM tumour and IHC analysis obtained for selected tumours................................................................................................................. 123

**Table 5.7.** Histopathological diagnosis by HE staining for 9 tumours derived from implantation of gliospheres obtained from a frozen piece of S912 GEM tumour and IHC analysis obtained for selected tumours................................................................................................................. 124

**Table 5.8.** Survival time (days, mean ±SD) of each experimental group of mice from the development of transplantable murine tumour model of low/intermediate grade experiment........................ 124

**Table 7.1.** Best overall response evaluation: animals following into each response category and corresponding RECIST criteria ......................................................................................... 141

**Table 7.2**. Tumour volume (acquired by MRI) and histopathological parameters (proliferation, apoptotic and mitotic rates) calculated for the test set cases...................................................... 162

## Abbreviations

| | |
|---|---|
| AIC | 5-aminoimidazole-4-carboxamide |
| Ala | Alanine |
| Arg | Arginine |
| AS | Surface area |
| ASR | Age-standardised rate |
| $B_0$ | External magnetic field |
| BBB | Blood-brain barrier |
| BER | Balanced error rate |
| bp | Base pair |
| ca. | *circa*, Approximately |
| CA | Contrast agents |
| CDK | Cyclin dependent kinase |
| CE | Contrast-enhanced |
| CNS | Central nervous system |
| CT | Computed tomography |
| Cho | Choline |
| Cr | Total Creatine |
| CR | Complete response |
| CSC | Cancer stem cell |
| CSI | Chemical shift imaging |
| DCE | Dynamic contrast enhancement |
| DMEM | Dulbecco's modified Eagle's medium |
| DMPM | Dynamic MRSI processing module |
| DMSO | Dimethyl sulfoxide |
| DMSO-MRSI | Dimethyl sulfoxide-perturbed Magnetic Resonance Spectroscopic Imaging |
| DT | Doubling time |

| | |
|---|---|
| DWI | Diffusion Weighted Imaging |
| EDTA | Ethylenediaminetetraacetic acid |
| EES | Extracellular extravascular space |
| EGF | Epidermal growth factor |
| EGFR | Epidermal growth factor receptor |
| EtBr | Ethidium bromide |
| FI | Fisher information |
| FID | Free induction decay |
| FOV | Field of view |
| GABA | γ-aminobutyric acid |
| GABRMN | *Grup d'Aplicacions Biomèdiques de la Ressonància Magnètica Nuclear* |
| GBM | Glioblastoma multiforme |
| Gd | Gadolinium |
| Gd–DTPA | Gadolinium–diethylenetriamine penta–acetic acid |
| GEM | Genetically engineered mice |
| GFAP | Glial fibrillary acid protein |
| Glc | Glucose |
| Gln | Glutamine |
| Glu | Glutamate |
| Glx | Glutamate and glutamine |
| Gly | Glycine |
| GPC | Glycerophosphorylcholine |
| GSH | Reduced Glutathione |
| HE | Hematoxylin-Eosin |
| HEPES | 4-(2-hydroxyethyl)-1-piperazineethanesulfonic acid |
| HIF-1α | Hypoxia-inducible factor 1-alpha |
| HR | High resolution |

| | |
|---|---|
| HSA | Heat-stable antigen |
| IDH | Isocitrate dehydrogenase |
| IHC | Immunohistochemistry |
| Inter-ST | Inter slice thickness |
| i.p. | Intraperitoneal |
| Ko | Knockout |
| Lac | Lactate |
| LDA | Linear discriminant analysis |
| LET | Long echo time |
| LOO | Leave-one-out |
| MAP2 | Microtubule-associated protein 2 |
| MCAO | Middle cerebral artery occlusion |
| MDM2 | Mouse double minute 2 |
| MGMT | O(6)-methylguanine-DNA methyltransferase |
| mI | Myo-inositol |
| ML | Mobile lipids |
| MLP | Multi-layer perceptron model |
| MM | Macromolecules |
| MR | Magnetic Resonance |
| MRI | Magnetic Resonance Imaging |
| MRS | Magnetic Resonance Spectroscopy |
| MRSI | Magnetic Resonance Spectroscopic Imaging |
| MSME | Multi-slice multi-echo |
| MTIC | Methyl-triazeno imidazole-carboxamide |
| MV | Multi-voxel |
| MW | Molecular weight |
| NA | Number of averages |

| | |
|---|---|
| NAA | N-acetylaspartate |
| NAAG | Nacetyl-apartyl-glutamate |
| NAD(P)$^+$ | Nicotinamide adenine dinucleotide (phosphate) |
| NAD(P)H | Nicotinamide adenine dinucleotide (phosphate) (reduced form) |
| NCAM1 | Neural cell adhesion molecule 1 |
| NMF | Non-negative matrix factorization |
| NMR | Nuclear Magnetic Resonance |
| NS | Number of slices |
| NT | Non-tumoural brain parenchyma |
| OA | Oligoastrocytoma |
| ODG | Oligodendroglioma |
| ODG2 | Oligodendroglioma grade II |
| ODG3 | Oligodendroglioma grade III |
| OLIG2 | Oligodendrocyte transcription factor |
| O6-meG | O6-methyl-guanine |
| p. | Passage |
| PBS | Phosphate Buffered Saline |
| PC | Phosphorylcholine |
| PCA | Principal Component Analysis |
| PCR | Polymerase chain reaction |
| PE-MRSI | Perturbation enhanced MRSI |
| PET | Positron emission tomography |
| PHD | Prolyl hydroxylase |
| p.d. | Post-detection |
| p.i. | Post-implantation |
| p.o. | *per os*, orally |
| ppm | Parts per million |

| | |
|---|---|
| PR | Pattern recognition |
| PRESS | Point-Resolved Spectroscopy |
| PSA | Polysialic acid |
| PUFA | Polyunsaturated fatty acids |
| q.d. | *quadue die*, every day |
| RARE | Rapid acquisition with relaxation enhancement |
| RB | Retinoblastoma |
| RECIST | Response Evaluation Criteria in Solid Tumours |
| RF | Radiofrequency |
| RMS | Rostral migratory stream |
| ROC | Receiver operating characteristic |
| RPMI | Roswell Park Memorial Institute |
| SC | Spectra Classifier |
| SET | Short echo time |
| SFFS | Sequential Forward Feature Selection |
| SGZ | Subgranular zone |
| SNR | Signal-to-noise ratio |
| spvs | Spectral vectors |
| ST | Slice thickness |
| STEAM | Stimulated-Echo Acquisition Mode |
| SV | Single voxel |
| SVZ | Subventricular zone |
| SW | Spectral width |
| T | Tesla |
| T1 | Longitudinal ("spin-lattice") relaxation time |
| $T_{1W}$ | T1-weighted |
| T2 | Transverse ("spin-spin") relaxation time |

| | |
|---|---|
| $T_{2W}$ | T2-weighted |
| TAT | Total acquisition time |
| Tau | Taurine |
| TBE | Tris-borate-ethylenediaminetetraacetic acid |
| TE | Echo Time |
| TF | Fourier Transform |
| Tg | Transgenic |
| TMZ | Temozolomide |
| TP53 | Tumour protein p53 |
| TR | Recycling time |
| UAB | *Universitat Autònoma de Barcelona* |
| UL | Unit Length |
| VAPOR | Variable Pulse Power and Optimized Relaxation Delays |
| VEGF | Vascular endothelial growth factor |
| VEGFR | Vascular endothelial growth factor receptor |
| VOI | Volume of interest |
| WHO | World Health Organization |
| Wt | Wild type |
| | |
| $\gamma$ | Gyromagnetic ratio |
| $\delta$ | Chemical shift |
| $\nu_0$ | *Larmor* frequency |
| $\nu_0$ | Frequency |
| $\Delta E$ | Energy difference |
| $\vec{M}$ | Net magnetization |

# 1. Introduction

## 1.1. Brain tumours

### 1.1.1. Epidemiology and classification

Tumours of the central nervous system (CNS) comprise less than 2% of all cancer cases diagnosed each year worldwide, but nevertheless, they account for a high mortality rate of 2.3% among all cancer patients [1] (Figure 1.1) in comparison with other tumours (e.g. for breast, prostate) for which mortality is lower than incidence.

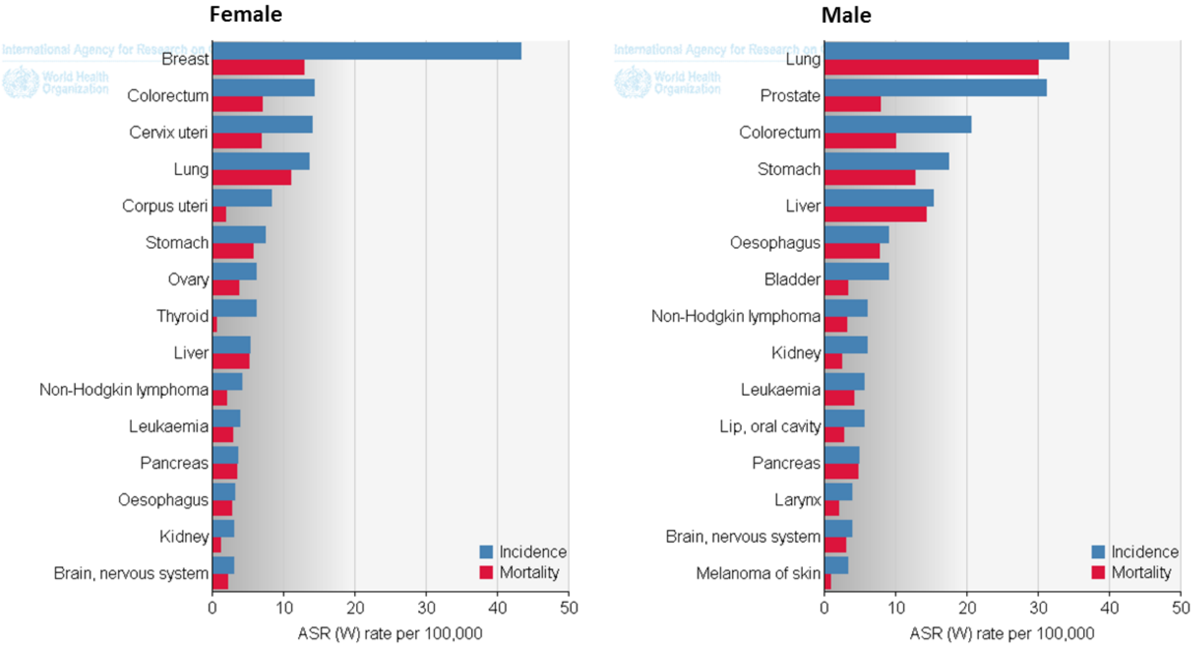

**Figure 1.1.** Age-standardised incidence (blue) and mortality (red) rates in women (left) and men (right) worldwide estimated by GLOBOCAN [1].

The worldwide incidence rate of CNS tumours in 2012, age-adjusted using the world standard population, was 3.4 per 100,000. Incidence rates by gender were 3.9 per 100,000 in males and 3.0 per 100,000 in females (Figure 1.2). The incidence rates were lower (3.0 per 100,000) in less developed countries than in more developed countries (5.1 per 100,000), probably due to the access to more sophisticated diagnostic techniques in the latter.

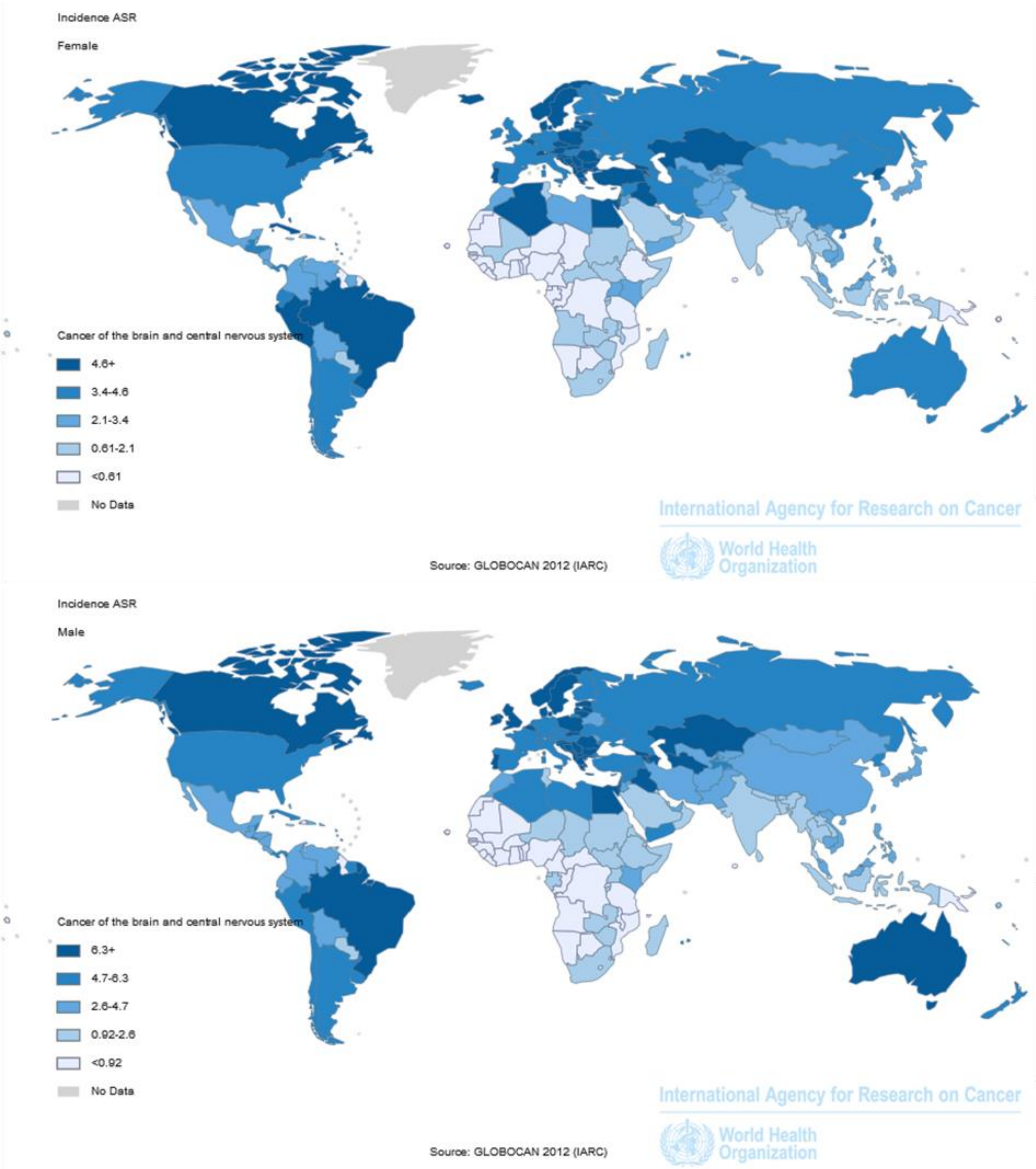
Incidence ASR
Female
Cancer of the brain and central nervous system
4.6+
3.4-4.6
2.1-3.4
0.61-2.1
<0.61
No Data
International Agency for Research on Cancer
World Health Organization
Source: GLOBOCAN 2012 (IARC)
Incidence ASR
Male
Cancer of the brain and central nervous system
6.3+
4.7-6.3
2.6-4.7
0.92-2.6
<0.92
No Data
International Agency for Research on Cancer
World Health Organization
Source: GLOBOCAN 2012 (IARC)

**Figure 1.2.** Incidence age-standardised rate (ASR) per 100,000 of brain and central nervous system tumours in female (top) and male (bottom) worldwide estimated by GLOBOCAN [1].

Among CNS tumours, brain tumours are a common designation for tumours arising in intracranial regions: brain itself (neurons, glial cells (astrocytes, oligodendrocytes and ependymal cells), lymphatic tissue or blood vessels), cranial nerves (Schwann cells), brain envelopes (meninges), skull, pituitary and pineal gland. These tumours, which originate in the brain, are called primary brain tumours. Secondary brain tumours, on the other hand, have a metastatic origin, i.e. they result from cancers primarily located in other organs that spread to brain by blood, mainly from lung or breast carcinomas, but some arise from melanomas, choriocarcinomas and renal carcinoma [2]. Still, metastatic tumours are the most common neoplasms of the CNS, occurring in 25% of the patients who die of cancer [3] with median survival from 2 to 16 months [4]. While primary brain tumours are named for cell type of origin or its location in the brain, the secondary brain tumours are named after the organ or the tissue in which they arose.

The tumours of CNS are classified according to criteria published by World Health Organization [2], based on the type and location of the cells that originate from, while the degree of malignancy is characterized by the grade. The grade of a tumour is based on four histopathological criteria, namely nuclear atypia, mitotic activity, endothelial hyperplasia and necrosis. These describe how abnormal the cancer cells are and how quickly the tumour is likely to grow and spread, determining the patient survival probability. All of this combined results in a scale of four grades of malignancy:

- **Grade I** tumours, have low proliferative potential, diffused nature and the tumour may be cured by surgery (e.g. pilocytic astrocytoma).
- **Grade II** tumours, are infiltrating tumours with low mitotic index and potential of recurrence after surgery; most tend to progress to high-grade lesions (e.g. astrocytomas and oligodendrogliomas (ODG)).
- **Grade III** tumours, present histological evidence of malignancy, such as nuclear atypia, elevated mitotic activity, clearly expressed infiltrative capabilities, and anaplasia (e.g. anaplastic ODG).
- **Grade IV** tumour, include lesions that are mitotically active with vascular proliferation, necrosis and generally associated with a rapid preoperative and postoperative progression of disease (e.g. glioblastoma multiforme (GBM)).

Gliomas, tumours that arise from glial cells, are one of the most prevalent CNS tumour types [5]. They are classified into different groups according to the cell (or stem cell, see Section 1.1.3) type they originate from (which include astrocytomas, derived from astrocytes; oligodendrogliomas (ODGs), derived from oligodendrocytes; and oligoastrocytomas (AOs), derived from astrocytes and/or oligodendrocytes) (Figure 1.3), their location (supratentorial, in the cerebrum; infratentorial, in the cerebellum) and grade.

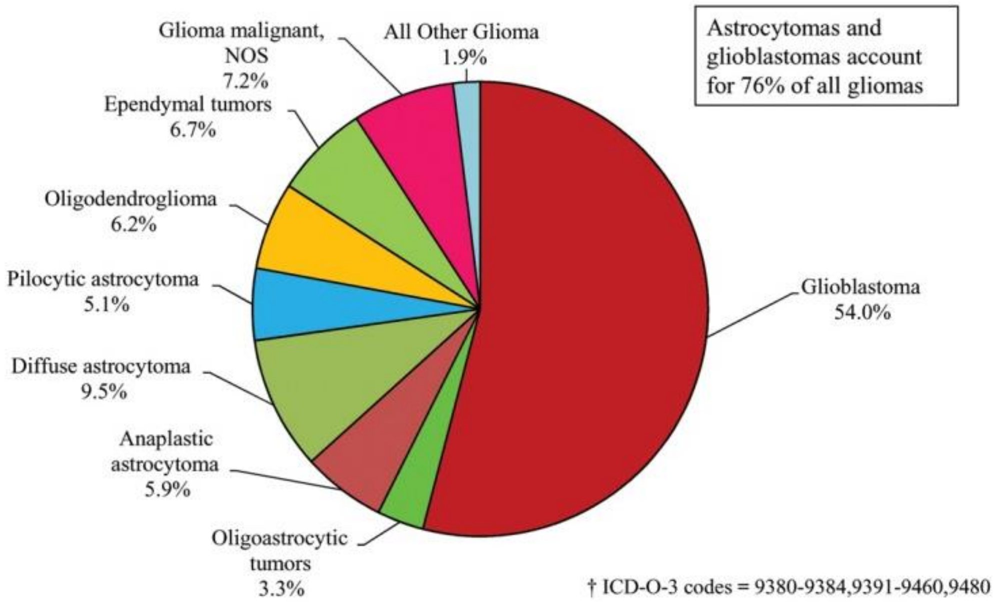

**Figure 1.3.** Distribution of primary brain and CNS gliomas by histology subtypes (CBTRUS Statistical Report 2006–2010 [6]).

Astrocytomas make up the most gliomas and represent 33.3% of all newly diagnosed brain tumour cases. They can be divided into: pilocytic astrocytoma (grade I), low-grade diffuse astrocytomas (grade II) and anaplastic astrocytomas (grade III). Pilocytic astrocytomas are slow-growing tumours with favorable prognosis and survival rates exceeding 5 years in 85% of cases. Diffuse astrocytomas, however, cannot be surgically resected as a whole and tend to evolve into more aggressive masses (of grade III) with the survival rate of 5 years or more in 60% of the cases.

Furthermore, ODGs are classified into low-grade ODG (grade II) and anaplastic ODG (grade III). They have a less favorable prognosis than diffuse astrocytomas, but also less likely to progress to more aggressive stages. The incidence rate of OAs can vary from 1.8% to 19% among all gliomas and this variation is due to different diagnosis criteria among laboratories, as they are often confused with

ODGs or astrocytomas. The prognosis and malignancy depends on the proportions of the different cell types that constitute these tumours.

The most aggressive type of glioma is GBM (grade IV) [7], which is also the most common malignant tumour in the CNS (Figure 1.3). They are highly resistant to chemo- and radiotherapy and only 3% of the affected patients survive more than three years [8, 9] with the median survival when both therapies are combined of 14.6 months [10]. The histopathological features of GBM include: nuclear atypia, cellular pleomorphism, vascular thrombosis, microvascular proliferation and necrosis, and is characterized by a diffuse tissue-distribution pattern, with extensive dissemination of the tumour cells within the brain that restricts complete surgical resection. GBMs can develop either *de novo* (primary GBM) or as the result of the malignant progression from any of the three main types of lower grade glioma (secondary GBM) [11] (Figure 1.4).

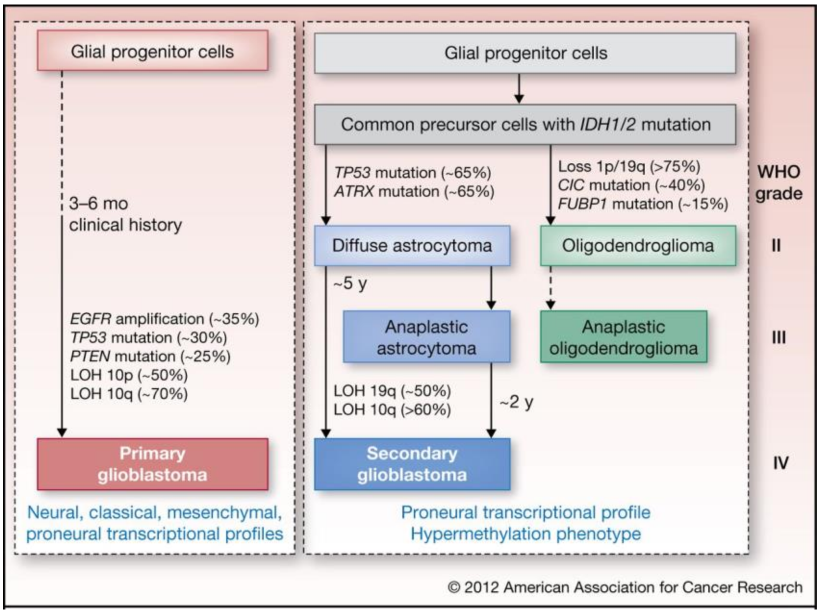
Glial progenitor cells
3–6 mo clinical history
EGFR amplification (~35%)
TP53 mutation (~30%)
PTEN mutation (~25%)
LOH 10p (~50%)
LOH 10q (~70%)
Primary glioblastoma
Neural, classical, mesenchymal, proneural transcriptional profiles
Glial progenitor cells
Common precursor cells with IDH1/2 mutation
TP53 mutation (~65%)
ATRX mutation (~65%)
Loss 1p/19q (>75%)
CIC mutation (~40%)
FUBP1 mutation (~15%)
WHO grade
Diffuse astrocytoma
Oligodendroglioma
II
~5 y
Anaplastic astrocytoma
Anaplastic oligodendroglioma
III
LOH 19q (~50%)
LOH 10q (>60%)
~2 y
Secondary glioblastoma
IV
Proneural transcriptional profile
Hypermethylation phenotype
© 2012 American Association for Cancer Research

**Figure 1.4.** Genetic pathways in the evolution of gliomas. Taken from [12].

### 1.1.2. Genetic pathways in the evolution of gliomas

Cancer development is a multistep process and morphologic changes observed during the process of malignant transformation reflect the sequential acquisition of genetic alterations [13]. It has been suggested that between four and seven independent alterations must occur within a normal somatic cell before a cancerous phenotype results [14]. These genetic alterations, that drive the development and progression of malignancies, include DNA sequence changes, copy number aberrations, chromosomal rearrangements and modification in DNA methylation, and some associated with gliomas are presented in Figure 1.4. Here, only those in the scope of this thesis are described.

*Tumour protein p53 (and retinoblastoma)*

The tumour protein p53 gene (TP53), along with the retinoblastoma protein (RB), is one of the main tumour-suppressor pathways that control cellular responses to potentially oncogenic stimuli. TP53 is a multiple functional transcription factor and a key regulator involved in the control of cell cycle progression, DNA integrity, and the survival of cells exposed to DNA-damaging agents as well as several non-genotoxic stimuli such as hypoxia [15]. TP53 mutations are frequent in low grade gliomas and secondary GBM derived therefrom (>65%), and less frequently found in primary GBM (<35%) [12]. Approximately 60% of mutations are located in the “hotspot codons” 248 and 273, encoding arginine (R248 and R273).

In turn, the INK4A locus encodes a second gene product p16$^{INK4A}$, as well as the alternative reading frame protein p14$^{ARF}$ (p19$^{ARF}$ in mice). Both are inhibitors of cell cycle progression, through RB and p53 pathways, respectively, but they act in two different ways. p16$^{INK4A}$ inhibits cyclin dependent kinases 4 (CDK4) [16] and P14$^{ARF}$ acts by binding directly to mouse double minute 2 (MDM, resulting in stabilization of both TP53 and MDM2 (Figure 1.5). Both p14$^{ARF}$ and MDM2 are upstream of the p53 pathway, such that loss of ARF or amplification of MDM2 leads to downregulation of p53 function. Both p16$^{INK4A}$ and CDK4 are upstream of the RB pathway, such that loss of INK4A or amplification of CDK4 leads to down regulation of the RB pathway. Deletion of INK4A is found in high-grade tumours.

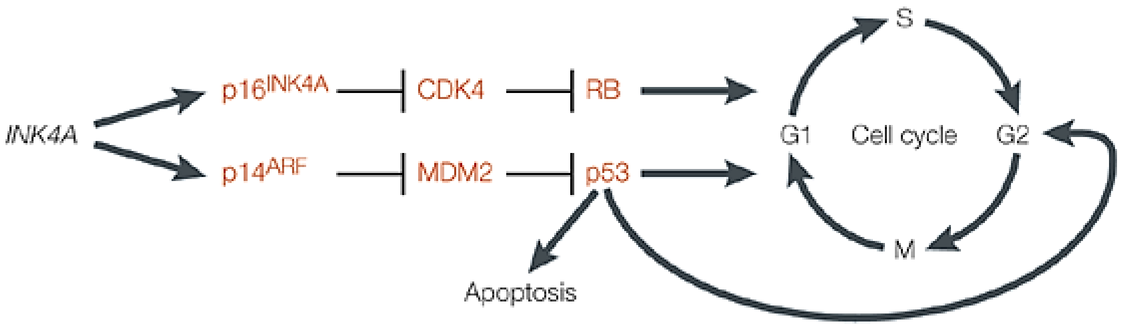

**Figure 1.5.** *INK4A* gene products, p16$^{INK4A}$ and p14$^{ARF}$, control the activity of RB and p53. RB promotes cell-cycle arrest in G1 and regulates entry into the S phase of the cell cycle through its effects on elongation factor 2. p53 has several effects, including causing G1 and G2 arrest and promoting apoptosis. Loss of p53 function also promotes genomic instability. Proteins encoded by genes that are frequently altered in human gliomas are highlighted in red. Taken from [17].

Because INK4A and ARF are transcribed from the same locus, and MDM2 and CDK4 are closely linked, these alterations cause loss of the p53 and RB pathways in a single chromosomal event and may explain why primary GBM progress so rapidly to WHO grade IV. In contrast, secondary GBM arise from lower grades of astrocytoma (WHO grades II and Ill) with sequential loss of p53 and RB signalling pathways.

### *Isocitrate dehydrogenase 1 and 2*

The NADP+-dependent isocitrate dehydrogenases 1 and 2 (IDH1 and IDH2) play functions in cellular metabolism in lipid synthesis, cellular defense against oxidative stress, oxidative respiration, and oxygen-sensing signal transduction. IDHs catalyse the oxidative decarboxylation of isocitrate into α-ketoglutarate (αKG) and reduce NAD(P)$^+$ to NAD(P)H. IDH1 is located in the cytoplasm and peroxisomes, where it participates in lipid metabolism and glucose sensing. IDH2 is located in mitochondria and it is involved in the Krebs cycle. However, the molecular pathogenesis of IDH1 and IDH2 mutations in the development of gliomas is still unclear. It is known that mutated IDH1 or IDH2 have significantly reduced enzymatic activity in catalysis of conversion of isocitrate to αKG and generate ᴅ-2-hydroxyglutarate [18]. Several theories have been proposed, including: increased angiogenesis because of accumulation of hypoxia-inducible factor 1-alpha (HIF-1α) [19] and increased vulnerability to oxidative stress because of depletion of antioxidants [18] (further details in described in Figure 1.6).

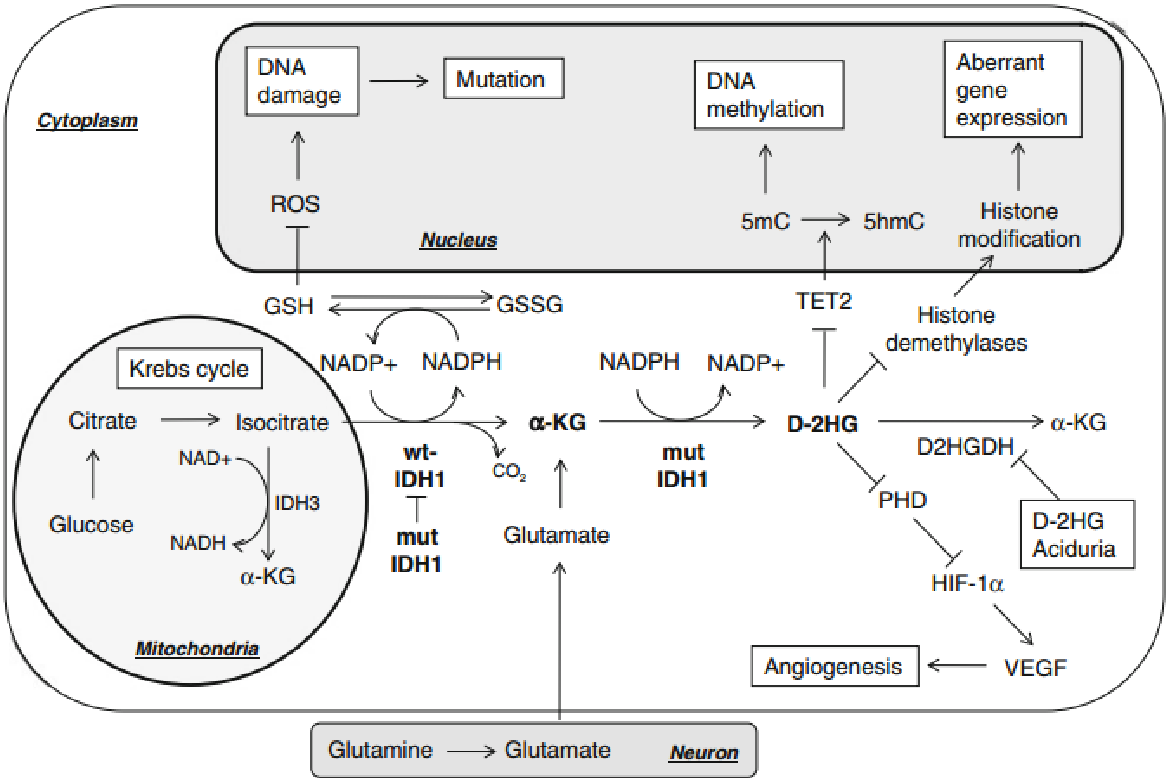
Cytoplasm
DNA damage
Mutation
DNA methylation
Aberrant gene expression
ROS
Nucleus
5mC
5hmC
Histone modification
GSH
GSSG
TET2
Histone demethylases
Krebs cycle
NADP+
NADPH
NADPH
NADP+
Citrate
Isocitrate
α-KG
D-2HG
α-KG
NAD+
IDH3
wt-IDH1
CO₂
mut IDH1
D2HGDH
Glucose
NADH
mut IDH1
Glutamate
PHD
D-2HG Aciduria
α-KG
HIF-1α
Mitochondria
Angiogenesis
VEGF
Glutamine
Glutamate
Neuron

**Figure 1.6.** Schematic diagram of the proposed molecular consequences of IDH1 mutation. Normal IDH1 converts isocitrate into αKG while reducing NAD(P)$^+$ to NAD(P)H. Mutant IDH1 converts αKG into D-2HG. D-2HG may inhibit a variety of dioxygenases including PHD (prolyl hydroxylase), TET2, and histone demethylases, which might trigger either aberrant angiogenesis, DNA methylation, or gene expression. Mutations of IDH1 may also reduce the cellular level of glutathione (GSH) by depleting NAD(P)H and rendering the cells vulnerable to oxidative DNA damage, leading to the development of mutations in other genes. Taken from [20].

IDH1 mutation at R132 and IDH2 at R272 are frequent in diffuse grade II and grade III gliomas and, within GBM, they have been proposed as a marker for GBMs that arise by transformation from lower-grade gliomas (secondary GBM), as they are rarely seen in primary glioblastomas [20-22].

### 1.1.3. Cancer stem cells hypothesis

Cancer arises from a series of the oncogenic and tumour suppressor mutations (see Section 1.1.2) that occurs in few or even a single founder cell, defining cancer as a DNA-associated disease. These cells eventually acquire unlimited and uncontrolled proliferation potential that drive tumour progression forward [14]. Two hypothetical models exist, which can explain this phenomenon.

Traditionally, cancer cells within tumours were portrayed as heterogeneous cell populations due to distinct clonal subpopulations, reflected in histopathological diversity and containing regions of various degrees of differentiation, proliferation, vascularity, inflammation, and/or invasiveness [23], but with all the cells in a tumour having a similar tumourigenic potential to proliferate extensively to form new tumours (Figure 1.7b). In the recent years, however, a hierarchical model has emerged (Figure 1.7c), pointing to the existence of a new dimension of intratumour heterogeneity and a subset of cells within the tumour that have significant proliferation capacity and the ability to generate new tumours, termed cancer stem cells (CSCs), with the remainder of the tumour cells representing terminally differentiated cells [24].

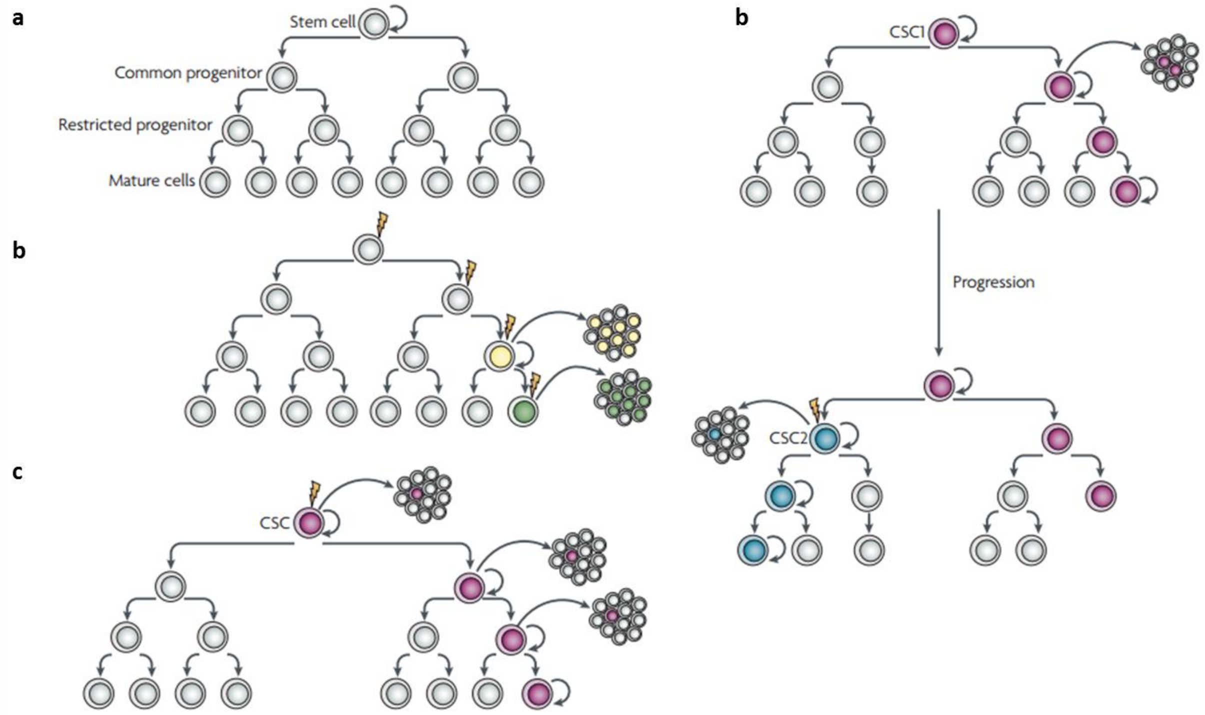

**Figure 1.7.** Two models for tumour heterogeneity and propagation in solid cancer cells. **a)** A normal cellular hierarchy comprising stem cells (at the apex), which progressively generate common and more restricted progenitor cells, ultimately yielding all mature cell types that constitute a particular tissue. **b)** In the clonal evolution model all undifferentiated cells have similar tumourigenic capacity. **c)** In the cancer stem cell (CSC) model, most cancer cells have only limited proliferative potential and only a subset of cancer cells consistently proliferate extensively in clonogenic assays and can form new tumours on transplantation [25, 26]. These cells, called cancer stem cells (CSC) can generate a tumour, based on their self-renewal properties and enormous proliferative potential. **d)** Both models of tumour maintenance may underlie tumourigenesis. Initially, tumour growth will be driven by a specific CSC (CSC1). With tumour progression, another distinct CSC (CSC2) may arise due to clonal evolution of CSC1. This may result from the acquisition of an additional mutation or epigenetic modification. This more aggressive CSC2 becomes dominant and drives tumour formation [27].

CSCs refer to a subset of tumour cells that has the ability to self-renew and generate the diverse cells that comprise the tumour [24, 28, 29]. They are termed cancer stem cells to reflect their stem-like properties and ability to continually sustain tumourigenesis. The origins of CSCs within tumours have not been clarified and may vary from one tumour type to another. In some tumours, normal tissue stem cells may serve as the cells-of-origin that undergo oncogenic transformation to yield CSCs; in others, may arise from restricted progenitors cells or more differentiated cells that have suffered oncogenic transformation and acquiring more stem-like character.

However, the concept of CSCs has significant clinical implications, as CSCs have been shown to be more resistant to chemotherapy and radiotherapy [30, 31].

In the adult mammalian brain, the largest neurogenetic regions are the subventricular zone (SVZ), which is located between the lateral ventricle and the parenchyma of the striatum (Figure 1.8a) and the subgranular zone (SGZ) of the dentate gyrus of the hippocampus (Figure 1.8b). These compartments, called neurogenic niches, contain highly undifferentiated, mitotically active stem and progenitor cells responsible for the whole process of tissue cell homeostasis throughout the life of the organism, yet these populations might function as a source of cells for transformation, giving rise to tumours.

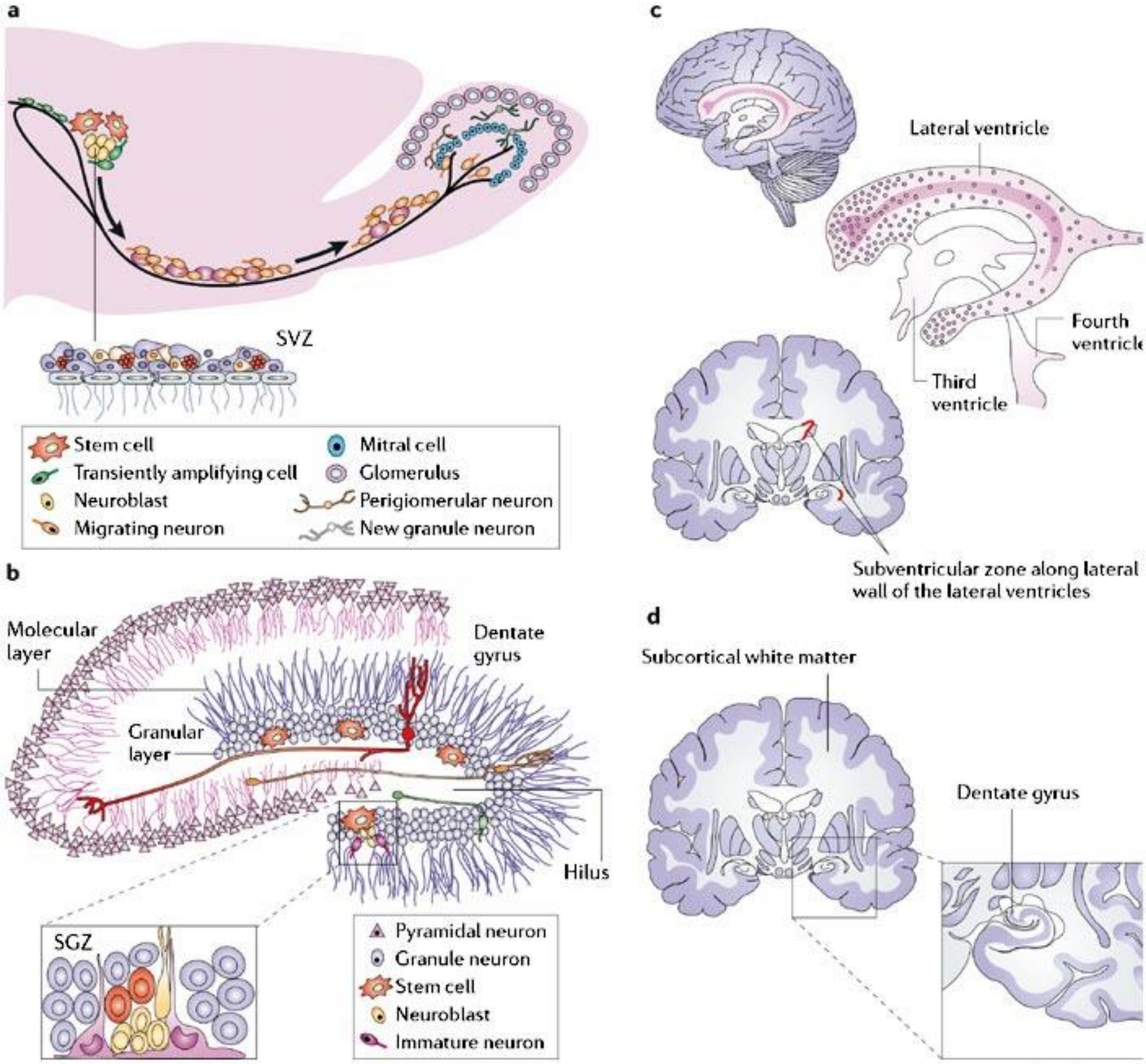
a
SVZ
Stem cell
Transiently amplifying cell
Neuroblast
Migrating neuron
Mitral cell
Glomerulus
Perigiomerular neuron
New granule neuron
b
Molecular layer
Dentate gyrus
Granular layer
Hilus
SGZ
Pyramidal neuron
Granule neuron
Stem cell
Neuroblast
Immature neuron
c
Lateral ventricle
Fourth ventricl
Third ventricle
Subventricular zone along lateral wall of the lateral ventricles
d
Subcortical white matter
Dentate gyrus

**Figure 1.8.** The anatomy and functioning of the subventricular zone and subgranular zone in humans and rodents. **a)** A sagittal section through the lateral ventricle that shows the larger area of adult neurogenesis; the subventricular zone (SVZ). This region lines the lateral ventricles of the forebrain and is comprised of three main cell types. The multipotent, type B astrocytes, that give rise to fast-cycling transiently proliferating precursor cells, called type C precursors and that, in turn, generate mitotically active type A neuroblasts. The type A cells, while dividing, migrate tangentially towards the olfactory bulbs where they integrate as new interneurons. **b)** An additional adult neurogenetic region is found in the subgranular zone (SGZ), which is located within the dentate gyrus of the hippocampus. A cellular hierarchy is similar to that of the SVZ and the type B astrocyte produces the intermediate type D precursor that eventually gives rise to the type G granule neurons. These neurons integrate functionally into the granule cell layer. **c)** In the adult human brain, a population of SVZ astrocytes that is organized as a periventricular ribbon has been identified as comprising neural stem cells. In contrast to the rodent SVZ, no signs of tangential neuronal chain migration were detected from the corresponding human area. **d)** The germinal zone of the adult human hippocampus is located within the dentate gyrus. Neurogenesis in this region has been demonstrated to take place in adult humans (taken from [32]).

Regarding the SVZ, various cells that are responsible for the generation of new neuronal or glial cells ordered progressively according to their differentiation capacity are shown in Figure 1.9b and they are:

- **Neural stem cells of type B**: multipotent, astrocyte-like adult neural stem cells with the morphology, ultrastructure and markers of astrocytes. They divide slowly (28 days) and possess ability to divide throughout the lifetime of the organism by symmetric divisions (both daughter cells are identical) and to generate transiently dividing progenitor cells through asymmetric cell divisions (one daughter cell of type B, other - progenitor cell, called type C cell).
- **Neural progenitor cells of type C**: These cells retain multipotency and have the property to divide rapidly (12 hours), although their ability to divide is limited. By asymmetric divisions give rise to maturer transiently dividing progenitors, i.e. migrating neuroblasts (type A cells).
- **Migrating neuroblasts or type A**: These cells migrate in bundles through the rostral extension of the SVZ into the olfactory bulb, where they integrate as new interneurons in the cortical layers (Figure 1.8a). At their destination maturation into neurons, glia or oligodendrocytes occurs.

Various studies provide compelling evidence that mitotically active precursors are the most likely source of many brain tumours; however, there is still a lot of controversy about the nature of the neural cell type that is targeted by transformation and results in subsequent tumourigenesis. Oncogenic mutations are rare, stochastic events, that are thought to accumulate over a considerable period of time and transiently dividing progenitors exist only briefly before differentiating into cells that are often quiescent or die because of normal turnover or damage. Therefore, mutagenic events might not have the opportunity to accumulate in transiently dividing progenitors and their terminally differentiated progeny. Conversely, somatic stem cells are perennial cells with a significant proliferation and self-renewal potential that lasts the lifetime, making them a preferential target for tumourigenesis.

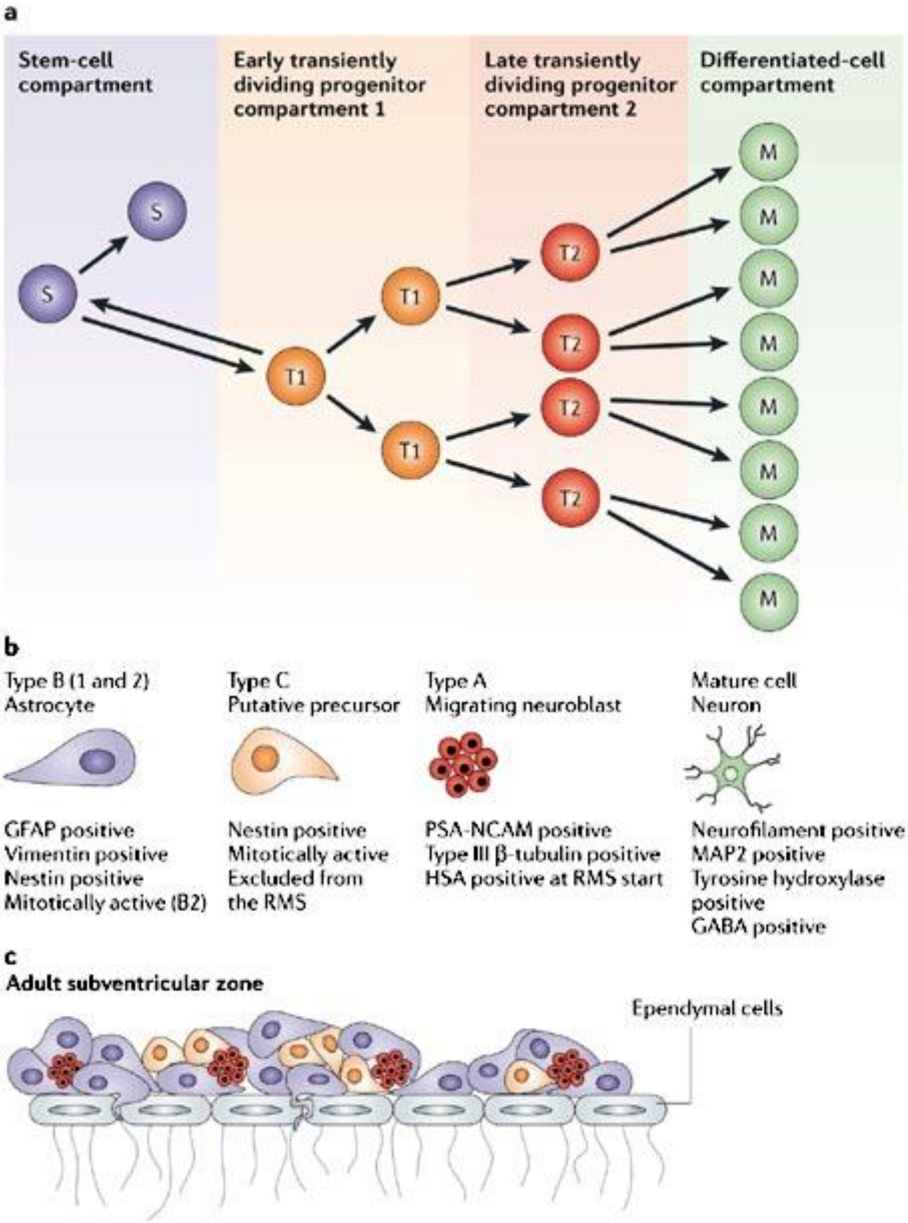
a
Stem-cell compartment
Early transiently dividing progenitor compartment 1
Late transiently dividing progenitor compartment 2
Differentiated-cell compartment
S
S
T1
T1
T1
T2
T2
T2
T2
M
M
M
M
M
M
M
M
b
Type B (1 and 2)
Astrocyte
Type C
Putative precursor
Type A
Migrating neuroblast
Mature cell
Neuron
GFAP positive
Vimentin positive
Nestin positive
Mitotically active (B2)
Nestin positive
Mitotically active
Excluded from the RMS
PSA-NCAM positive
Type III β-tubulin positive
HSA positive at RMS start
Neurofilament positive
MAP2 positive
Tyrosine hydroxylase positive
GABA positive
c
Adult subventricular zone
Ependymal cells

**Figure 1.9.** Hierarchical organization of the functional compartments in renewing tissues. **a)** The stem-cell compartment (purple), early transiently dividing progenitor compartment (orange), late transiently dividing progenitor compartment (red) and differentiated-cell compartment (green) are schematically described. Cells in the stem-cell and transiently dividing progenitor compartments could be the target of the onco-transformation that leads to the formation of tumour stem cells. **b)** The neural precursors that make up similar functional compartments in the neurogenetic regions of the adult brain and that might be the source of brain tumour stem cells. **c)** The structure of the subventricular zone, showing how these precursors fit and are organized in the germinal neuroepithelium of the largest neurogenetic region of the adult brain. GABA, γ-aminobutyric acid; GFAP, glial fibrillary acid protein; HSA, heat-stable antigen; MAP2, microtubule-associated protein 2; NCAM1, neural cell adhesion molecule 1; PSA, polysialic acid; RMS, rostral migratory stream (taken from [32]).

### 1.1.4. Detection

Detection of brain tumours does not take place until evident clinical symptoms occur in affected patients, which is usually a late event, because of the absence of pain receptors in the brain, allowing tumours to grow ‘silently’. Persistent headache, nausea, vomiting, seizures, visual disturbances, memory loss and altered mental functions, e.g. personality changes, respiratory arrest, elliptic fit or even an episode of coma, are common signs that can manifest once the intracranial pressure rises due to the mass effect of the lesion [33]. Often more than one symptom is present, and these hint clinicians to evaluation the patient for a brain tumour. Diagnosis begins with appropriate brain imaging. Techniques such as Computed Tomography (CT), Positron Emission Tomography (PET), Magnetic Resonance Imaging (MRI) and Magnetic Resonance Spectroscopy (MRS) are used to perform the initial assessment and localization of the tumour, as well as to perform the follow-up of treatment and determine tumour progression. Initial diagnosis is usually followed by histopathological analysis of the tumour biopsy, which is the gold standard method to confirm the diagnosis, tumour grading and classification (as per Section 1.1.1).

### 1.1.5. Therapy

#### Surgical resection

The standard therapy for newly diagnosed brain tumours is surgical resection. The primary objective of the surgery is to remove as much tumour mass as possible to achieve a better overall survival [34, 35] with complete removal being the ideal outcome without compromising the neurological functions of the patient. This may be the best strategy and provide a cure in some cancer cases, for example meningiomas, which are usually well-circumscribed lesions, but may be insufficient or impossible in others, due to the extension and/or localization or the infiltrative nature in case of high grade gliomas. Current advances in neurosurgery, such as minimally invasive techniques [36], intraoperative brain mapping [37], intraoperative MRI [38, 39] and labelling of tumour cells with 5-aminolevulinic acid that causes them to fluoresce for intraoperative identification of tissue [40] , have led to an improved safety and an increased extent of resection in glioma patients. However, complete surgical resection of high grade gliomas is impossible, because of their infiltrative nature. As a result, surgery must be followed by adjuvant radiotherapy, chemotherapy, or both.

### Radiotherapy

Radiotherapy is an important tool in the treatment and improvement of prognosis and survival of patients. The main aim of radiation therapy is to kill tumour cells, while leaving normal brain tissue unharmed, so that the vital functions and the patient's quality of life is not affected.

Radiation therapy involves administration of ionizing radiation (photon or a charged particle) to the location of the tumour from an external source (the most common approach), from a source placed inside the body (brachytherapy), or through the use of radioactive drugs (systemic). Radiation directly or indirectly ionizes the atoms which make up the DNA chain (Figure 1.10), blocking their ability to divide and proliferate further and thus resulting in cell death.

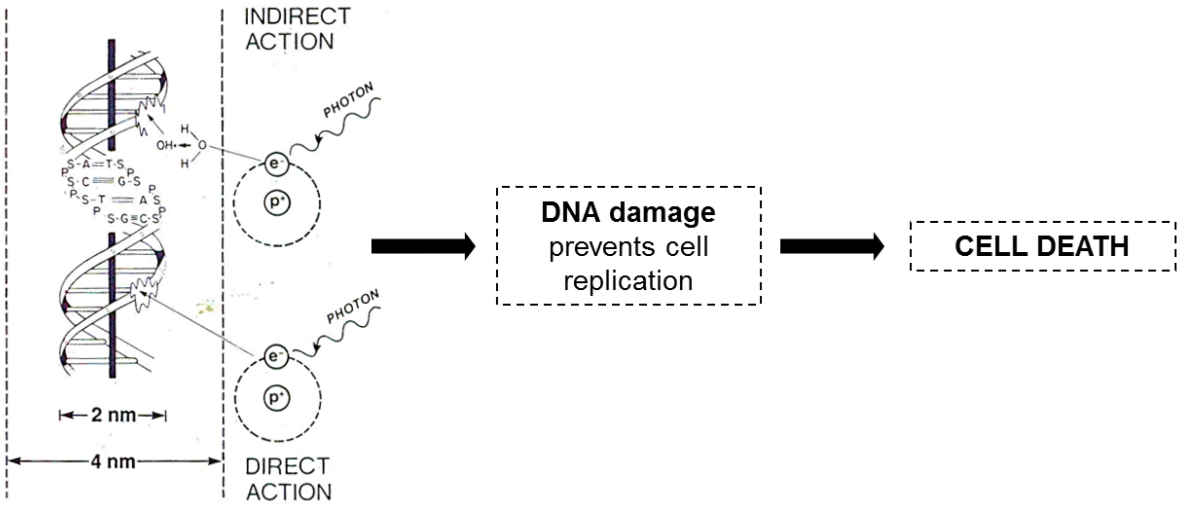

**Figure 1.10.** Direct and indirect action of radiation therapy. DNA damage is caused by one of two types of energy, photon or charged particle. This damage is either direct or indirect ionization of the atoms the DNA chain. Indirect ionization happens as a result of the ionization of water, forming free radicals, notably hydroxyl radicals, which then damage the DNA strand, preventing cell replication and resulting in cell death.

Although radiation damages both normal cells as well as tumours cells, normal cells usually can repair themselves at a faster rate and retain its normal function status than the tumour cells. Tumour cells in general are not as efficient as normal cells in repairing the damage caused by radiation treatment resulting in differential cancer cell killing [41].

Radiotherapy may be used following or, in some cases, in place of resection of the tumour and it is the most common treatment for secondary brain tumours. Radiation with an external beam irradiation has been shown to be effective in the treatment of newly diagnosed malignant gliomas increasing the median survival of the treated patients from 5 months to 9 months with adjuvant RT compared to surgery alone [42, 43]. Advances in stereotactic radiosurgery and computerized calculations allow focusing the radiation at the site of the tumour while minimizing the radiation dose to the surrounding brain and prove useful especially in cases of metastasis [44]. Regarding high-grade gliomas, radiotherapy dose needed to halt the progression of disease carries risks of harming the normal tissue. Therefore, it is advisable to complement MRI diagnosis with other non-invasive techniques, such as MRI, MRS, MRSI, perfusion or diffusion MRI, in order to adequately discriminate between healthy and tumoural tissue and develop the most appropriate therapy protocol for a given case to improve the prognosis and increase survival [45, 46]. Perfusion MRI is a potential technique for predicting survival in patients with glioma. Data obtained can be used to calculate the cerebral blood volume, which is associated with microvasculature of the tumour, and to distinguish between residual and recurring tumour, and necrosis induced by radiotherapy. The MRI diffusion technique allows mapping of water diffusion patterns and therefore reveals microscopic details about tissue architecture, either normal or in a diseased state, and the proportion of intra and extra cellular space, allowing approximating tumour cell content. The combination of these techniques has proven to effectively predict survival of patients with gliomas and detect response to therapy [47].

However, gliomas are heterogeneous tissues and some cells seem to be resistant to radiotherapy [48, 49], implicating that even after application of the clinically best tolerated maximum dose tumours, will not be eradicated completely.

### Chemotherapy

The use of therapeutic agents poses a major challenge for neuro-oncologists, because CNS tumours represent a variety of growth patterns and response to therapy, making it difficult to find a specific therapeutic target. The main objective of these agents is not only to cure, but also to stabilize the disease, controlling tumour growth and improving the quality of patients' life. However, the fundamental problem with systemic chemotherapy for brain tumours is reaching an effective dose within the tumour. The unique physiology of tumour tissue and mechanisms at the blood-tumour interface, i.e. increased intratumour colloid (oncotic) pressure, bad perfusion/tortuosity, collapsed vessels, etc., make it difficult for blood-borne drugs to reach the tumour's inner core.

Standard chemotherapies are based mainly on alkylating agents, such as temozolomide (TMZ), which is considered the most effective drug for the treatment of glioblastomas. This group of medications is also one of the few with the ability to penetrate the blood–brain barrier (BBB), achieving cytotoxic concentrations in cerebrospinal fluid and brain parenchyma, which may be of interest with tumours with yet intact BBB. Following oral absorption, TMZ in aqueous solution is spontaneously hydrolysed to its active form, methyl-triazeno imidazole-carboxamide (MTIC). MTIC is rapidly converted to the inactive 5-aminoimidazole-4-carboxamide (AIC) and to the electrophilic alkylating methyldiazonium cation that may transfer a methyl group to DNA. The DNA-methyl adducts are responsible for cytotoxicity. The N7 of guanine and the N3 of adenine represent the majority of DNA-methyl adducts. Alkylation of the O-6 position of guanine accounts for only about 5% of DNA adducts, but is the primary responsible for the cytotoxic effects of TMZ. The O6-methyl-guanine (O6-meG) lesion leads to DNA double strand breaks and subsequent cell death via apoptosis and/or autophagy.

MGMT (O6-meG-DNA methyltransferase) repairs the O6-meG lesion and it is thought to contribute to resistance to TMZ. The repair occurs by transferring the methyl group from the adduct to its own cysteine residue. Methylated MGMT is then degraded. Thus, MGMT is considered a 'suicide' repair protein, and new MGMT must be synthesized in order to continue DNA repair. The resistance to alkylating agents is mainly due to overexpression of the MGMT protein, and it is a major, currently unresolved problem with TMZ therapy. Therefore, mechanisms to deplete MGMT in tumour cells are being developed in an attempt to increase sensitivity to TMZ (Figure 1.11).

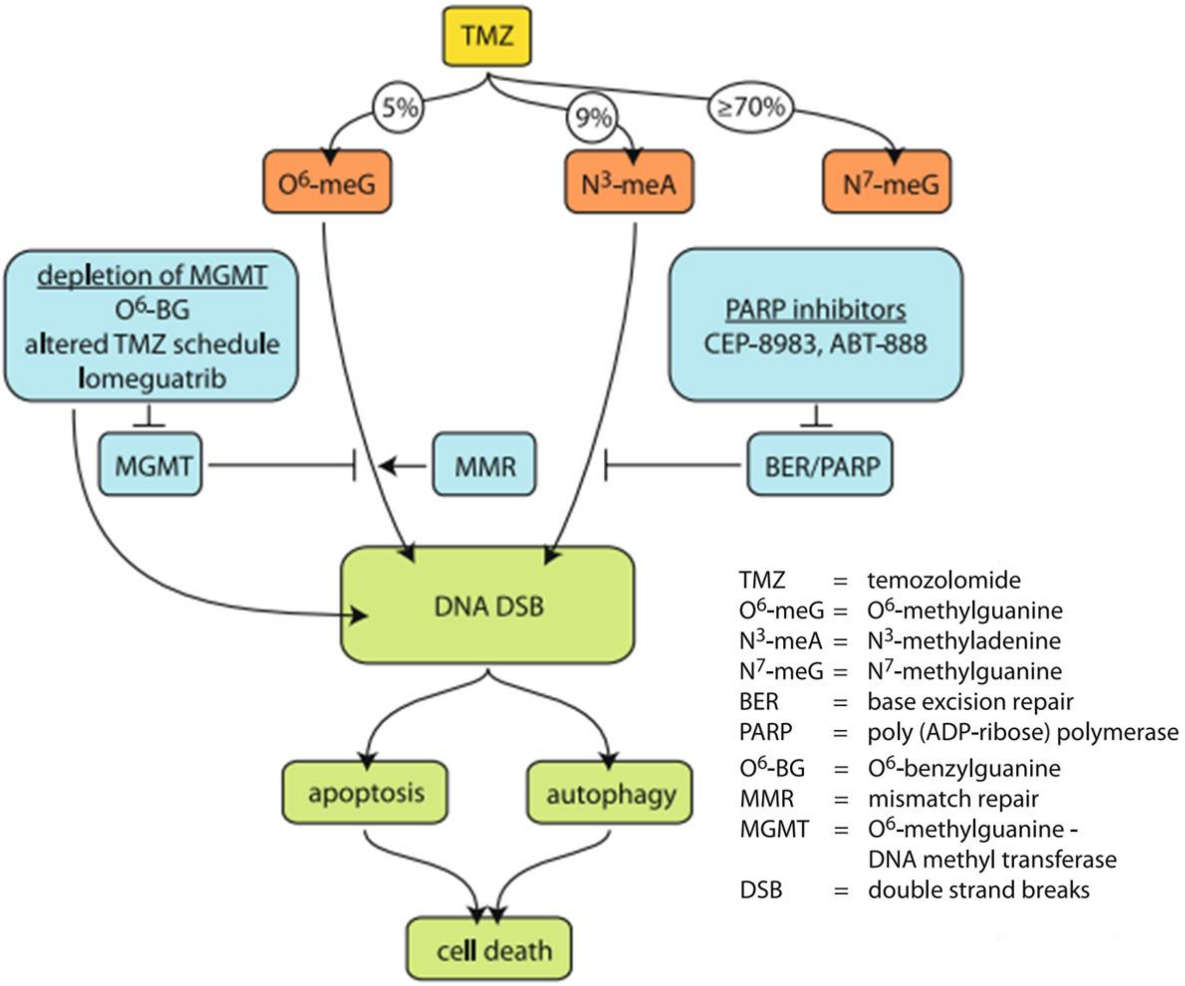
TMZ
5%
9%
≥70%
O6-meG
N3-meA
N7-meG
depletion of MGMT
O6-BG
altered TMZ schedule
lomeguatrib
PARP inhibitors
CEP-8983, ABT-888
MGMT
MMR
BER/PARP
DNA DSB
apoptosis
autophagy
cell death
TMZ = temozolomide
O6-meG = O6-methylguanine
N3-meA = N3-methyladenine
N7-meG = N7-methylguanine
BER = base excision repair
PARP = poly (ADP-ribose) polymerase
O6-BG = O6-benzylguanine
MMR = mismatch repair
MGMT = O6-methylguanine - DNA methyl transferase
DSB = double strand breaks

**Figure 1.11.** Temozolomide: site of action and targets for regulation with other agents. O$^6$-meG DNA adducts account for only 5% of TMZ-induced DNA lesions, but they are responsible for the cytotoxic effect. MGMT repairs the lesions, resulting in resistance to TMZ. When MGMT is depleted (such as by O$^6$-BG or varied dosing schedules) or suppressed by methylation of the gene promoter, cytotoxicity of TMZ is enhanced. MMR recognizes the abnormal base pairs containing O$^6$-meG, eventually leading to DNA DSB and cell death. N$^3$-meA adducts are also cytotoxic, but are usually repaired by the BER system. Pharmacologic inhibition of PARP inhibits the functioning of the base excision repair system, potentially enhancing TMZ cytotoxicity (figure taken from [50]).

TMZ improves outcome in treated patients when administrated on their own or in combination with irradiation [51] or with other agents like procarbazine [52] or lomustine [53]. In preclinical studies in animal models, TMZ is usually dissolved in dimethyl sulfoxide (DMSO), before being administered intragastrically [54-56], whereas for clinical patients, it is available in capsules pharmaceutical form.

Besides TMZ therapy, there are other therapeutic strategies that target intracellular signaling pathways determining the key functions of tumour biology, such as proliferation and apoptosis or angiogenesis. Two main pathways that are targeted are the vascular endothelial growth factor (VEGF) or signalling of the endothelial growth factor (EGF) and its receptor (EGFR), which is a promoter of numerous effects at cell proliferation, invasion and angiogenesis levels. Among the drugs, developed to act on these signalling pathways, we find Bevacizumab for VEGR and Erlotinib or Gefitinib for EGF/EGFR [57]. Bevacizumab is a humanized VEGF monoclonal antibody that targets angiogenesis and is under study in first-line glioblastoma treatment, added to chemoradiotherapy with temozolomide. Results demonstrated an increase in progression-free survival, but not in overall survival with the addition of Bevacizumab [58, 59].

## 1.2. Preclinical models of human glioma

Due to evident ethical restrictions, it is not possible to perform repeated exams in patients afflicted with a brain tumour or to repeatedly collect biopsy samples at given time points of tumour growth / progression for research purposes, especially if surgical resection or chemotherapy are feasible. For this reason, animal models of human brain tumours have been developed to facilitate the studies of tumour characterisation, progression and response to therapy.

### 1.2.1. GL261 murine model

Currently, many of the advances in the characterization of brain tumours, as well as improved diagnosis and treatment are being carried out in animal models that develop disease in a very similar way to humans. For GBMs, the most widely used preclinical murine models are those induced by stereotactic injection of glioma cells into the brain parenchyma, either mouse cell lines (allograft models) or samples obtained from human tumour biopsies (xenograft models). The GL261 mouse glioma line is one of the most widely used to study GBM and is usually inoculated into

C57BL/6 strain, resulting in tumours with invasive and infiltrative characteristics similar to those of human GBMs [60]. These tumours grow exponentially for about four weeks, killing of animals from mass effect at the end of this period. Furthermore, studies that correlate the findings on tumour angiogenesis obtained by MRI techniques (relative cerebral blood volume measurements) and histopathology (markers of vascular density) in this model have shown that MRI is a noninvasive technique able to characterize the evolution of this model and therefore applicable in studies to improve diagnosis and response to therapy [61]. Studies on gene alterations, immunological characteristics and radiation sensitivity demonstrate the utility of the GL261 model to investigate the anti-tumour effect of various treatment strategies: immunotherapy, gene therapy, chemotherapy, radiotherapy or antiangiogenic therapy [60].

On the other hand, transplantable models, despite having the advantage of rapid tumour development and reproducibility, do no fully resemble the characteristics of angiogenesis and invasiveness of human brain tumours. For this reason, genetically engineered models have been developed.

### 1.2.2. Genetically engineered mice (GEM) models

Transgenic models in which the tumours arise spontaneously throughout the life of animals, are known to more precisely emulate the evolution of the disease in humans [62, 63]. These models are based on transgene expression or silencing knock-out of certain genes involved in the development of primary human brain tumours, which are capable of reproducing their patterns of progression [64].

#### RasB8 mice model

GFAP-$V^{12}$ HA-*ras* (referred to as RasB8 mice) is a genetically engineered germ line astrocytoma mouse model. RasB8 is characterised by the presence of the $V^{12}$ HA-*ras* transgene, which expression is regulated by the astrocytes-specific glial fibrillary acid protein (GFAP) promoter [65]. RasB8 mice are obtained by the transfection technique of a retrovirus, which carries the gene of interest and a selection marker, into cultured mouse embryonic stem cells. After positive selection, cells are transferred to a pseudo-pregnant female mouse in order to create chimeric embryos. The chimeric mice are then cross-bred with normal mice and those which incorporated the transgene in their germ-line generate transgenic offspring [66]. The overexpression of $V^{12}$ HA-*ras* gene, although not a primary molecular aberration of human astrocytoma, initiates the sequence of genetic events that lead to the development of astrocytoma in mice [66]. RasB8 mice exhibit pathological as well as molecular progression features similar to human astrocytoma [65, 67]. Namely, mice expressing this transgene develop astrocytomas with mitotic, polymorphic and infiltrative astrocytes, and are also associated with increased vascularity and necrosis [65]. Moreover, several genetic alterations associated with human low and high grade astrocytoma are noted in this mouse model, including gain-of-function alterations evidenced by increased expression of EGFR and vascular endothelial growth factor receptor (VEGFR), as well as loss-of-function mutations, including changes in TP53 expression or TP53 mutations [67].

#### S100β-v-erbB / INK4A/ARF(+/-) mice model

S100β-v-erbB is a genetically engineered mice model of oligodendroglioma, expressing v-erbB, a transforming homologue of the EGFR, under the control of the S100 promoter. Because S100βis expressed in central nervous system stem cells, the S100β-v-erbB transgene recapitulates high-level expression of EGFR during the pathogenesis of glioma and causes development of oligodendroglioma with pathognomonic histology and pathology observed in human oligodendroglioma [63]. Tumours are highly infiltrative, invaded along white matter tracts, and developed branching thin-walled capillaries, reflecting histopathologic features characteristic of human oligodendroglioma. Aditionally, transgenic animals heterozygous for INK4A/ARF (corresponding to the deletion of two tumour suppressors affecting RB and p53 pathways that are found to be mutated in human gliomas, as described in Section 1.1.2) or p53 develop high-grade tumours.

## 1.3. Nuclear Magnetic Resonance (NMR)

Nuclear Magnetic Resonance, better known in clinical practice as Magnetic Resonance (MR), is a valuable research tool that has been used for past decades to non-invasively investigate human tumours. It was since 1970's, when Paul Lauterbur (Nobel Prize 2003) generated the first NMR images and Raymond Damadian invented the first whole-body MR scanner and performed a full body scan of a human being to "diagnose" cancer. Since then tremendous progress has been made in both technological improvements of the method itself and its applications, including MRI, MRS and MRSI, which provide *in vivo* medical images and metabolomics information about tissues aiding everyday clinical diagnostics.

### 1.3.1. Overview of basic MR principles

*Physical properties of nucleus*

The NMR phenomenon is based on the physical properties of atoms and was first described by Bloch and Purcell in 1946. Some atoms have the property of absorbing radiofrequency (RF) energy and re-emitting it during the transition to their original state when they are placed in a magnetic field. This property is determined by another quantum property, present within nuclei of atoms with an odd number of protons or neutrons, and called the nuclear spin. These nuclei are said to be MR active. In the MR biomedical research the most prominent are proton ($^{1}H$), carbon ($^{13}C$) and phosphorus ($^{31}P$) due to their spin $I = ½$ and natural abundance. Since nuclei are charged particles in motion, those with non-zero spin have a magnetic moment ($\vec{\mu}$) that has a magnitude and direction specific for each type of nucleus (Figure 1.12).

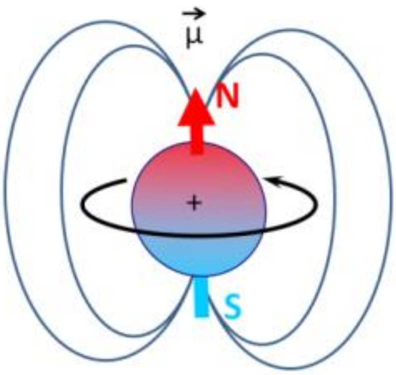

**Figure 1.12.** Diagram representing a magnetic moment of a nucleus (caused by the rotation of the nucleus with a nuclear spin different than zero) resembling a magnet with north (N) and south (S) poles. Blue and red arrow shows the magnetic field direction. Black circular arrow represents the rotation of the $\vec{\mu}$ around its axis. Circular blue lines represent magnetic field.

In the absence of an external magnetic field ($B_0$), the magnetic moments are randomly oriented and the net magnetization is zero (Figure 1.13). When an external field $B_0$ is applied they orient parallel or anti-parallel to the applied field, in the case of nuclei with spin ½. In this situation, the $\vec{\mu}$ of the nuclei will precess along an axis parallel to the direction of the $B_0$ field, with frequency $\nu_0$, called Larmor frequency (Figure 1.14). In a sample containing a large number of nuclei, the more populated state is the lower energy orientation parallel to the $B_0$, as oppose to the upper energy anti-parallel state.

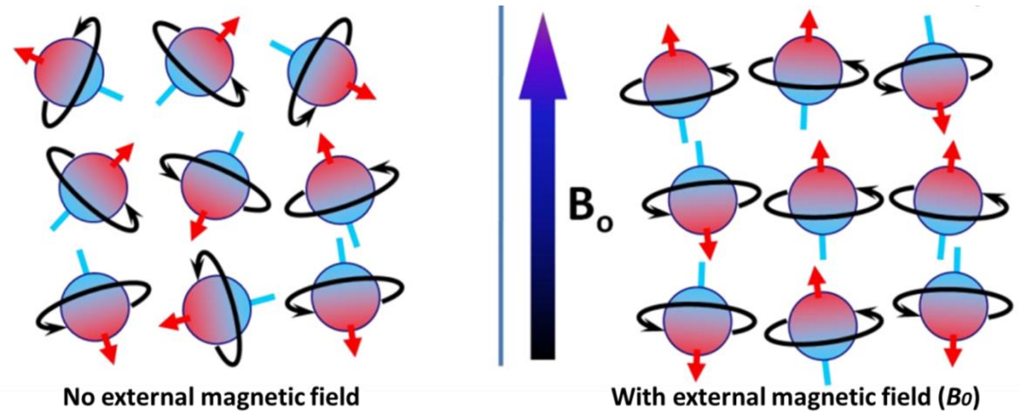
$B_o$
No external magnetic field
With external magnetic field ($Bo$)

**Figure 1.13.** Effect of an external magnetic field ($B_0$) on the spins. Due to Brownian motion the population of nuclei is oriented in all possible directions (left). Applying a magnetic field $B_0$ nuclei align in two different directions: parallel or anti-parallel to the field (right).

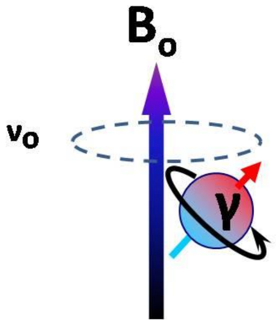

**Figure 1.14.** Graphical representation of the *Larmor frequency*. The $\vec{\mu}$ of nuclei in the sample precess around the magnetic field ($B_0$) with precession frequency ($v_0$) dependent of the gyromagnetic constant (γ) and the value of $B_0$.

The resonance phenomenon is based on the ability of nuclei to transition between energy states. If an amount of energy equal to the difference in energies (ΔE) of the two nuclear spin orientations is applied to the nucleus (or more likely, group of nuclei), transition between energy levels is induced. This is obtained by applying an additional magnetic field ($B_1$) in the electromagnetic RF range as short pulses in the plane perpendicular to $B_0$. The absorption of energy by the nuclear spins causes transitions, usually from lower to higher energy state.

The energy required to induce flipping and obtain an NMR signal is just the energy difference between the two nuclear orientations and is shown in Figure 1.15b and Equation 1 to depend on the strength of the magnetic field *Bo* in which the nucleus is placed:

$$\Delta E = \frac{\gamma h B_0}{2\pi}, \qquad \text{Eq.1}$$

where h is Planck's constant and $\gamma$ is the gyromagnetic constant of the nucleus (varies from one nuclear isotope to another). The Bohr condition ($\Delta E = hv_0$) enables the frequency $v_0$ of the nuclear transition to be written as:

$$v_0 = \frac{\gamma h B_0}{2\pi}, \qquad \text{Eq.2}$$

Equation 2 is often referred to as the *Larmor equation*, and $\omega_0 = 2\pi v_0$ is the angular *Larmor resonance velocity*, while $v_0$ is the resonance frequency. The *gyromagnetic ratio γ* is a constant for any particular type of nucleus and is directly proportional to the strength of the tiny nuclear magnet.

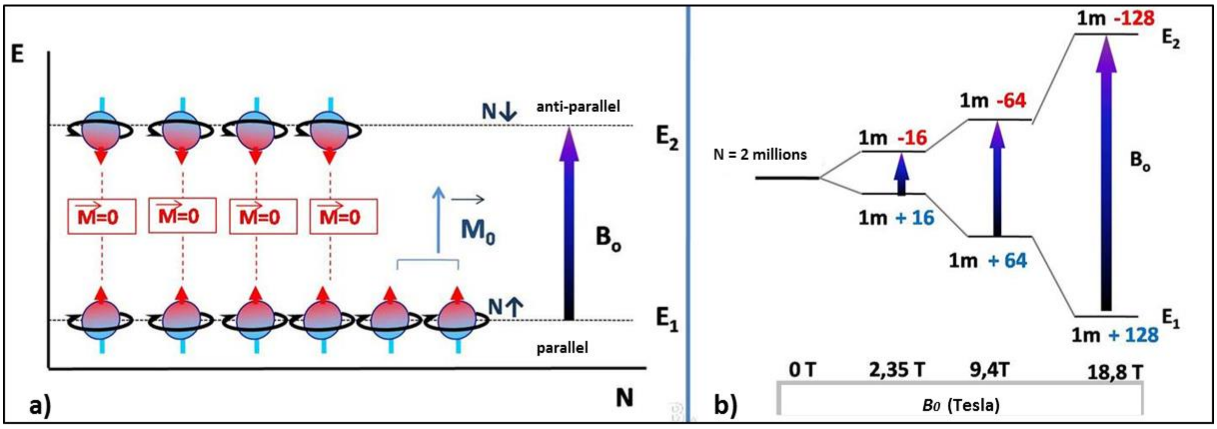

**Figure 1.15.** Graphical representation of the spins in thermal equilibrium in the presence of an external magnetic field $B_0$. **a)** Distribution of the spins between low energy level (E1) and high energy (E2) levels, which is in favor of low energy level resulting at net magnetization $\overrightarrow{M_0}$ parallel to the external magnetic field ($B_0$). **b)** Dependence on magnetic field strength $B_o$ of the separation of nuclear energy levels (ΔE) for spin I= 1/2 and the relative populations of the energy levels assuming one has approximately two million protons in the sample. N↑: cores with parallel orientation, N↓: nuclei with antiparallel orientation, m: million, T: Tesla.

Applying $B_1$ in the direction of the xy plane, the net magnetization of the nuclei changes by an angle θ (flip angle), changing the orientation of the net magnetization of the nuclei in thermal equilibrium ($\overrightarrow{M_0}$ = Mz) to the transverse plane (Mxy) (Figure 1.16). When the RF ceases, the magnetization recovers its initial orientation emitting the energy absorbed during the transition through relaxation processes, described later in this section, while an electrical signal is picked up by the receiving coil. Namely, the transverse component of the magnetization of the sample (Mxy) revolves around $B_0$ with the Larmor frequency and induces a small alternating current in a detection coil surrounding the sample. Thus, the detected signal is obtained as an attenuated sinusoid, called free induction decay (FID), and must be processed mathematically by Fourier Transform (TF), which untangles all the different frequency components of the FID, representing them in the frequency domain rather than in the time domain. Then, an NMR spectrum (Figure 1.17) is obtained. NMR studies detect a current intensity proportional to the initial magnetization of the sample signal. This signal is quite low considering the small differences between low and high energy populations, and an amplification is needed before processing.

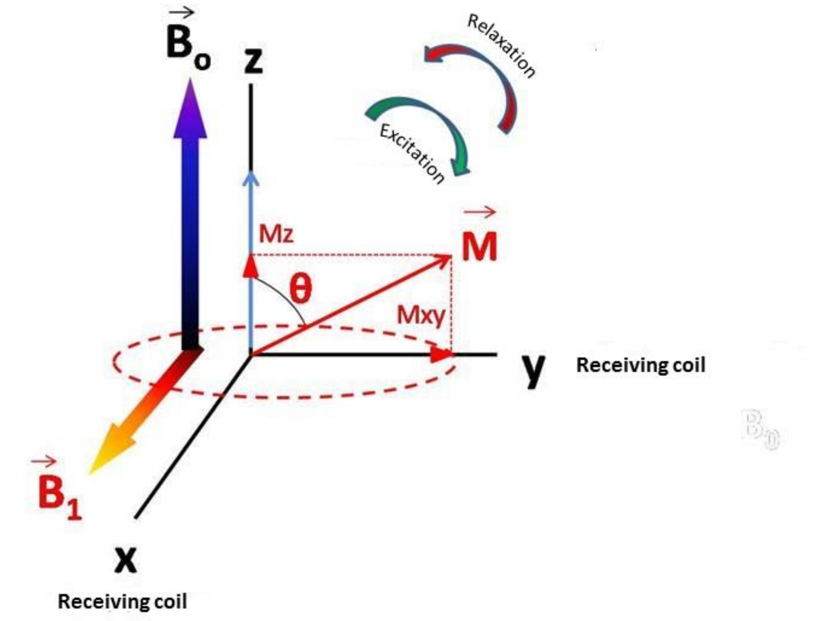

**Figure 1.16.** Representation of the perturbation of the macroscopic magnetization of a sample in a coordinate system (rotating at the resonance frequency). Applying an additional magnetic field ($B_1$) perpendicular to $B_0$ (excitation) causes net magnetization $\vec{M}$ to move by an angle θ, flipping it into the *Mxy* (transverse) plane. When $B_1$ is removed, the system returns to its initial thermal equilibrium (relaxation).The *Mxy* component will be captured by the receiver coils as alternating electrical current signal.

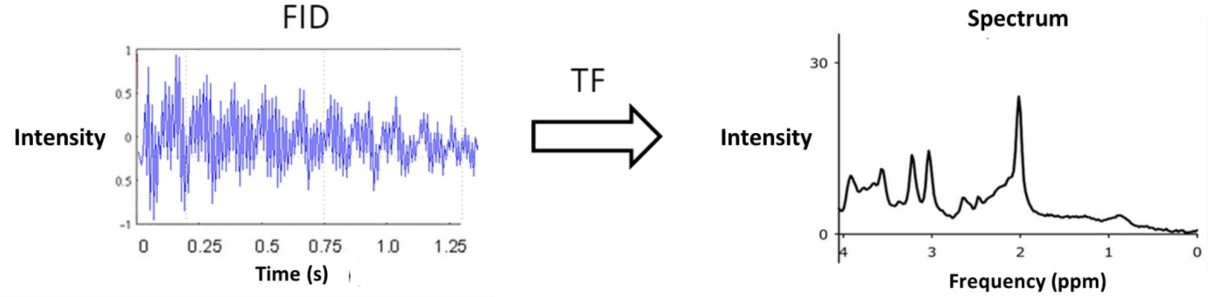

Figure 1.17. FID transformation (left, time domain) recorded in an NMR experiment, to a spectrum (frequency domain), after application of the TF.

### Relaxation times

The processes that determine the return to equilibrium of both longitudinal and transverse magnetisation are called "spin-lattice" and "spin-spin" interactions, respectively. These two processes cause T1 relaxation and T2 relaxation respectively, and are exponential in nature with time constants T1 and T2. These two time constants are important for tissue and spectral characterisation in MRI and MRS.

*T1 relaxation time*

T1 relaxation describes the transfer of energy from the spin system to its surroundings, otherwise known as the lattice. The energy transfer process causes the longitudinal magnetisation, *Mz* to gradually recover exponentially towards its initial equilibrium value (Figure 1.18). Thus T1 relaxation is also known as longitudinal relaxation or T1 recovery. The time it takes to recover 63% of the initial magnetization is called T1 relaxation constant.

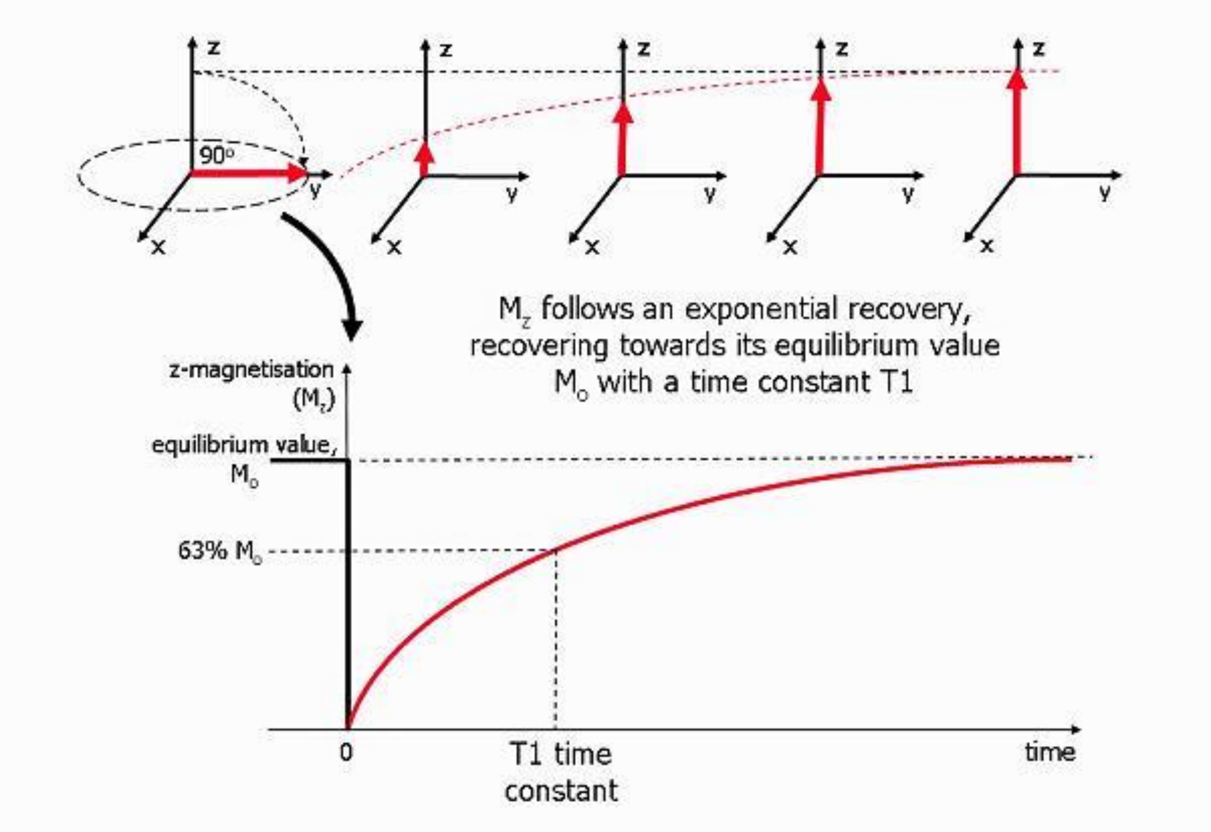
z
90°
y
x
$M_z$ follows an exponential recovery, recovering towards its equilibrium value $M_0$ with a time constant T1
z-magnetisation ($M_z$)
equilibrium value, $M_0$
63% $M_0$
0
T1 time constant
time

**Figure 1.18.** T1 relaxation process after a 90° RF pulse is applied at equilibrium. The longitudinal magnetisation $M_z$ is reduced to zero, but then recovers gradually back to its equilibrium value if no further RF pulses are applied. The recovery of $M_z$ is an exponential process with a time constant T1. This is the time at which the magnetization has recovered to 63% of its value at equilibrium. Taken from [68].

The T1 rate constant depends on the strength of the applied magnetic field $B_0$, tissue composition, structure, molecular motion and surroundings. Protons in different tissues and metabolites therefore have different T1 recovery rates. For instance, at 1.5 T, the T1 relaxation time of the water resonance of grey matter tissue is about 1138 ms whereas that of white matter tissue is about 649 ms.

*T2 relaxation time*

T2 (transverse) relaxation describes the loss in phase coherence between neighbouring spins with time. Each spin experiences the external magnetic field, $B_0$. However, one spin affects the other by slightly altering the magnetic field experienced by the second spin. The precession rate of the second spin will change slightly, causing an increase or decrease in its phase coherence relative to the first spin. Thus, these dipole-dipole interactions cause the precession rates of the individual spins to vary slightly. The result is that they lose phase coherence (i.e. they no longer precess at the same rate as before) and the resultant transverse magnetisation *Mxy* decays gradually to zero as shown in Figure 1.19. The time it takes the magnetization to decay to 37% of the initial phase coherence (*Mxy*) is called T2 relaxation constant. However, the actual decay of global coherence is usually faster due local static variations (inhomogeneities) in the applied magnetic field, $B_o$. Therefore, the actual time the system takes to lose 63% of the initial magnetization is called T2* relaxation constant (Figure 1.19).

This type of relaxation involves energy exchange among only the spins and so is called spin-spin relaxation. Spin-spin relaxation time depends on the molecular environment of the spins, and so T2 for the resonance of interest vary between tissues. Free molecules (i.e. spins) in fluids influence the phase of each other less than if they were close to one another as in solids. Thus, spins in fluids take longer to dephase than those in environments with restricted motion. Fluids therefore mostly have longer T2 relaxation times than solids. For instance, in tumours where there is more unbound water than in normal tissues, water spins take longer to dephase. Therefore at 1.5 T, in white matter tissue, lesions have longer water T2 relaxation times (e.g. 165 ms) compared to normal tissue (98 ms).

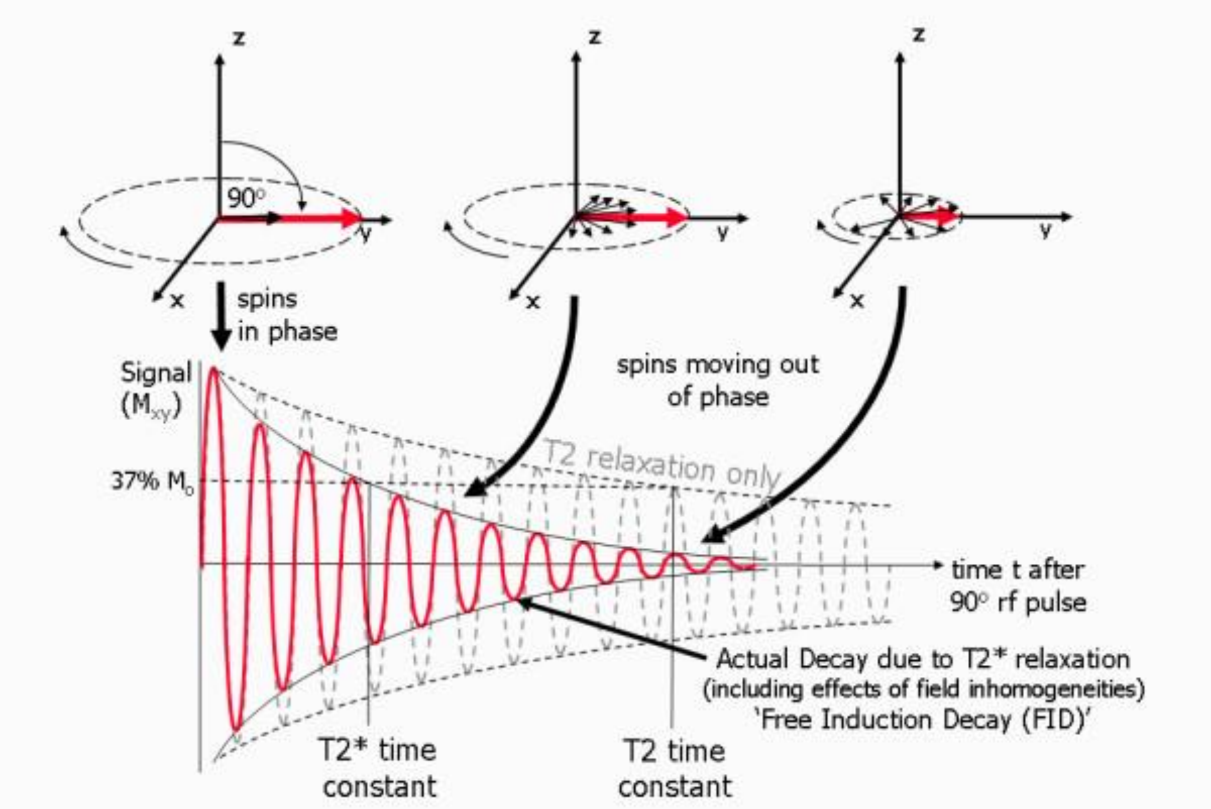
z
z
z
90°
y
y
y
x
x
x
spins in phase
Signal ($M_{xy}$)
37% $M_o$
spins moving out of phase
T2 relaxation only
time t after 90° rf pulse
Actual Decay due to T2* relaxation (including effects of field inhomogeneities) 'Free Induction Decay (FID)'
T2* time constant
T2 time constant

**Figure 1.19**. T2 and T2* relaxation processes after a 90° RF pulse is applied at equilibrium. Initially the transverse magnetisation (*Mxy*) (red arrow) has a maximum amplitude as the population of proton magnetic moments (spins) rotate in phase. Then the amplitude of the net *Mxy* (and therefore the detected signal) decays as the proton magnetic moments move out of phase with one another (shown by the small black arrows). The resultant decaying signal is known as the Free Induction Decay (FID). The overall term for the observed loss of phase coherence is T2* relaxation, which combines the effect of T2 relaxation and additional de-phasing caused by local variations (inhomogeneities) in the applied magnetic field. Both T2 and T2* are exponential processes with times constants T2 and T2* respectively. This is the time at which the magnetization has decayed to 37% of its initial value immediately after the RF pulse. Taken from [68]

T1 and T2 relaxation occur simultaneously but are independent of each other. Nonetheless, the dephasing of the spins occurs much faster than the recovery of longitudinal magnetisation (T2 ≤ T1). For this reason, longitudinal magnetisation can never be re-established until all the transverse magnetisation has decayed away. Hence for a given tissue, water T2 is usually about a tenth of T1. The T1 and T2 values of water in cerebrospinal fluid however are close at a given field strength: for example, T1 = 3302 ms and T2 = 2269 ms at for water 1.5 T.

### 1.3.2. Applications of NMR in biomedical research of brain cancer

Conventional MR imaging (MRI) is the most popular means of diagnosing brain tumours. Apart from providing a spatial anatomic location of the tumour, it provides an opportunity to noninvasively follow gross tumour morphology and how it evolves over time. Additionally, it can be used to measure parameters of biophysical interest, such as the apparent diffusion coefficients of water or cerebral blood volume. As an adjunct to MRI, MR spectroscopy (MRS) obtains biochemical information and metabolomics profile of the tissue under investigation. Finally, MR spectroscopic imaging (MRSI) combines both techniques and provides a 2D or 3D mapping of the spatial distribution of the metabolites in the region of interest (ROI). And since tumours are commonly heterogeneous, this allows characterisation of different parts of the tumour and/or its surrounding tissue.

#### 1.3.2.1. Magnetic Resonance Imaging

MRI is based on the magnetic properties of hydrogen nuclei, which is abundant in the human body and its solitary proton which has a large magnetic moment. The images are obtained from the $^{1}H$ signal present in the tissue (mostly $^{1}H$ from water and fat) are dependent on its concentration and mobility. The remaining metabolites do not contribute significantly in obtaining the images, because they are in a much smaller concentration in comparison to the fat and water. The intrinsic contrast of images obtained in MRI is primarily achieved due to differences in proton density (hydrogens) between tissues of the sample under study, and also to their characteristic relaxation times T1 and T2. Those differences, for example, between normal tissues and tumours result in contrast differences on the image, and that provides the basis for distinguishing tumours from normal tissues. There are three major types of images, defined by the parameter in which the contrast is based, that can be generated during the classical MRI acquisition: weighted by T1, T2 and proton density. This is usually achieved changing acquisition parameters as the echo time (TE) (Section 1.3.2.2) and the recycling time. Moreover, the intrinsic contrast can be modified or enhanced with the use of contrast agents (CA).

### Contrast agents

While MRI has high specificity for correctly detecting abnormal or pathological morphology, it cannot determine the degree of progression of established tumour. The CA used in MRI were developed in order to increase the specificity and sensitivity of this detection, as sometimes the intrinsic contrast is not enough.

CA are compounds that, when placed in the vicinity of resonant nuclei, can alter their relaxation behaviour. Thus, once administered to the subject, CA can selectively affect the T1 and/or T2 relaxation times of water in tissues and therefore increase contrast, namely between pathology and normal zone. Gadolinium ($Gd3^+$), a trivalent lanthanide with positive magnetic susceptibility (paramagnetic properties), is one of the examples of CA widely used in the MRI examinations in the clinics. Most CA used in patients are based on this metal, which is a T1 enhancement agent, used at small concentrations (0.1 – 0.2 mmol/Kg). This means that the T1 relaxation time of the nearby water protons are reduced, resulting in increased signal intensity on T1 weighted images (positive T1 contrast enhancement (CE)). Because of its elevated toxicity in free form [69], this metal ion is normally administrated during MRI exams in the form of a chelated compound (e.g. Gd-DTPA).

Most of the clinically available CA are not able to cross an intact BBB, but they can reach a lesion if BBB is broken.

### 1.3.2.2. Magnetic Resonance Spectroscopy

MRS is a technique which can be combined with magnetic resonance imaging to measure the concentration of a multitude of metabolites and macromolecules, and allows the biochemical characterization of tissues *in vivo* non-invasively. MRS can also be performed with nuclei that are MR active (due to their magnetic spin properties) and abundant in a given sample. Examples of these nuclei are mentioned in Section 1.3.1.

For performing *in vivo* MR spectroscopy it is of utmost importance to accurately obtain the NMR signal from a defined volume of tissue within an anatomical region of the body. The so-called "localisation techniques" are used for this purpose. These can be divided into two types, single voxel (SV) (a voxel being a small cubic based volume element for the region to be sampled with MRS) and multi-voxel techniques (MV), also named chemical shift imaging (CSI) techniques. In SV spectroscopy, a spectrum is acquired from a small volume of tissue defined by the intersection of three orthogonal planes. MV localization techniques can be in one dimension (1D), in two (2D) or in three (3D) dimensions and produce a matrix of contiguous voxels. In clinical MRS, SV spectroscopy and 2D and 3D MV or CSI are normally used.

For volume definition in SV, one approach is to excite only the volume of interest with frequency selective radiofrequency pulses. This can be achieved in *in vivo* spectroscopy in different ways, among which there are the stimulated-echo acquisition mode (STEAM) [70] or the point-resolved spectroscopy (PRESS) [71]. In both STEAM and PRESS, three selective RF pulses are applied, but they differ in other parameters, such as the sequence timing and the placement of the pulses. From a practical point of view, in *in vivo* MR spectroscopy, spectra acquired using a PRESS sequence will have double signal-to-noise ratio (SNR) than those acquired using STEAM sequences and will thus be preferable for comparable TE when provided by the scanner manufacturer.

### *Chemical shift*

The chemical shift phenomenon makes it possible for metabolites to be distinguishable in a spectrum, and in turn differences in spectral pattern allow distinguishing not only between different tissue types, but also classes of tumours, due to differences of their metabolism.

When a nucleus is placed in a magnetic field, $B_0$, its electrons circulate in such a manner that there is an induced magnetic field, $B_i$, aligned opposite to the main field. This is known as the shielding effect. The effective field, $B_{eff}$, experienced by the nucleus is then reduced by a fraction, $\delta$ of $B_0$ given by: $B_{eff} = B_0 (1-\delta)$, so that for the mentioned nucleus, the Larmor frequency now becomes:

$$\nu_0 = \gamma B_0(1-\delta) \qquad \text{Eq. 3}$$

A nucleus with a greater electron cloud density experiences a greater shielding effect and thus has a lower Larmor frequency at a given field in comparison with another nucleus which doesn't have a similar electron cloud. In a chemical bond, nuclei share their electron clouds and the more electronegative of the pair tends to 'steal' charge from around the other one. In this case, the nucleus whose charge density is reduced by the more electronegative one is said to be deshielded. The deshielded nucleus experiences a higher *Beff* value and so resonates at a higher frequency than its unbound state. Hence, the chemical environment of a given nucleus affects its resonance frequency.

The shielding effect is expressed in terms of the chemical shift, $\delta_{cs}$, in a part per million (ppm) scale independent of $B_0$, with respect to an internal or external reference.

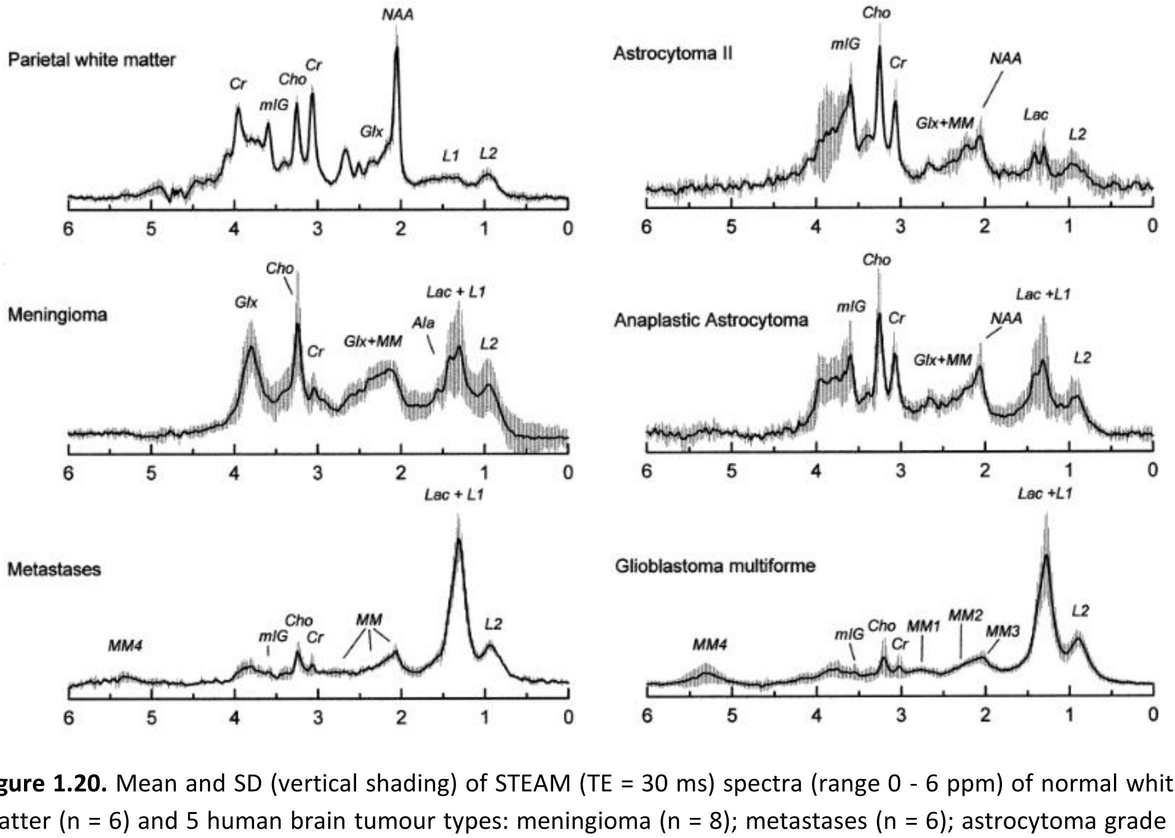

**Figure 1.20.** Mean and SD (vertical shading) of STEAM (TE = 30 ms) spectra (range 0 - 6 ppm) of normal white matter (n = 6) and 5 human brain tumour types: meningioma (n = 8); metastases (n = 6); astrocytoma grade II (n = 5); anaplastic astrocytoma (n = 7); glioblastoma (n = 13). Ala: alanine (at 1.47 ppm), Cho: choline (at 3.22 ppm), Cr: total creatine (at 3.03 ppm), Glx: glutamate and glutamine (at , L1 and L2: lipids (at ca. 1.3 and 0.9 ppm, respectively), Lac: lactate (at 1.33 ppm), mI: myo-Inositol and glycine (at 3.56 ppm), MM1, MM2, MM3 and MM4: macromolecules (at ca. 2.8, 2.25, 2.05 and 5.4 ppm, respectively), NAA: N-acetyl aspartate (at 2.01 ppm). Taken from [72].

*Relaxation times and use of different Echo Times*

The various metabolites have different molecular structures and so their protons are said to reside in different chemical environments. MRS signals from these metabolites therefore have different T1 and T2 relaxation times. Collecting MRS data at different TE provides complementary information from the tissue metabolome.

The TE in a MR sequence is basically the time elapsed between excitation and collection of the MR signal. A short TE (STE) acquisition, typically 20 - 40 ms, will be able to offer more information in the spectrum because less metabolite signals will have decayed. The spectrum will therefore contain more peaks (Figure 1.21). For *in vivo* acquisition, the problem with STE spectra is that several metabolite resonances overlap (due to limited spectral resolution) and it also contains large contributions from lipids and macromolecules which can make the interpretation of some spectra complex.

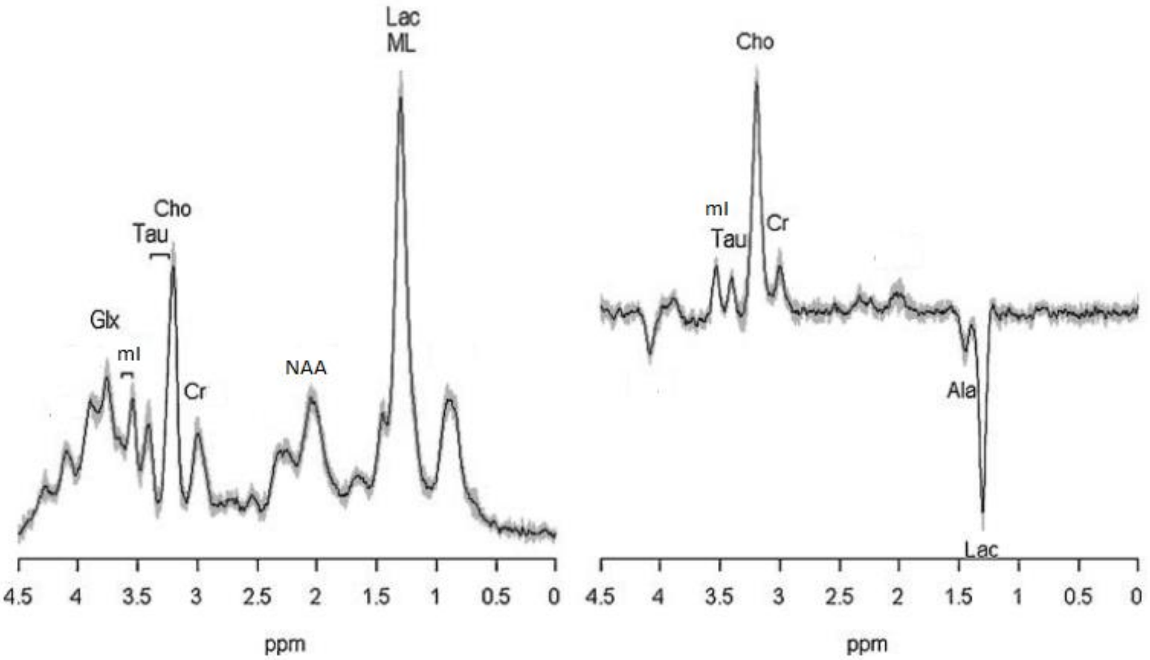

**Figure 1.21.** Spectral patterns and SD (grey shading) of GL261 tumours at two TEs (12 ms, left, and 136 ms, right) obtained from MRS explorations of C57BL/6 tumour bearing mice (n = 6). Ala, alanine (1.45 ppm); Cr, total creatine (3.93 and 3.03 ppm); Cho, choline (3.21 ppm); Glx, glutamine and glutamate (3.77/3.75 ppm); Lac, lactate (1.31 ppm); Lac/ML, lactate and methylene group of fatty acyl chains in ML (1.31 ppm) ; mI, myo-inositol (3.62 ppm); NAA, N-acetyl-containing compounds (2.01 ppm); Tau, taurine (3.42 ppm). Modified from [73].

A longer TE acquisition (typically TE ≥135ms) on the other hand will result in significant signal decay of short T2 metabolites, resulting in fewer peaks in the spectrum (Figure 1.21). Lipids and macromolecules have short T2 relaxation times in comparison with other metabolites; their signals will therefore decay, eliminating their contribution in the spectrum. However, also potentially interesting metabolite peaks are lost from the spectrum.

The choice of TE time in an acquisition therefore depends on the aim of the examination. In some cases, if it is possible, it may be beneficial to use both long and short TE times in the same examination.

### *Resonances and biological significance of the major compounds of brain tissue*

#### *N-Acetylaspartate*

N-Acetylaspartate (NAA) is the largest signal in the normal adult brain spectrum, resonating at 2.01 ppm, with a small and usually unresolved contribution from N-acetylaspartylglutamate (NAAG) at 2.04 ppm. NAA is one of the most abundant amino acids in the CNS and it is often referred to as a “neuronal marker,” since immunocytochemical studies have suggested that NAA is predominantly restricted to neurons, axons, and dendrites within the CNS [74, 75]. Even though its exact function is unclear, brain NAA has been speculated to act as an osmolite in the nerve cell, a storage form of aspartate, a precursor of NAAG and an acetyl donor for myelin synthesis [76]. Because of its specificity to neurons, NAA is commonly considered to be a marker of healthy neuronal density. A decrease in the NAA peak intensity has been reported in a number of neurological disorders including multiple sclerosis [77] , ischemia [78], acute head injury [79], inflammation and tumours [80].

#### *Choline*

The choline-containing metabolites include glycerophosphorylcholine (GPC), phosphorylcholine (PC) and free choline. They contribute to a prominent peak at 3.2 ppm [81] and combined resonance is often reported as total choline (Cho). These compounds are involved in membrane synthesis and degradation [82, 83] and are considered to be a marker of membrane turnover, which is elevated in disease states, e.g. tumours. Other pathological processes which lead to Cho elevation include active demyelination [84] or inflammation [85]. Low brain Cho has been observed in hepatic encephalopathy [86].

*Creatine*

The creatine methyl resonance at 3.03 ppm is a composite peak consisting of both creatine and phosphocreatine, therefore this combined resonance is often reported as total creatine (Cr). A resonance from the CH2 of creatine can also be observed at 3.91 ppm. These compounds are involved in energy metabolism via the creatine kinase reaction, generating ATP. Total Cr is therefore thought to be a marker of the energetic status of cells. Because the Cr peak is relatively stable with no age- [83] or disease-related changes, it is commonly used as the concentration reference in quantifying the other metabolites, e.g. for calculating metabolite ratios such as Cho/Cr, NAA/Cr, myo-inositol (mI)/Cr or mobile lipids (ML)/Cr [87]. However, this practice should be used with caution since decreased Cr levels have been observed in hypoxia, tumours [88] and stroke [89], and increased levels in trauma and myotonic dystrophy [90].

*Myo-inositol*

Among isomers of inositol, myo-inositol (mI) is the predominant form found in tissue and one of the larger signals in short SET spectra occurs at 3.5–3.6 ppm, which contains smaller contributions from inositol monophosphate, inositol polyphosphates and glycine (Gly). The function of mI is unclear, but it is believed to play a role in various neuronal signalling systems, metabolism of membrane-bound inositol phospholipids [83], cell growth , an osmolite (particularly in the cerebellum) and a storage form of glucose [91]. It has been proposed as a glial marker [92]. Increased levels of mI have been associated with Alzheimer’s dementia and demyelinating diseases, while decreased levels have been reported in hepatic encephalopathy [93]. mI + Gly levels has also been shown to decrease with astrocytic grade *in vivo* between low-grade astrocytoma and GBM [94, 95].

*Glutamate and Glutamine*

At clinical field strengths (typically 1.5 - 3 T), glutamate (Glu) and glutamine (Gln) signals almost completely overlap and are difficult to be distinguished, and they are detected as a composite Glx peak. At higher fields (4T and above), Glu and Gln become better resolved and can be quantified individually [96, 97] with the resonance of Glu occuring within 2.04 - 2.35 ppm and of Gln within 2.12 - 2.46 ppm. Glu acts as the major excitatory neurotransmitter in the CNS and so is found in higher concentrations in neurons than in glia. Gln on the other hand is a precursor and storage form of glutamate located in astrocytes. A large increase of Gln occurs is commonly observed in patients with liver failure (for example, hepatic encephalopathy) when the Glu/Gln cycle is altered and in such cases Gln is an indicator of liver disease by monitoring it in the brain [91]. Increased Glu and Gln concentrations have also been observed in severe ischaemia and hypoxia [98].

*Lactate*

Lactate is an end product of anaerobic glycolysis, usually present in brain tissue at low concentrations under normal conditions. Its resonance doublet at 1.31 ppm becomes inverted at long TE, while in shorter TE acquisitions *in vivo* it may be difficult to distinguish from resonances of lipids and macromolecules (MM). Its signal increases in cases of hypoxia and blood flow impairment such as stroke, trauma, tumour, necrotic tissue and cystic masses [99, 100].

*Lipids and macromolecules*

Lipid and MM resonances occur at various regions of the spectrum: around 0.9, 1.3 - 1.4 and 2.0 -2.6 ppm. They could sometimes be more pronounced particularly at shorter TE and in the presence of tumours. Lipids are all known to be significant markers of tumour malignancy. Their levels correlate with necrosis which is a histopathological feature of high grade gliomas caused by hypoxic stress [72].

#### 1.3.2.3 Magnetic Resonance Spectroscopic Imaging

While SV MRS produces a signal from a certain volume, MRSI is able to acquire multiple signals from a grid of voxels (Figure 1.22). MRSI is a powerful technique since it allows simultaneous visualization of the metabolic state of different regions of the tissue of interest, and it has been consistently used in both clinical [101] and preclinical studies [102].

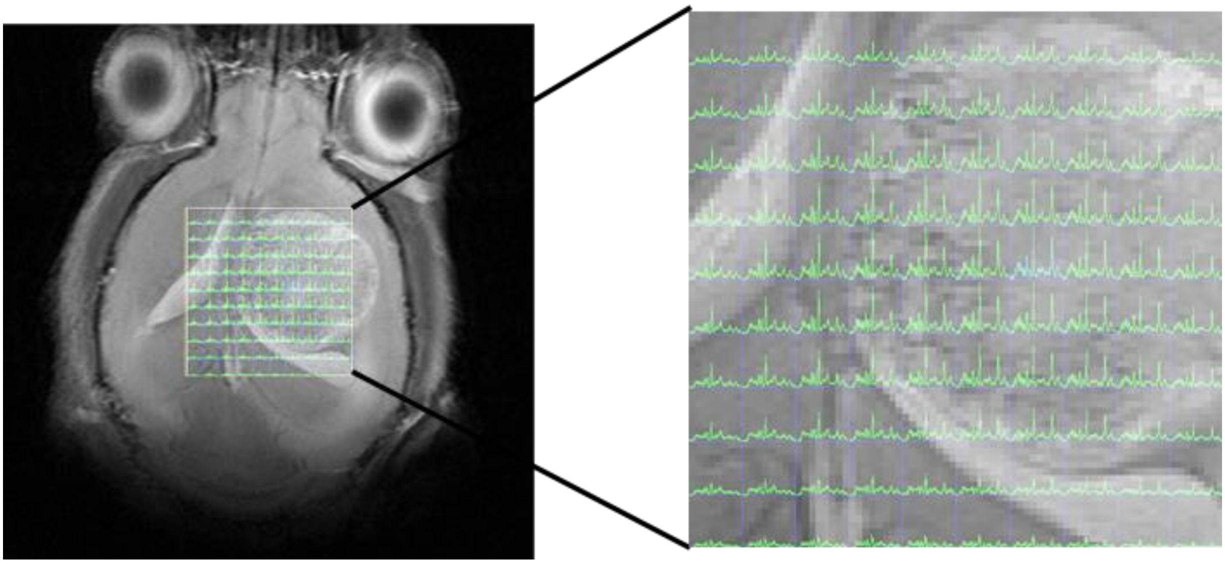

**Figure 1.22.** CSI obtained from a mouse brain bearing GL261 tumour *in vivo* at 7T (right): TR/TE = 2500/12 ms; 4.8 µl nominal voxel size, with PRESS localization, Variable Pulse Power and Optimized Relaxation delays (VAPOR) water suppression and outer volume suppression. On the left, reference $T_{2W}$ image of mouse brain (C57BL/6 strain) showing the PRESS voxel position (centre of field of view (FOV)); taken from group results.

**PE-MRSI**

MRS and MRSI have been invaluable tools for improving brain tumour characterisation [103-105]. However, MRS alone is still non fully specific with respect to grading of some tumours (aggressiveness), which suggests that the differences in the basal MRS specific patterns of these lesions are not sensitive enough to perfectly recognize tumour progression stages. Preclinical studies described earlier [73, 106] indicated that perturbing these basal patterns with defined metabolic challenges improves MRS sensitivity for staging tumour progression. These perturbation patterns then should be recognized and separated by pattern recognition (PR) techniques and a mathematical classifier [107].

*PE-MRSI with glucose under mild hypothermia*

Glucose is the major substrate for normal cerebral metabolism in both men and animals, and it is transported across the BBB by facilitated diffusion [108]. However, in gliomas glucose metabolism is remarkably enhanced in comparison to normal brain parenchyma [109, 110] while other *in vivo* MRSI studies show its heterogeneity in different regions of the tumour. In C6 rat gliomas regional differences in the distributions of lactate and extracellular acidity, both before and during transient hyperglycaemia due to glucose infusion were found [111]. Glycolysis has also been found to be consistently more prominent in hypoxic areas of human gliomas in mice than in regions of diffuse infiltrative growth [112]. Taking into account these differences, our group proposed a new method to improve tumour heterogeneity evaluation *in vivo*, perturbing the basal MRSI metabolic pattern of mouse gliomas with acute hyperglycemia [107]. This method showed higher glucose uptake and regional differences in glucose accumulation in GL261 gliomas than in normal brain parenchyma, after intraperitoneal injection of glucose in mice under moderate brain hypothermia (~30°C).

*PE-MRSI with DMSO*

Recently, DMSO was pointed out as a potential CA for brain tumours [113] that could be used to perturb their basal pattern of tumours. DMSO is a solvent which dissolves both nonpolar and polar compounds. Therefore, DMSO has several uses as inhibition of the formation of secondary structures of DNA and primers during PCR; a cryoprotectant for freezing organs, tissues and cell suspensions [114] and as a topical analgesic to reduce pain caused by muscle injury and neutralize free radicals (hydroxyl groups) [115]. In preclinical studies in mice models it is also used to dissolve temozolomide. DMSO was shown to be well detected in MRS and MRSI spectral patterns of tumour-bearing and normal mouse brain and also its differential accumulation in those tissues could serve as a CA for brain tumour detection, even in those tumours ‘invisible’ to standard gadolinium-enhanced MRI.

#### 1.3.2.4. Pattern recognition analysis of NMR data

The analysis of metabolites through MRS allows obtaining biochemical information about specific processes affected by pathology. However, the richness of information contained in MRS spectra poses difficulties to interpret the measurements and associate changes in more than a few metabolites with a particular clinical condition. Coupling the techniques of MRS with reliable algorithms of pattern recognition (PR) and machine learning permits to identify relationships between the quantitative changes of different metabolites simultaneously and detect even subtle differences in metabolic profiles.

In summary, PR is the process of classifying input data into categories or classes based on key features. In the case of brain tumours, spectra obtained by MRS or MRSI, the PR analysis includes two concepts: the grade or class to which each spectrum is associated, and the mathematical process which quantifies certain characteristics of the spectra to associate with a particular category or class. There are two classification methods in PR: supervised and unsupervised classification.

#### Supervised PR

The supervised PR methods involve the use of a known training group of cases to develop a mathematical model. The investigator assigns the spectra to a certain class based on a previous classification, which in the case of brain tumour spectra in normally done by histopathological analysis. This is called training. Once trained, the classifier and the mathematical algorithms can be applied to a set of independent test for validation assigning the input data to appropriate class label.

Supervised classification basically consists of three steps: 1) dimensionality reduction, 2) learning phase on a training set and classification of the spectra in different classes based on the differential descriptive characteristics and 3) evaluation of the robustness of the classification in terms of their descriptive characteristics (which allows discrimination of differences between groups) and predictive (allowing to assign a new spectrum to one of the previously established classes) [107, 116]. There exist several types of supervised techniques that can be applied to MR data, but the most classical one is Linear Discriminant Analysis (LDA).

#### Unsupervised PR

The main difference between the unsupervised and supervised methodology is the learning process. In the unsupervised classification, the researcher does not assign cases to a particular class.

Unsupervised techniques try to group cases based on their similarities between each other, without knowing the exact grouping. The similarity measure can be based on the distance of the samples in the multi-dimensional feature space constructed by the observed data features. Clustering techniques, Principal Component Analysis (PCA) [117] or non-negative matrix factorization [118] are examples of common unsupervised techniques.

Such techniques have the advantage that each class instead of being represented by a number of features, spectroscopic characteristic pattern of a given "metabolic state" is obtained and called source. From the biochemical point of view, the source extraction technique to classify MRS data assumes that in each voxel there is a mixture of heterogeneous tissues pattern and contribution of each source can be presented [102]. The obvious advantage of this approach lies in the fact that the labeling procedure becomes independent of the availability of labeled MRSI datasets and the negative effect of mislabeled cases on the generalization capabilities of the model will be prevented.

**Semi-supervised PR**

The semi-supervised methodology in [132] proposes to take benefit from the use of prior knowledge derived from class membership of the spectra to guide the source extraction. It involves three main stages:

I. The definition of a Fisher Information (FI) metric [133] to model pairwise similarities and dissimilarities between data points, using a Multi-Layer Perceptron (MLP) classifier to estimate the conditional probabilities of class membership.

II. The approximation of the empirical data distribution in an Euclidean projective space in which Non-negative Matrix Factorization (NMF)-based techniques can be applied. This is done in this work with Multidimensional Scaling methods, specifically with the iterative majorization algorithm [134, 135].

III. The application of Convex-NMF for the source decomposition of the data.

# 2. General objectives

1. Characterisation of brain abnormal masses in GEM colonies available in the GABRMN laboratory using MR-based techniques (Section 4)

2. Improvement of brain tumour incidence rate in preclinical murine models to be used in future therapy protocols, through:

    2.1. MR systematic screening of GEM colonies (Section 4)

    2.2. Developing a transplantable murine tumour model of low/intermediate grade (Section 5)

    2.3. Evaluation of selected driver mutations in different tumour models used by the GABRMN laboratory (Section 6)

3. Improvement of non-invasive protocols for therapy response monitoring using MRSI-based PR techniques and nosological imaging (Section 7)

# 3. General materials and methods

This section describes the common materials and methods used in different experiments presented in this thesis. Further on, each section contains material and methods specific for the work described in that particular section with the cross reference between the general material and methods to avoid redundancy by not repeating methods already described in previous sections.

### 3.1. GL261 cells

The murine GL261 glioma cell line was obtained from the Tumour Bank Repository at the National Cancer Institute (Frederick/MD, USA) at a declared passage of 8. These cells had been previously used and characterised by our group [73, 106] and this was continued due to their highly reproducible behaviour (close to 100% penetrance) in generating high grade gliomas (grade IV) when implanted into wild type C57BL/6 mice.

The cells were cultured in flasks of 75 $cm^2$ (Nunc, LabClinics SA, Barcelona) using RPMI-1640 (Roswell Park Memorial Institute) (Sigma, Madrid) supplemented with 2.0 g/L of sodium bicarbonate, 0.285 g/L glutamine, 1% penicillin-streptomycin (all from Sigma-Aldrich, Madrid) and 10% fetal bovine serum (Gibco, Invitrogen, UK). The time period to reach confluence (i.e. cells covering 75 -85% of the flask surface) was 7 days from the time of subculture (day 0). The medium was changed on the day 3 and 5. Cell cultures were incubated at 37°C in a 5% $CO_2$ and 95% humidity (incubator HERAcell, 150i, Thermo Scientific). Upon reaching confluence, cells were subcultured; the medium was removed by aspiration with a vacuum pump and the cells were washed with 10 ml of sterile PBS. Then, after removing PBS, cells were detached from the flask using 2 ml of trypsin-EDTA (0.5 g/L and 0.2 g/L, respectively) (Sigma, Madrid) and resuspended in 8 ml RPMI medium (10 ml total volume of resuspension). The resuspension, containing ~7 x $10^5$ cells, was seeded into new flasks containing 25 ml RPMI medium. Cells were subcultured until passage 40, at which time they were discarded to avoid possible accumulation of genetic alternations and a new aliquot thawed from the initial amplification made in the lot and cultured as above.

### 3.2. Gliospheres

Tumours of interest were excised from animals sacrificed by cervical dislocation and cells disaggregated mechanically. Gliospheres were generated, frozen and thawed in collaboration and according to the protocols established by the group of Josep M Canals (*Institut d'Investigacions Biomèdiques August Pi i Sunyer*, *Hospital Clínic*, Barcelona).

Gliospheres cultures were obtained by seeding 75 $cm^2$ flasks with 10,000 cells/$cm^2$ in Dubelcco's Modified Eagle's Medium (DMEM; Sigma Chemical Co.):F12 (GIBCO) (1:1); supplemented with 0.6 mM D-(+)-glucose (Sigma Chemical Co.), 2 mM glutamine, 50 U/ml penicillin/streptomycin (GIBCO), 5 mM HEPES (GIBCO), 0.2 % heparin (Sigma Chemical Co.), 4 mg/ml bovine serum albumin (Sigma Chemical Co.), 1× N2 Supplement (GIBCO), 10 ng/ml fibroblast growth factor (Sigma Chemical Co.) and 20 ng/ml epidermal growth factor (Invitrogen SA). Every 5 days gliospheres were collected, detached from the layer with Trypsin treatment: TrypLE™ Express (Gibco) at 37°C for 5 min and dissociated by pipetting approximately 40 times with a P100 micropipette (10-100 µl range) and re-plated in fresh media at a density of 10,000 cells/$cm^2$ as described in [119]. All cell cultures were incubated at 37°C in a 5% $CO_2$ atmosphere.

Some gliospheres were frozen to check the reliability, robustness and repeatability of generated cells for transplantation purposes. Dissociated cells from harvested gliospheres after pipetting were then transferred to the freezing medium: 90% DMEM with 10% DMSO (Sigma–Aldrich Co.). Between 30,000 – 100,000 cells were loaded into a cryovial and frozen (at the rate of −1°C/min until −80°C) using a freezing container (Nalgene Europe Ltd., Hereford, UK), and then stored in liquid nitrogen. When cells from gliospheres were needed again they were rapidly thawed in a water bath at 37°C, washed twice in DMEM and derived cultured as described above.

### 3.3. Cell count

The cell counts were performed in a Neubauer haemocytometer using Trypan Blue dye to distinguish viable from dead cells, since the latter are not able to extrude the dye and appear dark blue in colour when viewed under a microscope. Aliquots of 40 µl of a cell suspension, obtained during the subculturing step described above (Section 3.1), were combined with 50 µl of Trypan Blue dye (0.4% preprepared in 0.81% sodium chloride and 0.06% potassium phosphate; Sigma-Aldrich) and 110 µl of PBS. To calculate the number of cells/ml, the average number of cells in the four corner squares of the chamber was counted and the following formula was used:

$$C_{no} = M\ x\ d\ x\ 10{,}000 \qquad \text{Eq. 4}$$

where $C_{no}$ , is the number of cells/ml ; $M$, is the average count of the squares; $d$ is the dilution factor (which in our case is 5).

### 3.4. Animal models

Each mice evaluated in the GABRMN is given a unique alphanumerical identifier. For example, identifiers of the type CXXX belong to mice bearing GL261 tumours, while SXXX belong to GEM of the S colony (see below for further details).

Throughout the studies described in this thesis, all mice were housed and bred at the animal facility of the *Universitat Autònoma de Barcelona* (*Servei d'Estabulari*). The detailed composition of the diet is shown in Annex 1. The protocol of supervision of laboratory animals described in Annex 2 was followed by the *Servei d'Estabulari* veterinary staff to assess their physical state and inform the investigator if sacrifice of an animal was recommended and halting of the experimental protocol needed to be considered.

The experiments were conducted according to experimental protocols, previously approved by the local ethics committee (*Comissió d'Ètica en l'Experimentació Animal i Humana*, protocol CEEAH 1176 and CEEAH 2449).

#### Wild type C57BL/6 mice

Female mice of 18-24g in weight, aged 16-20 weeks, were obtained from Charles River Laboratories (Charles River Laboratories International, L'Arbresle, France). The wt C57BL/6 mice were used either as control animals or to generate the stereotactically induced tumours tumour as described in Section 3.6.

**Genetically engineered mice**

***S colony: S100B-v-erbB/INK4A-ARF(+/-)***

Founders of this colony were obtained through the Mouse Models of Human Cancer Consortium Repository at the National Cancer Institute (MMHCC-NCI, Frederick, MD, USA). This transgenic mice model is a low/intermediate grade ODG model and expresses a truncated allele for EGFR, *v-erbB* under the control of the S100ß promoter, which overexpression causes ODGs [63]. Furthermore, the genetic alternation of INK4A-ARF(+/-), corresponding to the deletion of two tumour suppressors (affecting RB and p53 pathways, as described in Section 1.2.2), allows transition of the tumours into a higher grade (anaplastic ODG, grade III) in transgenic animals heterozygotic for INK4A/ARF deletion.

The S colony was developed and maintained under supervision of the *Servei d'Estabulari* staff by crossing Tg/Ko+/- females (of age between 8 and 64 weeks) with Tg/Ko+/- males (of age between 10 and 96 weeks). If Tg/Ko+/- males were not available for breeding, Tg/wt males were used. The possible genotypes of the progeny are presented in Table 1 below.

***R colony: GFAP-$V^{12}$HA-ras***

Transgenic (Tg) GFAP-V12 HA-*ras* B8 (RasB8) [65] mice founders, expressing a single copy of oncogenic $V^{12}$ HA-*ras*, were obtained from the Dr A. Guha's Laboratory in Toronto, Ontario, Canada.

The R colony was maintained and bred under supervision of the *Servei d'Estabulari* staff by crossing Tg females (of age between 8 and 64 weeks) with Tg males (of age between 10 and 96 weeks). The possible genotypes of the progeny are either Tg or wt (Table 1.1).

In order to differentiate animals in the same cage, 3 weeks after the birth, unique ear notches were made by an ear punch device - 1, 2 or 3 notches and their combinations in both ears, as shown in Figure 3.1. Then each animal was given a specific alphanumeric identification number starting with a letter S in case of the S colony, e.g. S912, and with R in case of the R colony, e.g. R279. The maximum number of animals per cage was 8.

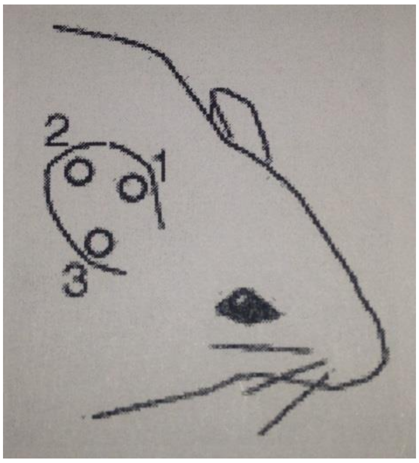

**Figure 3.1.** Scheme for marking mice by ear punching.

When marked by ear punches, animals of both S and R colonies were checked for the transgene presence (and knockout mutation, in case of S colony). For this a small piece of tail (3-4 mm) was cut off from each animal and the tail end of the animal immediately cauterized to prevent excessive bleeding. The tail samples were then stored at -20°C until used for DNA extraction, as described in section 3.5.

The animals with detected transgene and/or with neurological symptoms, indicative of possible tumour pathology, were explored by MRI (Section 3.10.1) to check for the possible presence of an abnormal mass.

**Table 3.1.** Possible expected genotypes of the progeny of the S and R colony crossings. Highlighted in green are the genotypes used in the pilot study described in Section 4.

| | **S colony** | **R colony** |
|---|---|---|
| **Possible genotypes** | Tg/Ko+/-<br>Tg/Ko-/-<br>Tg/wt | Tg |
| | wt/Ko+/-<br>wt/Ko-/-<br>wt/wt | wt |

### 3.5. Genotyping for GEM

***S colony***

The presence of the transgene and the knock-out mutation were confirmed by PCR analysis by slightly modifying protocols designed by Dr. David Goldberg (University of California San Francisco, USA) and Dr. Dave Sims (MMHCCNCI, USA). Briefly, DNA was extracted from a piece of tail with a standard lysis solution (50mM Tris-HCl pH 8, 1 mM EDTA, 0.2% SDS, 20 mM NaCl, 100 mg/L proteinase K) and incubating at 55 ˚C overnight. For amplification of the gene S100β-v-erbB the primers 5-'CTCACAGCAATCTCAAAGCTCCCC-3 'and 5'-AGCCTCCAAAGTCAGGTTGATGAGC-3' (Thermo Fisher Scientific GmbH, Ulm, Germany) were used, as described in [63]. For identification of INK4A-ARF (+/-) 3 different primers were used (to evaluate the absence/presence of both tumour suppressors): 5'-GTGATCCCTCTACTTTTTCTTCTGACTT-3', 5'-CGGAACGCAAATATCGCAC-3' and 5'-GAGACTAGTGAGACGTGCTACTTCCA-3 '. The PCR protocol was as follows: ([temperature (°C) / duration (min)] / number of cycles): [95/5] / 1; [(95/1) (60/0.5) (72/2)] / 29; [72/10] / 1).

***R colony***

The presence of the transgene was detected by PCR analysis by modifying protocols described in [65]. A tip of a mouse tail was lysed as described above for the S colony. GFAP-$V^{12}$ HA-*ras* transgene was identified using the following primers (Isogen): 5'-ACTCCTTCATAAAGCCCTCG -3' located in the GFAP promoter and5'-CTCGAATTCTCAGGAGAGCACACACTT-3' located in the 3' region of the HA-*ras* cDNA. The PCR protocol was as follows: ([temperature (° C) / duration (min)] / number of cycles): [94/10] / 1; [(94/1) (58.7/1) (72/2)] / 39; [72/5] / 1.

**Gel electrophoresis of PCR products**

The PCR-products were analysed in a 2% (w/v) horizontal agarose gel in the 1xTBE electrophoresis buffer system (ApllliChem GmbH). Ethidium bromide (EtBr) was added to the molten agarose to a final concentration of 0.1 µg/ml to allow visualization of the DNA under ultraviolet light (UV). Into each 10µl of the PCR amplified DNA sample, 2 µl of the loading buffer (Ecogen) was added before loading 10 µl of the mixture onto the gel. DNA size markers of up to 1kb (BioVentures,Inc.) were loaded in the same way as a sample into a well on each gel to enable sizing and quantification of DNA fragments. Stained DNA was visualized on a Bio-Rad transilluminator at 260 nm and imaged using the Quantity One (v.4.6.9) software by Bio-Rad Laboratories, Inc. (USA). The presence of bands on the gel was interpreted as explained in Figure 3.2.

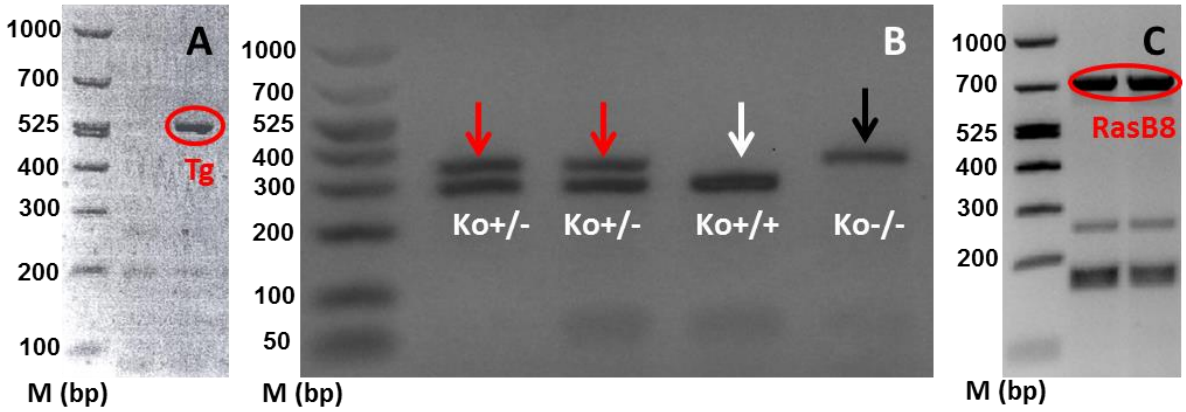

**Figure 3.2.** Gel electrophoresis of PCR products for genotyping of S and R colonies. **S colony: A)** 525 bp product proves the presence of transgene (Tg), **B)** 278 bp represents a wild type INK4A-ARF (white arrow), while 313 bp band is an indication of a mutated INK4A-ARF (black arrow). Presence of both bands indicates an animal heterozygous (Ko+/-) for INK4A-ARF (red arrow). **R colony: C)** 700 bp fragment indicates a transgenic mouse (RasB8).

### 3.6. Generation of tumours by stereotactic injection of cells

After the cell count (Section 3.3), the cell suspension was transferred into a 15ml Falcon tube (Deltalab SLU, Barcelona, Spain) and centrifuged 1.5 minutes at 1,400 x g (Centrifuge Selecta S-240, ALCO, Terrassa, Spain). The supernatant was removed and the pellet resuspended in the RPMI medium, so that each 4µl contained $10^5$ of cells, according to the equation:

$$V_f = \frac{(4\mu l \; x \; Cf)}{10^5} \qquad \text{Eq. 5}$$

where $V_f$ is the volume of the medium for cells to be resuspended in (µl) and *Cf* is the total number of cells in the pellet calculated according to Eq. 4 (Section 3.3).

Analgesia was administered subcutaneously to each animal 15 minutes prior to anaesthesia and also 24 and 48 hours after surgery (Meloxicam, 1.0 mg/kg), whereas Buprenorphine (0.1 mg/kg) was given directly after animal recovery from anaesthesia. The animals were anesthetized with a mixture of ketamine (Parke-Davis SL, Madrid) and xylazine (Carlier, Barcelona, Spain) (80 and 10 mg/kg, respectively) administered intraperitoneally, and immobilized in a stereotaxic holder (Kopf Instruments, Tujunga / CA, USA), as shown in Figure 3.3 After the head area was shaved, the incision site was sterilized, a 1 cm incision was made exposing the scull, and a 1 mm hole was drilled 0.1 mm posterior to the Bregma and 2.32 mm lateral (right) to the midline using a microdrill (Fine Science Tools, Heidelberg, Germany). A 26 G Hamilton syringe (Reno/NV, USA), positioned on a digital push-pull microinjector (Harvard Apparatus, Holliston/MA, USA) was then used for injection of 4 µl RPMI medium containing $10^5$ GL261 cells or cells from gliospheres at a depth of 3.35 mm from the skull surface at a rate of 2 µl/min. Once the injection was completed, the syringe was left for two minutes before the removal to allow the cells to settle and to prevent them from leaking outside the scull. Then the Hamilton syringe was gently taken out, the scission site closed with suture silk 5.0 (Braun, Barcelona, Spain) and the animal left to recover in a warm environment (~25 ˚C) in close approximation to an infrared lamp, to recover from anaesthesia.

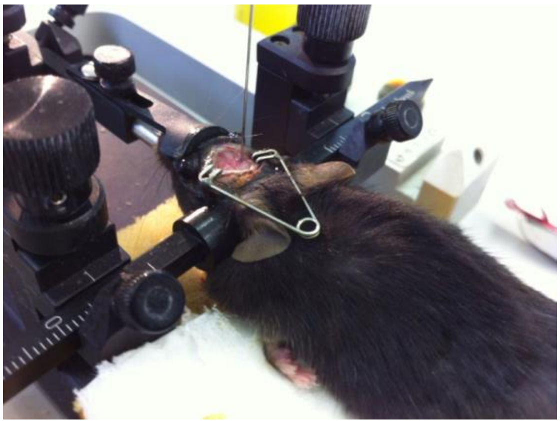

**Figure 3.3.** A C57BL/6 mouse with a scull incision immobilized in a stereotactic holder.

### 3.7. Tissue preservation for post-mortem procedures

When tumour-bearing animals died or were sacrificed by cervical dislocation (refer to annex 2 for the criteria used to decide about animal sacrifice) after *in vivo* MR studies (see Section 3.10) due to symptoms of suffering, the brains were excised and either fixed or frozen. In case of fixation, tissue was preserved in 4% formaldehyde and embedded in paraffin; while if freezing was the strategy chosen, tumours were dissected away and sliced. Pieces of about 2 mm$^3$ ware placed in cryotubes containing 1ml of 10% DMSO in Phosphate Buffered Saline (PBS) and kept for one hour in liquid nitrogen atmosphere before placing in a liquid nitrogen container.

## 3.8. Histopathological analysis

### 3.8.1. Analysis of brain/tumour tissue

Histopathological analysis was done with the collaboration and supervision of Dr. Martí Pumarola (*Departament de Medicina i Cirurgia Animals*, *Universitat Autònoma de Barcelona*).

Once fixed and embedded in paraffin, serial sections of the tissue (5 µm) were performed to correlate the histological preparations with the orientation of reference image in the MRSI studies. The sections were analysed by classical Hematoxylin-Eosin (HE) staining to distinguish the areas of normal and tumour tissue and, in the case of transgenic animals, to diagnose the type and grade of tumours.

Caspase 3 (Cell Signaling Technology, Izasa, Barcelona, Spain) and Ki67 (BD Biosciences, Madrid, Spain) immunohistochemical stainings were used for detecting apoptosis and cell proliferation, respectively, in brain samples of GL261 tumour bearing mice, either control or treated with TMZ. The preparations were digitized for further quantification (Hamamatsu Photonics France, Massy, France). Representative regions of 0.1 mm$^2$ were selected from the periphery and the core of the tumoural masses, at 20x magnification, using NDPview 1.2.53 software (Hamamatsu Photonics France SARL, Massy, France). The number of selected regions depended on tumour size (between 4 and 17 in the periphery and between 1 and 14 in the core of the tumours). Immunopositive cells for Caspase 3 and positive and negative cells for Ki67 were counted in each field using Image J 1.47d software (NIH, USA) and the “Cell Counter” plugin.

The number of mitoses in selected TMZ-treated GL261 tumours was counted and evaluated at 40x using an Axioskop 40 microscope (Carl Zeiss, Goettingen, Germany) on the original HE stained slices at selected areas by Dr. Martí Pumarola.

### 3.8.2. Analysis of gliospheres

Assessment of prepared gliospheres (Section 3.2) was done by the Josep M Canals group (*Institut d'Investigacions Biomèdiques August Pi i Sunyer*, *Hospital Clínic*, Barcelona). The samples were fixed in 4% paraformaldehyde for minimum 30 minutes and the analyses were performed by confocal microscopy using Leica (Mannheim, Germany) TCS SL laser scanning confocal spectral microscope with argon and helium–neon lasers attached to a Leica DMIRE2 inverted microscope.

## 3.9. Therapy protocol for GL261 GBM

The therapy administration protocol used in our studies was based on previous work from others [120-122] and optimized previously in our group, proving the TMZ therapy consisting in three cycles alternating drug/rest periods to be the most effective in the investigated preclinical GBM system [123]. One dose per day was administered for 5 consecutive days during the first cycle (60mg/kg q.d. × 5 p.o.), followed by 3 days of rest, then 2 consecutive therapy days of the second cycle (60mg/kg q.d. x 2 p.o.), 3 days of rest and finally a third cycle, identical to the second (60mg/kg q.d. x 2 p.o.), as schematized in Figure 3.4.

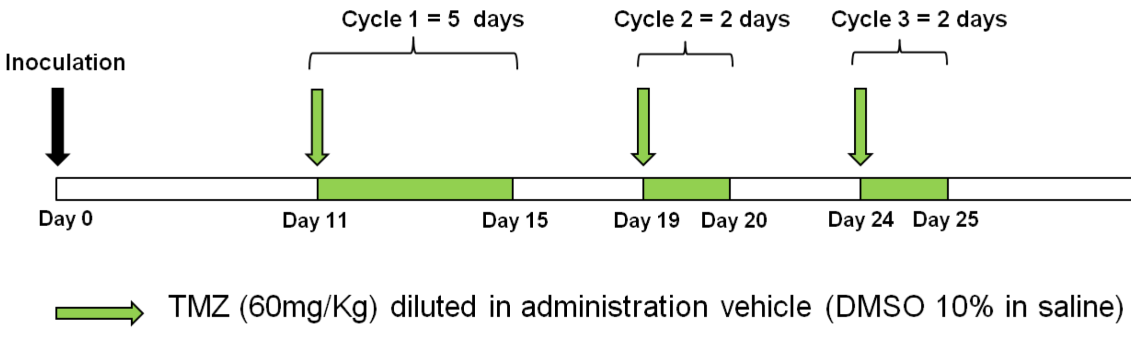

**Figure 3.4.** General scheme of the pre-established TMZ therapy protocol. The therapy consists of three daily treatment cycles with TMZ. The black arrow indicates the day of GL261 cells implantation into C57BL/6 mice. The green arrows indicate the start of each therapy cycle and green sections show each therapy cycle duration.

A stock solution (200 mg/ml) of TMZ (Sigma-Aldrich, Madrid, Spain) was prepared by dilution in 10% DMSO (AppliChem, Barcelona, Spain) in saline solution and sonication: 4 pulses of 5 s at 30% of amplitude, interleaved with rest periods of 5 s (Ultrasonic Processor VCX750, Sonics & Materials, Inc., Newtown, CT 06470-1614 USA). Then, the stock TMZ solution was further diluted in the administration vehicle (DMSO 10% in saline) at a concentration of 6 mg/ml. The volume administered with an intragastric probe (20 G, 38 mm, Popper & Sons, New York, USA) was 10 µl per 1g of animal weight.

## 3.10. In vivo MRI/MRS/MRSI

MR studies were carried out at the joint NMR facility of the Universitat Autònoma de Barcelona and CIBER-BBN (Cerdanyola del Vallès, Spain) with a 7T horizontal magnet (BioSpec 70/30, Bruker BioSpin, Ettlingen, Germany) equipped with actively shielded gradients (B-GA12 gradient coil inserted into a B-GA20S gradient system) and a quadrature receive surface coil, actively decoupled from a volume resonator with 72 mm inner diameter.

Mice were placed in the scanner bed and anesthetized with 0.5-2.0% isoflurane in $O_2$, keeping the respiratory frequency at 60-80 breaths/min. The body temperature was controlled using a recirculating water system incorporated to the animal bed and measured by a rectal probe and maintained between 37-38 °C, except in the case of PE-MRSI glucose studies, when the temperature was maintained between 28.5 - 29 °C. Breathing and temperature were constantly monitored (SA Instruments, Inc., New York, USA).

### 3.10.1. MRI acquisition

GEM animals as well as mice implanted with GL261 cells or gliospheres were screened by acquiring high resolution (HR) coronal $T_{2W}$ images ($TR/TE_{eff}$ = 4200/36 ms) using RARE (Rapid Acquisition with Relaxation Enhancement) sequence to detect brain tumour presence and monitor its evolution stage. The acquisition parameters were as following: turbo factor, 8; FOV, 19.2 x 19.2

mm; matrix, 256 x 256 (75 x 75 µm/pixel); number of slices, 10; slice thickness (ST), 0.5 mm; inter-ST, 0.6 mm; number of averages (NA), 4; total acquisition time (TAT), 6 min and 43 s.

#### Contrast Enhanced MRI (CE MRI)

The BBB integrity was assessed by CE MRI and detection of contrast uptake, acquiring standard $T_{1W}$ images (TR/TE=350/8.5ms) before and 20 minutes after intraperitoneal *(ip)* injection of gadoterate meglumine (DOTAREM®, Guerbet, Roissy, France) as a bolus (200 µl, 50µmol/ml in saline solution - a sterile solution of sodium chloride (0.9% NaCl)). Acquisition parameters were as follows: FOV, 17.6 x 17.6 mm; matrix 128x128 (138×138µm/pixel); NS, 3; inter-ST, 0.1 mm; TR / TE, 350/8.5 ms; NA, 1; ST, 1 mm; TAT, 44 s 800 ms.

#### Dynamic Contrast Enhancement (DCE)

Dynamic contrast enhancement (DCE) studies were performed using gadopentate dimeglumine (Gd-DTPA, Magnevist®, Schering, Madrid, Spain) as a CA. After acquiring three pre-contrast standard $T_{1W}$ images, the CA was injected intravenously (0.2 mmol $kg^{-1}$) and a series of 38 dynamic images was acquired with temporal resolution of 51.2 s per frame. For this, the multi-slice multi-echo (MSME) sequence was used with: FOV; 17.6×17.6 $mm^2$; matrix, 128x128 (138×138µm/pixel); TR/TE, 350/8.5 ms; NA, 2; ST, 1 mm; TAT, 34 min 59 sec.

DCE MRI data were processed using an in-house developed software, DCE@urLAB [124]

### 3.10.2. SV-MRS acquisition

Once tumours reached a volume sufficient for setting a voxel of the size $(2 - 3\ mm)^3$ without contaminating the metabolic profile with normal brain parenchyma, SV spectra were acquired at short and long TE, 12 and 136 ms respectively, using PPRESS localization and VAPOR water suppression [125], with the parameters described in [113]: spectral width (SW), 4006.41 Hz; TR, 2500 ms; NA, 128; TAT, 5 min and 30 s.

### 3.10.3. PE-MRSI

Mice implanted with GL261 cells and GEM animals were studied by MRSI, which allowed obtaining metabolomic information from different parts of a tumour, revealing its heterogeneity, and also from the surrounding tissue, gathering both metabolic and anatomical information. Additionally, PE-MRSI techniques with substances such as DMSO and glucose [73, 106, 113] were used in order to increase the dynamic range for *in vivo* brain tumour characterization in preclinical studies. Both substances used in PE-MRSI studies were injected intraperitoneally as a bolus (10 µl per g of animal, 10% (v/v) DMSO and 25% (w/v) D-glucose in saline, respectively), while the animals were inside the magnet, to avoid re-shimming needs.

For the PE-MRSI with DMSO, a coronal $T_{2W}$ HR reference image and 14 ms TE basal MRSI were initially acquired. DMSO was then injected, followed by three repeated 14 ms TE MRSI acquisitions.

For the PE-MRSI with glucose in hypothermia (about 30°C) studies, a coronal $T_{2W}$ HR reference image and two reference MRSI scans were initially acquired, one with 14 ms TE, followed by another acquisition at 136 ms TE. Then hyperglycemia was induced and consecutive MRSI scans were acquired as follows: 14 ms TE, 14 ms TE, 14 ms TE, 136 ms TE and 14 ms TE.

The PE-MRSI experiments were performed using a 2D CSI sequence with PRESS localization, where: FOV, 17.6 x 17.6 mm; ST, 1 mm: Volume of Interest (VOI), 5.5 x 5.5 x 1.0 mm, positioned in the way that most tumour was covered and including a part of the nearby normal/peritumoural brain parenchyma; TR, 2500ms; SW, 4006.41Hz; NA, 512; TAT, 21m 30 s.

Water suppression was performed with VAPOR, using a 300 Hz bandwidth. Linear and second order shims were automatically adjusted with FASTMAP in a 5.8 x 5.8 x 5.8 mm volume which contained the VOI region. Six saturation slices (ST, 10 mm; sech-shaped pulses: 1.0 ms/20250 Hz) were positioned around the VOI to minimize outer volume contamination in the signals obtained. Spatial resolution was defined by a 8 x 8 voxel matrix over the FOV (4.84 µl nominal resolution) reconstructed after Fourier interpolation to a 32 x 32 matrix, as described in [106]. The selected VOI (10 x 10 voxels) was interpolated in this matrix.

### 3.10.4. MR data processing and post-processing

*Tumour volume calculation from MRI acquisitions*

Tumour volumes in evaluated mice were calculated from $T_{2w}$ HR coronal images using the equation:

$$\mathrm{TV}\,(\mathrm{mm}^3) = \left[(AS_1 \;\mathrm{x}\; \mathrm{ST}) + \left[(\mathrm{AS}_2 + (...) + \mathrm{AS}_{10}) \;\mathrm{x}\; (\mathrm{ST} + \mathrm{IT})\right]\right] \mathrm{x}\; 0.075^2 \qquad \text{Eq. 6}$$

where *TV* is the tumour volume, *AS* is the number of pixels contained in the region of interest delimited by the tumour boundaries in each slice of the MRI sequence, ST is 0.5 mm, inter-ST is 0.1 mm and 0.075 $\mathrm{mm}^2$ is the individual pixel surface area.

The tumour area was calculated in pixels in each slice, using an automated system for generating regions of interest (ROIs) available in the Paravision 5.0 software (Bruker BioSpin, Ettlingen, Germany). The inter-slice volume was not registered and it was estimated adding the inter slice thickness (inter-ST) to the corresponding ST in Equation 6 (Figure 3.5).

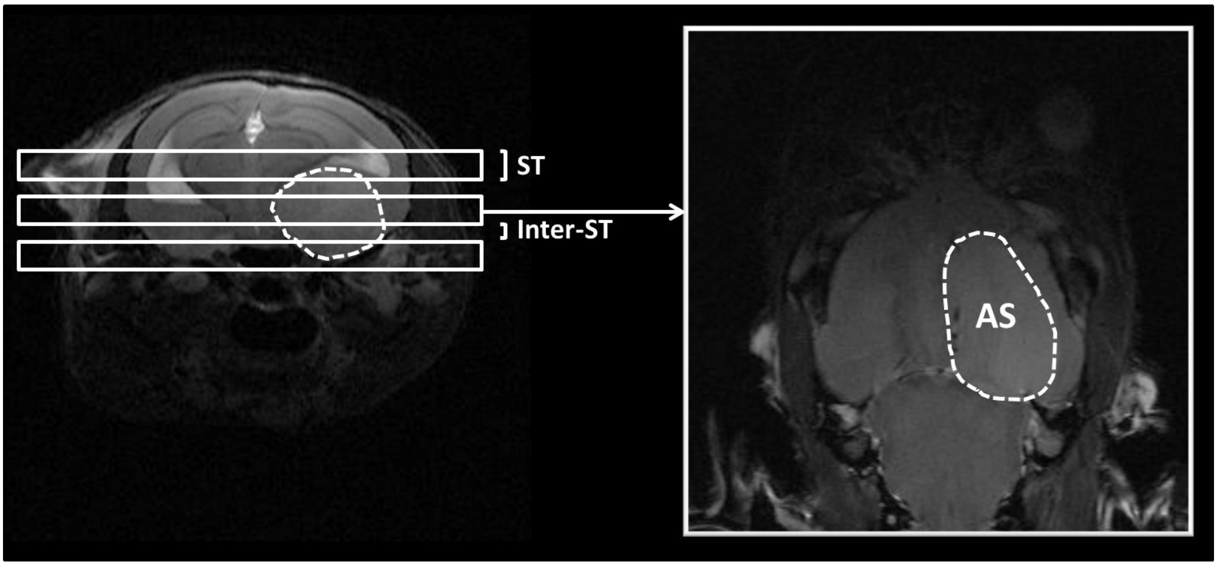

**Figure 3.5.** Scheme of the volume measurement carried out in mice. HR coronal $T_{2W}$ images were acquired for this purpose (image on the right). The surface area (AS) of the tumour (white dashed line contour) was measured in each slice of the coronal sequence, and the ST and the inter-ST (represented by horizontal slices over an axial image on the left) were taken into account for final volume calculation.

### *Calculation of tumour doubling time*

Doubling time (DT) of abnormal masses was calculated using the following formula (taken from [126]):

$$DT = \frac{(T-T_0)x\ ln2}{\ln(V-V_0)} \qquad \text{Eq.7}$$

where $T$-$T_0$ indicates the length of time between two measurements and $V_0$ and V denote the tumour volume at two points of measurement, the initial and the final, respectively.

### *MRS in vivo data processing*

In vivo MR SV spectra were processed with the TopSpin v1.3 software (Bruker Daltonik, GmbH): Lorenzian filter, 4 Hz of line broadening before Fourier transformation, manual zero- and first-order phase correction were applied and chemical shift was referenced to total creatine (3.03 ppm). The resulting spectra were exported in ASCII format and analysed with the software R v2.15.2 (The R Foundation for Statistical Computing) using home-written scripts for UL2 normalization (where each intensity was divided by the square root of the sum of squares of each spectra data point, Equation 8) [107]. Scripts for average spectra and SD calculation were also available. Spectral metabolite heights for major resonances were normalized for the region from 0 to 4.5 ppm for each spectrum.

$$I_{norm}i = \frac{I_{real}i}{\sqrt{\sum_0^{4,5}(I_{real}i)^2}} \qquad \text{Eq. 8}$$

where $I_{norm}i$ is the normalized intensity for each data point of the spectrum and $I_{real}i$ is the initial intensity for each data point between 0 and 4.5 ppm.

### *MRSI and PE-MRSI data processing*

MRSI data were post-processed essentially as described in reference [106]. In summary, data were initially processed with ParaVision 5.0 (Bruker BioSpin, Ettlingen, Germany). Then post-processing with 3D Interactive Chemical Shift Imaging v1.9.10 (3DiCSI) (Department of Radiology, Columbia University, NY, USA) was performed for line broadening adjustment (Lorentzian filter, 4 Hz), zero-order phase correction and exporting the data from individual voxels in ASCII format.

The dynamic MRSI processing module (DMPM) [127] running over MatLab (The MathWorks Inc., Natick, MA, USA) developed by the GABRMN was used to align all spectra within each MRSI matrix (using the choline peak as reference, 3.21 ppm), quantify the relative peak intensity changes in comparison with the basal unperturbed spectra in case of PE-MRSI (chemical shift of interest was 2.72 ppm for DMSO and 3.43 ppm for glucose) and display these changes as colour-coded maps (10 x 10 voxels). The 0 – 4.5 ppm region of each spectrum in the MRSI matrix was individually normalized to UL2 and the normalized matrix was exported in ASCII format, which is compatible with the Spectra Classifirer software [128] for performing the PR analysis of the spectra, and also with the scripts of the R program, and used to calculate the average spectra of different tissues types present in the VOI acquired.

### 3.11. Pattern recognition analysis

The PR analysis of different spectra was used to classify which voxels from MRSI matrices corresponded to normal brain tissue, ODG or GBM. In case of the therapy protocol (Section 3.9), it was used to distinguish between normal brain tissue, treated/responding and untreated/unresponsive tumour. In both cases, it was carried out using *SpectraClassifier* software [128] (available at http://gabrmn.uab.es/sc) and previously developed classifiers based on LDA, as described in [107] and [123], respectively. Voxel selection was carried out as described in Section 3.11.1. For the analysis, each individual voxel in the MRSI grid was referred to as spectral vector (spv) and considered as an individual case. After the PR studies, the classification result obtained for each voxel was colour-coded and represented as nosological maps for each matrix (see Section 3.11.2.3).

### 3.11.1. Voxel data selection and labelling for MRSI data grids

Considering an initial grid of 100 voxels from the MRSI VOI of each animal, those located in the edges of the grid were discarded due to possible low SNR; and those located in the tumour boundaries with normal tissue were also discarded to avoid spectral pattern mixing or contamination from different tissue types, essentially as described in [102, 107]. Others were labelled accordingly as normal tissue or tumour as shown in Figure 3.6. This labelling based in the $T_{2W}$ anomaly region will be known in other sections as "original tags" labelling.

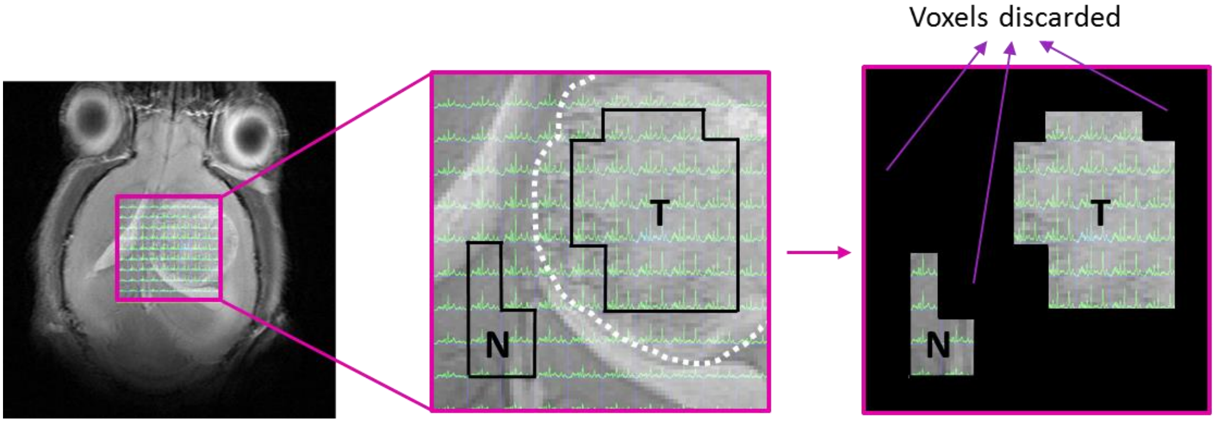

**Figure 3.6.** Voxel selection and labelling. N: normal brain parenchyma. T: tumour (could be labelled differently depending on tumour grade or type of protocol, i.e. treated or untreated tumour in case of therapy studies). Black area (on the right) summarizes discarded voxels for classifier training purposes.

### 3.11.2. Semi-supervised methodology for source extraction

#### 3.11.2.1. Non-negative Matrix Factorization

Non-negative Matrix Factorization (NMF) [129, 130] methods is a group of multivariate data analysis techniques aimed to estimate meaningful latent components, also known as sources, from non-negative data. Standard NMF methods decompose the data matrix *V* into non-negative matrices *W* (the sources) and the mixing matrix *H* (see Figure 3.7). The differences between them are given by the different cost functions used for measuring the divergence between *V* and *W*H* In [131] the authors present a variant of NMF, namely convex-NMF, in which the basis vectors of S are constrained to be convex combinations of the data points. Convex-NMF relaxes the NMF constraints to allow negative value use both in the data matrix and the sources.

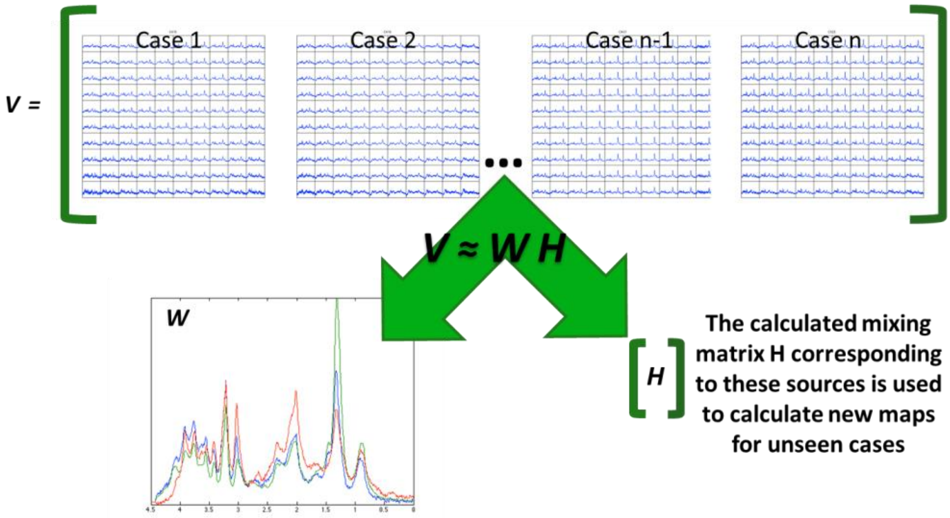
V =
Case 1
Case 2
Case n-1
Case n
V ≈ W H
W
H
The calculated mixing matrix H corresponding to these sources is used to calculate new maps for unseen cases

**Figure 3.7.** Scheme of Non-negative Matrix Factorization method: the data matrix *V* is decomposed into non-negative matrices *W* (the sources) and the mixing matrix *H*.

#### 3.11.2.2. Semi-supervised extraction of source signals

The diagram of the main steps followed in the semi-supervised source extraction methodology is shown in Figure 3.8.

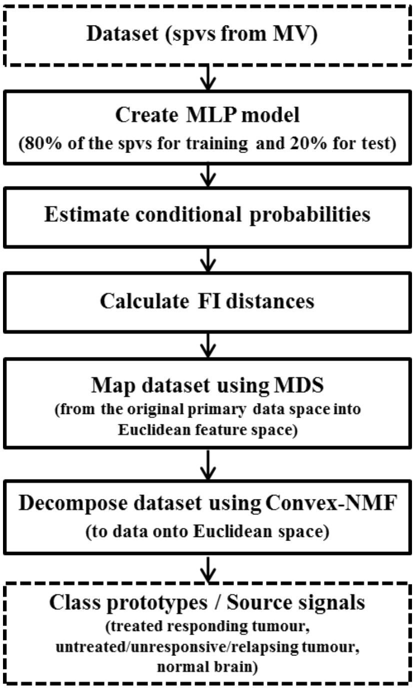
Dataset (spvs from MV)
Create MLP model
(80% of the spvs for training and 20% for test)
Estimate conditional probabilities
Calculate FI distances
Map dataset using MDS
(from the original primary data space into Euclidean feature space)
Decompose dataset using Convex-NMF
(to data onto Euclidean space)
Class prototypes / Source signals
(treated responding tumour, untreated/unresponsive/relapsing tumour, normal brain)

**Figure 3.8.** Diagram showing the main steps followed in the semi-supervised source extraction methodology, from the collection of MRSI data grids to the generation of the three main sources describing the metabolic profile of the tumours analysed.

From the 100 voxels included in the MRSI VOI of each animal, those located in the edges of the grid, with a SNR (calculated as in [104]) lower than 57.2 ± 26.04 were discarded; and those located in the tumour boundaries with normal tissue were also discarded (as also described in Section 3.11.1) to avoid spectral contamination from different tissue types essentially as described in [102, 107]. Voxels outside the tumoural mass (as shown by $T_{2w}$ MRI), showing a high accumulation of DMSO in the color-coded maps calculated from PE-MRSI sequences, were also discarded for training purposes [123]. A total of 508 spectral vectors from the training set were included in the analysis. The selected spectral vectors were labelled as tumour (responding and control) and normal parenchyma, initially assuming that all the voxels inside each tumour belonged to the same category (responding or control). The robustness of this assumption was later on evaluated using an independent test set.

Regarding the source calculations, this was done in collaboration with Sandra Ortega-Martorell (from the Department of Mathematics and Statistics Liverpool John Moores University Liverpool, United Kingdom). The 80% of those 508 spectra (randomly selected) were used to create the MLP model, which was assessed with the remaining 20% of them. This model was used to estimate the conditional probabilities of class membership for each case, which were then used to define the Fisher Information (FI) metric. Three sources were calculated then, following the three steps of the semi-supervised methodology mentioned before, one of them to represent the responding tumour, another to represent the tumour without treatment, and third for the normal tissue.

#### 3.11.2.3. Nosological imaging of the response to therapy

For the generation of colour-coded nosological images of each individual mouse the values of the mixing matrix were used (calculated as in Section 3.11.2.1), as it represents the proportions in which each source is contributing to each voxel (as shown in Figure 3.9, middle). Then the final resulting nosological image was produced, which shows the highest correlation of each voxel to the sources, being either responding or untreated/unresponsive/relapsing or normal brain (Figure 3.9, at right). Nosological images were produced throughout the course of therapy to track full or partial response changes (in case of treated animals), as presented in Figure 3.9 (on the right). Nosological images were also produced for untreated control animals for comparison.

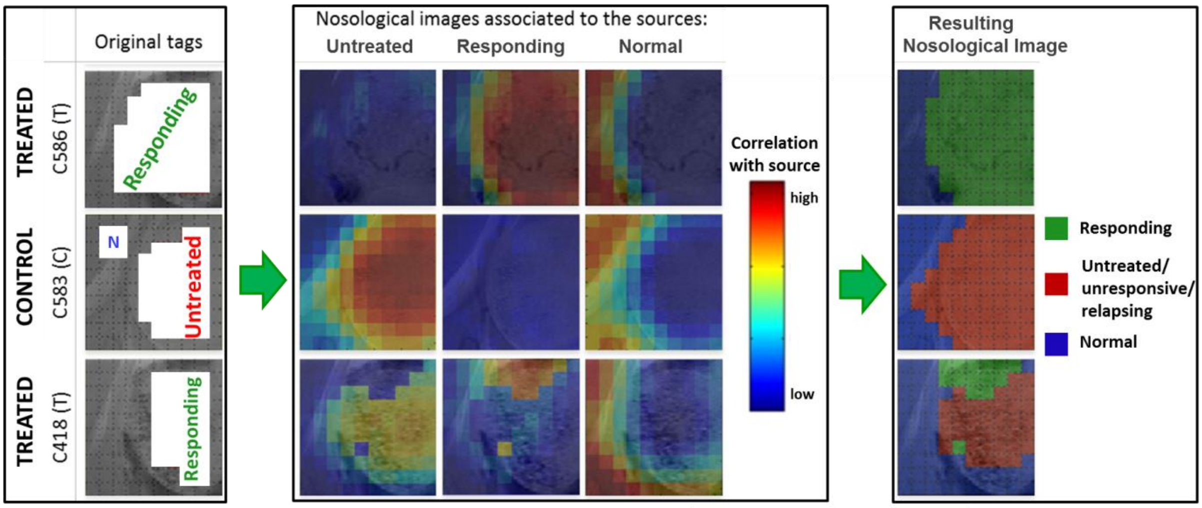
Original tags
TREATED
C586 (T)
Responding
CONTROL
C583 (C)
N
Untreated
TREATED
C418 (T)
Responding
Nosological images associated to the sources:
Untreated
Responding
Normal
Correlation with source
high
low
Resulting Nosological Image
Responding
Untreated/ unresponsive/ relapsing
Normal

**Figure 3.9.** Nosological imaging of response to therapy. **On the left:** Original labelling of voxels of the MV grid, based on the MRI (normal brain parenchyma vs tumour tissue) and therapy status (untreated and treated, i.e. responding). **In the middle:** Nosological images showing correlation of the voxels to each source (red being high and blue being low correlation). **On the right:** Resulting nosological image showing the source with the highest correlation with each voxel, i.e. green – voxels with the highest correlation with the responding source, red – voxels with the highest correlation with untreated/unresponsive source and blue – voxels with the highest correlation with normal brain tissue.

### 3.12. Statistical analysis

The statistical analysis was carried out using IBM SPSS Statistics v.20 software. Data was evaluated for compliance with the normal distribution using the Shapiro–Wilk and Kolmogorov–Smirnov tests. The survival rate of mice was calculated using Kaplan-Meier analysis, whose significance was calculated using the log-rank tests and Tarone-Ware. Metabolite height ratios from SV MRS spectra and tumour volumes were inspected for normality with the Kolmogorov-Smirnov test, compared using the Student's t-test for paired samples, in case of samples following a normal distribution, and the Mann-Whitney U-test was applied to non-normal distributions, while variance homogeneity was evaluated with the Levene's test. The ANOVA test applying Bonferroni correction was used to compare DMSO accumulation (seen in colour-coded maps) from MRSI sequences between normal brain parenchyma, treated and control tumours. This test was also applied for comparing the immunohistochemical quantifications for Ki67, caspase 3 and mitoses between control and treated groups. The presence of outliers in samples was tested with Grubb's and Dixon'stests. A contingency analysis based on Chi-Square tests and Phi and Cramer´s V symmetric measures, determined the correlation between histopathology markers and the response detected by the sources methodology. Student's t-test was applied to compare Ki67 staining between responding and non-responding tumours. Finally, for the PR analysis the Sequential Forward Feature Selection (SFFS) method was used for feature selection and the classifier was developed by Fisher's LDA. The performance of each classifier was evaluated for the training set and for the independent testing set, using bootstrapping method and balanced error rate (BER), implemented using the ROC curves (receiver operating characteristic) and the leave-one-out (LOO) method.

# 4. Pilot study and characterisation of GEM

(Objective 1)

## 4.1. Specific objectives

**4.1.1.** To genotype animals from the two different colonies of GEM previously described in Section 1.2.2 (S and R colonies) in order to identify animals carrying out the desired genetic modification for further crosses or evolution monitoring.

**4.1.2.** MRI systematic screening of GEM colonies to assess the ability of detection of abnormal brain masses before symptoms onset and to estimate non-invasively tumour incidence rate in each colony.

**4.1.3.** Identification of animals with low/intermediate grade tumours for potential further use in the disaggregation protocol of Section 5.

## 4.2. Specific Materials and Methods

Mice from the S and R colony were genotyped as described previously in Section 3.5 and only those possessing the desired transgene were further screened by MRI as in Section 3.10.1. In principle mice were scanned randomly, unless some individuals showed brain tumour symptoms reported by the housing facility staff (the protocol for animal inspection for brain tumour symptoms can be found in Annex 3). In this instance, those animals had priority for screening. Once an abnormal mass was detected by MRI it was further explored using some or all of the following protocols, depending on the condition of the animals and/or the BioSpec scanner availability: SV MRS (as per Section 3.10.2), CE MRI (as per Section 3.10.1), PE-MRSI with DMSO and glucose in hypothermia (as per Section 3.10.3) and DCE (as per Section 3.10.1). All the experiments were conducted according to experimental protocols, previously approved by the local ethics committee (CEEAH 1176).

## 4.3. Results and Discussion

At the start of this section, it needs to be mentioned, that the pilot studies of the GEM colonies included in this section are continuation of the protocol previously performed by other GABRMN group members and some results are shared with those colleagues that initiated this work. In this thesis only the representative, previously not described cases, and studies for the S and R colonies, in which the PhD text author participated, are presented in a retrospective view.

### 4.3.1. Genotypic characterisation

Since 11/2011, when the pilot study carried out within this PhD work was started, until 04/2013, when the pilot study was finished, the number of animals genotyped from each colony, as well as the number of animals confirmed to be transgenic for potential MR screening are presented in Table 4.1 below. The information on the genotype was also used for breeding and maintenance of the colonies.

**Table 4.1**. Number of GEM animals genotyped and found to be transgenic by PCR genotyping (as per Section 3.5), and transgenic rate in each colony.

| Colony | No. of animals genotyped | No. of transgenic animals in each colony | Transgenic rate in each colony (%) |
|---|---|---|---|
| **S** | **130** | **56** | **43 %** |
| **R** | **139** | **71** | **51 %** |

The overall number of genotyped animals was 130 and 139 for the GEM S and R colonies, respectively. The genotypes found for the S colony were as follows: Tg/Ko+/-, Tg/Ko-/-, Tg/wt, wt/Ko+/-, wt/Ko-/- and wt/wt. The percentage of the transgenic offspring (including genotypes Tg/Ko+/-, Tg/Ko-/-, Tg/Wt ) was of 43% of all genotyped animals, and the transgenic genotype with a higher percentage was Tg/Ko+/- (Figure 4.1) with a total of 24%, which agrees with previous group results and animals genotyped during the period from 09/2005 until start of this study (Figure 4.2). However, the percentage for all transgenic, which was initially 56%, decreased to 47% during the period of 3 years during, which the studies of this PhD were performed. According to the Breeding Strategies for Maintaining Colonies of Laboratory Mice by Jackson Laboratory, 50% of the offspring should be transgenic, when breeding is done correctly [136]. Both values are close to the expected 50%.

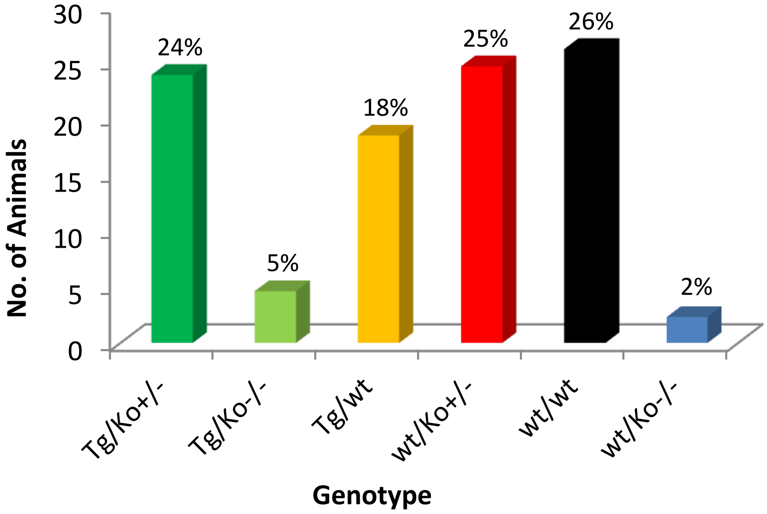

**Figure 4.1.** Total number of animals from the colony S genotyped (n = 130) during the pilot study within this PhD work, and their genotype distribution (percentage of total on top of the bar).

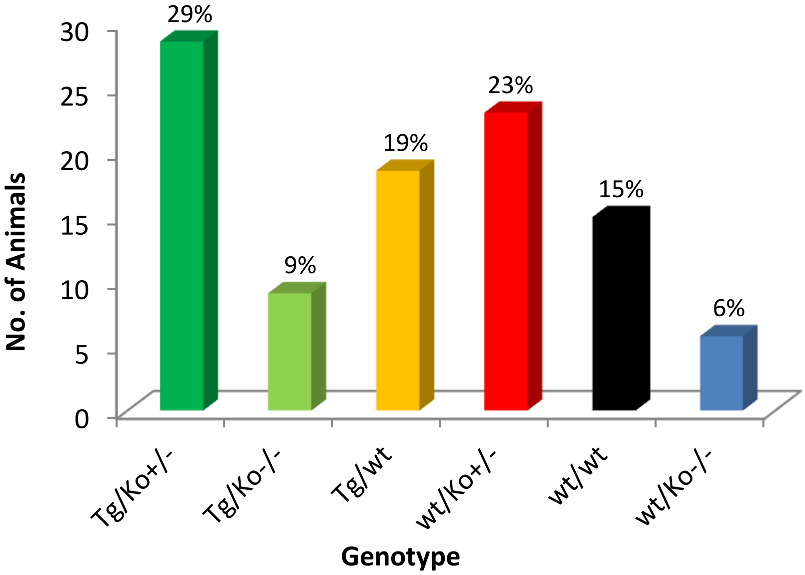

**Figure 4.2.** Total number of animals from the colony S genotyped (n = 781) prior to the pilot study of this PhD work since the establishment of the colony, and their genotype distribution (percentage of total on top of the bar).

Regarding the R colony, there were two possible genotypes: Tg and wt, The distribution of these genotypes is presented in Figure 4.3. It can be seen that the breeding was done correctly and around 50% of all offspring was confirmed to be transgenic.

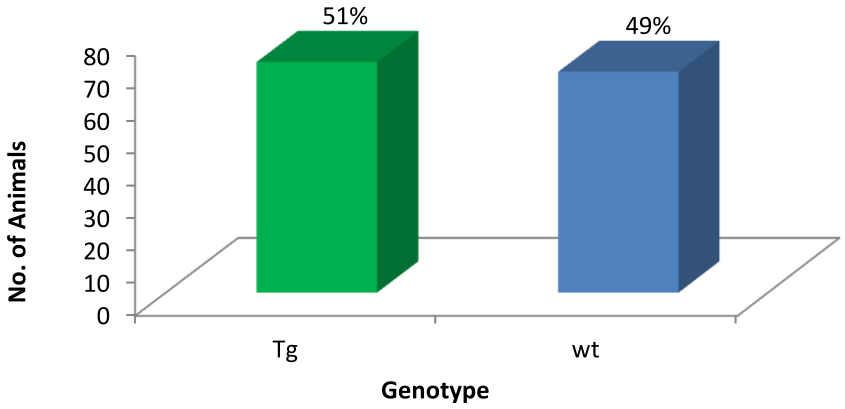

**Figure 4.3.** Total number of animals from the colony R genotyped (n = 139) during the pilot studies within this PhD work, and their genotype distribution (percentage of total on top of the bar).

### 4.3.2. MR screening and tumour incidence

The mice that were genotyped and found to be transgenic continued to the pilot study and were explored by MR (as described in Section 3.10). However, the health status of the animals was assessed visually by the veterinary staff of the UAB *Servei d'Estabulari* according to Annex 3 and those with reported specific abnormal symptoms had the priority for the MR screening, as the symptoms could be an indication of the presence of an abnormal brain mass. The most common symptoms developed by mice of both, S and R colonies, were: impaired mobility or paralysis, kyphosis, cachexia or piloerection. Additionally, R colony animals, found later to be affected by brain tumour, were typically smaller than the other mice in the same litter and had abnormal motion behaviour, i.e. running in circles. The distribution of these symptoms can be seen in Figure 4.4. As the pilot study and MRI screening was performed on most of Tg animals, regardless of the presence of abnormal symptoms and behaviour, the number of animals in Figure 4.4 is smaller than Table 4.1.

If MRI screening did not detect a tumoural mass and some animals with clear suffering symptoms were sacrificed, while the reaming mice returned to the animal facility and continued in the pilot protocol.

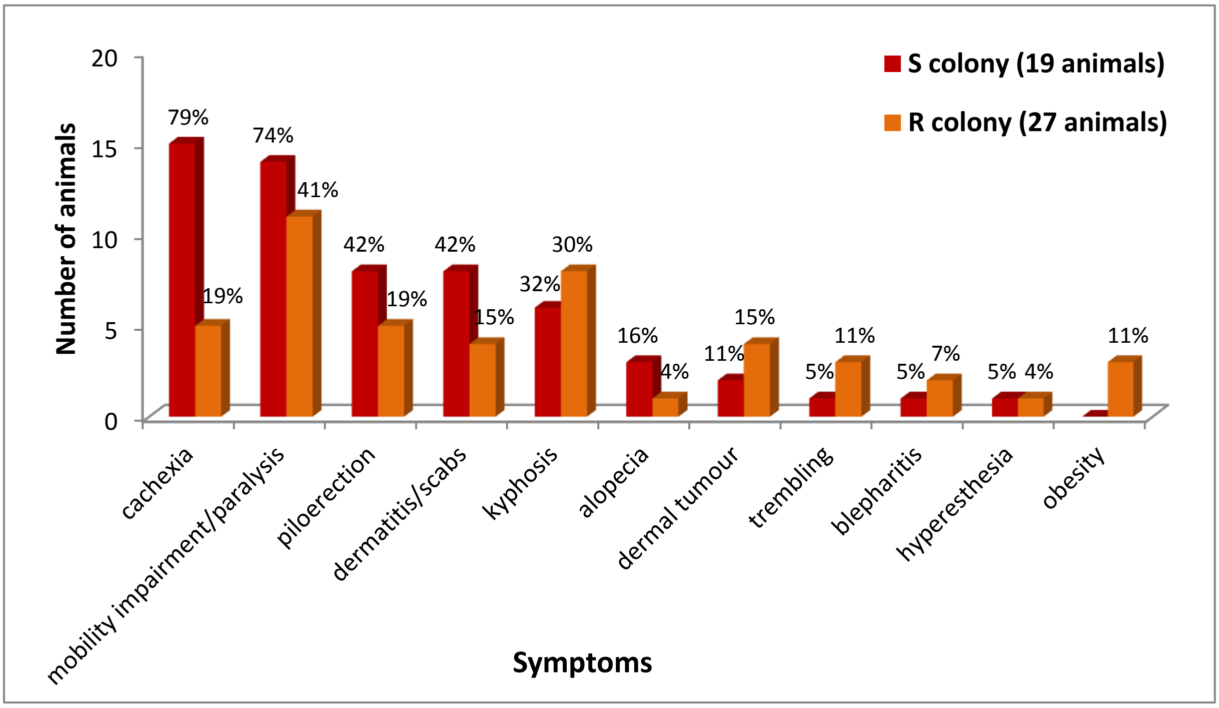

**Figure 4.4.** Distribution of abnormality symptoms developed by mice among S and R colonies prior to abnormal brain mass detection by MRI.

The total number of the animals screened by $T_{2W}$ MRI in order to investigate a potential presence of brain lesions is shown in Table 4.2. It can be noticed that the number of the animals screened during this pilot study is higher that the number of animals genotyped (Table 4.1) and this is because of the animals that were previously genotyped by the group prior to 11/2011 and were also included in the pilot MRI evaluation described in this section.

Despite having a high number of animals explored (Table 4.2), the tumour incidence detected by MRI is far from the initially described by the developers of the S colony (>90%, as reported in [63]) and for the present pilot study it reached a value of 16%. This was considering only the animals with the inherited transgene. However, it should be noted that the percentage of tumours in [63] was assessed by histopathological analysis of all transgenic animals, which was not carried out in our case. In this work, only animals that were previously explored by MR and for which an abnormal mass had been detected were analysed by histopathology. This could partially explain the lower tumour incidence detected, but the fact that the remaining non-explored/non-histopathologically analysed animals did not show the symptoms of disease, could be interpreted as indication that they did not develop tumoural mass during the investigated time span of 18 months, which was longer than the span of the investigated evolution time in [63] of 12 months. The majority of lesions (8 out of 9) detected by MRI during this work developed in the animals with the genotype Tg/Ko+/-, while one was in a Tg/wt mouse.

**Table 4.2.** Number of animals screened and tumour incidence rate among transgenic animals in each colony during the period of this work, as well as during the whole pilot studies.

| Colony | No. of transgenic animals | No. of animals MR-screened | No. of animals with MR-detectable abnormal mass | Tumour incidence among Tg animals (%) |
|---|---|---|---|---|
| *Time frame of this PhD work* | | | | |
| **S** | **56** | **138** | **9** | **16 %** |
| **R** | **71** | **54** | **1** | **1 %** |
| *Pilot study prior to this PhD work* | | | | |
| **S** | **439** | **363** | **70** | **16%** |
| **R** | **47** | **68 *** | **6** | **13%** |

* Symptomatic wt animals were included in MR-screening, hence the higher number of animals screened than numbe of transgenic animals.

The tumour occurrence for the R colony was even lower and during this thesis work only one lesion was detected, which corresponds to ca. 1% incidence rate among the transgenic animals. It did not confirm the expected tumour incidence rate reported previously by the original researches (>90% developed by 4 months of age [65]) and the majority of transgenic animals either with (23 animals) or without neurological symptoms explored in the pilot protocol showed no presence of abnormal brain masses by MRI during the 12 months of investigation time frame.

The differences between the incidence observed during this pilot study and the values reported in the literature could be due to environmental factors such as stress, as described in [137], although possible additional genetic alternation linked to the transgene and passed on to the progeny could also play a role in the decrease of tumour incidence. One of such alterations could be instability of the number of transgene copies in the progeny mice. The developers of both colonies noted increased penetrance with an increased dosage of the transgene, and although in the S colony it had no direct influence on penetrance [63], the increased gene dosage may require fewer additional genetic events for transformation, as in [138].

### 4.3.3. MRI/MRS/MRSI/PE-MRSI/DCE-MRI characterisation

The animals, in which a mass was detected, underwent further explorations as described in Section 3.10, trying to obtain non-invasively as much information on the tumour type and tumour evolution as possible. This protocol was applied to the S and R colonies and as a result various explorations were performed (Table 4.3). Out of the two colonies studied, the colony S had the larger number of lesions detected (during the 18 months period of this work, 9 as opposed to 1 for the R colony), therefore the total number of individual explorations performed was also higher.

**Table 4.3.** Number and type of MR studies performed additional to $T_{2W}$ MRI.

| Colony/Exploration | CE | SV | PE-MRSI with DMSO | PE-MRSI with D-glucose | DCE-MRI |
|---|---|---|---|---|---|
| S | 6 | 14 | 6 | 4 | 1 |
| R | 1 | 1 | 1 | 1 | - |

For some animals, various explorations of the same kind were performed, e.g. SV or DMSO-MRSI, at different time points along the tumour development time, so that in some cases we could gather a fairly complete longitudinal monitoring of tumour progression, including tumour volume growth curve and spectroscopic characteristics. To measure the tumour volume, the high-resolution $T_{2W}$ sequences were used in the coronal plane and also 3D sequences were sometimes used (see section 3.10.4 for details). In general, low doubling time could suggest low tumour grades, while high grade ones tend to duplicate mass faster. Additionally, $T_{1W}$ CE studies reveals whether the BBB is intact or broken and the latter is also indication of the presence of a high grade tumour. When the lesion volume was large enough to position a voxel of $(2.5\text{mm})^3$ (i.e. 2.5 x 2.5 x 2.5 mm, 15.6 µl) therein, these animals were studied by MRS to analyse the spectroscopic pattern of the mass and provide additional information as to whether they were low grade or high grade tumours. Low grade tumours are characterized by low choline/creatine ratio, quite preserved NAA and low mobile lipid content, whereas high grade tumours present a specific spectral pattern, which included high choline/creatine ratio, NAA level greatly decreased and a significant presence of mobile lipid signals [72, 139]. All animals, whenever possible, underwent scans at two TE, SET and LET (12 and 136 ms, respectively), although in some specific cases not sufficient homogeneity was reached to acquire a usable spectrum, i.e. lesions were located in areas of tissue-air interface (as shown in Figure 4.5), there was a presence of bleeding (Figure 4.6), etc.

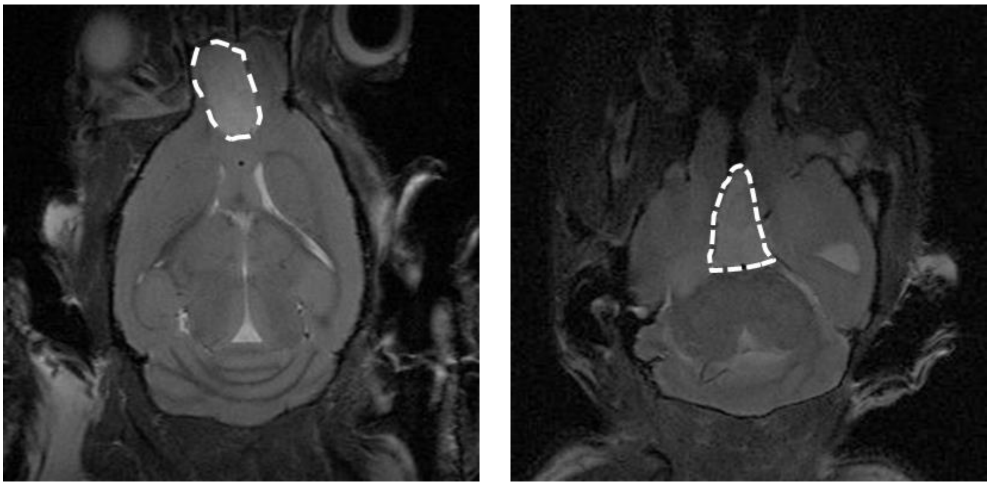

**Figure 4.5**. $T_{2W}$ images of cases S851 (on the left) and S857 (on the right) with tumour location (white dotted line), respectively in the olfactory bulb and the brainstem, compromising possible MRS/MRSI explorations.

If the location and size of the mass permitted it, also MRSI with and without metabolic perturbations were acquired and this helped to get additional information about tumour grade and tumour segmentation. The type and grade of most tumours was confirmed by post-mortem histopathological analysis based on haematoxylin-eosin staining performed within the region correlating with MRSI (Section 3.8). Results of representative animals are presented below.

**R colony**

The mouse R279 (transgenic, male) had an abnormal brain mass detected at 14 weeks of age when it was MRI screened due to the presence of symptoms of suffering, i.e. piloerection, hunched posture and decreased activity. At the day of the MRI detection, the abnormal mass already was large in size (126 mm$^3$) with clear haemorrhage (seen in Figure 4.6, and pointed with a red arrow, black region showing shortened T2 possibly due to iron in blood). The MR explorations were performed within 6 days since detection until the animal was sacrificed (see Figure 4.7). A piece of the mass was frozen for potential tumour disaggregation (as in Section 5), while other piece went for histopathological analysis and was diagnosed as GBM.

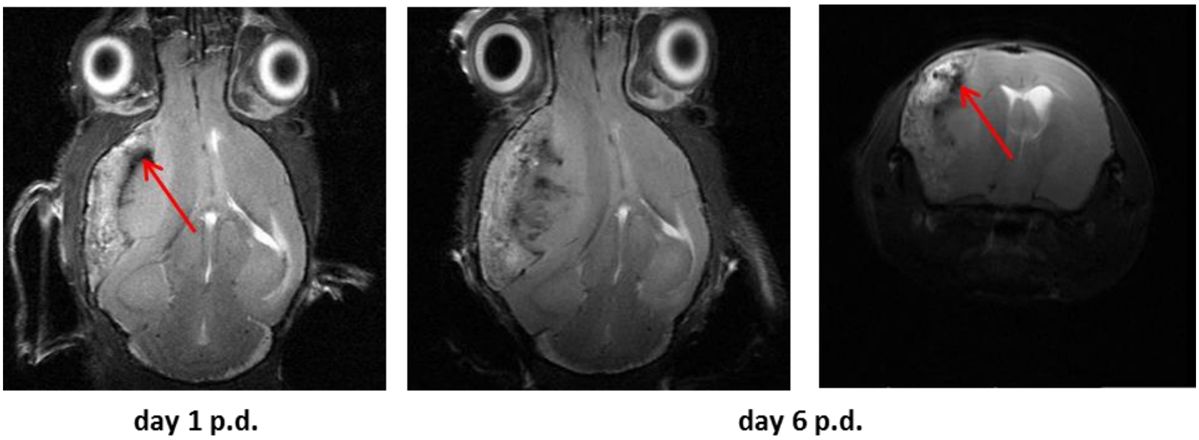

**Figure 4.6.** $T_{2W}$ MRI of R279 mouse brain at coronal orientation acquired on the day of detection (on the left) and at 6 days post-detection (p.d.) (in the middle), and at axial orientation (on the right) acquired at 6 days p.d. Red arrows indicate possible haemorrhage within the tumoural mass.

Figure 4.7 shows mass progression for this tumour within 6 days from the initial mass detection and explorations performed at each time point. It can be noticed that within this short period of time the mass volume increased nearly doubled (the calculated doubling time of 7.2 days). However, it needs to be stressed that the doubling time can vary depending on the growth curve point and in this particular case it was fast because of the late detection of the mass.

Due to the relatively large time needed for some explorations (e.g. MRSI and PE-MRSI), they could not be performed at the same day, due to restrictions related too long anaesthesia periods inside the magnet.

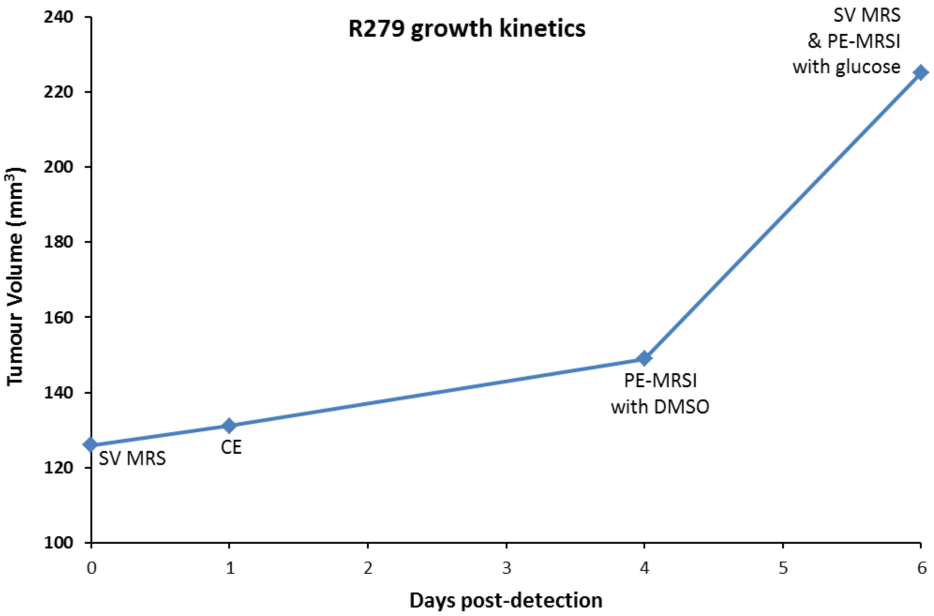

**Figure 4.7.** R279 tumour mass growth from the day of detection until the sacrifice of the animal, and type of explorations performed on each day. $T_{2W}$ MRI explorations were also performed at every time point listed.

On day one p.d. of the abnormal mass, the $T_{1W}$ CE exploration showed a partially broken BBB, suggesting possible transition to a higher grade tumour (Figure 4.8). Transition from low/intermediate to high grade was expected for these tumours, as described by the researchers who developed this transgenic model [65]. When comparing the SV MR spectra from the day of the abnormal mass detection with the spectra obtained on the last day of exploration, i.e. 6 days p.d., some spectral pattern changes may be detectable (Figure 4.9), although the MRS quality was borderline. These changes could include decrease in the NAA signal (2.01 ppm) with high Lac/ML resonances (ca. 1.3 ppm) visible at both explorations times for SET (Figure 4.9.A). The LET spectra had even worse SNR and only a possible increase at day 6 p.d. for the signal at 3.42 ppm, which could correspond to taurine. Also the doubling time calculated (7.2 days) was much faster than, for example, that of case S871 from the S colony (22.7 days) shown below and it was closer to the doubling time of the GL261 tumours (2.6 ± 0.3 days, n = 17), which could indicate a high grade tumour.

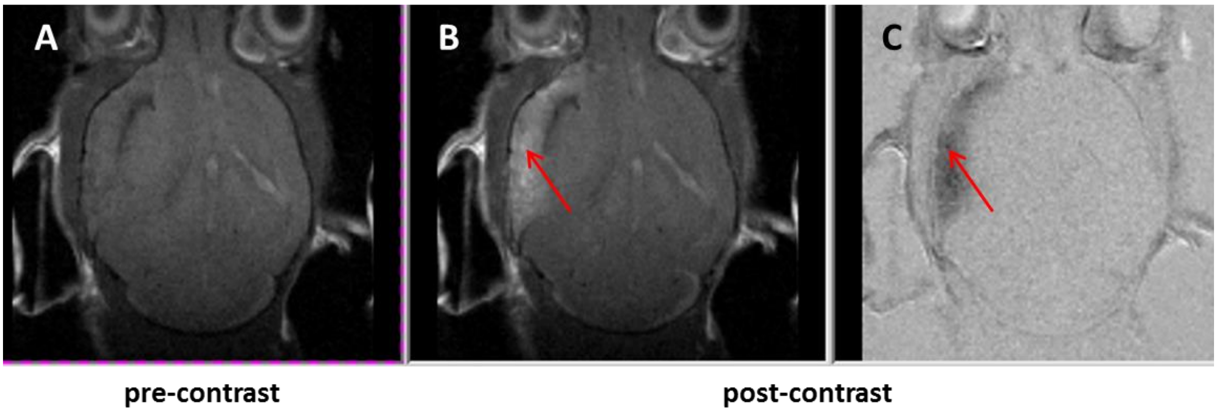

**Figure 4.8.** $T_{1W}$ coronal images of R279 **A)** pre- intraperitoneal contrast administration and **B)** post-intraperitoneal contrast administration acquired one day p.d. **C)** Difference image between A) and B) showing the zone of contrast intake as hipointense region. Red arrows indicate the broken BBB region.

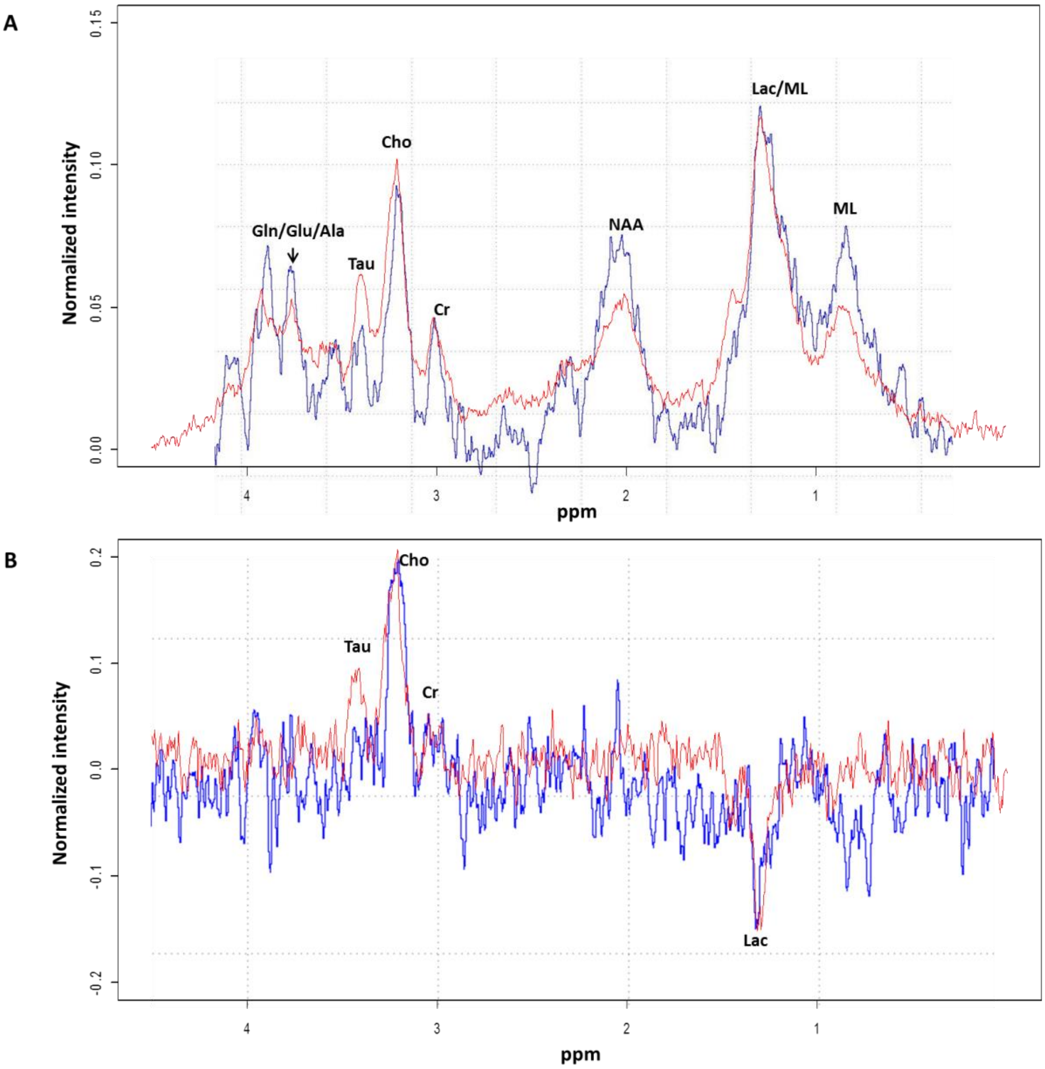

**Figure 4.9.** Comparison of the R279 tumour MR spectra on the day of the abnormal brain mass detection (blue spectra) and on the day 6 p.d. (red spectra) at **A)** SET (12 ms) and **B)** LET (136 ms). Cho: choline, Cr: total creatine, Gln: glutamine, Glu: glutamate, NAA: N-acetylaspartate, Lac: lactate, ML: mobile lipids, Tau: Taurine.

In previous studies, our group had demonstrated the differential accumulation and wash-out kinetics of DMSO in normal versus tumour-afflicted brain parenchyma, providing an efficient CE in glial tumours independent of tumour grade and state of BBB permeability [113]. The mentioned study was performed with both the GL261 GBM tumour bearing mice and also mice from the S GEM colony, which presented DMSO "hotspots" inside the tumoural mass and the close-by surrounding parenchyma. During this pilot study, PE-MRSI with DMSO perturbation was also performed on the R279 case, belonging to R colony, on the day 4 p.d. of the brain mass.

The MRSI spectra acquired for the R279 case in the relevant volume (VOI) were used to calculate maps of DMSO accumulation detectable with MR in comparison with basal spectra (Figure 4.10). As in the previously described cases [113], there was clear accumulation of DMSO on the tumour boundaries and a "hotspot" can also be seen in Figure 4.10A. The maximum apparent DMSO accumulation in the "hotspot" was detected 44 minutes post-injection. It is unclear as of now the differential origin of the R279 DMSO "hotspot" accumulation in its tumour border, especially without a histopathology correlate. Among possible causes for this "hotspot" we could cite: (i) the tumour mass may infiltrate in some occasions beyond the $T_{2W}$ hyperintensity zone, (ii) there may be some differential DMSO retention in the periventricular zone, (iii) peritumour cells attracted to the tumour mass (inflammatory cells, neural stem cells) may also show differential DMSO retention (text adopted from [123]).

PE-MRSI with glucose (hyperglycaemia) under mild hypothermia was also performed for the case R279 as shown in Figure 4.11. We can observe a "hotspot" of glucose, as well as lactate, accumulation inside the tumoural mass, and its location seems also different from the DMSO accumulation "hotspot", reinforcing possible different biological reasons for differential MRS pattern change caused by each perturbation. The glucose PE-MRSI study allowed the case to be tested with an automated classifier for spectral MR data previously developed by our group [107], which allows to distinguish normal brain tissue, ODG (grade II) and GBM (grade IV). Most of the voxels from the MRSI of R279 were classified as GBM (Figure 4.12). Unfortunately, no robust classifier was available yet for ODG of intermediate grade. Accordingly, we cannot discard grade III from the PE-MRSI based classier. Still, grade III/IV would be in agreement with previous explorations indicating an intermediate/higher grade tumour, i.e. spectral characteristics and CE MRI showing BBB disruption by contrast intake in the abnormal mass, and in agreement with histopathological diagnosis as GBM.

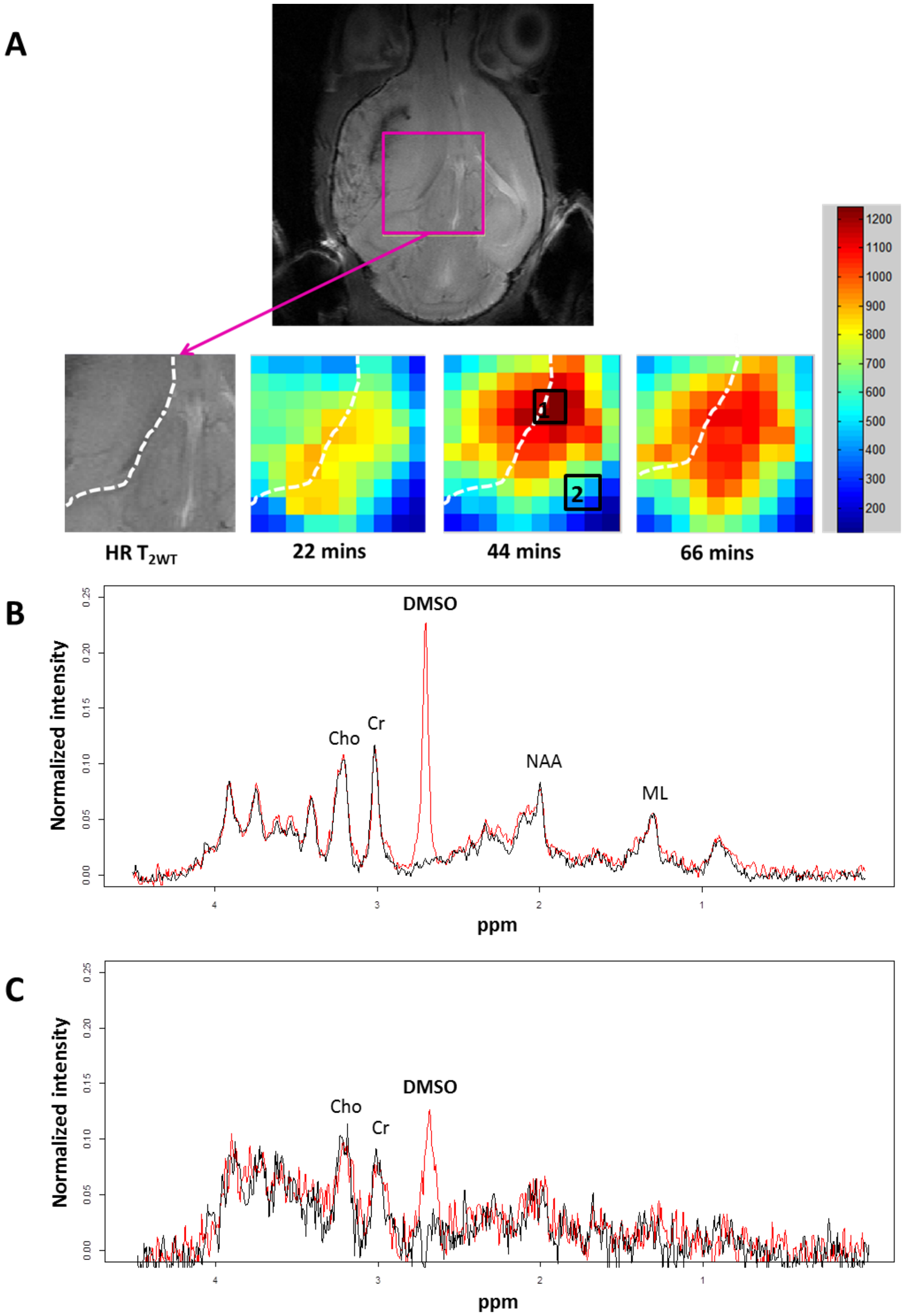
A
HR $T_{2WT}$
22 mins
44 mins
66 mins
1
2
1200
1100
1000
900
800
700
600
500
400
300
200
B
DMSO
Cho
Cr
NAA
ML
Normalized intensity
0.00
0.05
0.10
0.15
0.20
0.25
4
3
2
1
ppm
C
Cho
Cr
DMSO
Normalized intensity
0.00
0.05
0.10
0.15
0.20
0.25
4
3
2
1
ppm

**Figure 4.10.** PE-MRSI with DMSO of the R279 mass. **A)** VOI on the reference $T_{2W}$ image (top) with enlargement of VOI and colour-coded intensity maps representing the DMSO signal detected after its i.p. administration (bottom) with the intensity scale (right) ranging from blue (low DMSO accumulation) to red (high DMSO accumulation); white dotted line labels the $T_{2W}$ defined tumoural mass borders and black squares 1 and 2 correspond to the voxels of the matrix from which individual spectra were extracted and shown in B) and C). **B)** Spectra of the voxel marked as 1 from the high accumulation zone and **C)** spectra of the voxel marked as 2 from the low accumulation zone in the MRSI grid acquired before (black spectra) and 44 minutes after (red spectra) the administration of DMSO. Cho: choline, Cr: total creatine, NAA: N-acetylaspartate, ML: mobile lipids.

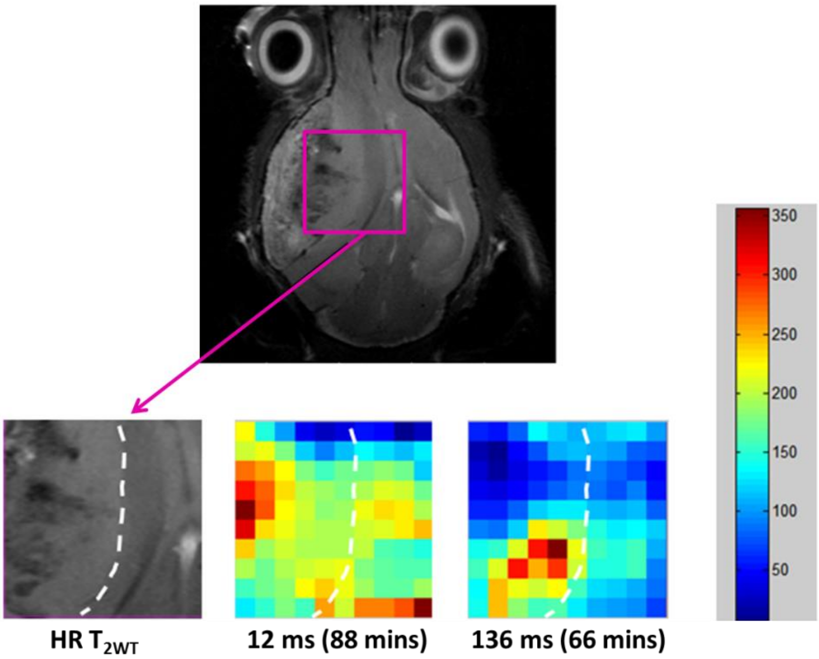

**Figure 4.11.** PE-MRSI: hyperglycaemia under mild hypothermia of R279. VOI on the reference $T_{2W}$ image (top) with enlargement of VOI and colour-coded intensity maps representing D-glucose signal changes detected at SET (12 ms) after 88 minutes post glucose i.p. administration and lactate signal detected at LET (136 ms) after 66 minutes post glucose i.p. administration (bottom); white dotted line labels the $T_{2W}$ defined tumoural mass borders. The signal intensity scale (right) ranges from blue (low signal) to red/brown (high signal).

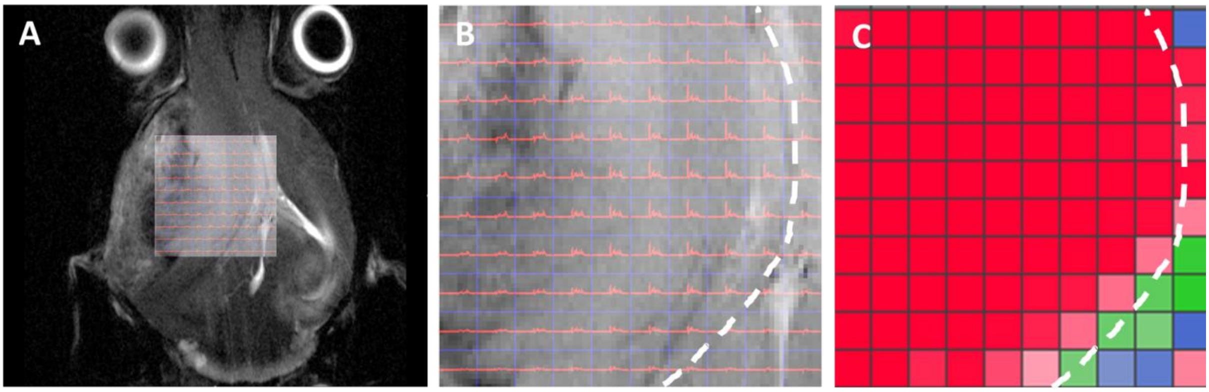

**Figure 4.12.** PR analysis for R279 mouse at day 6 p.d. **A)** VOI superimposed with the reference $T_{2W}$ image. **B)** Enlargement of VOI shown in A with spvs for short TE shown in red. **C)** Nosological map obtained with the automated classifier results - blue voxels are assigned to normal brain parenchyma, red voxels to GBM and green voxels to ODG. Tumour boundaries from $T_{2W}$ images are marked with a white dotted line.

**S colony**

As it can be seen in Table 4.2, the S colony produced a larger number of detectable masses than the R one. During this pilot study 9 abnormal masses were detected. Here we present the results obtained for one representative case S871. The animal S871, male, of genotype Tg/Ko+/- had an abnormal brain mass detected at 42 weeks of age, with no previous symptoms of abnormal behaviour. Since the day of detection, explorations performed included: SV, CE, as well as PE-MRSI with DMSO and with glucose in hypothermia. Figure 4.13 shows growth kinetics of the tumour and time points for each exploration acquired and Figure 4.14 presents $T_{2W}$ images, showing visible changes in growth volume between day 2 and 51 p.d., as this tumour presented a slow-growing pattern.

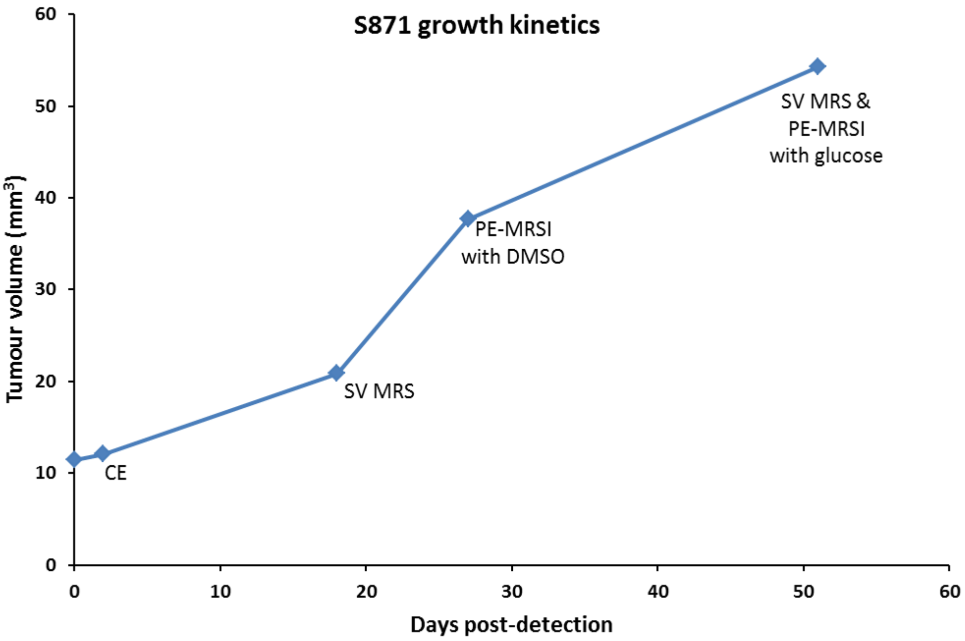

**Figure 4.13.** S871 tumour volume growth profile measured from $T_{2W}$ images from the day of the abnormal mass detection until the sacrifice of the animal and the additional type of explorations performed on each day.

The abnormal mass had a volume of 11 mm$^3$ at the time of detection and developed in the temporal lobe. It was possible to monitor tumour progression by MR for 51 days from the time of initial detection. As it can be seen, the size of the abnormal brain mass displayed a slow volume growth (doubling time of 22.7 days) as compared with GL261 GBM tumours (see Section 5) and for which mass doubling time was 2.3 ± 0.4 days (n = 17). This suggested a less aggressive nature of this tumour compared to the GL261 GBM, although controversial information was obtained from the $T_{1W}$ CE exploration, which revealed a somewhat compromised BBB (red arrow in Figure 4.15). Altogether, these data could be indicating the presence of a grade III tumour.

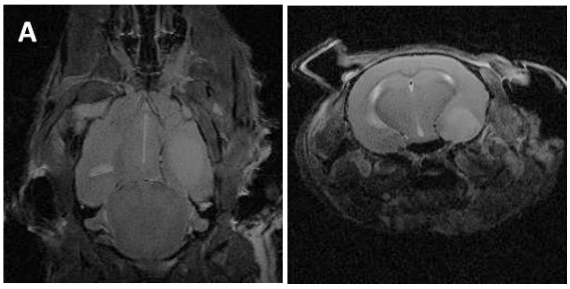

**day 2 p.d.**

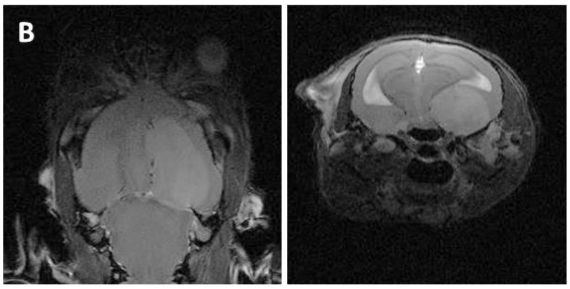

**day 51 p.d.**

**Figure 4.14.** $T_{2W}$ HR MRI of S871 mouse brain at acquired on **A)** the day 2 p.d. and **B)** 51 p.d. Coronal orientation (on the left) and at axial orientation (on the right) are shown for each day.

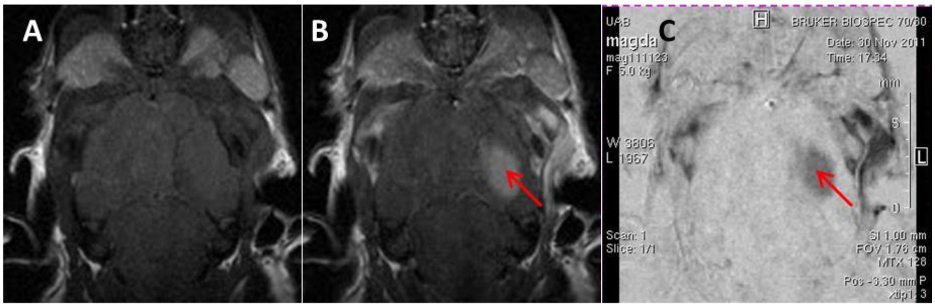
A
B
C
UAB
magda
mag111123
F 5.0 kg
H
BRUKER BIOSPEC 70/30
Date: 30 Nov 2011
Time: 17:34
mm
5
0
L
W 3806
L 1967
Scan: 1
Slice: 1/1
SI 1.00 mm
FOV 1.76 cm
MTX 128
Pos -3.30 mm P
zdp1: 3

**pre-contrast** **post-contrast**

**Figure 4.15.** $T_{1W}$ coronal images of S871 **A)** pre-intraperitoneal contrast administration and **B)** post-intraperitoneal contrast administration acquired on the day 2 p.d. of the abnormal mass. **C)** Difference image between A) and B) showing the zone of contrast intake (red arrows).

Regarding the MR spectra obtained (refer to Figure 4.16), those acquired on the day 51 p.d. did not show major changes from the ones obtained on the day 18 p.d. However, because of the poor quality of the SV MRS, this was checked also by quantitative evaluation of some metabolites peaks ratios (Table 4.4), which confirmed that the values on the day 18 day 51 p.d. were similar. This could be interpreted as suggesting that there was no clear progression in tumour aggressiveness. Therefore, once all explorations were completed the animal was sacrificed and the tumour frozen for potential generation of gliospheres, as was for the case S912 (described in Section 5).

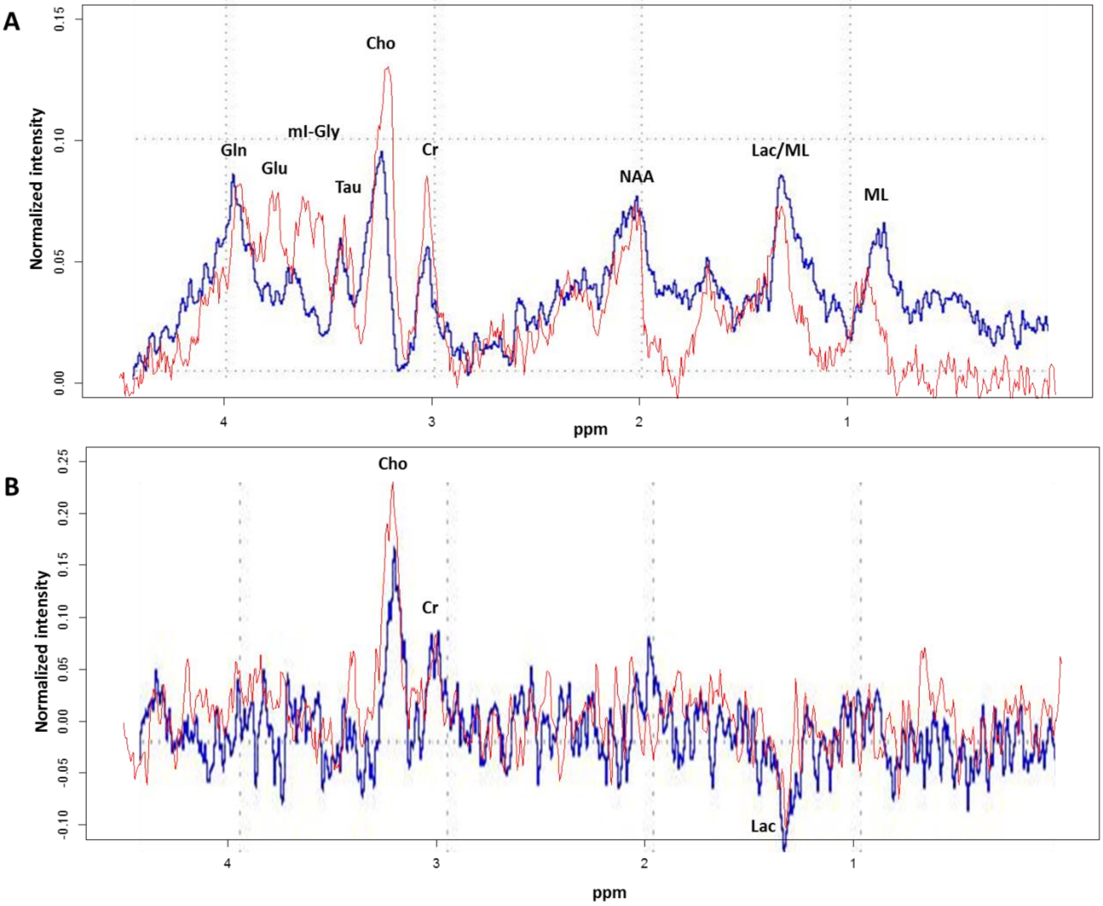

**Figure 4.16.** Comparison of the S871 tumour spectra on the day 18 p.d. (blue spectra) and on the day 51 p.d. (red spectra) at **A)** SET (12 ms) and **B)** LET (136 ms). Cho: choline, Cr: total creatine, Gln: glutamine, Glu: glutamate, mI-Gly: NAA: N-acetylaspartate, Lac: lactate, mI-Gly: myo-inositol + glycine ML: mobile lipids, Tau: Taurine.

**Table 4.4.** Comparison of main ratios at SET between day 18 and day 51 p.d. for S871 case. Cho: choline, Cr: total creatine, NAA: N-acetylaspartate, Lac/ML: Lactate and mobile lipids (at STE their resonances overlap at about 1.31 ppm).

| Ratio at SET | Day 18 p.d. | Day 51 p.d. |
|---|---|---|
| **Cho/Cr** | 2.21 | 2.27 |
| **Cho/NAA** | 2.03 | 2.29 |
| **Lac-ML/Cr** | 1.43 | 1.29 |

In addition to SV MRS studies, DMSO-MRSI was performed on the day 27 p.d. and a clear "hotspot" of higher differential DMSO accumulation was observed especially at 66 minutes post DMSO administration (Figure 4.17A).

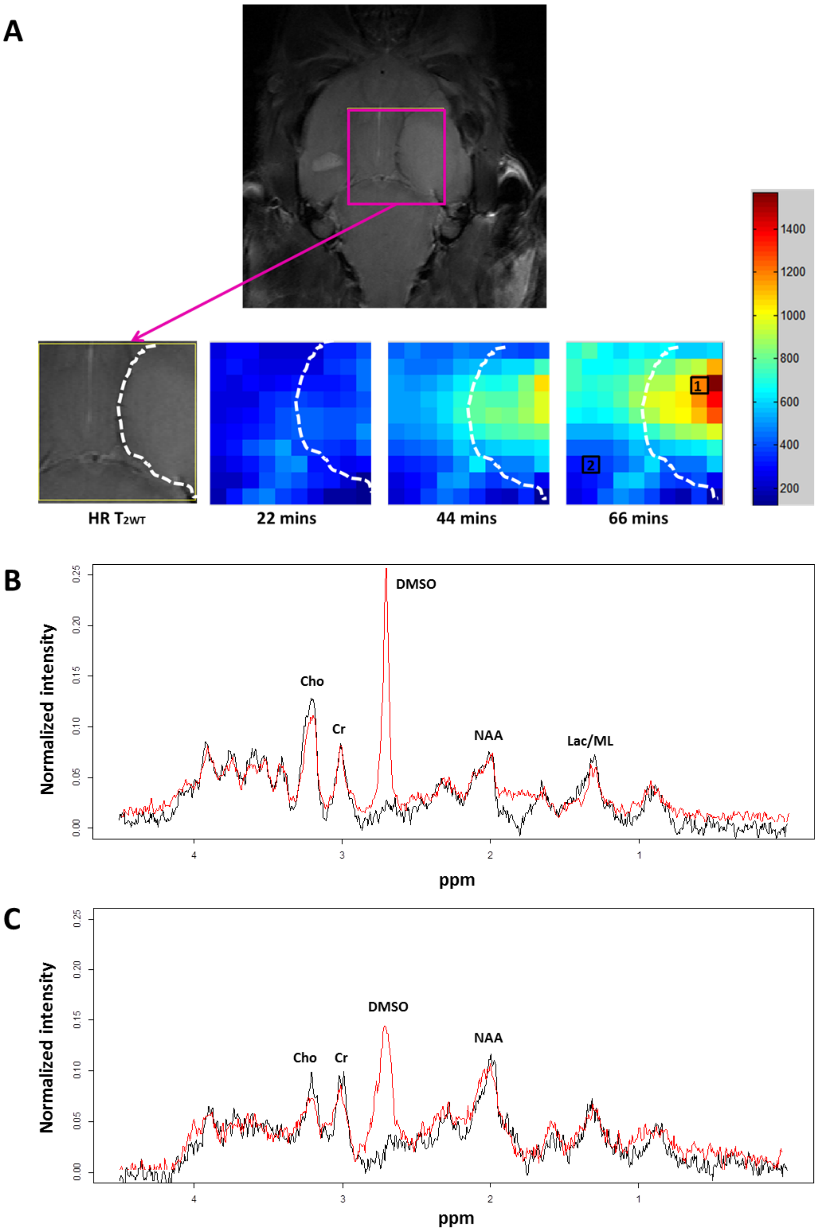
A
HR T2WT
22 mins
44 mins
66 mins
1400
1200
1000
800
600
400
200
1
2
B
Normalized intensity
0.00
0.05
0.10
0.15
0.20
0.25
DMSO
Cho
Cr
NAA
Lac/ML
4
3
2
1
ppm
C
Normalized intensity
0.00
0.05
0.10
0.15
0.20
0.25
DMSO
Cho
Cr
NAA
4
3
2
1
ppm

**Figure 4.17.** PE-MRSI with DMSO of the abnormal mass of the S871 mouse at the day 27 p.d. **A)** VOI on the reference $T_{2W}$ image (top) with enlargement of VOI and colour-coded intensity maps representing the DMSO signal detected after its i.p. administration (bottom) with the intensity scale (right) ranging from blue (low DMSO accumulation) to red (high DMSO accumulation); white dotted line labels the tumoural mass and black squares 1 and 2 correspond to the voxels of the matrix from which SV spectra were extracted and shown in B) and C). **B)** Spectra of the voxel marked as 1 from the high accumulation zone inside the tumour and **C)** spectra of the voxel marked as 2 from the low accumulation zone in the MRSI grid before (black spectra) and 66 minutes after (red spectra) the administration of DMSO. Cho: choline, Cr: total creatine, NAA: N-acetylaspartate, Lac: lactate, ML: mobile lipids.

To complete the studies, PE-MRSI with hyperglycaemia under mild hypothermia was performed (Figure 4.18) showing a clear "hotspot" of glucose accumulation detected inside the abnormal mass, although the "hotspot" location does not seem to correlate with the DMSO accumulation "hotspot" (seen in figure 4.17). As previously stated for the case R279, this allowed this case to be classified with the automated classifiers for spectral MR previously developed by our group, based on the glucose PE-MRSI with high overall accuracy of the classifier (94%) [107] for distinguishing between GBM, ODG (grade II) and normal brain parenchyma. As it can be seen in Figure 4.19, the mass was recognized as heterogeneous and classified mainly as ODG grade II with some voxels assigned to GBM. This suggested transition to higher grade and was confirmed histopathologically post-mortem, as the tumour was diagnosed as anaplastic ODG (grade III). This points that a classifier trained to distinguish grade III cases, whenever available, should be used in this case.

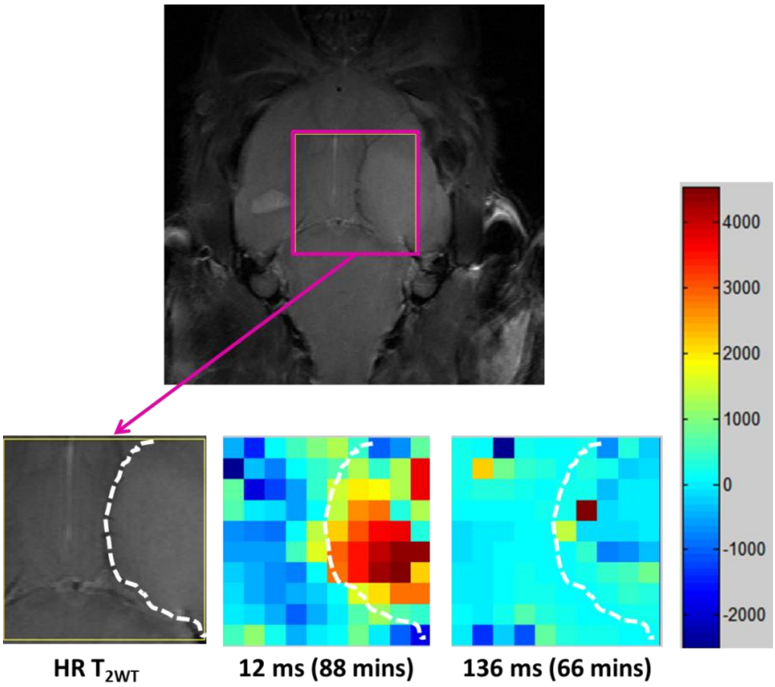

**Figure 4.18.** PE-MRSI: hyperglycemia under mild hypothermia of the S871 case. VOI on the reference $T_{2W}$ image (top) with enlargement of VOI and colour-coded intensity maps representing D-glucose signal accumulation detected at SET (12 ms) after 88 minutes post glucose i.p. administration and lactate signal accumulation detected at LET (136 ms) after 66 minutes post administration (bottom); white dotted line labels the $T_{2W}$ defined tumoural mass borders. The signal intensity scale (right) ranges from blue (low signal) to red/brown (high signal).

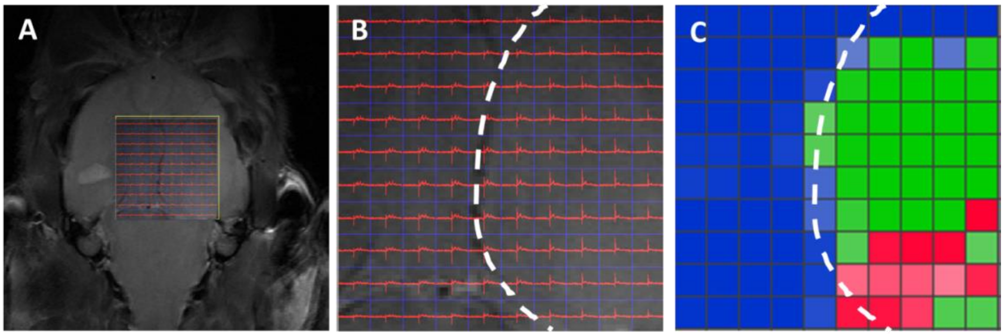

**Figure 4.19.** PR analysis for one representative animal from the S colony, S871 at day 51 p.d. A) VOI superimposed with the reference image ($T_{2W}$ HR). B) Enlargement of VOI shown in A with spvs for short TE in red. C) Nosological map obtained with the automated classifier results - blue voxels are assigned to normal brain parenchyma, red voxels to GBM and green voxels to OD2. Tumour boundaries from $T_{2W}$ images are marked with a white dotted line.

An additional exploration performed for some pilot study animals was DCE-$T_{1W}$ (as described in Section 3.10.1.), which allows to evaluate quantitatively perfusion of tumours and their surroundings. The DCE study was not however done for S871, therefore another example, the case S910, is presented. Reference images along with the Kep perfusion map are shown in Figure 4.20. The signal enhancement due to the effect of the CA is shown by comparing the reference $T_{1W}$ image (before injection of Gd-DTPA) with the $T_{1W}$ CE image at the time of maximum signal enhancement and also with the Kep perfusion map.

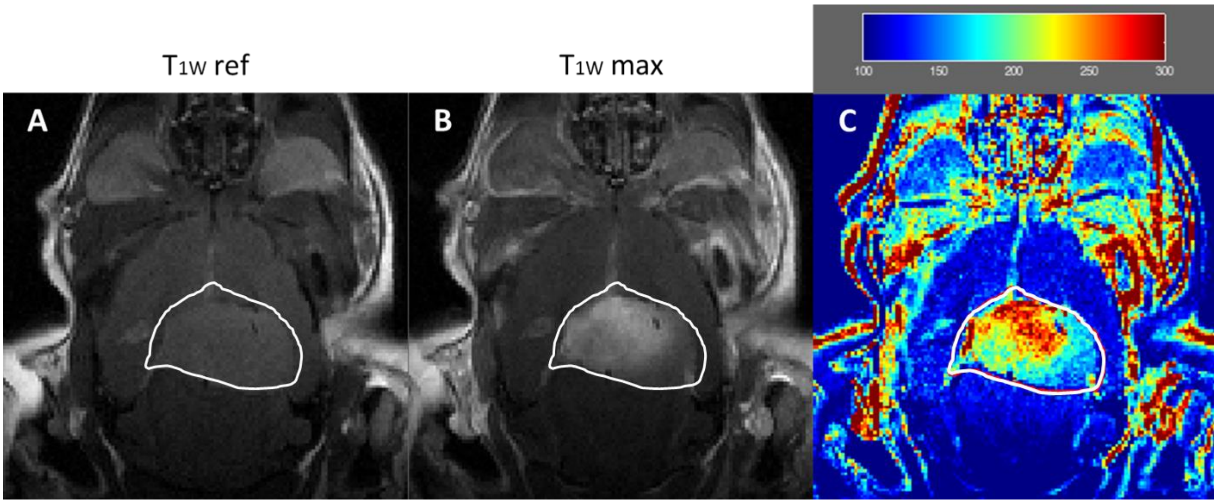

**Figure 4.20.** Entire FOV view for $T_{2W}$ images and DCE-T1 data of the S910 mouse: **A)** $T_{2W}$ reference image of DCE-T1 MRI study ($T_{1W}$ ref). **B)** $T_{2W}$ CE image at the time of maximum signal enhancement ($T_{1W}$ max). **C)** Color-coded Kep perfusion map. Tumour boundaries are marked with a white line.

In Figure 4.21, the time-course of the average signal enhancement in the tumour region (manually defined and seen as a white in in Figure 4.20) from the 3 slices acquired during DCE-T1 studies after the bolus injection of the CA is shown. The maximum signal intensity (160 - 175%, taking the basal pre-CA injection as 100%) was reached about 6 minutes after injecting the CA and was rather stable throughout the course of the study the DCE-T1 study. In comparison, in GL261 GBM tumours maximum intensity is reach between 2.6 – 4.3 minutes after injection, and decreased to 117 - 128 % until the end of the study group studies (GABRMN group results). This suggests that S871 was less well perfused than classical GBM GL261 tumours, at the investigated time point [124, 140, 141].

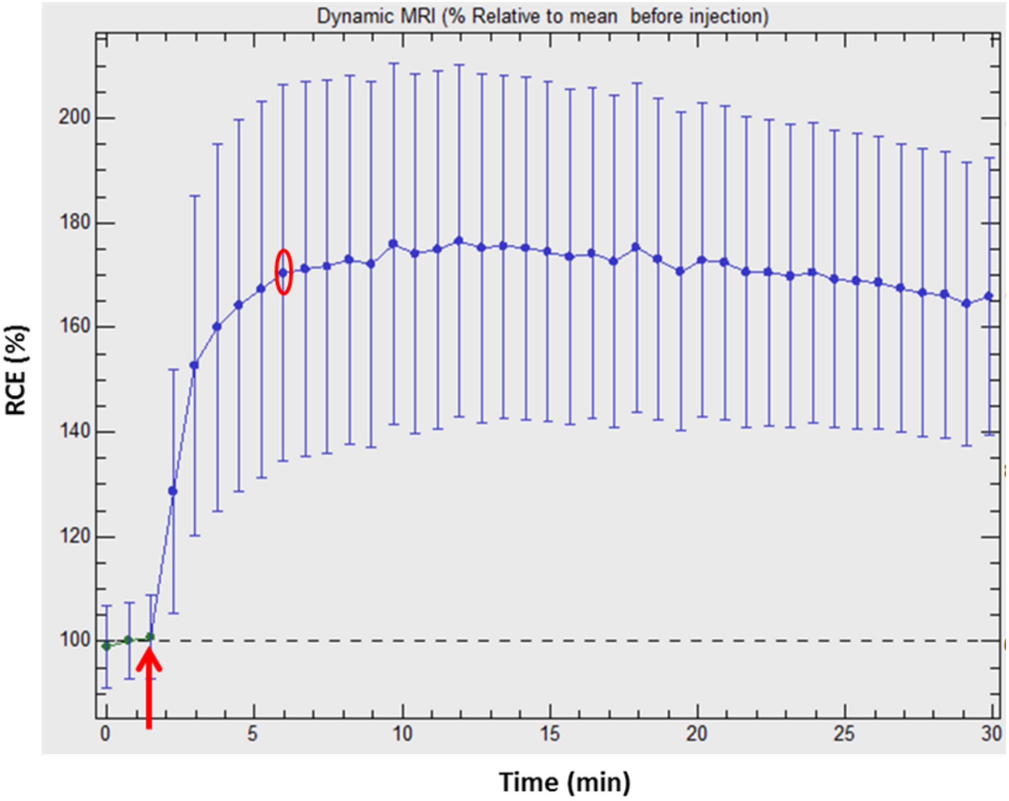

**Figure 4.21.** Time-course curve for the S910 case, showing the average signal enhancement in the tumour region, from the 3 slices studied, after bolus injection of the CA; Vertical bars show ±SD intervals; red arrow in the time axis indicates the moment of the injection; red circle indicates the moment of reaching the maximum signal intensity.

### 4.3.4. Histopathology of tumours

To complete the pilot studies, histopathological analysis was carried out, as it is still the gold standard method used for tumour grading and classification. This way MR preliminary characterisation and classification could be validated in most cases.

Figure 4.22 shows distribution of the histopathological diagnosis for the R colony. It can be seen that the number of cases that underwent histopathological analysis is higher than the number of abnormal brain masses stated in Table 4.2 This is due to the fact, that some mice developed lesions that could not be clearly MR-identified by the investigator (not being a professional radiologist) as a brain tumour, therefore they were also sent for histopathological expertise and were mostly identified as neuronal dysplasia (50% of all studied cases). We also found that some mice of the R colony developed GBM, which disagrees with the literature that describes this GEM as an astrocytoma model [65]. On the other hand, predominant type and grade of the S colony cases studied histopathological during the pilot study was oligodendroglioma of grade II (57%) (see Figure 4.23), which is coherent with the literature information about this model [63].

Cases R279 and C871 described above were diagnosed respectively as GBM and anaplastic ODG, which agrees with the initial MR characterisation and partially with the classification by the automated classifier based in PE-MRSI spectral data (refer to Section 4.3.3).

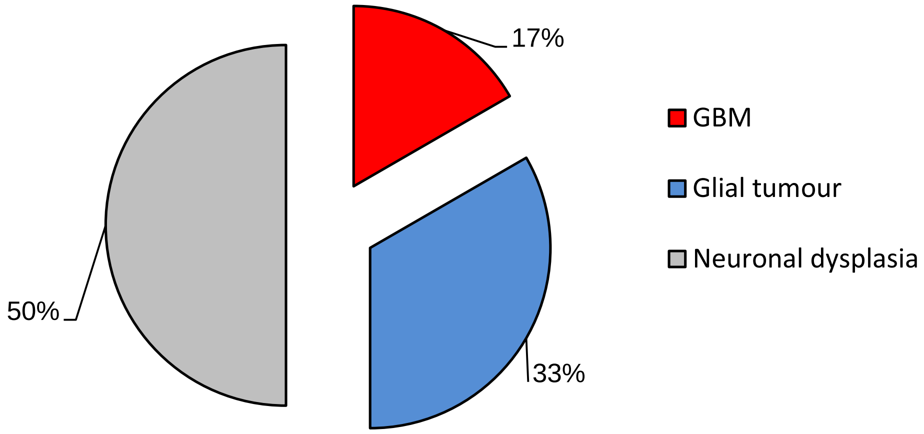

**Figure 4.22.** Distribution of histopathological diagnosis found for abnormal brain lesions of the R GEM colony

(n = 11).

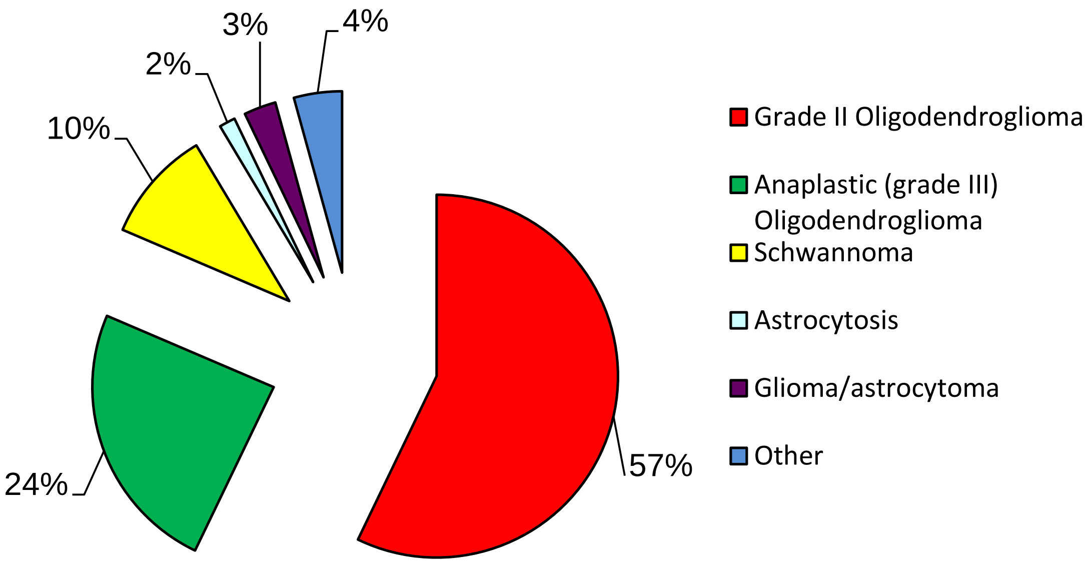

**Figure 4.23.** Distribution of histopathological diagnosis found for brain masses of the S GEM colony (n =70).

### 4.4. General discussion for this section

The pilot study performed during the work course of this PhD was mostly based on screening animals for masses by MRI, regardless of possible symptoms. This strategy in comparison to the previous one used in the group (e.g. Milena Acosta's PhD work), based on screening of solely symptomatic mice, did not increase the penetrance rate to the values reported by founders [63, 65]. Additionally, growth volume curves, time of appearance of the detected masses, as well as their grade and type, varied among cases of abnormal masses detected in the same colony, which can be especially seen looking at the histopathological diagnosis summary (Figures 4.22 and 4.23). Some tumours had very aggressive evolution pattern, developing rapidly after initial MRI detection or being already detected at a very advanced stage (volume of ~125 $mm^3$), when severe neurological symptoms were noticed, preventing the execution of the full set of possible MR explorations, because the animals had to be sacrificed for ethical reasons. Other animals had masses detected in places that compromised proper shimming (adjustment of the magnetic field homogeneity over the

VOI inside the MR scanner), e.g. brainstem or olfactory bulb (Figure 4.5), so that the explorations could not be done. This highlighted the fact that we did not have in our hands, unfortunately, a stable and reproducible model with predictable onset of low/intermediate grade brain tumours. Additionally, the maintenance of such a large number of animals (the total number of mice populating the GABRMN maintained GEM colonies at peak times was over 500) and human labour involved in their characterisation resulted in a very large economic cost, which was not sustainable and not proportional to the results obtained. This led us to consider the possibility of generating a transplantable tumour line from one of these GEM spontaneous tumours. Therefore, the work presented in this section was used for the screening and selection of an appropriate GEM candidate, which was later used for preliminary studies by other GABRMN members (Milena Acosta) and collaborators to generate gliospheres (the contribution of this thesis to this work will be described in Section 5). The explorations gathered during Section 4 work served then for general characterisation of masses with future potential use in tumour disaggregation experiments (Section 5) and for the characterisation of the colonies.

### 4.4. Conclusions

1. Two different GEM colonies (S and R) were maintained and genotyped for the specific genetic modifications expected. The information gathered was used for maintaining and breading of these colonies, as well as for the pilot study of the screening for tumoural masses. A total of 269 mice were genotyped during this PhD work, with results being consistent with work previously developed by our group.

2. The tumour incidence rate (1% for R and 16% for S), nevertheless was found to be much smaller than the one reported by founders (>90%). The evaluation technique used for diagnosis (MRI screening of transgenic mice versus histopathological analysis) could at last partially explain this difference.

3. Distribution of histopathological diagnosis was coincident with previous group analysis, however for the R colony histopathology reviled presence of some GBM cases, which disagrees with the literature information about this model, describing it as astrocytoma model.

4. Variability in tumour growth patterns and in the type of tumours developed by the GEM indicates that they would not be good models for therapy response studies requiring several homogenous diseased mice for comparable evaluation. Additionally, their overall maintenance cost does not make them advisable in periods of economic restriction.

5. Despite the low incidence rate and large variability, GEM tumours developed were characterized using MR-based techniques and selected cases considered of interest were used for development and training of tumour type grade classifiers based in MRSI perturbed spectra.

6. Finally, the screening of the GABRMN GEM colonies during this PhD work also helped to select for tumours suitable for disaggregation protocols and generation of potentially transplantable models of low/intermediate grade glioma.

# 5. Developing a transplantable murine tumour model of low/intermediate grade

**(Objective 2)**

## 5.1 Rational and Objective

The aim of this study was to generate a transplantable glial tumour model of low/intermediate grade by disaggregation of a spontaneously appearing tumour in GEM, in order to increase tumour incidence rate in comparison to the S GEM colony previously studied by the group (Section 4). This should allow us to obtain an improved model for brain tumour progression and therapy studies.

## 5.2 Specific Materials and Methods

The studies began by a preliminary attempt of tumour generation from disaggregated GL261 tumours (both freshly resected and frozen), as already described in Sections 3.2 (gliospheres generation) and 3.6 (generation of tumours), respectively. Once the technique proved feasible and implantation of GL261 cells from gliospheres generated from disaggregated GL261 masses into C57BL/6 mice produced tumours, the procedure was repeated using a spontaneously appearing GEM tumour from the S colony (described in Section 1.2.2), namely S912, detected by standard MRI screening as described in Section 3.10.1. Once generated, the S912 gliospheres (either fresh gliospheres, frozen gliospheres from fresh tumour or gliospheres generated from a frozen piece of tumour) were used for implantation of further groups of C57BL/6 mice as presented in Table 5.1 below.

**Table 5.1.** Distribution of experimental animals depending on the source of cells used for the tumour generation protocol and identifiers of animals in each group.

| Group | No. of animals | Source of cells for tumour generation | Alphanumeric identifier of animals in the group |
|---|---|---|---|
| A | 6 | Standard GL261 cells | C(unique number) |
| B | 6 | Gliospheres generated from fresh GL261 tumour | |
| C | 7 | Gliospheres generated from frozen GL261 tumour | |
| D | 29 | Gliospheres generated from fresh S912 tumour | G(unique number)-S912 |
| E | 29 | Frozen gliospheres generated from fresh S912 tumour | Gc(unique number)-S912 |
| F | 9 | Gliospheres generated from frozen S912 tumour | Gtc(unique number)-S912 |

*In* vivo progression and follow up of S912-derived tumours was performed by MR as described in Section 3.10 until animals died or were sacrificed, due to animal welfare standard protocol, by cervical dislocation. The brains of 49 mice in total (S912 and its derivatives) were excised and fixed (as a whole or a piece of tumour) in 4% formaldehyde and diagnosed histopathologically by classical HE staining (Section 3.8.1). For selected cases, immunohistochemistry (IHC) analysis for oligodendrocyte transcription factor (OLIG2) protein and GFAP was also performed. In case of tumours with an apparent low/intermediate grade by MRI/MRSI (i.e. no BBB breakdown; typical MRS SV pattern features) (n=5 out of 49), these were extracted and halved - one part was frozen in liquid nitrogen in a cryotube containing 1ml of 10% DMSO in RPMI medium for future disaggregation and potentially obtaining second generation gliospheres.

Tumours were also sampled for some randomly chosen animals (n = 7) in order to perform genotype check as per Section 3.5 (S colony).

It should be mentioned that the preliminary studies of this section were performed in collaboration with Milena Acosta, a former member of the GABRMN, who started this particular protocol and which was continued in this PhD period.

## 5.3 Results and discussion

### 5.3.1. Disaggregated tumour model using GL261 derived gliospheres

We used the GL261 murine glioma model for our preliminary studies, because it is a well characterised model [60, 106] with a well-known growth pattern evaluation of the performance of the standard tumour generation protocol described in the literature [106]. Furthermore, the disaggregation technique of solid tumour tissue has been widely used in the previous decades for establishment of new glioma cell lines [142].

For this disaggregation protocol, GL261 tumour bearing mice were sacrificed once masses reached a volume of 140 ± 20 mm$^3$ (n = 6, day 18 ± 2 post-implantation (p.i.)) and tumour tissue, either fresh or frozen, was used to generate gliospheres as per Section 3.2. The appearance of gliospheres prepared is presented in Figure 5.1A).

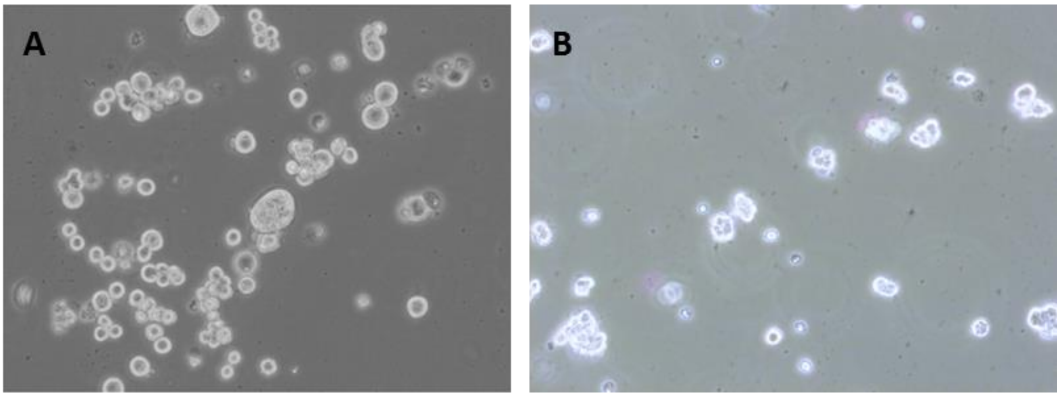

**Figure 5.1.** Image from confocal microscopy (100X) of gliospheres generated from **A)** GL261 tumour and **B)** S912 GEM tumour.

Regarding tumours derived from GL261 gliospheres obtained from fresh GL261 tumours, masses were detectable by MRI on the day 8 p.i. in all implanted mice and their growth presented a similar pattern to the standard GL261 tumours, with mean survival of 21 ± 3 days (Figure 5.2.) without significant difference in comparison with 21 ± 2.5 days observed for the standard GL261 tumours ($p = 0.058$). The final mean volume of those tumours generated from gliospheres was in average 101 ± 26 $mm^3$ ($n = 6$) and significantly smaller ($p = 0.005$) in comparison to 201 ± 37 $mm^3$ ($n = 6$) in control GL261 tumours from previous work of the group [123]. The penetrance was 100% in both cases.

Regarding tumours derived from GL261 gliospheres obtained from frozen GL261 tumours, abnormal masses were already detectable by MRI on the day 10 p.i., which resulted in a slightly longer (although non-significant, $p = 0.106$) survival (25 ± 2 days) in comparison with the group implanted with freshly disaggregated tumours (Figure 5.2). The penetrance was also 100% and the mean final tumour volume was of 119 ± 32 $mm^3$ non-significantly different from control GL261 ($p = 0.078$) and fresh tumours ($p = 0.295$).

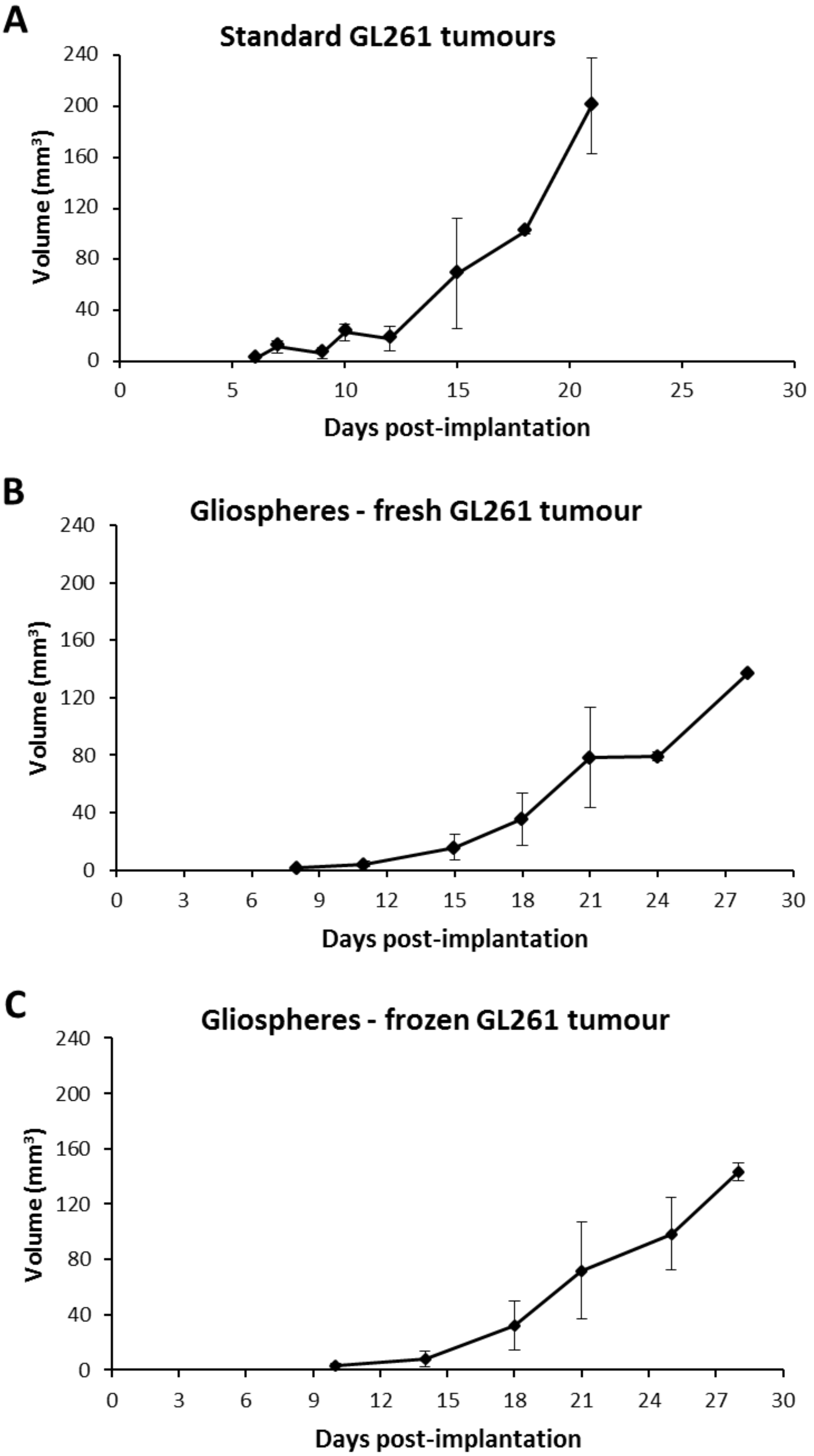

**Figure 5.2.** Average growth curves representing the mean ± SD of tumour volumes (mm$^3$) grown from implanted: **A)** GL261 cells (n = 6); **B)** cells from gliospheres obtained from fresh GL261 tumour (n = 6), **C)** cells from gliospheres obtained from frozen GL261 tumour (n = 7).

These results are in agreement with studies carried out by other researchers that produced gliospheres from the same cell model and did not find significant difference in survival time between animals implanted with $5x10^4$ GL261 cells from gliospheres (23.4 ± 4 .6 days) and those implanted with the same amount of GL261 cells directly from cell culture (29.8 ± 6.4 days) [143]. However, when concentration of the cell inoculum used was decreased to $5x10^3$ cells was used, the cells from gliospheres were confirmed to have more aggressive behaviour displaying a reduced survival time significantly (48.8 ± 11.8 days versus > 100 days for 3 out of 4 mice investigated by them).

Furthermore, our results proved possible that generation of gliospheres from a frozen GL261 mass aliquot was as successful as for a freshly resected tumour, with the ful tumour penetrance in implanted mice. This finding is in line with literature that demonstrates that using frozen tissue material for establishment of stable outgrowing cells does not significantly decrease take rates after cryopreservation for establishing stable outgrowing cells lines in comparison to fresh material [144]. This should be useful, as it is not always possible to carry out gliospheres preparation work with freshly excised masses. Still, authors in [144] did not evaluate performance in allograft transplantion experiments.

By completing the above experiment, we believe that the methodology was optimized and ready to continue with the next step, i.e. generation of a transplantable brain tumour model by disaggregation of a spontaneous GEM tumour of an intermediate grade.

### 5.3.2. Disaggregated tumour model from a GEM anaplastic ODG: the S912 tumour

The systematic MRI screening of the S GEM colony detected a tumoural mass in the brain of the S912 female mouse at 14 weeks of age, later confirmed to display the genotype S100β-v-erbB/INK4A-ARF (+/-). The $T_{2W}$ images showed a circumscribed mass (about 22 $mm^3$ in volume) located in the hypothalamus (Figure 5.3.A). The CE MRI $T_{1W}$ studies (Figure 5.3.B and 5.3.C) showed a partially compromised BBB integrity when the tumour volume was < 30 $mm^3$, indicating a heterogeneous nature of the mass and possibly transition between intermediate and high grade in the region, where the contrast enhancement was clear.

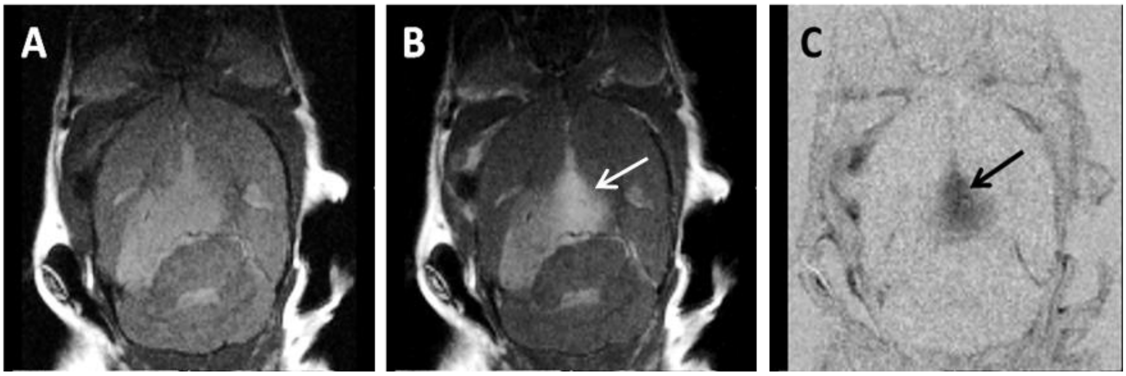

**Figure 5.3.** Coronal $T_{1W}$ MRI of the S912 mouse brain **A)** pre- and **B)** post- pre-intraperitoneal contrast administration, as well as **C)** subtraction of the two previous images, acquired at 7T 32 days after initial tumour detection. The black arrow in C indicates the area of contrast enhancement.

The grade and type of the tumour were confirmed later on after sacrifice at day 61 post tumour detection by histopathological analysis of a piece of abnormal mass, as anaplastic OA (grade III).

Gliospheres generated from freshly resected S912 tumour tissue are shown in Figure 5.1B.

#### 5.3.2.1. MRI assessment of tumour growth and estimation of penetrance

The first batch of 29 C57BL/6 mice implanted with cells derived from gliospheres obtained from a disaggregated piece of fresh S912 mass had a tumour incidence rate of 55%, i.e. 16 animals developed tumours in the evaluated time frame of 3 months during which mice were monitored for symptoms and explored by MRI in case of need. Masses showed two distinct growth patterns and for this reason they were classified into two groups: ‘short latency’ and ‘intermediate latency’. Average time of first detection by $T_{2W}$ MRI and final tumour volume for both groups can be seen in Table 5.2. ‘Short latency’ refers, arbitrarily, to tumours with similar initial detection day and growth curve time course than tumours from GL261 gliospheres (as in Figure 5.2). On the other hand ‘intermediate latency’ refers to tumours with clearly delayed detection time with respect to those GL261 tumour gliospheres (25 versus 9 days average values). An arbitrary cut-off boundary at 16 days of latency before detection was chosen for this.

**Table 5.2.** Number of animals assigned into each group, time of tumour detection, average final volume and doubling time of masses.

| **Animal group** | | **No. of mice** | **Time of first mass detection by MRI (days p.i.)** | **Final volume ($mm^3$) [a]** | **Doubling time (days)** |
|---|---|---|---|---|---|
| Fresh S912 gliospheres | Short latency [d] | 9 | 9 | 101.4 ± 58.9 | 4.3 ± 0.4 |
| | Intermediate latency [d] | 7 | 25 ± 28 | 181.0 ± 74.0 | 9.8 ± 12.1 |
| Frozen S912 gliospheres | Short latency | 13 | 15 ± 3 | 106.2 ± 59.4 | 3.4 ± 1.3 |
| | Intermediate latency | 9 | 21 ± 3 | 139.1 ± 71.2 [b] | 9.1 ± 2.8 |
| | Long latency [d] | 5 | 75 ± 104 | 155.2 ± 50.1 | 9.5 ± 4.8 |
| Gliospheres from frozen S912 tumour | | 9 | 10 ± 3 [c] | 181.0 ± 74.0 | 3.5 ± 5.9 |

[a] This measure is a rough estimate, because some animals were not screened immediately before their death/sacrifice (up to 8 days time gap).

[b] Excluding Gc29-S912, because its last volume check was done 27 days before its death.

[c] Excluding Gtc6-S912, in which the abnormal mass was only detected by MRI on the day 80 p.i.

[d] See text for definition of ‘short latency’, ‘intermediate latency’ and ‘long latency’.

Regarding the animals implanted with gliospheres that were previously frozen and then disaggregated and recultured, all implanted animals developed a mass. Detection of masses by $T_{2W}$ MRI was very spread out in time, having also a more diffuse/irregular appearance (Figure 5.4.B and Figure 5.4.C) in comparison to those generated by GL261 cells or fresh S912 gliospheres. Most masses were detected between day 14 and 21 p.i., although some tumours were detected as late as 8 months p.i. The tumour grow rate, expressed as tumour doubling time (calculated with equation 7 as described in Section 3.10.4), also varied, as in the batch of animals implanted with fresh gliospheres (refer to Table 5.2). As previously, based on the kinetics of tumour growth, animals were arbitrarily divided into three different groups - ‘short latency’, ‘intermediate latency’ and an additional ‘long latency’ group (Table 5.2) with cut-off boundaries between the groups of 20 and 53 days, respectively. In the ‘intermediate latency’ group, some tumours did not show detectable volume increase for extended periods of time (e.g. 10 weeks for the Gc15-S912 mouse) until they started growing again. ‘Long latency’ refers to abnormal mass detected not earlier than day 53 p.i. and tumour evolution ranging between 12 – 29 days after then.

Masses that developed late in p.i. time, i.e. both from the 'intermediate' and 'long latency' groups, tended to grow inside ventricles (this also applies to masses grown from the frozen tumour S912 gliospheres described below), as can be seen in Figure 5.4.D.

The evolution of tumours grown from implanted gliospheres obtained from a frozen S912 mass sub-sample (n = 9) mostly resembled the growth pattern of animals implanted with GL261 cells, apart from two animals: one of them developed a tumour of the 'intermediate latency' type (Gtc2-S912), and in another one, the mass was not detected until day 80 p.i. (Gtc6-S912, 'long latency' sub-type). Still, tumour incidence was 100%, i.e. 9 out of 9 animals developed tumours. In most mice, the initial mass was already detectable by $T_{2W}$ MRI on the day 10 p.i.

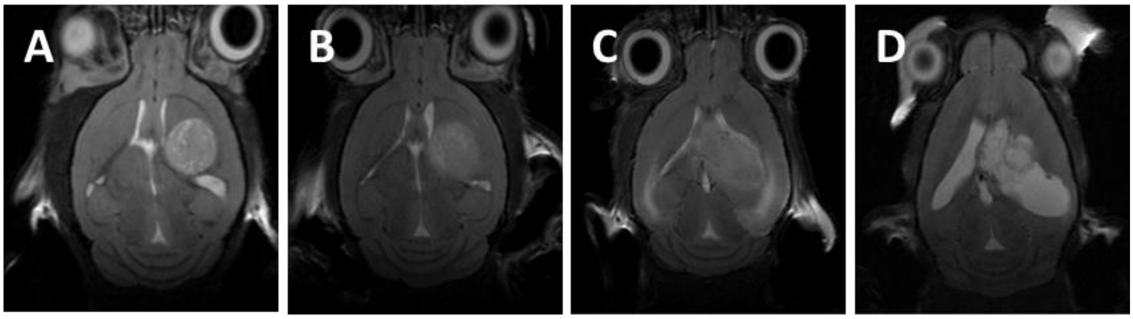

**Figure 5.4.** Coronal $T_{2W}$ MRI of mice brains with different appearance of tumours, depending on type of cells implanted **A)** tumour C482 generated with standard GL261 cells, 15 days post tumour detection **B)** tumour G10-S912 from the 'short latency' group generated from fresh S912 gliospheres, 19 days post tumour detection **C)** tumour Gc5-S912 from the 'short latency' group generated from frozen S912 gliospheres, 20 days post tumour detection **D)** Gc8-S912 tumour growing inside ventricle from 'intermediate latency' group generated with cells from frozen S912 gliospheres, 46 days post tumour detection.

As can be seen above, applying the disaggregation method established on GL261 tumours to the GEM fresh tumour showed substantial increase in the penetrance in comparison to the GEM S colony and reached 55% versus >90% described by the S colony mice providers [63]. However, this penetrance was much lower than 96% for the standard GL261 model (GABRMN unpublished results for n=832) or full penetrance in the GL261 setup experiments (n = 6) shown in this work. When repeating the studies with frozen GEM gliospheres/tumour the penetrance increased up to 100%. A possible explanation for this would be that the process of culturing, freezing, thawing and growing in new mice helps selecting for a more aggressive cellular subtype, possibly having accumulated additional driving mutations, resulting in higher grade tumours being favoured and progression from ODG grade III to grade IV GBM. This would be in line with the available literature in the matter, which describes that it is very difficult to obtain a low/intermediate grade stable cell line. In this respect, Shimada et al. [145] showed that aggressive tumours allow to establish continuous stable cell lines from primary culture, while it proves difficult to achieve the same for non-aggressive tumours. These authors [145] also suggested that the mutational status of p53 and MDM2 played an important role in the development of stable tumoural cell lines usable for new tumour generation. Other authors that succeeded in developing low/intermediate grade cell lines, have reported that the expansion of tumour cells via *in vitro* culture can affect the characteristics of developed masses in comparison with the original tumour. In this respect, Barker et al. [146], after 6 months of cell culture, observed that the implanted tumours, which were originally diagnosed as an astrocytoma grade III, classified as mixed GBM and sarcoma, or gliosarcoma (grade IV). Halfter et al. [147] established cell lines derived from a mixed astro-oligodendroglioma and an astrocytoma, both of grade II/III, and only the astrocytoma cell line induced tumour growth following injection into the hind leg of athymic mice. Onda et al. [148] established two glioma cell lines from two surgical specimens obtained at different times from the same patient; one was derived from the primary tumour (slightly anaplastic astrocytoma, grade II/III), while another was from the recurrent tumour (GBM, grade IV), and subcutaneous tumours developed only after inoculation into nude mice of the higher grade GBM cells, confirming their more aggressive nature. However, in contrast to what was described by Shimada et al. [145], neither of the cell lines used by Onda et al. [148] had the mutational status of the p53 gene altered.

On the other hand, other authors reported that cryopreserved human spheroids retain their histological characteristics after thawing [149] and when xenografted into nude mice after freezing and thawing they preserve their essential phenotypic traits and their gene expression profiles do not change significantly [150, 151]. However all the evaluated gliospheres reported in the study were originally derived from GBM tumour, already grade IV.

Therefore, further investigation is needed in order to clarify the cause of the recorded grade progression in our case (see also Section 5.3.2.4 on this) and possibly the mutational status of the crucial driver genes will need to be evaluated.

It may also be wise for future work to ascertain tumour type and/or grade of a disaggregation candidate before embarking in the full gliosphere generation/transplantation procedure. However, an important conclusion from the experiment was that the implantation of cells from previously frozen gliospheres or frozen tissue material did produce glial tumours in the receiving animals with optimal (100%) penetrance.

#### 5.3.2.2. MRS/CE MRI/ PE-MRSI

Regarding MR evaluation of S912-derived tumours spectra, this allowed preliminary *in vivo* assessment of their grade, which was eventually validated by histopathological analysis. The average spectra for each group of tumours/animals at short and long TE can be seen in Figures 5.5 and 5.6, while average metabolite ratios at both TEs are presented in Table 5.3 and 5.4. It can be seen that tumours developed from fresh S912 gliospheres showed features associated with oligodendrogliomas (Figure 5.5), i.e. moderate increase in Cho/Cr ratio in comparison to normal brain parenchyma, moderate decrease in NAA which is usually associated with a decrease of viable neurons [152-154], and increased lactate signal and detection of mobile lipids [154, 155], while patterns of tumours derived from frozen S912 (Figure 5.6) have clearly higher lactate (LET) and mobile lipids signals usually associated with GBM [107]. Additionally, box-plots presented in Figure 5.7 show increasing trend of Cho/Cr ratio with time p.i. (for the ‘normal latency’ group implanted with fresh S912 gliospheres) and with increasing latency. Same increasing trend can be observed for ML/Cr ratios (Figure 5.8). This could possibly indicate progression in tumour grade.

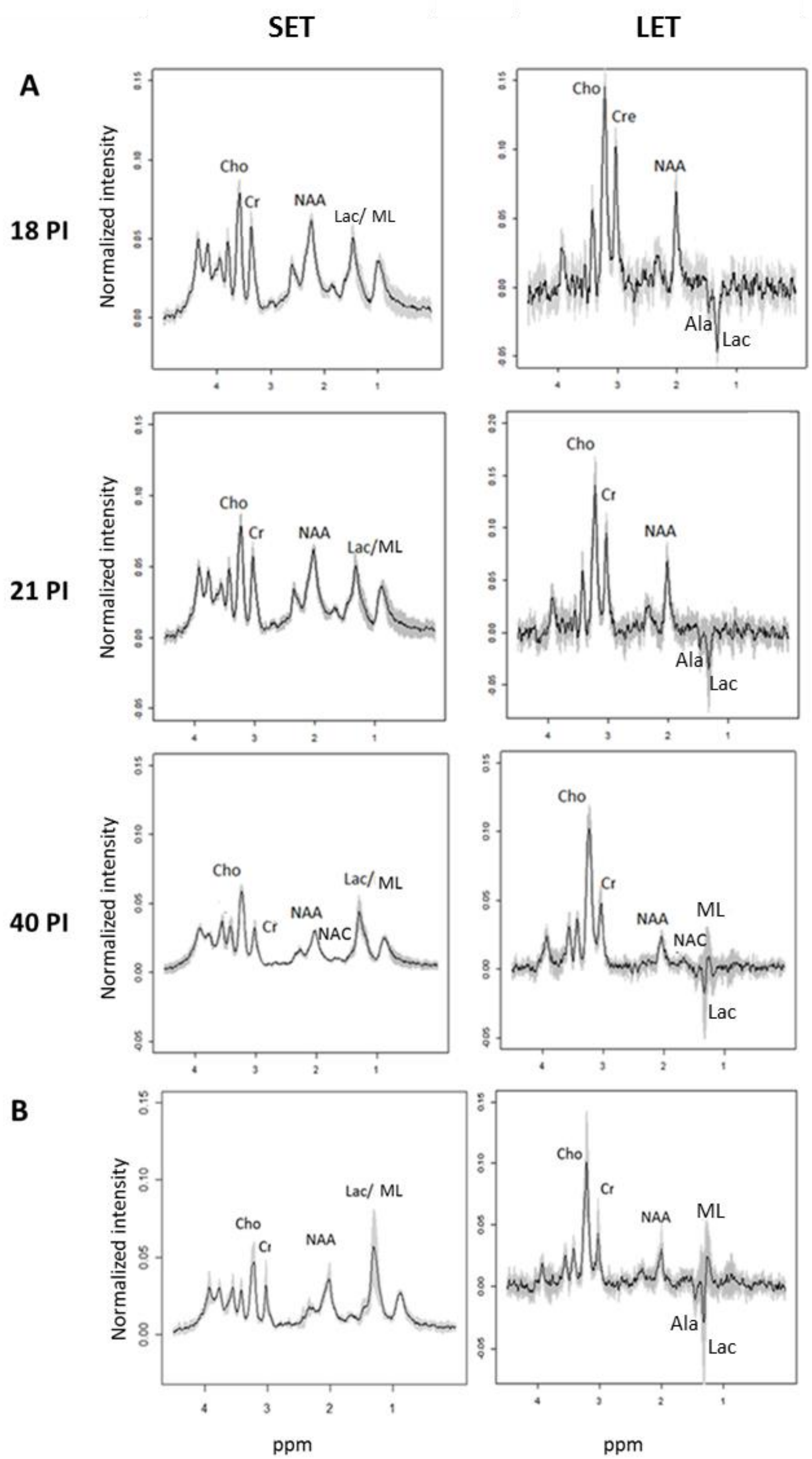

**Figure 5.5.** Average SV MR spectra (± SD, grey shading) at SET(12 ms) and LET (136 ms) obtained from (1.5 - 3.0 mm)$^3$ voxels of tumours generated from GEM S912 fresh gliospheres of: **A)** 'short latency' group of animals acquired at day 18 (n = 9), 21 (n = 9) and 40 (n = 7) p.i. and of **B)** 'intermediate latency' group of animals (n = 5) acquired between days 35 and 42 p.i. Ala: alanine, Cho: choline, Cr: total creatine, NAA: N-acetylaspartate, Lac: lactate, ML: mobile lipids.

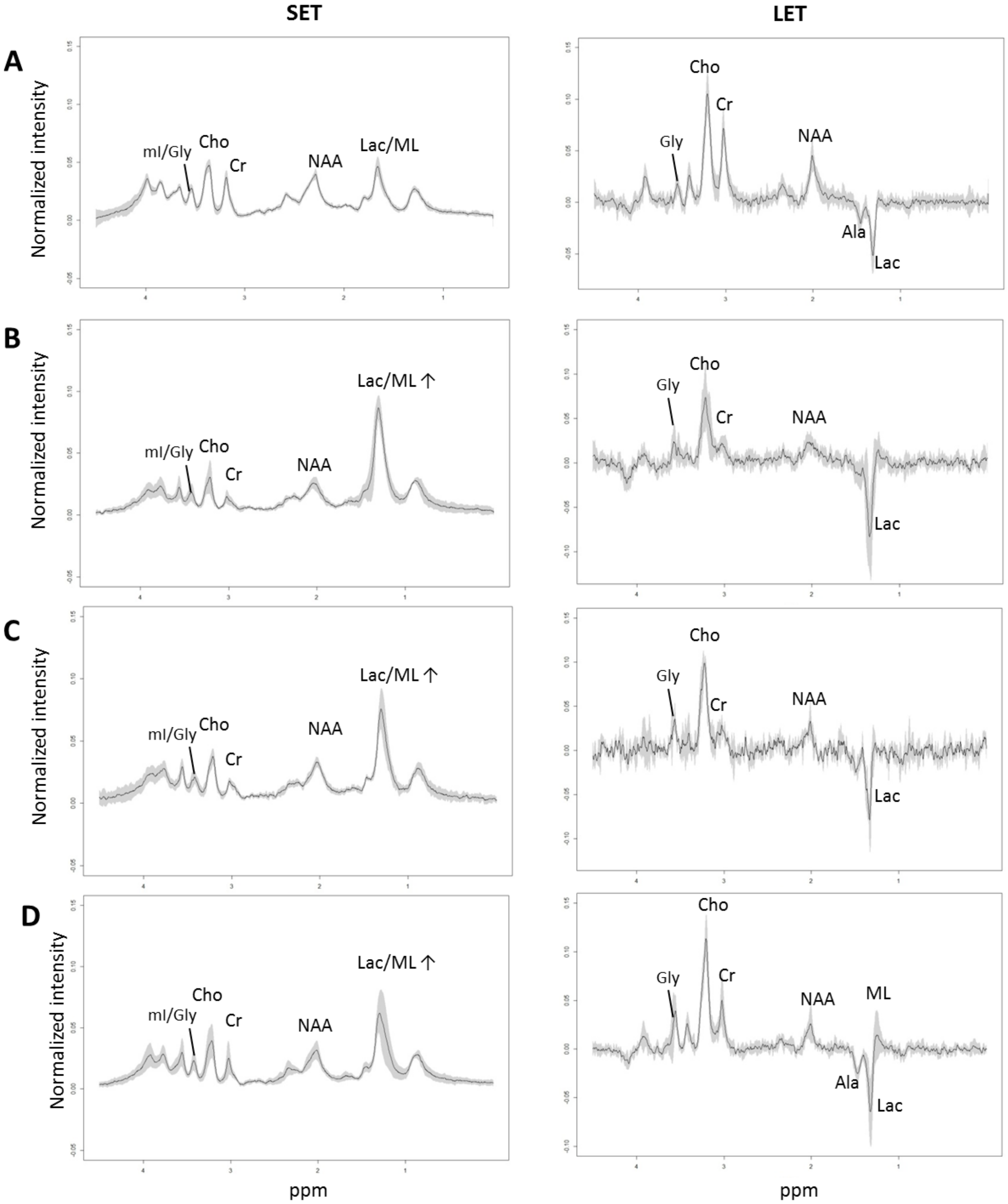

**Figure 5.6.** Average SV MR spectra (± SD, grey shading) at SET (12 ms) and LET (135 ms) obtained from tumours generated from frozen GEM S912 gliospheres (A, B, C) and tumours generated from gliospheres obtained from a frozen piece of GEM S912 tumour (D): **A)** ‘short latency’ group of animals (n = 13), SV acquired between days 21 and 34 p.i., **B)** ‘intermediate latency’ group of animals (n = 6), SV acquired between days 59 and 77 p.i., **C)** ‘long latency’ group of animals (n = 4), SV acquired between days 53 and 253 p.i., **D)** group of animals implanted with gliospheres obtained from a frozen piece of S912 tumour (n = 8), SV acquired between day 26 and 80 p.i. Cho: choline, Cr: total creatine, Gly: glycine, mI: myo-inositol, NAA: N-acetylaspartate, Lac: lactate, ML: mobile lipids. Black arrows in A, B and C indicate visible Lac/ML increase in comparison to ‘short latency’ group.

**Table 5.3.** Average metabolite peak height ratios at both short and long TE normalized spectra for tumours generated from fresh S912 gliospheres: 'short latency' (SL) group at day 18, 21 and 40 p.i. and 'intermediate latency' (IL) group 35-42 days p.i.; and normal brain parenchyma (NB) of C57BL/6 mice. The main resonances, used for ratio calculations are labelled as follows: Cho (choline) at 3.21 ppm; Cr (total creatine) at 3.03 ppm; Lac (lactate) at 1.32 ppm; ML (mobile lipids) at 1.28 ppm; NAA (N-acetylaspartate) at 2 ppm; Tau (taurine) at 3.42 ppm. Significant differences for peak height ratios between SL day 21, SL day 40 and IL in comparison to SL day 18 are marked with *, and significant difference between SL day 18, SL day 21,SL day 40 and IL in comparison to NB are marked with $^{\dagger}$. See also references [106, 107, 113] for further details about resonance assignment.

| | | **SL (n=9) day 18** | | **SL (n=9) day 21** | | **SL (n=7) day 40** | | **IL (n=5) day 35-42** | | **NB (n=4)** | |
|---|---|---|---|---|---|---|---|---|---|---|---|
| | | **Average** | **SD** | **Average** | **SD** | **Average** | **SD** | **Average** | **SD** | **Average** | **SD** |
| **SET** | **Cho/Cr** | 1.35$^{\dagger}$ | 0.09 | 1.40$^{\dagger}$ | 0.11 | 1.80*$^{\dagger}$ | 0.25 | 1.92*$^{\dagger}$ | 0.40 | 0.96 | 0.20 |
| | **ML/Cr** | 0.90 | 0.12 | 0.81 | 0.21 | 1.38* | 0.37 | 4.45$^{\dagger}$ | 3.86 | 0.74 | 0.12 |
| | **NAA/Cr** | 1.06 | 0.11 | 1.02 | 0.24 | 0.97 | 0.12 | 2.86$^{\dagger}$ | 3.00 | 1.06 | 0.03 |
| **LET** | **Cho/Cr** | 1.47 | 0.32 | 1.78*$^{\dagger}$ | 0.27 | 2.30*$^{\dagger}$ | 0.50 | 3.02$^{\dagger}$ | 1.96 | 1.29 | 0.38 |
| | **Lac/Tau** | 0.76$^{\dagger}$ | 0.28 | 0.91$^{\dagger}$ | 0.24 | 1.11 | 0.82 | 2.85 | 2.29 | 1.81 | 0.44 |
| | **Lac/Cr** | 0.46$^{\dagger}$ | 0.17 | 0.58 | 0.16 | 0.70 | 0.38 | 2.07* | 1.47 | 0.76 | 0.19 |
| | **NAA/Cr** | 0.71 | 0.13 | 0.64 | 0.15 | 0.50 | 0.20 | 0.96 | 0.78 | 1.00 | 0.22 |

**Table 5.4.** Average metabolite peak height ratios at both short and long TE normalized spectra for tumours generated with frozen S912 gliospheres: 'short latency' (SL) group, 'intermediate latency' (IL) group and 'long latency' (LL); tumours generated from S912 gliospheres obtained from frozen tumour (FT) and normal brain parenchyma (NB) of C57BL/6 mice. The main resonances, used for ratio calculations are labelled as follows: Cho (choline) at 3.21 ppm; Cr (total creatine) at 3.03 ppm; mI-Gly (Myo-inositol + glycine) at STE or Gly (glycine) at LET at 3.55 ppm; Lac (lactate) at 1.32 ppm; ML (mobile lipids) at 1.28 ppm; NAA (N-acetylaspartate) at 2 ppm, Tau (taurine) at 3.42 ppm. Significant differences for peak height ratios between SL, IL, LL and FT in comparison to NB are marked with $^{\dagger}$.

| | | **SL (n=13)** | | **IL (n=9)** | | **LL (n=5)** | | **FT (n=8)** | | **NB (n=4)** | |
|---|---|---|---|---|---|---|---|---|---|---|---|
| | | **Average** | **SD** | **Average** | **SD** | **Average** | **SD** | **Average** | **SD** | **Average** | **SD** |
| **SET** | **Cho/Cr** | 1.40$^{\dagger}$ | 0.27 | 2.15$^{\dagger}$ | 0.31 | 1.45$^{\dagger}$ | 0.46 | 1.63$^{\dagger}$ | 0.77 | 0.96 | 0.20 |
| | **ML/Cr** | 1.32 | 0.53 | 8.43$^{\dagger}$ | 2.86 | 2.77$^{\dagger}$ | 1.85 | 3.54$^{\dagger}$ | 2.46 | 0.74 | 0.12 |
| | **NAA/Cr** | 1.15 | 0.22 | 2.37 | 0.78 | 1.39 | 0.77 | 1.46 | 0.37 | 1.06 | 0.03 |
| | **mI-Gly/Cr** | 0.81 | 0.26 | 1.62$^{\dagger}$ | 0.37 | 0.98 | 0.57 | 1.33$^{\dagger}$ | 0.36 | 0.43 | 0.01 |
| **LET** | **Cho/Cr** | 1.46 | 0.23 | 3.13$^{\dagger}$ | 0.44 | 4.58$^{\dagger}$ | 4.29 | 2.89$^{\dagger}$ | 0.98 | 1.29 | 0.38 |
| | **Lac/Tau** | 1.62 | 0.47 | 7.84$^{\dagger}$ | 6.16 | 1.81 | 1.01 | 3.23 | 1.94 | 1.81 | 0.44 |
| | **Lac/Cr** | 0.76 | 0.26 | 4.24$^{\dagger}$ | 2.47 | 3.79 | 4.53 | 2.03 | 1.36 | 0.76 | 0.19 |
| | **NAA/Cr** | 0.69 | 0.11 | 1.48 | 1.00 | 1.87 | 1.82 | 0.58 | 0.23 | 1.00 | 0.22 |
| | **Gly/Cr** | 0.23 | 0.10 | 1.25$^{\dagger}$ | 0.39 | 1.92$^{\dagger}$ | 2.57 | 1.08$^{\dagger}$ | 0.71 | 0.31 | 0.17 |

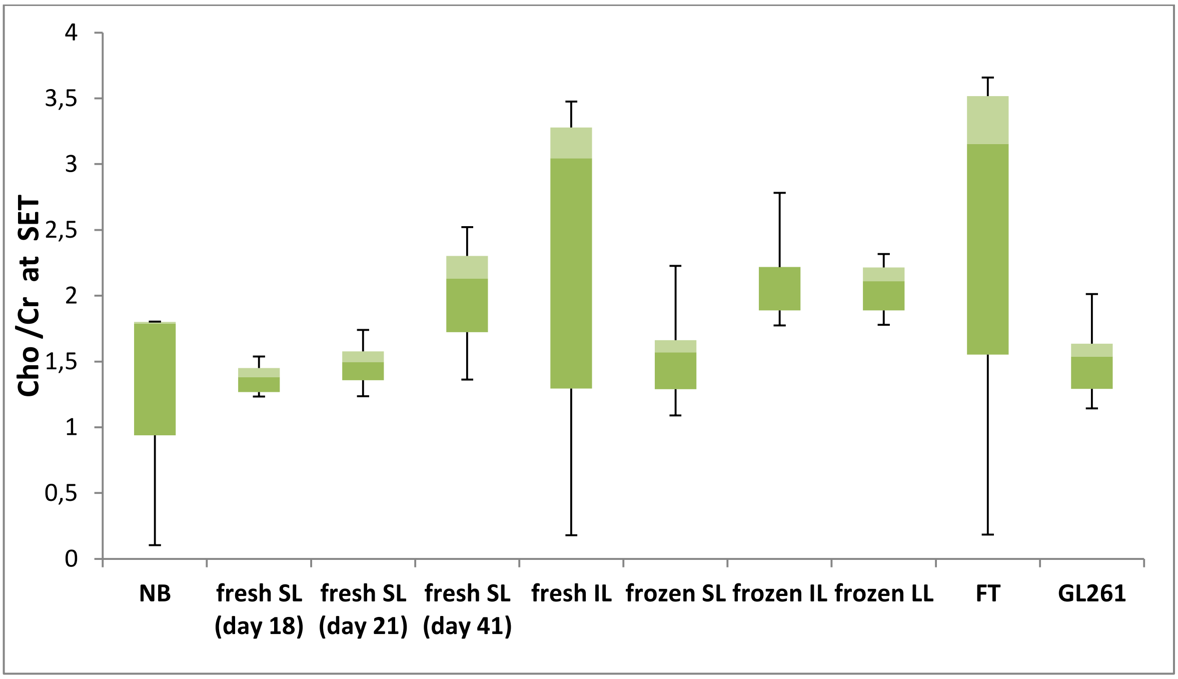

**Figure 5.7.** Box-plots representing Cho/Cr ratios at SET for normal brain parenchyma (NB) of C57BL/6 mice, tumours generated from fresh S912 gliospheres: ‘short latency’ (SL) group at day 18, 21 and 40 p.i. and ‘intermediate latency’ (IL) group at 35-42 days p.i.; tumours generated from frozen S912 gliospheres: ‘short latency’ (SL) group, ‘intermediate latency’ (IL) group and ‘long latency’ (LL); tumours generated from S912 gliospheres obtained from frozen tumour (FT) and standard GL261 tumours. The upper and the lower boxes represent the quartiles 1 and 3 of each distribution, respectively, and they are divided with the quartile 2 (median). The upper and lower whiskers show the maximum and minimum values for non-outliers of each distribution. See Table 5.3 and 5.4 for n values.

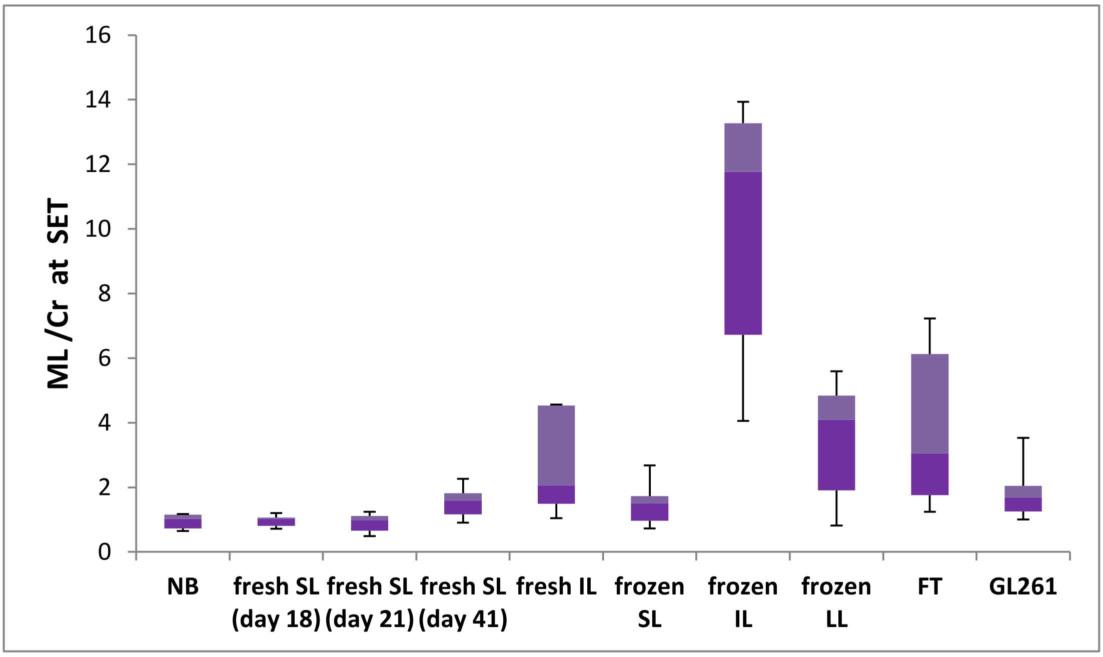

**Figure 5.8.** Box-plots representing ML/Cr ratios at SET for normal brain parenchyma (NB) of C57BL/6 mice, tumours generated from fresh S912 gliospheres: ‘short latency’ (SL) group at day 18, 21 and 40 p.i. and ‘intermediate latency’ (IL) group at 35-42 days p.i.; tumours generated from frozen S912 gliospheres: ‘short latency’ (SL) group, ‘intermediate latency’ (IL) group and ‘long latency’ (LL); tumours generated from S912 gliospheres obtained from frozen tumour (FT) and standard GL261 tumours. See Table 5.3 and 5.4 for n values.

Besides MRS studies, CE MRI allowed assessment of the state of BBB integrity and accordingly, a qualitative orientation of a possible transition to higher grade. Regarding animals implanted with fresh S912 gliospheres, 12 out of 16 animals were studied with CE MRI. It was observed that 7 out of the 8 animals screened during the initial mass development period (average volume 32 ± 9 $mm^3$ at day 28 p.i.) had intact BBB; 2 out of those 7 were also studied at the final stages of tumour development and displayed compromised BBB (average volume 136 ± 33$mm^3$), which suggested the undergoing transition from an original grade III tumour to a higher (grade IV). One of the latter is presented in Figure 5.9. Comparison of the spectra obtained at the initial and the final stages of tumour progression may also suggest this transition, as increased Cho/Cr ratio, elevated ML and Gly (at the resonance coresonating with mI at SET) can be observed. The remaining 4 animals implanted with fresh S912 gliospheres had BBB compromised at an average tumour volume of 144 ± 57 $mm^3$.

For animals implanted with frozen gliospheres, animals were studied at the initial stages of mass development (23 ± 14 $mm^3$, n = 27); 22 of them displayed broken BBB (22 ± 13 $mm^3$), while for 5 mice, all from the ‘short latency’ group, the BBB was intact (25 ± 23 $mm^3$), but no further CE MRI was obtained. The remaining 2 animals died before the CE MRI exploration could be performed; therefore their BBB status at death is unknown.

In the last batch of mice implanted with gliospheres obtained from a frozen S912 tumour piece, 3 out of 9 animals had intact BBB (average volume 25 ± 3 $mm^3$), but as above no further explorations were performed. The masses with compromised BBB were on average 33 ± 31 $mm^3$ (n=6).

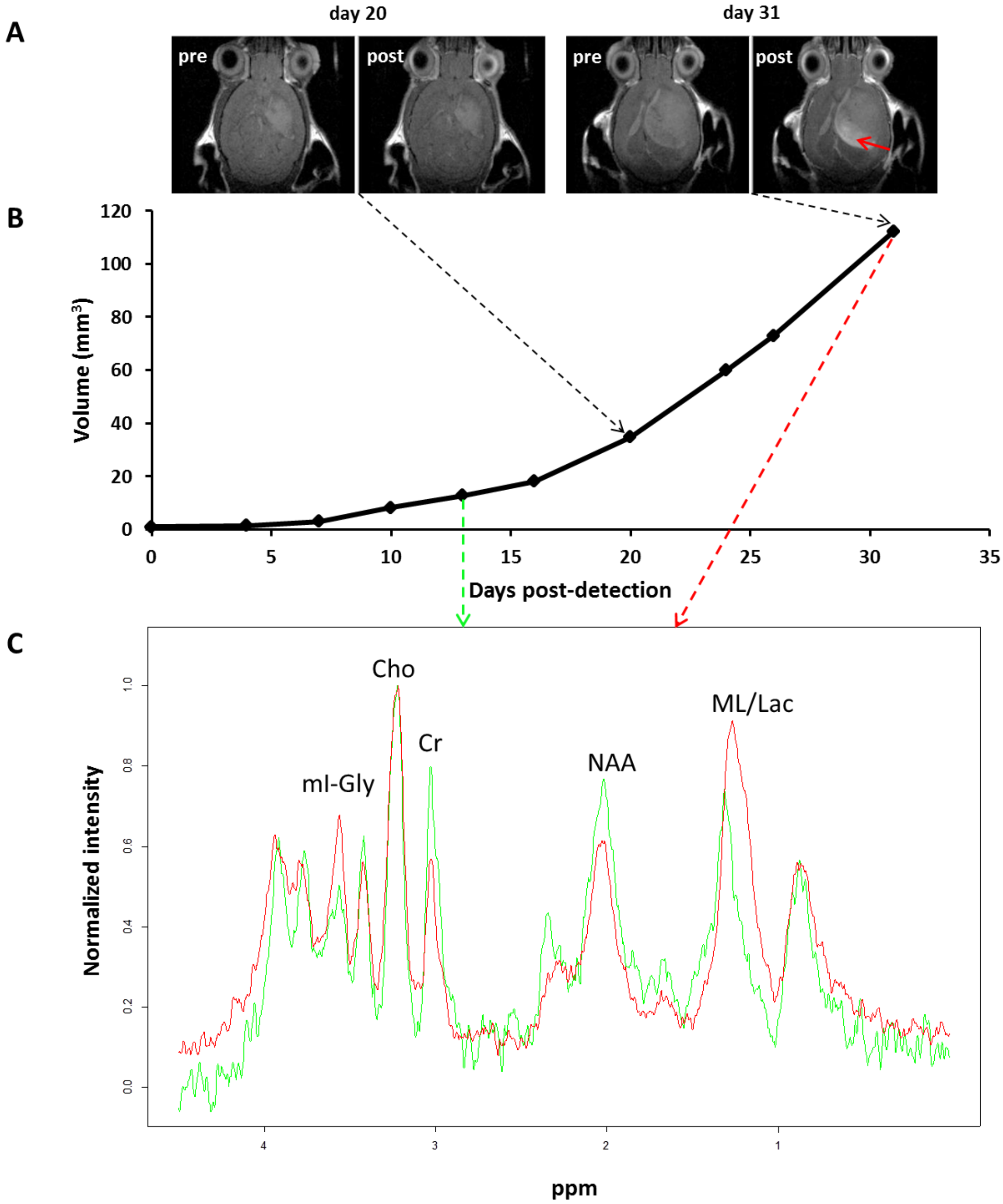

**Figure 5.9.** Changes in contrast intake and spectral pattern of G5-S912 tumour during its growth curve. **A)** Coronal $T_{1W}$ MRI pre and post CE on the day 20 (left) and 31 p.i. (right). Red arrow indicates the zone of contrast intake. **B)** Growth curve of the tumour. Black arrows indicate time points of the CE studies; while green and red arrows with dashed lines show time points at which SV SET MRS spectra presented in C) were acquired. **C)** Comparison of the SET spectra acquired at initial (green) and final (red) stages of tumour progression. Cho: choline, Cr: total creatine, NAA: N-acetylaspartate, Lac: lactate, ML: mobile lipids.

Moreover, the PE-MRSI classifier accessible at GABRMN allowed non-invasive evaluation of the tumour grade. The PR analysis was used to classify voxels from the glucose-perturbed MRSI matrices for the comparison of normal brain parenchyma, ODG (grade II) and GBM (grade IV). The classifier used was the one described in [107]. Representative nosological maps of classification for mice from groups D and E (see Table 5.1) are presented in Figure 5.10. The MSRI based classifier applied to tumour G1-S912 at day 39 p.i. shows a heterogeneous classification pattern compatible of transition between grade II, with OD component, and grade IV. As the used classifier does not contain the grade III class, the classification could be interpreted as suggesting a heterogeneous high grade glioma in transition between grade II/III and III/IV. Histopathology for G1-S912 after sacrifice at day 39 p.i. classified it as oligodendroglioma grade III (see also Section 5.3.2.4). Furthermore, Gc26-S912 evaluated by MRSI at day 35 p.i. suggested a mostly homogeneous grade IV glioma, which agreed with final histopathology performed after sacrifice at the same day.

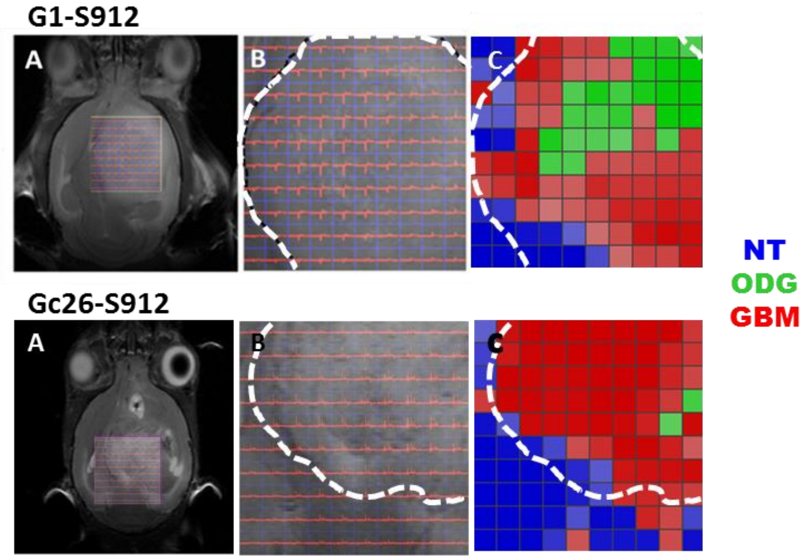

**Figure 5.10.** PR analysis for representative mice from groups D and E of animals, implanted with fresh gliospheres, G1-S912 (top) at day 39 p.i., and frozen gliospheres, Gc26-S912 (bottom) at day 35 p.i. **A)** VOI superimposed with the reference image ($T_{2W}$ HR). **B)** Enlargement of VOI shown in A with spvs for short TE in red. **C)** Nosological maps. Blue voxels are assigned to normal brain parenchyma (NT), red voxels to glioblastoma (GBM) and green voxels to oligodendroglioma (ODG). Tumour boundaries from $T_{2W}$ images are marked with a white dotted line.

#### 5.3.2.3. Genotyping

Nine randomly chosen animals with implanted gliospheres had their genotype checked in order to confirm the accordance with the original S912 GEM genotype. All tumours checked presented the expected transgene (Tg; S100B-v-erbB) as in the initial S912 mouse. However, three of the analysed masses presented loss of heterozygosity for the knockout gene (INK4A-ARF (+/-)), that is to say, they were homozygotic (Ko-/-). Two of these animals (G1-S912 and G4-S912) belonged to the batch of animals implanted with cells from fresh gliospheres ('short latency' group) while one (Gc18-S912) belonged to the 'intermediate latency' group from the batch of mice injected with cell from frozen gliospheres. The homozygous deletion of INK4A-ARF in humans is often associated with malignant progression in high-grade gliomas [156, 157] being also one of the most frequent mutations found in human gliomas [158, 159] associated with short survival times [156]. In transgenic mice it has been described that animals homozygous for loss of INK4A-ARF, develop tumours with similar tumour incidence, but with decreased latency and survival in comparison to heterozygous animals [63]. In our studies, the phenotypic consequences for the loss of heterozygosity for the original S912 knockout were not obvious, as the animals with homozygous deletion detected fall into the 'short latency' and the 'intermediate latency' groups. However, this genomic difference is not negligible and should be taken into account in future studies.

#### 5.3.2.4. Histopathological diagnosis

The original S912 tumour, as well as 48 out of 54 tumours generated from it, underwent histopathological analysis. From the total of 16 animals, with tumours developed post injection of cells from gliospheres obtained from a fresh piece of S912 tumour, 12 were analysed histopathologically and diagnosed as anaplastic ODG grade III (Table 5.5). The studied tumours were heterogeneous and showed two regions: one of grade II, characterized by having circumscribed neoplastic proliferation of isomorphic cells and another of grade III with proliferation of glial cells and GFAP positive. Studied tissues showed moderate pleomorphism anisocariosis, low mitosis, with neoplastic cells growing in a honeycomb pattern and blood vessels of irregular distribution and endothelial hyperplasia. Furthermore, populations of pleomorphic neoplastic cells with evident nuclear atypia, anisokaryosis and eosinophilic cytoplasm growing in groups were observed in the regions of transitions from grade II to III, in which the vascular component was more noticeable. In Figure 5.11 an example of an abnormal mass highly positive for oligo 2 and less for GFAP is shown.

The remaining 4 tumours developed from gliospheres derived from a fresh piece of S912 tumour were saved for future gliospheres generation and further transplantation.

**Table 5.5.** Histopathological diagnosis by HE staining for 12 tumours derived from implantation of gliospheres obtained from a fresh piece of S912 GEM tumour and IHC analysis obtained for selected tumours.

| ID | HE | IHC: Olig2 and GFAP |
|---|---|---|
| **S912** | anaplastic oligoastrocytoma | anaplastic oligoastrocytoma (grade III) |
| **G2-S912** | **poorly differentiated glioma / ODG (grade III)** | anaplastic oligoastrocytoma (grade III) |
| **G3-S912** | | |
| **G5-S912** | | |
| **G6-S912** | | |
| **G8-S912** | | |
| **G9-S912** | | highly pyknotic |
| **G10-S912** | | anaplastic oligoastrocytoma (grade III) |
| **G11-S912** | | anaplastic oligoastrocytoma (grade III) |
| **G12-S912** | | |
| **G13-S912** | | anaplastic oligoastrocytoma (grade III) |
| **G14-S912** | | |
| **G15-S912** | | |
| **G16-S912** | | |
| **G17-S912** | | |
| **G18-S912** | | |
| **G19-S912** | | |

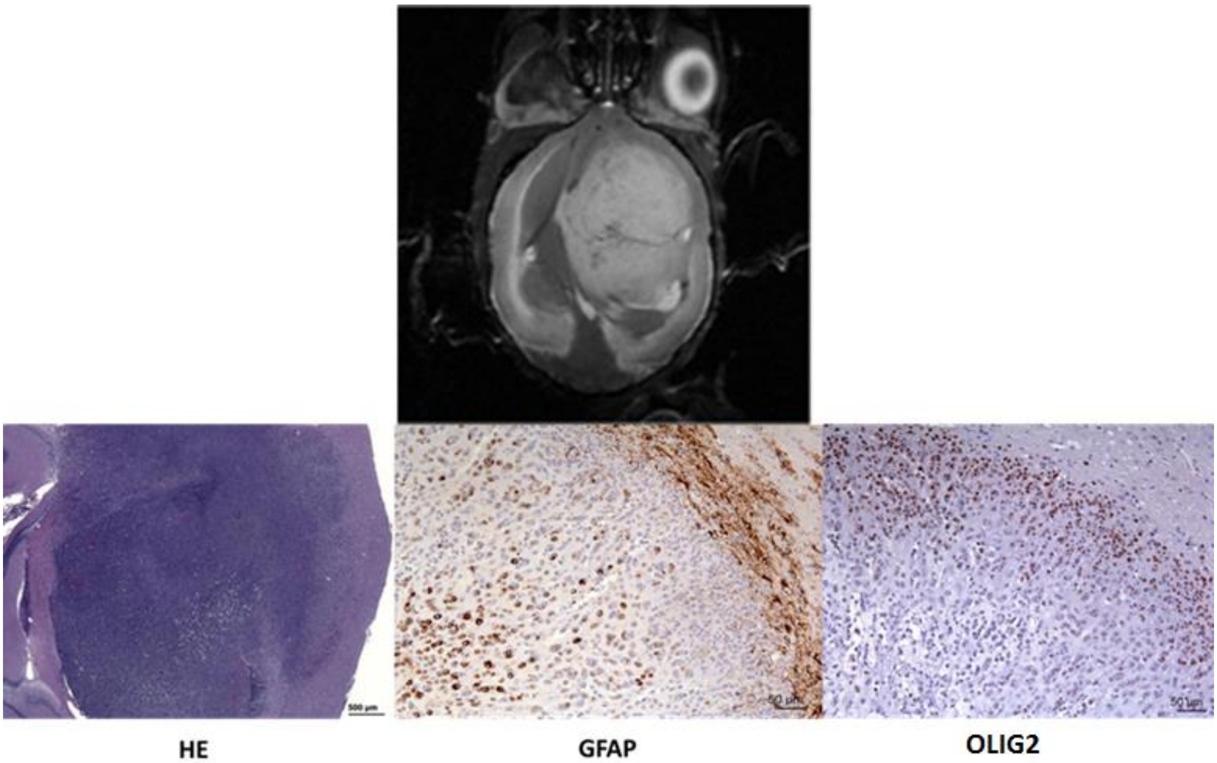

**Figure 5.11.** $T_{2W}$ coronal MRI of G2-S912 tumour 43 days p.i (top) and images of histological immuno-preparations of the tumour tissue done after the animal was sacrificed on day 62 p.i. with comparable orientation with respect to the reference MRI image.

The diagnosis for 27 out of 29 tumours derived from implantation of previously frozen gliospheres and all 9 tumours derived from implantation of gliospheres obtained from a frozen piece of GEM S912 tumour showed clear progression and all samples corresponded to the same type of tumour classified as GBM (grade IV) (see Tables 5.6 and 5.7). Brains of two animals were lost, because they died during the night and were not suitable for histopathological analysis due to tissue deterioration. Some tumours demonstrated differences in relation to their architecture, namely they had a “chondroid”/solid and microcystic pattern (refer to Table 5.6 and 5.7), and were more infiltrative than other tumours. However, they did not belong to one particular group of animals and were found in the short, intermediate and late latency groups, as well as in the group of animals implanted with gliospheres derived from a frozen piece of S912. Multifocal tumours were found to be more closely related to the presence of necrosis and the “chondroid” pattern. Mitotic index varied among tumours and in some tumours was very high (2-5 mitosis in x40 field). Presence of necrosis also varied from individual to multiple cells. The immunohistochemical study using GFAP and Olig2 as markers for astrocytes and oligodendrocytes, respectively, in selected cases confirmed that, in general, Olig2 a stained greater number of tumoural cells. On the other hand, GFAP identified tumour cells with the "chondroid" pattern.

**Table 5.6.** Histopathological diagnosis by HE staining for 27 tumours derived from implantation of frozen gliospheres obtained from a fresh piece of S912 GEM tumour and IHC analysis obtained for selected tumours.

| ID | HE | IHC: Olig2 and GFAP |
|---|---|---|
| **Gc1-S912** | **GBM (grade (IV)** | |
| **Gc2-S912** | | |
| **Gc3-S912** | | Olig2 positive tumour cells, some GFAP positive |
| **Gc4-S912** | | cells of "chondroid" part GFAP positive,<br>minority Olig2 positive |
| **Gc5-S912** | | |
| **Gc6-S912** | | Most Olig2 positive; minority of GFAP positive cells, including "chondroid" part |
| **Gc7-S912** | | |
| **Gc9-S912** | | |
| **Gc11-S912** | | Most Olig2 positive; minority of GFAP positive cells, including "chondroid" part |
| **Gc12-S912** | | |
| **Gc13-S912** | | |
| **Gc14-S912** | | |
| **Gc15-S912** | | |
| **Gc16-S912** | | |
| **Gc17-S912** | | |
| **Gc18-S912** | | |
| **Gc19-S912** | | |
| **Gc20-S912** | | |
| **Gc21-S912** | | |
| **Gc22-S912** | | |
| **Gc23-S912** | | |
| **Gc24-S912** | | |
| **Gc25-S912** | | |
| **Gc26-S912** | | |
| **Gc27-S912** | | Most Olig2 positive on the periphery; minority of GFAP positive cells, including "chondroid" part in the centre |
| **Gc28-S912** | | |
| **Gc29-S912** | | |

**Table 5.7.** Histopathological diagnosis by HE staining for 9 tumours derived from implantation of gliospheres obtained from a frozen piece of S912 GEM tumour and IHC analysis obtained for selected tumours.

| ID | HE | IHC: Olig2 and GFAP |
|---|---|---|
| **Gtc1-S912** | **GBM (grade (IV)** | |
| **Gtc2-S912** | | |
| **Gtc3-S912** | | |
| **Gtc5-S912** | | |
| **Gtc6-S912** | | |
| **Gtc7-S912** | | |
| **Gtc8-S912** | | most (40%) GFAP positive on the periphery; minority Olig2 positive in the periphery |
| **Gtc9-S912** | | |

### 5.3.3. Survival

Survival of the animals implanted with S912 gliospheres ranged between 31 and 318 days. This range was above the range for animals bearing GL261 tumours originated from cultured cells or cells from GL261 gliospheres (see Table 5.8). There were significant differences between S912 tumours derived from fresh gliospheres (short and intermediate latency) and GL261 fresh gliospheres derived tumours, as well as between the intermediate and long latency group of tumours derived from frozen gliospheres and fresh S912 gliospheres derived tumours. Kaplan-Meier survival curves are presented in Figure 5.12.

**Table 5.8.** Survival time (days, mean ±SD) of each experimental group of mice. There was a significant difference detected between: tumours derived from fresh S912 gliospheres (either, short or intermediate latency) and tumours derived fresh GL261 gliospheres (*); between either intermediate latency or long latency tumours derived from frozen S912 gliospheres and tumours derived from fresh S912 gliospheres (**). The difference in survival time was non significant ($p > 0.05$) between tumours derived from GL261 gliospheres (either fresh or frozen) and standard GL261 tumour, and neither between tumours derived from S912 gliospheres obtained from a frozen piece of tumour and tumours derived from fresh S912 gliospheres.

| Group of animals | GL261 tumours (n=7) | GL261 gliospheres | | S912 gliospheres | | | | | |
|---|---|---|---|---|---|---|---|---|---|
| | | | | Fresh | | Frozen | | | Frozen tumour (n=9) |
| | | Fresh (n=6) | Frozen tumour (n=7) | Short latency (n=9) | Intermediate latency (n=7) | Short latency (n=13) | Intermediate latency (n=9) | Long latency (n=5) | |
| Mean survival (days) | 19 ± 2.9 | 23 ± 2.5 | 25 ± 2.4 | 40 * ± 4.9 | 61 * ± 20.6 | 41 ± 10.6 | 103 ** ± 42.4 | 163 ** ± 124.2 | 45 ± 15.3 |

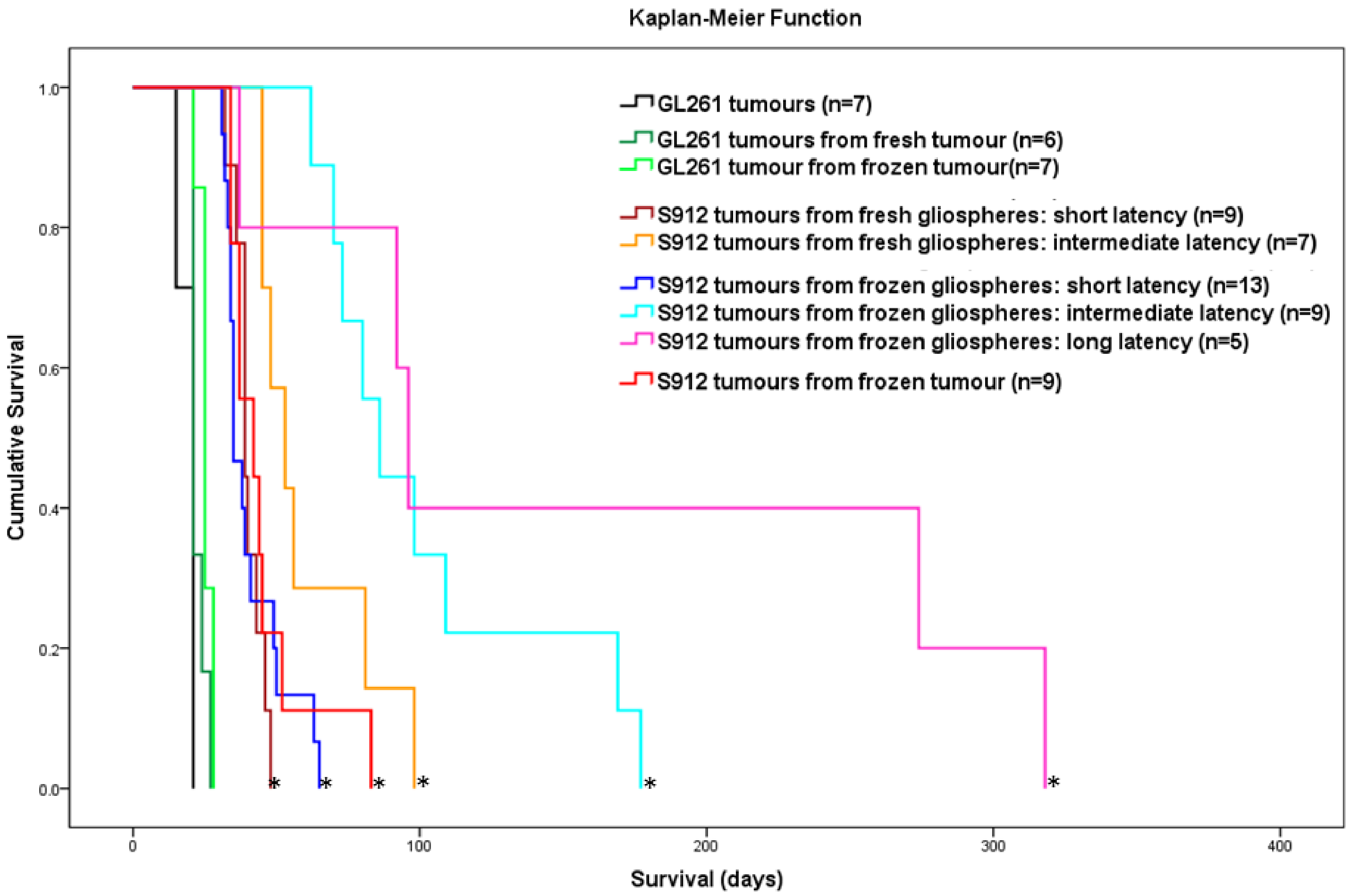

**Figure 5.12.** Kaplan-Meier survival curves of C57BL/6 mice implanted with cells/gliospheres of different origin or different preparation protocol. Survival of the animals implanted with cells from S912 gliospheres was significantly higher (marked with asterisk) in comparison with those implanted with GL261 cells or cells from GL261 gliospheres. See Table 5.4 for further details.

### 5.4. Conclusions

1. We successfully generated gliospheres from an anaplastic OA (grade III) GEM tumour. However, freezing and cell culture protocols produced a progression to grade IV glioblastoma (GBM). This makes the developed transplantable model qualify as potential secondary GBM model in mice.

2. Tumours derived from GEM gliospheres presented 100% penetrance, which is significantly higher that the penetrance obtained for the local S GEM colony (about 17%).

3. The survival time of the S912 derived cells implanted animals (range 31 - 318 days) was significantly higher than of the standard GL261 GBM tumour model (15 – 21 days).

4. There was an increasing trend of Cho/Cr and ML/Cr ratios with time p.i. (for the 'normal latency' group implanted with fresh S912 gliospheres) and with increasing latency, possibly indicating progression in tumour grade.

5. The PE-MRSI classifier accessible at GABRMN allowed non-invasive evaluation of the tumour grade in selected animals, which only partially agreed with the histopathological diagnosis, as the classifier did contain the grade III class. However, heterogeneous classifications could be interpreted as suggesting a heterogeneous high grade glioma in transition between grade II/III and III/IV.

6. Loss of heterozygosity for the knockout gene was detected in 3 out of 9 tumours analysed, but clear phenotypic consequences due to this loss were not observed.

# 6. Sequencing of selected genes in different tumour models

**(Objective 1, 2 and 3)**

## 6.1. Specific objectives

Restricted genomic evaluation of selected murine tumour models by checking the possible presence of particular driver mutations commonly occurring in gliomas (IDH1, IDH2 and p53).

## 6.2. Specific Materials and Methods

### 6.2.1 Selection of samples

Several tumour samples from different models/animals were selected for the gene sequencing protocol and in total 16 samples were sequenced for the DNA sequences of interest: 6 GL261 tumours, 3 GL261 cells of early passage (p.22), 3 wt C57BL/6 brains, 2 S colony tumours, namely S407 and S885 (both histopathologically diagnosed as anaplastic astrocytoma grade III), and 2 tumours developed during the GEM tumour disaggregation protocol (refer to Section 5), namely Gc4-S912 and Gtc-S912, that progressed to grade IV from the original grade III tumour.

### 6.2.2 Sample obtention and DNA extraction

GL261 tumours were resected from 6 animals on the day 16-21 p.i., when the tumour reached the desired volume (between 70-130 $mm^3$), evaluated by volumetric $T_{2W}$ MRI. For the wild type C57BL/6 animals, healthy brain parenchyma was extracted instead. Regarding the S colony tumours and S colony GEM derived tumours, a piece of each tumour was obtained in previous experiments (Section 4 and 5, respectively). All tumours were frozen after dissection as previously described in Section 3.7.

In case of the GL261 cell line, cells were subcultured into corning flasks. On the day 7 post-cultivation, when they reached confluence, they were washed twice with PBS and detached with 2ml of trypsin-EDTA solution (1X) per flask. To stop the action of trypsin 8ml of RPMI media was added and cells from each flask were centrifuged at about 1,100g for 8 minutes into a 15ml Falcon tube. Each pellet was resuspended with 1ml of PBS with 10% DMSO, put into -80ºC for 4 hours and then stored in liquid nitrogen until further processing. Just before extractions cells were pelleted again by centrifugation as above and 150µl of PBS was added to each tube.

The tissue or cell pellets were homogenised following steps illustrated in Annex 4 and genomic DNA was extracted according to the protocol provided by the DNA extraction kit supplier (refer to the QIAamp® DNA Mini Handbook, found on the QIAGEN website http://www.qiagen.com). Then, primers were designed for the amplification of specific DNA regions with of IDH1, IDH2 and p53 genes containing sites where mutations occur frequently in gliomas (i.e. R132, R172 and R273 respectively). This was done using online primer design tools and the resulting primers were as follows: for IDH1 gene: 5’-TCACCAAAGATGCTGCAGAG-3’ and 5’-ACCACTGATCTGAGCGTATGG-3’; for IDH2 gene: 5’- AAGAGCCCTAACGGAACGAT-3’ and 5’- AGTTCAAGCCAAGGCTTCCT-3’, for p53 gene: 5’-CGGGAAATAGAGACGCTGAG-3’, and 5’- GTGACTTTGGGGTGAAGCTC-3’. Samples were amplified by PCR and electrophoresed to check for the presence of the desired products as seen in Figure 6.1. The final optimized PCR conditions for maximum amplification of the regions of interest can be found in Annex 5.

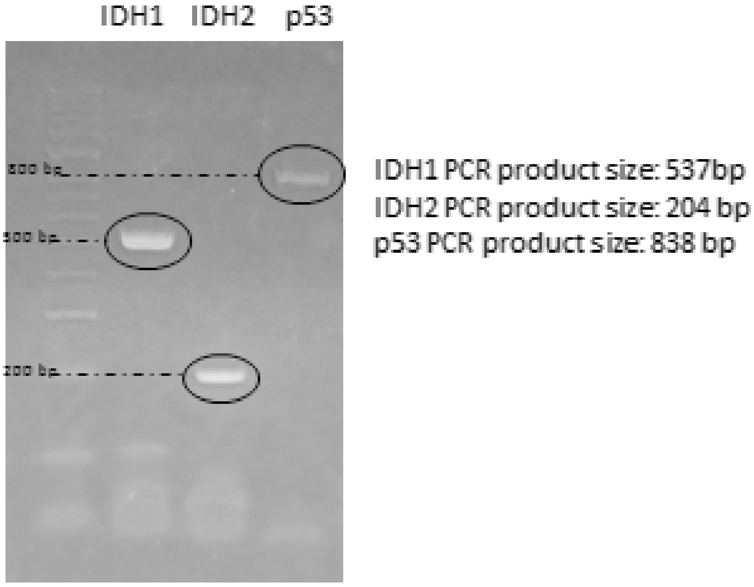
IDH1
IDH2
p53
800 bp
500 bp
200 bp
IDH1 PCR product size: 537bp
IDH2 PCR product size: 204 bp
p53 PCR product size: 838 bp

**Figure 6.1.** PCR amplification of the regions of interest of IDH1, IDH2 and p53 of murine DNA

Sequences were analysed for the possible presence of mutations using the Sanger method at *Servei de Genòmica i Bioinformàtica* at the Institut of Biotechnology and Biomedicine, UAB in collaboration with Dr. Anna Barceló. Sequences and chromatograms were viewed using the DNA baser software version 3.5.4 (available to download from http://www.dnabaser.com/download/download.html) and mutations searched using online alignment tools (www.ncbi.nlm.nih.gov/BLAST/).

## 6.3. Results and discussion

We decided to try to identify three mutations that frequently occur in human, namely IDH1, IDH2 and p53 at R132 [160-162], R172 [163, 164] and R273 [165], respectively. The rationale for this very preliminar genomic characterisation of our tumour models was to evaluate whether the status of three genes (IDH1, IDH2 and p53) were wt or mutated and, accordingly close to primary (wt) or secondary (mutated) human GBM.

When the DNA extraction was concluded and 3 PCR products obtained (for IDH1, IDH2 and p53 genes) for each sample, the amplicons were sequenced using the Sanger method. Obtained sequences from the tumoural masses were aligned with the sequences of the normal brain parenchyma of a C57BL/6 mouse, as well with the sequences found in the online *Genome Bank* (http://www.ncbi.nlm.nih.gov/nuccore/) to check for the possible presence of mutations. However, there were no mutations were detected in any of the tumour samples for the selected genes regions, as shown in Figure 6.2).

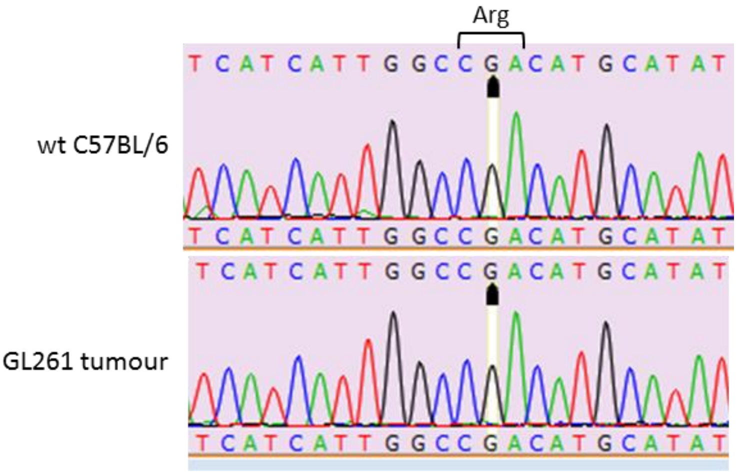

**Figure 6.2.** Comparison of IDH1 sequences at the region of expected mutation site (R132) for normal brain parenchyma of wt C57BL/6 mouse and a GL261 tumour showing no mutation detected in the tumour. Arg - Arginine (R).

A possible explanation for this could be that the driver mutations found in humans do not correspond to the same gene location in the investigated murine tumour genes. Some authors [161] suggest that an IDH1 oncogene mutated at codon R132 could also be a tumour driver in mice, but this has never been found in murine GBM, which seems also to be the case in our models (Figure 6.2). Regarding p53, a tumour suppressor gene, many mutations “hotspots” and truncations can take place, but R273 is the most frequently altered codon reported [165, 166] in humans. The p53 primers designed to check for this alteration in our murine models, also included in the product amplicon the R153 codon, which was reported to possess a homozygous point mutation in the GL261 model [60]. However, neither mutation was detected in our models, which include the GL261 GBM.

For future studies, the whole genome/exome sequencing should be performed instead of punctual studies in order to detect the gene driving mutations in the murine tumour models investigated in our case.

### 6.4. Conclusions

1. PCR and sequencing methods were optimized for the analysis of IDH1, IDH2 and P53 mutations in preclinical samples and cultured samples.

2. Different samples from our glioma models, including GL261 tumours, GL261 cells line, S colony tumours and tumours developed during the GEM tumour disaggregation protocol (refer to Section 5) were sequenced and no IDH1, IDH2 and p53 mutations at particular sites reported for human or GL261 murine gliomas were detected.

# 7. Longitudinal studies of the GL261 GBM model response to temozolomide (TMZ) therapy

(Objective 3)

## 7.1. Specific Objectives

The aim of this section was to obtain *in* vivo, in a non-invasive way, biochemical information from the preclinical GL261 tumour (GBM, grade IV) through MRSI studies along the TMZ therapy. This should be performed at different time points of a previously established TMZ therapy protocol in order to search for molecular biomarkers indicating therapy response or tumour relapse. For this, PR analysis of the MRSI matrixes, using source extraction, was performed and transformed into colour-coded nosological images of response or relapse after therapy.

## 7.2. Specific Materials and Methods

A total of 28 female C57BL/6 mice of age 16-18 weeks were implanted with GL261 cells, as described in Section 3.6. To allow sufficient scanner time for MRSI exploration protocols, the study was divided into four parts, each time implanting 7 animals. On day 10 p.i. $T_{2W}$ MRI screening was performed (see Section 3.10.1) and 3 mice with homogenously growing tumours (according to their tumour volume) from each group of 7 (total n = 12, considering the overall experiment) were chosen to proceed into the TMZ therapy protocol (as per Section 3.9) and DMSO-MRSI protocols (Section 3.10.3). DMSO-MRSI explorations were performed every second day, starting on day 10 p.i., with 6 consecutive 14ms TE MRSI acquisitions for the first group of 3 animals and 4 consecutive 14 ms TE MRSI acquisitions for the remaining mice. The explorations were performed until the animals died or were sacrificed due to symptoms (see Annex 2). The brains were dissected and fixed in 4% formaldehyde for histopathological diagnosis, apart from mice C817 and C819, which were frozen in liquid nitrogen (as per Section 3.7) for gene sequencing, as it was also described for other tissues in Section 6.

All data obtained was processed according to *MRSI and PE-MRSI data processing* of Section 3.10.6 and the MV MRSI matrices acquired prior to and post DMSO administration, exported in ASCII format, were used for source extraction and segmentation using a semi-supervised approach, as described in Section 3.11.2. This was done for each animal and for each time point of exploration using scripts developed by the GABRMN and running over MatLab (The MathWorks Inc., Natick, MA, USA), that automatically extract sources and produce colour-coded maps of possible response.

The response to TMZ therapy (for use in the semi-supervised approach in pattern recognition) was evaluated using the Response Evaluation Criteria In Solid Tumours (RECIST) 1.1 [167].

A group of 16 tumour bearing mice not chosen for the therapy and the DMSO-MRSI evaluation were used as controls for survival and tumour growth for this study and were sacrificed when symptoms of suffering occurred. Tumours were then excised and frozen in liquid nitrogen to be used for the protocol of sequencing of selected genes (Section 6).

## 7.3 Results and Discussion

A total of 12 C57BL/6 wt mice with GL261 implanted tumours were subjected to the 3 cycle therapy previously optimized in our group [123] , which was designed based on previous literature on toxicology [168], efficacy [169] and repeated cycles scheduling [121, 122] of TMZ in GBM therapy in preclinical studies.

Among the 12 studied mice, masses showed different growth kinetics, suggesting variable response to the standard therapy protocol applied. Therefore, this part of the study was focused on tracking and detecting potential local changes in GL261 tumours induced by TMZ administration non-invasively, through MRI, MRS and MRSI along tumour evolution and course of therapy in the individual investigated tumours.

### 7.3.1. Growth kinetics of GL261 tumours subjected to therapy

The therapeutic strategy applied in this work to GL261 GBM was based on previous publications [123] were it was reported that TMZ therapy produces a transient response detectable by MRI after the second cycle of treatment (as per Section 3.9). Tumour volume of 12 cases in the treated group was calculated at the same day the MRSI sequences were acquired (see Section

3.10.6), in order to correlate the potential therapy response sampled by changes observed in the spectral pattern and described by the sources, with a standard response indicator - the tumour growth assessed volumetrically by MRI. This MRI-based volume calculation strategy has been applied by other authors for evaluating therapy response in GBM preclinical models [170, 171], although it has some limitations related to the size of the mouse brain, which requires high field MR scanners (7 - 12 T) or micro-imaging sets suitable for scanning small animals [172].

MRSI acquisitions started on the day 10 post-inoculation (mean tumour volume 10.53 ± 5.6 mm$^3$) and were performed, when possible, every second day until the animals died or were sacrificed, due to mass effects and according to animal welfare protocol criteria. As it can be seen in Figure 7.1, the volume kinetics of tumours treated with TMZ, is quite variable, also suggesting possible differences in response to the therapy protocol used. However, the average growth curve of the treated animals combined (refer to Figure 7.2) shows characteristic transient response that is detectable by MRI as volume growth arrest in comparison with untreated tumours, as seen in [123] (Figure 7.3). The tumour volume at day 20, 22, 24, 28, 30 and 32 post-inoculation in treated animals was found to be significantly lower than the GL261 untreated control at day 21 p.i. ($p < 0.05$). To validate the general growth pattern of treated animals in this work, their average growth curve was also compared to the average growth curve of responders from previous studies of our group [123] and no significant differences were observed in comparison with previous results (refer to Figure 7.4). In both cases tumours showed a characteristic volume growth arrest starting already at the end of the second cycle, i.e. between days 20 and 34 p.i.

With respect to the case C817, it was excluded from the mean growth rates curves in Figures 7.2 and 7.4, as its volumes has outlier values at three different time points detected by Dixon's test.

Treated animals with significantly longer survival and decrease in tumour volume, namely C817 and C819, were decided to be treated with additional two-day therapy cycles, once the regrowth of the tumour occurred and reached about 75 mm$^3$ – the average volume at which the animals started to respond to TMZ. The sufficient regrowth only occurred for the case C819, but the animal died on the second day of the fourth cycle (refer to Figure 7.1).

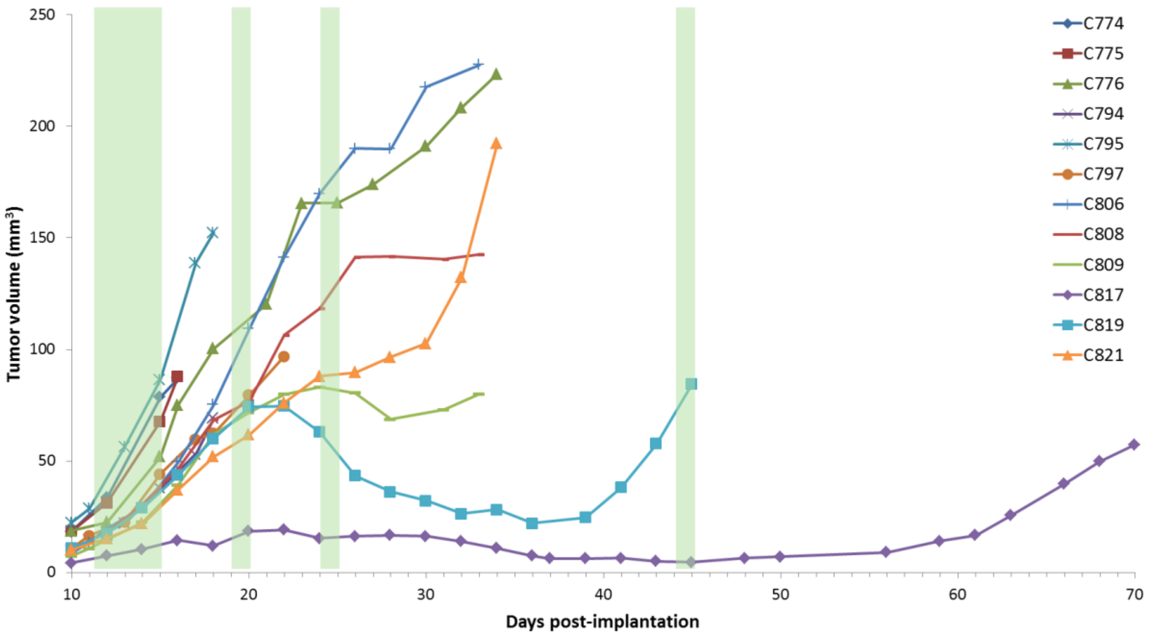

**Figure 7.1.** Volume growth dynamics of GL261 tumours treated with TMZ (n = 12). Green sections show each therapy cycle duration.

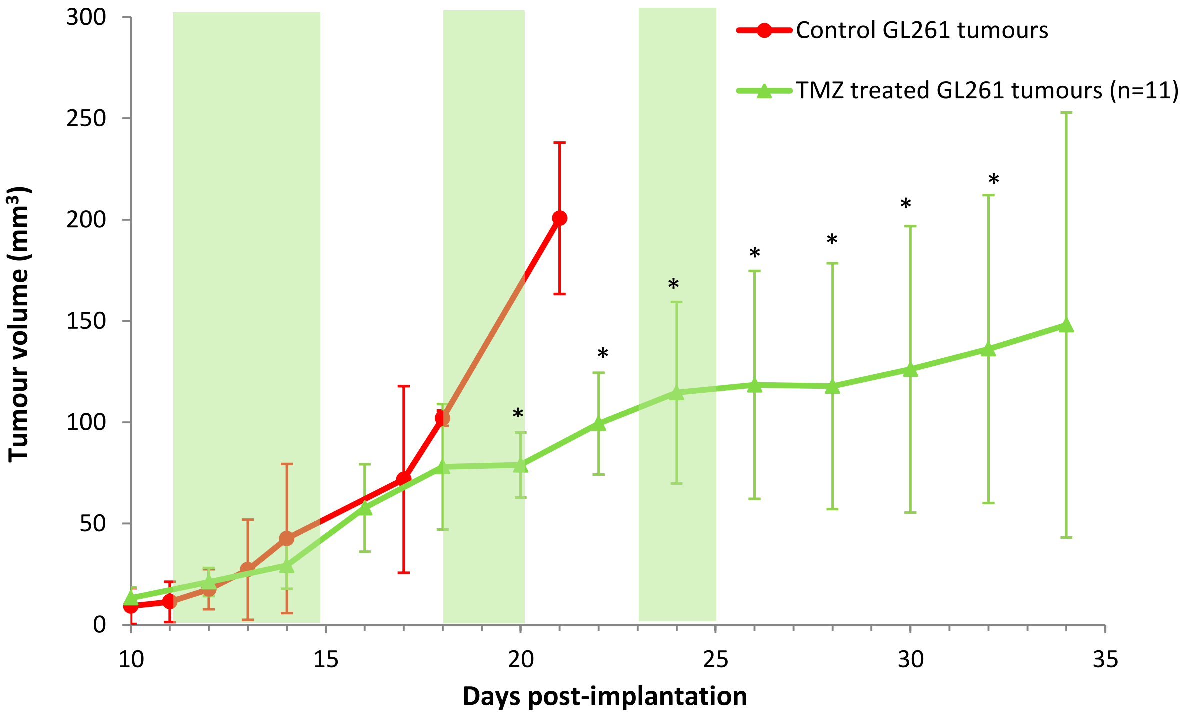

**Figure 7.2.** Mean growth rate (±SD) of GL261 tumours treated with TMZ (green bar columns) in this thesis (n = 11, green symbols), excluding case C817, in comparison to the standard growth kinetics of untreated GL261 tumours (n = 6, red symbols). Asterisks (*) indicate the significant difference ($p < 0.05$ ) in volume between treated animals and untreated GL261 control group on the 21 p.i.)

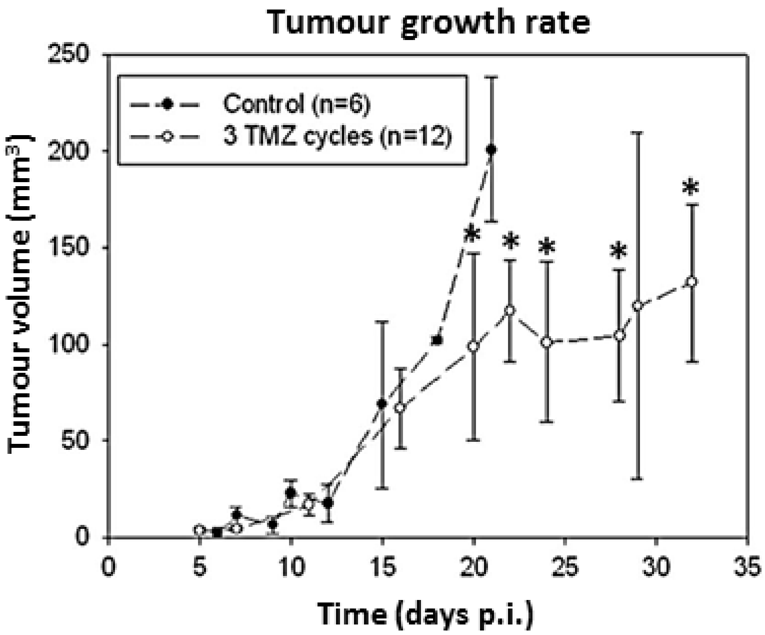

**Figure 7.3.** Tumour growth rate (average values ± SD) of control (untreated) GL261 tumours (n = 6) and tumours treated with three TMZ cycles (n = 12). Treated tumours showed a significantly lower volume (marked with an asterisk) at days 20, 22, 24, 28 and 32 of evolution, in comparison with control tumour volumes at day 21 (Figure taken from [123]).

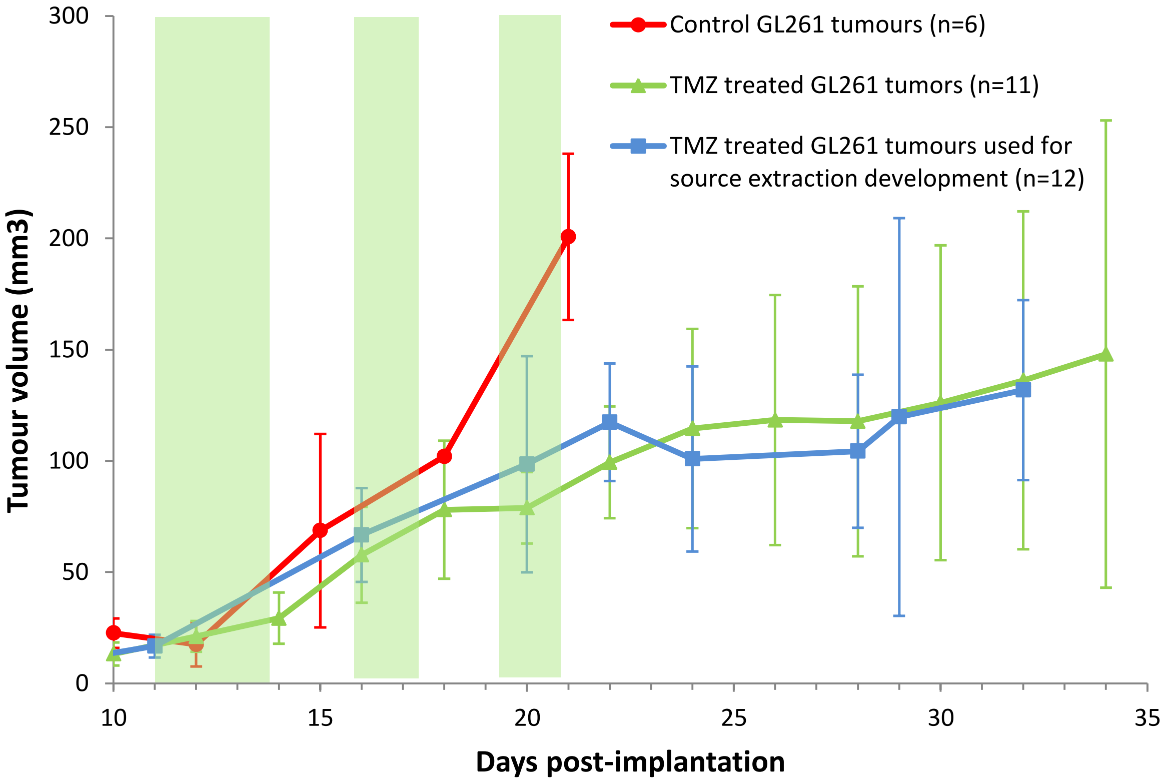

**Figure 7.4.** Mean growth rate ±SD of GL261 tumours treated with TMZ (blue symbols), excluding case C817, in comparison to both, previous results of the group [123] (green symbols) and the standard growth kinetics of untreated GL261 tumours (red symbols).

It has to be noted that in Figures 7.2 and 7.4 above, the growth until day 34 p.i. is shown, however the mice C817 and C819 survived past that day, until day 70 and 45 p.i., respectively (as seen in Figure 7.1).

### 7.3.2. Evaluation of tumour response to TMZ according to RECIST criteria

Based on volumes and growth curves of treated tumours, response was evaluated according to the published RECIST criteria [167, 173], that define when tumours in cancer patients improve (i.e. respond), stay the same (i.e. stabilize), or worsen (i.e. progress) during treatment. Initially, baseline was defined and tumour burden estimated at this time point in order to use it as a reference for subsequent measurement and to assess objective response. The baseline was defined according to the previous results of the group [174]; i.e. GL261 tumour bearing mice treated with one TMZ cycle do not respond to treatment, demonstrating no significant difference in growth in comparison to the untreated control group, therefore for assessing the three cycles TMZ protocol, the baseline was defined as the volume at the beginning of the second cycle (namely day 20 p.i.). The reason for this choice is that it was already known for our preclinical model that one TMZ cycle was not effective and a reduction in volumes of the investigated tumours was not expected during the period of the first cycle of therapy (stable disease according to RECIST criteria [167]). Using this baseline, the best overall response according to the RECIST criteria was evaluated, i.e. the best response measured as the smallest increase or largest decrease in each tumour volume recorded from and compared to the baseline volume. The response categories and animals falling into them are presented in Table 7.1 below. The volume was measured based on MRI $T_{2W}$ hyperintensity abnormal brain mass detection (as described in Section 3.10.4).

**Table 7.1.** Best overall response evaluation: animals following into each response category and corresponding RECIST criteria.

| **Response Category** | **Animals** | **Criteria** |
|---|---|---|
| Complete response | none | Total disappearance |
| Partial response | C817, C819 | At least 30% decrease in volume * |
| Stable disease | C776, C806, C808, C809, C821 | Neither sufficient shrinkage nor sufficient increase to qualify for partial response or progressive disease, respectively |
| Progressive disease | C797 | At least 20% increase in volume * |
| Not evaluable for response | C774, C775, C794, C795 | Early death |

* best response recorded from and compared to the baseline volume on day 20 p.i.

According to the RECIST criteria and considering the best response observed, none of the animals included in this study showed complete response with a total disappearance of the tumour. Two masses, namely C817 and C819, showed decrease in volume by more than 30% before recurrence, what classifies them into the partial response group and five tumours (C776, C806, C808, C809 and C821) were categorised as stable disease, which means that response to TMZ resulted in a growth arrest. One tumour was classified as progressive disease with more than 20% increase in volume (case C797), while the remaining 4 masses (C774, C775, C794, C795) could not be evaluated using those criteria due to early death of the animals, i.e. between days 16 and 18 p.i., which is before the defined baseline.

The average curves for each group of response considering the RECIST criteria are presented in Figure 7.5. It should be noted that animals belonging to the progressive disease and not evaluable groups were given just two or one therapy cycle, respectively, due to early death (refer to Figures 7.5 and 7.6).

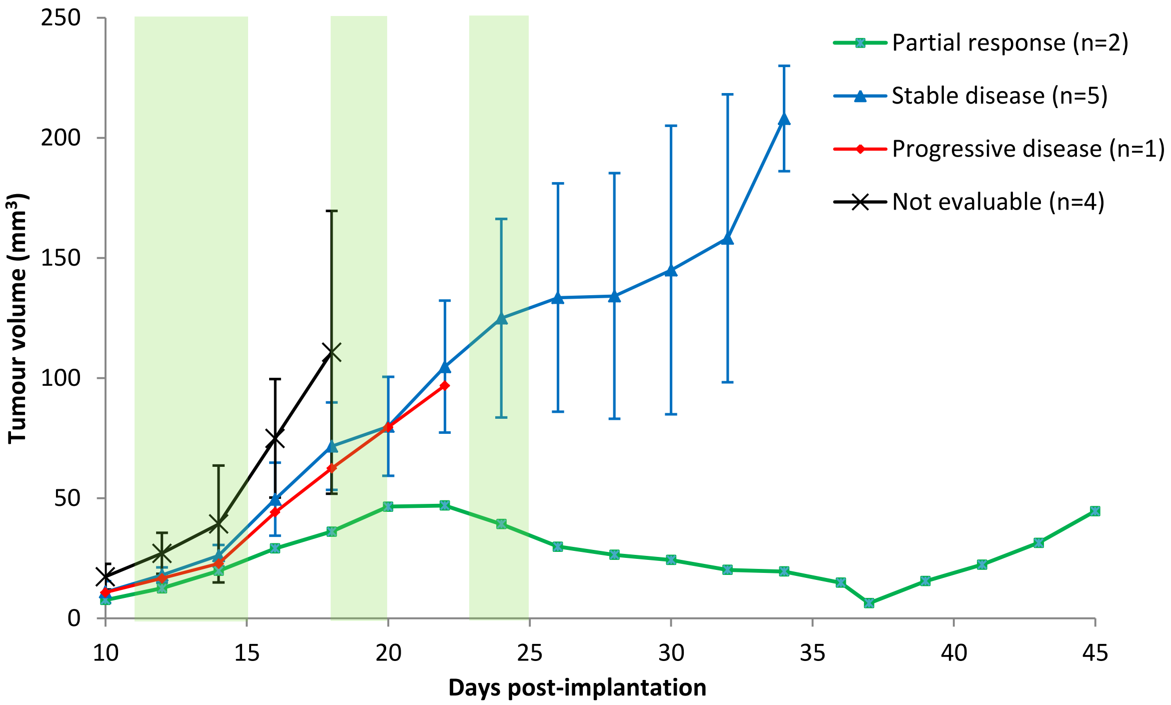

**Figure 7.5.** Average growth curves of each group of response defined by RECIST criteria.

These data suggest a high variability in tumour response, taking into account the tumour volume criteria, which is one of the main systems used in the clinical practice, with possible anatomic and metabolomic relevant changes taking place before anatomical changes could be seen (see Sections 7.3.4 – 7.3.7)).

### 7.3.3. Survival

The survival rates of the animals treated with three cycles of TMZ were also analysed and correlated with volumetric MRI studies. There was significant difference in survival ($p < 0.05$) between the survival of the control mice harbouring GL261 tumours not treated with TMZ (n = 16, mean survival 23.5 ± 5.3 days, with a final mean tumour volume of 178.7 ± 116.7 $mm^3$) and the group defined as partially responding (see Table 7.1), in which animals lived 45 (C819) and 70 days (C817) and the final volumes measured were 84.6 $mm^3$ and 57.3 $mm^3$, respectively. Also, there was significant survival increase in the partial response group when compared to the stable disease group (see Table 7.1) (n = 5, mean survival 33.4 ± 0.5 days, with a final volume of 225.5 ± 2.9 $mm^3$).

However, there were no significant differences between control and stable disease groups. Figure 7.6 below shows the Kaplan-Meier survival curves of the different groups.

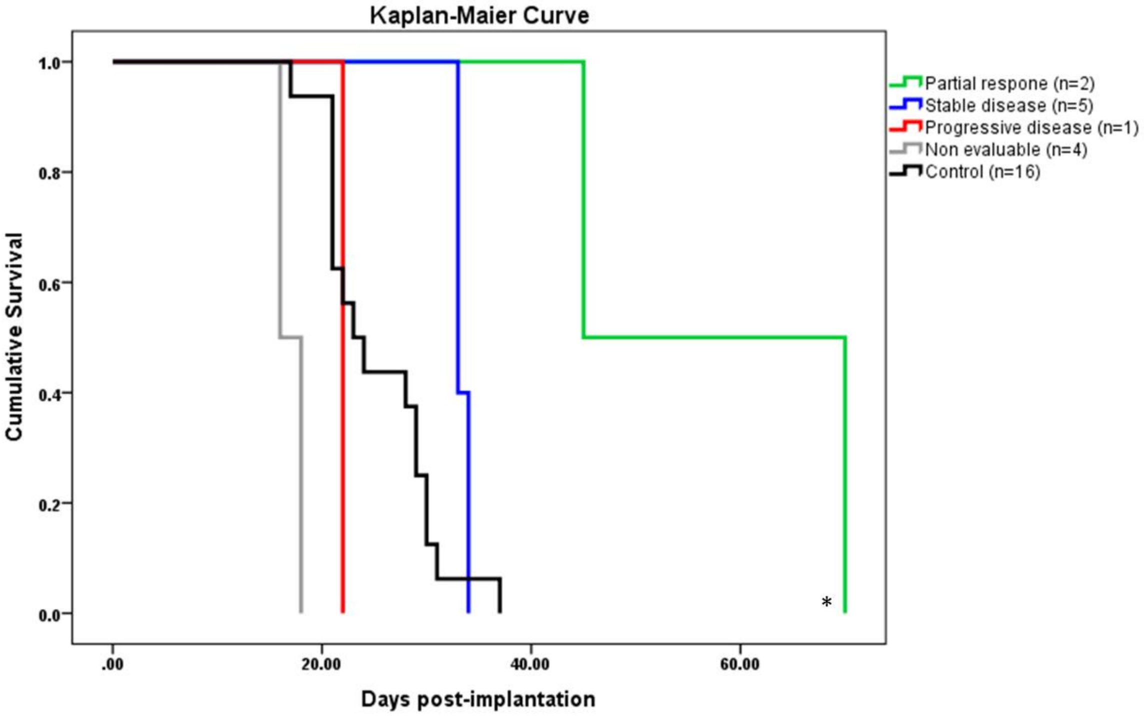

**Figure 7.6.** Kaplan-Meier survival curves of animals harbouring GL261 tumours subjected to TMZ therapy classified as partially responding (green), stable disease (blue), progressive disease (red), non-evaluable group (grey) and control GL261 group (black). There was significant difference in survival detected between the partial response group and control group, as well as between the partial response and stable disease groups.

To increase the number of cases and obtain more representative results, the above survival rates were combined with previous results of our research group [123], which produced increased number of animals in the stable disease group (n =17) and in the control group (n = 22). Taking these numbers into account resulted in minor modifications in average survival of both the stable disease group (27.9 days) and control group (21 ± 5.5 days), and with the significant differences between the groups remaining as described in previous paragraph. Survival of the non-evaluable group was 18 ± 2.4 days. Kaplan-Meier curves are presented in Figure 7.7 below.

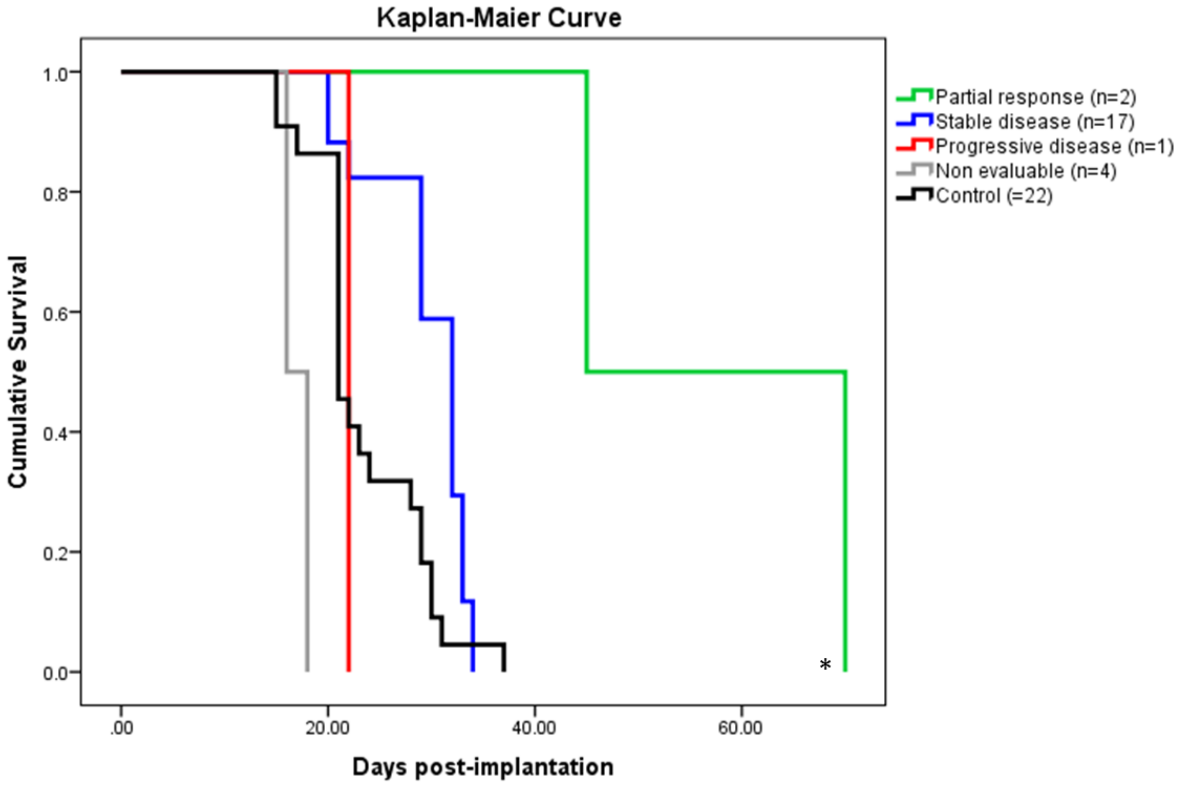

**Figure 7.7.** Kaplan-Meier survival curves of animals harbouring GL261 tumours subjected to TMZ and also control mice, from the current work and from previous group work [123], classified as partially responding (green), stable disease (blue), progressive disease (red), non-evaluable group (grey) and control GL261 group (black). There were significant differences in survival detected between the partial response or stable disease groups and the control untreated GL261 group. There was no significant difference between the stable disease and control groups.

### 7.3.4. MRI

Apart from the volume measured using MRI and difference in survival in the treated GL261 animals in comparison with mice from the control group, changes in tumour appearance of the $T_{2W}$ images were also observed along the longitudinal experiments. Representative MRI acquisitions along the evolution of the C819 tumour, which was defined as partially responding, are shown in Figure 7.8. On the day 18 p.i., apart from visible volume increase in comparison with day 10 p.i., the heterogeneity of the tumour mass is clear with hyper-intense zones within the tumour boundary. This could be an early indication of cell death necrosis due to the therapy response, as seen by other authors upon treatment in GEM [56] or human gliomas [175], although the shrinkage of the whole mass volume does not become apparent until past the day 22 p.i., when also possible tissue haemorrhage, visible as hipo-intense stretches, is noticeable. The possible bleeding disappears later on and recurrence of the mass, with mass volume increase occurs (as observable by day 45 p.i.).

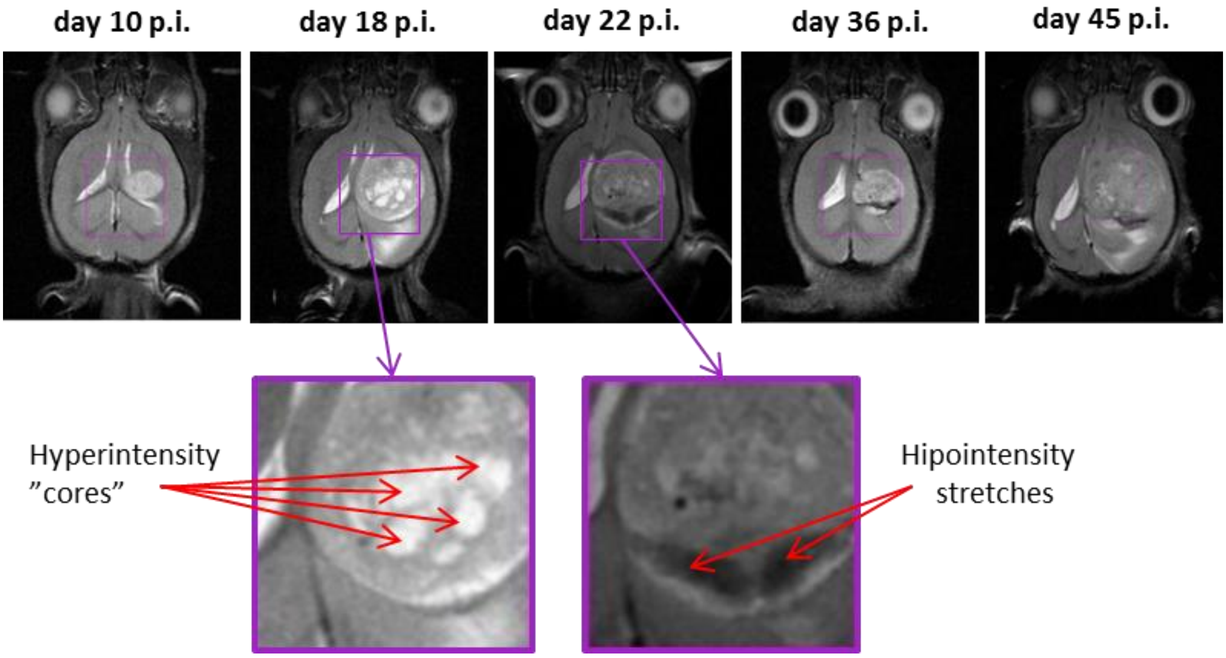

**Figure 7.8.** $T_{2W}$ coronal MRI of C819 tumour (classified as partially responding to the therapy) at selected time points along the tumour evolution.

### 7.3.5. PE-MRSI and DMSO maps

MRSI techniques have been previously used for assessing tumour changes due to effective treatments [176-178], besides of superimposing the metabolomic and anatomical information, they also provide the advantage of obtaining more data (i.e. spvs, spectral vector elements) with the same number of animals (in our case, each study provides 100 voxels, spvs, for the same animal). And since tumours are commonly heterogeneous, MRSI can be used to characterise different parts within a tumour and its surrounding tissue [73, 179]. The application of PR techniques to these data vectors provide us with the possibility of calculating nosologic images to correlate anatomic changes (detected by MRI) with metabolic features/changes. In addition, the use of spectral perturbation techniques, as described in [113], was also applied with the goal to increase the dynamic range of the changes observed in each experimental group. In this work, PE-MRSI sequences were performed every 2 days, starting on the day 10 p.i., before and after DMSO i.p. injection (Section 3.10.3).

DMSO is a polar aprotic solvent, which is commonly used to dilute TMZ in preclinical studies [54-56] and recent studies of our group have shown that DMSO-MRSI produces differential accumulation of DMSO in brain tumours, regardless the grade of the detected lesion [113]. This finding was detected as a high DMSO signal intensity in MRSI grids inside or close to the tumoural masses, which turns into colour-coded maps extracted from PE-MRSI experiments which reflect “hotspots” in some tumours/experimental conditions.

In the longitudinal studies with GL261 tumours presented in this work, the DMSO accumulation varied at the different time points of the TMZ therapy protocol for different groups of animals. At day 10 post cell inoculation and before the TMZ treatment, DMSO was retained mainly inside the tumoural mass for all cases. Nevertheless, DMSO accumulation was also partially detected outside the limits of the tumoural mass detected by $T_{2W}$ MRI, as in some control and low-grade oligodendroglioma cases described in [113]. The origin of this DMSO retention beyond the limits of the $T_{2W}$ hyperintensity mass is still unknown and different hypothesis could be considered in this respect, i.e. 1) the tumour mass may infiltrate in some occasions beyond the $T_{2W}$ hyperintensity zone, 2) some differential DMSO retention could take place in the periventricular zone, which is near the GL261 cells injection point (striatum) or 3) peritumour cells attracted to the tumour mass (like inflammatory cells or neural stem cells) may also show differential DMSO retention. In spite of this, the DMSO “hotspot” in majority of tumours, defined as stable disease or partially responding, decreased and/or moved outside the well-defined mass around days 20 - 22 of evolution, i.e. after the second TMZ cycle (see Figure 7.9 and Section’s 7.3.7 figures). This decrease/displacement generally correlates with the time in which growth arrest and tumour shrinkage detected in stable disease and partial response group, respectively. Representative colour-coded maps for DMSO accumulation acquired at selected time points for the case C817 are displayed in Figure 7.9 (DMSO accumulation for all exploration days can be also seen in Section 7.3.7). This phenomenon is in line with previous results of the GABRMN group, which showed that treated tumours accumulate significantly less DMSO than untreated ones [113] and that DMSO detected by PE-MRSI is a potential surrogate biomarker for detecting early response to treatment in our GBM model.

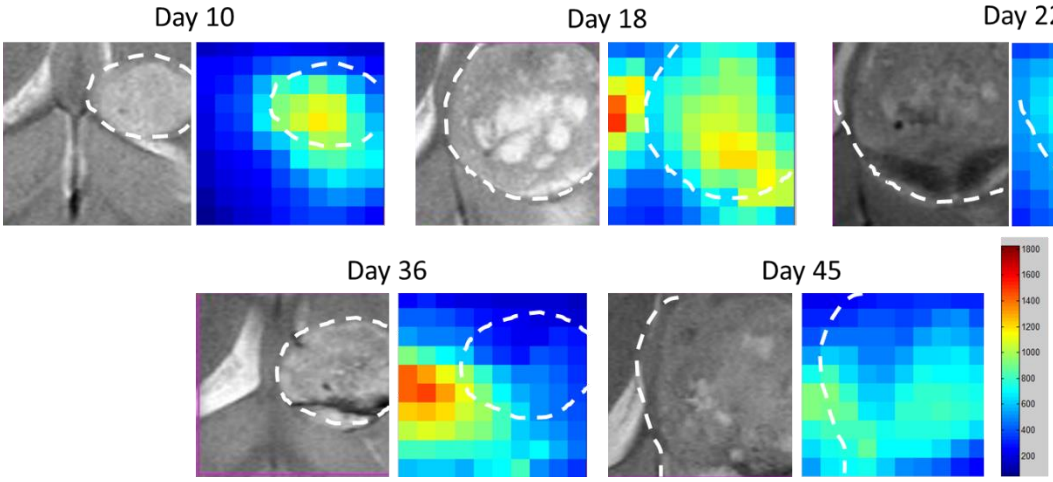

**Figure 7.9.** Representative $T_{2W}$MRI and MRSI colour-coded maps of DMSO accumulation acquired at different time points p.i. for mouse C817. The DMSO accumulation (calculated as in [113]) is higher inside the tumoural mass and the close-by surrounding parenchyma until around day 22 p.i., when thereon it decreases and the major “hotspot” moves outside of the tumour boundaries. Dashed lines label the $T_{2W}$ abnormal mass contour, also shown in MRI images on the left for each time point investigated.

On the other hand, DMSO accumulation persisted inside the masses of animals that died early, i.e. their response to TMZ could not be defined, or in those defined as progressive disease (refer to Section 7.3.7 figures).

### 7.3.6. Source extraction in the training data set

In previous studies of our group [123] a classification system, based on the MRSI-sampled metabolome of normal brain parenchyma, untreated and TMZ-responding GL261 GBM bearing mice with a 93% accuracy, was developed. Classifications correlated well with both tumour volume changes detected by MRI after therapy and with the histopathological data. A surrogate response biomarker based on the linear combination of 12 spectral features has been found in the MRS/MRSI pattern of treated tumours, allowing the non-invasive classification of growing and responding GL261 GBM.

The training data set (8 treated animals and 6 untreated controls), previously included in [123], was used to calculate the source signals using a semi-supervised methodology (described in [132] and Section 3.11.2), which represents the three tissue types studied: normal brain parenchyma (N), GL261 tumours treated with 3 TMZ cycles, that showed response by growth arrest (R), and untreated control GL261 tumours actively proliferating (T). Figure 7.10 illustrates sources calculated from a training set of animals, which are part of previous results from our group (manuscript in preparation). These were the sources finally used to analyse the set of 12 animals studied in this work.

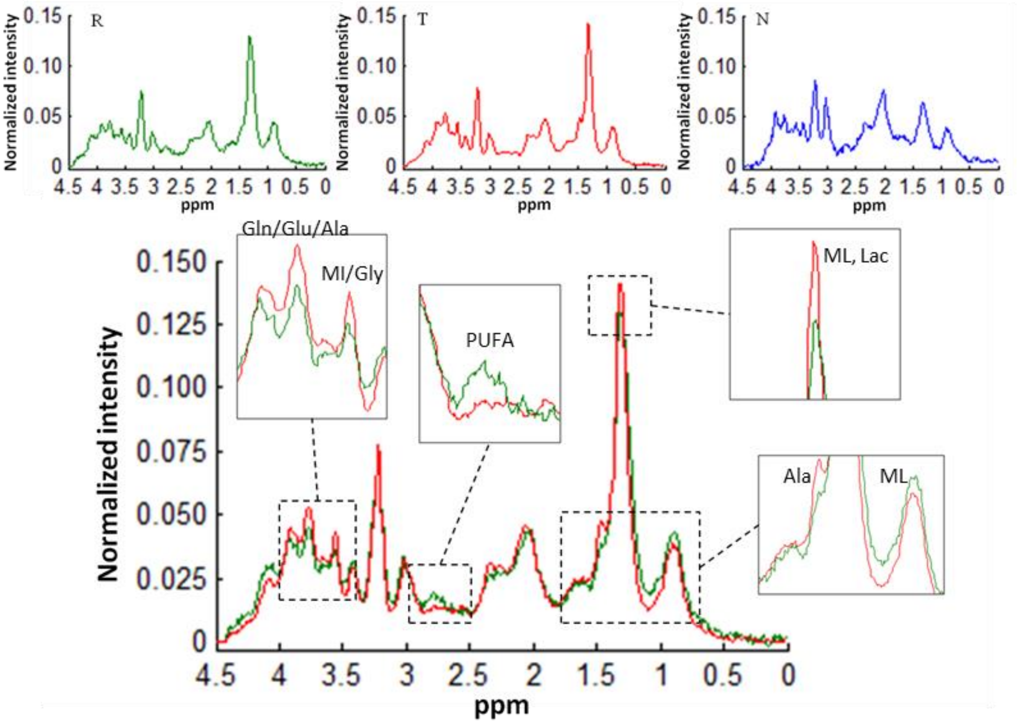

**Figure 7.10.** The three sources calculated with the semi-supervised methodology (top row): green represents treated responding tumour (R); red, untreated/unresponsive tumour (T); and blue, normal tissue (N). The main differences between sources R and T are also highlighted (bottom). Horizontal axes indicate the frequencies measured in ppm. See text and abbreviation list for acronyms.

As it can be seen in Figure 7.10 the nature of the changes in the spectral pattern of treated tumours, in comparison to control tumours, are mainly due to mobile lipids (ML) (0.9 and 1.3 ppm) and PUFA (2.8 ppm) in ML resonances, which are very sensitive and accurate biomarkers for detecting therapy-related metabolic changes and increase their intensity upon apoptosis [180]. This PUFA resonance increase upon response has also been detected in human glioma under different therapeutic regimes [176]. Additionally PUFA MRS detectable accumulation has been detected upon increased cumulative apoptosis in rat brain tissue upon MCAO (middle cerebral artery occlusion) induced stroke [181]. Still, other contributions (as lactate (1.3 and 4.1 ppm), glutamine, glutamate, alanine (3.8 ppm), and myo-inositol/glycine (3.5 ppm) may be helping discrimination among tumour sources (see Figure 7.10). On the other hand, the differences between sources from normal tissue and tumoural masses are mainly based on higher choline/creatine ratios (at 3.21 and 3.03 ppm, respectively), higher lactate and ML signals and lower NAA contribution for the tumours in comparison to normal brain parenchyma. All these metabolic changes regarding spectral intensities were previously characterized in [123], comparing intensity ratios among the different type of tissues, and these significant changes correlate well with the differences shown in the sources profiles.

### 7.3.7. Nosological maps

As explained in Section 3.11.2.1, the new mixing matrixes were calculated for each mouse and the extracted sources were used in this Section 7 to generate colour-coded nosological images, as described in Section 3.11.2.3. Figure 7.11 shows the results of three characteristic mice from the training set, two of them treated and one from the control group. The first column represents the region of interest of each mouse with the original labels (“tags”) selected for training the semi-supervised methodology, as described per Section 3.11.1, followed by three nosological colour-coded maps associated to the sources T, R and N. The resulting nosological image (right column), combines the information of the three maps (T, R and N) and shows the highest correlation of each voxel to the source, green representing response to therapy, red representing tumour (untreated or without response), and blue representing normal brain parenchyma. This example summarizes how response to therapy can be monitored at a particular time point and throughout the course of therapy and illustrates the three main groups of response detected by the source methodology in the training set.

Considering cases treated with 2 TMZ cycles, namely C586 and C418, the first one shows clear response, while the latter indicates a partial or heterogeneous response within the tumour. On the other hand, the control case C583 shows a clear progressive pattern compatible with untreated tumour, as expected. Nosological images for the eleven remaining cases from the training set, obtained on the day just prior to death/ethical sacrifice, are shown in Annex 6.

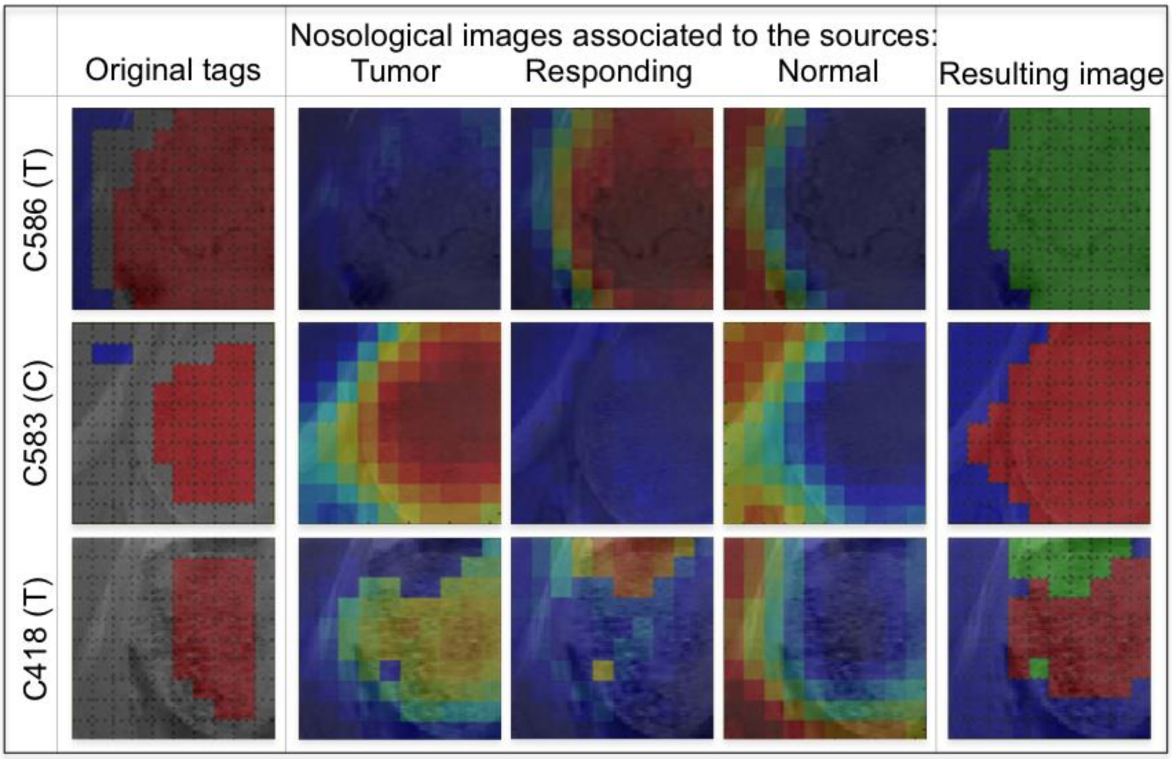

**Figure 7.11.** Nosologic imaging for three mice from the training set for source extraction: C418 and C586 at day 22 p.i. – treated with TMZ (T) and C583 at day 18 p.i. – untreated GL261 tumour control (C). First column shows the map of original tags with labels selected for training the semi-supervised methodology, where red means (treated/untreated) tumour and blue means normal brain. The three colour-coded maps from the middle are the nosological images associated to each source, where the scale of colours moves from red to blue, red indicates high values in the mixing matrix meaning high probability of belonging to a certain class, while blue indicates low values. Last column compiles the results from the previous three maps into one, in which the red colour codes for untreated tumour, green for responding tumour, and blue for normal brain. All the maps are superimposed using a “transparency” view over the corresponding $T_{2W}$ MR images.

To test the validity of the source-based methodology to detect non-invasively response to treatment in the GL261 GBM model, 12 independent cases of this thesis work treated with TMZ were analysed using the sources extracted from the training set to generate new mixing matrices.as described in Section 3.11.2.2 (see also Section 7.3.of the results). Nosologic colour-coded maps were produced for each case every second day, during and after the course of therapy, and these maps were overlaid with the corresponding MRI images and correlated with the RECIST criteria of response. The response throughout of two cases belonging to the partial response group C819 and C817 are presented in Figures 7.12 and 7.13, respectively; the stable disease cases C796, C808, C809 and C821 are shown in Figures 7.14, 7.15 and 7.16; while the progressive disease case C776 and non-evaluable cases can be seen in Figure 7.17 and 7.18, respectively. The nosological maps allowed convenient tracking of response to treatment and made clear the intratumoural heterogeneity of response, hinting the growth arrest and relapse. Tumours response to treatment started to be detectable between days 16 and 22, even before changes in tumour volume, with respect to average values of control untreated tumours, were observed (e.g. at day 24 for cases C819 and C821 and day 26 for case C808). The response regions enlarged and continued along time with either a homogeneous (cases C808, C809 and C819) or heterogeneous pattern (cases C776, C817, C821).

Considering for example the case C819, the nosologic images obtained at various time points during and after therapy are presented in Figure 7.12. Until the day 16 the tumour was recognized as fully unresponsive and the evidence of response started to be observed at day 18. This preceded the growth arrest and the nosological image demonstrated full response on the day 22, followed by decrease of the mass volume. On the other hand, the image produced on the day 36 indicates signals of relapse, just before a relative increase in tumour volume was detected at day 41 (increase by 55% in two days) and finally on the day 45 it was recognized as mostly fully growing again.

For more informative visual correlation of response by nosological imaging with the RECIST criteria, apart from the best overall response as assessed and shown in Table 7.1, each individual time point was evaluated for the RECIST criteria as well and shown as coloured bars for each case in Figures 7.12 – 7.18. Considering again the case C819 (Figure 7.12), until the day 16 it was recognized by nosological images as fully unresponsive and the evidence of response started to be observed at day 18, before the RECIST criteria and the tumour volume indicated that it entered the stable disease state at day 22 (neither 30% of volume reduction nor 20% of volume increase with respect to the previous measurement) in agreement with fully responding spvs in the nosological image, and remained in a transient response state until day 26, when it showed partial response (30% of volume reduction with respect to the previous measurement). Then it remained stable according to RECIST until day 41 (when it showed more than the 20% of volume increase with respect to day 39), which agrees with mostly responding spvs in the tumour mass during this period, and an active proliferation pattern at day 45. Stable disease periods could also be found for mice C776, C808, C809, C817 and C821, which agreed with their nosological images displaying response. However, the case C821 during the final period of the tumour evaluation, namely days 32 and 34, is categorised as a progressive disease according to RECIST (Figure 7.16), while nosological images show an almost fully responding tumour, in the MRSI sampled ROI. Another such “abnormal” case is C795 (Figure 7.18), categorised as a non-evaluable case considering overall response, as this mouse died at day 18, before starting the second therapy cycle. The nosological image at day 18 shows an almost fully responding tumour, but it remained stable with respect to the previous measurement regarding the RECIST criteria. This could be possibly be explained by histopathological analysis of these tumours (refer to Section 7.3.8).

Additionally to the longitudinal studies of this thesis, the source methodology was also validated with two additional groups: 7 retrospective GL261 control mice [102] and a group of 11 treated animals (manuscript in preparation), for all of which nosologic images were produced at an individual time point, just before their sacrifice and correlated with the histopathological studies (refer to Section 7.3.8). The seven control cases were classified as not responding tumours, being the tumour source the one with the highest correlation within the voxels contained in the tumoural mass and recognized as tumour (see Annex 7). One out of eleven treated animals was administered to 3 TMZ cycles and displayed full response coherent with volume changes (results not shown). The remaining ten treated animals were administered to just one TMZ cycle, therefore according to [123] were not supposed to respond to therapy, however they were retrospectively included in order to assess the ability of the classifier to properly distinguish them. Eight of them were recognized as not responding (nosological images for majority of them can be seen in Annex 8), while two had partial response (refer to cases C414 and C419 in Annex 8).

The performance of the proposed method was compared for a selected number of cases to the previously developed method based in supervised classifier development [123] and found better performing (Figures 7.12 - 7.14 and 7.16 - 7.18). The nosologic images obtained using the source extraction methodology seemed to more accurately distinguish the tumour boundaries when compared with $T_{2W}$ MRI, predict the relapsing C819 tumour (Figure 7.12) and generally agreed more with the RECIST criteria.

The approach to create nosologic images and maps of the brain using MRSI data has also been reported in literature by other researchers. For example, an unsupervised nosologic imaging for glioma diagnosis is presented in [182], where different tissue patterns were identified from the MRSI data from GBM patients using non negative matrix factorization, distinguishing normal, tumour and necrotic tissue. A supervised methodology for segmentation and classification of different brain tumours is described in [183]. On the detection of tumour response to treatment using hyperpolarization MRSI-based images of was described in [184, 185].

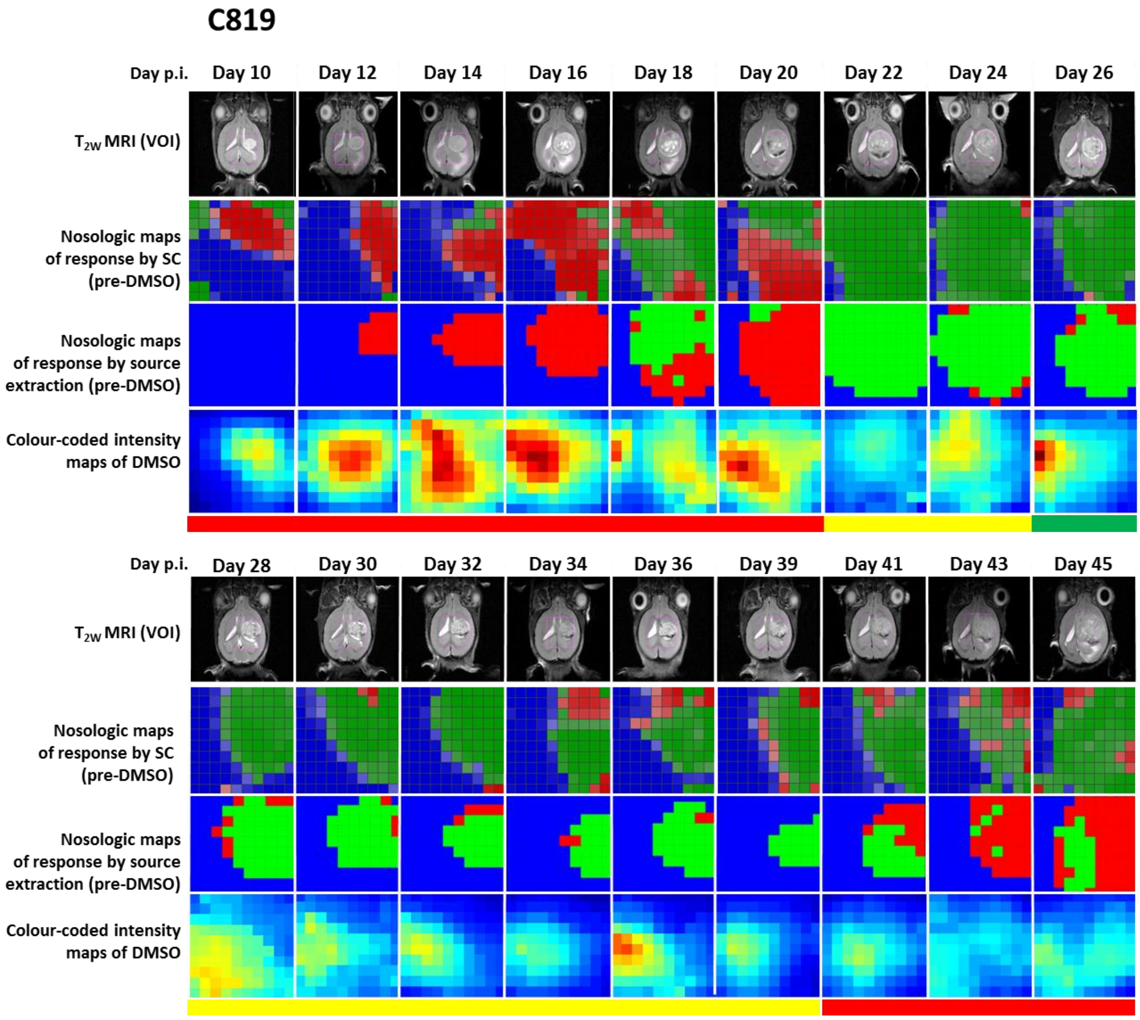
C819
Day p.i.
Day 10
Day 12
Day 14
Day 16
Day 18
Day 20
Day 22
Day 24
Day 26
T2W MRI (VOI)
Nosologic maps of response by SC (pre-DMSO)
Nosologic maps of response by source extraction (pre-DMSO)
Colour-coded intensity maps of DMSO
Day p.i.
Day 28
Day 30
Day 32
Day 34
Day 36
Day 39
Day 41
Day 43
Day 45
T2W MRI (VOI)
Nosologic maps of response by SC (pre-DMSO)
Nosologic maps of response by source extraction (pre-DMSO)
Colour-coded intensity maps of DMSO

**Figure 7.12.** Nosologic colour-coded maps corresponding to the partially responding case C819 obtained by using Spectra Classifier (SC), developed in [123], in comparison to the source extraction method described in Section 7.3.6 -7.3.7, with corresponding HR $T_{2W}$ images (top). ROI obtained prior to DMSO injection at different time points of the tumour evolution are also shown, during and after the course of therapy. The green voxels were predicted as responding tumour, red voxels as untreated/unresponsive tumour, and blue voxels as normal parenchyma. Refer to Figure 7.1 for a comparison with the tumour volume evolution. Bottom row represents the MRSI colour-coded maps of DMSO accumulation (calculated as in [113]) acquired at different time points. Under the maps there is a colour-bar showing the response stage determined by the RECIST criteria along the therapy protocol (red means progressive disease; yellow, stable disease and green partial response).

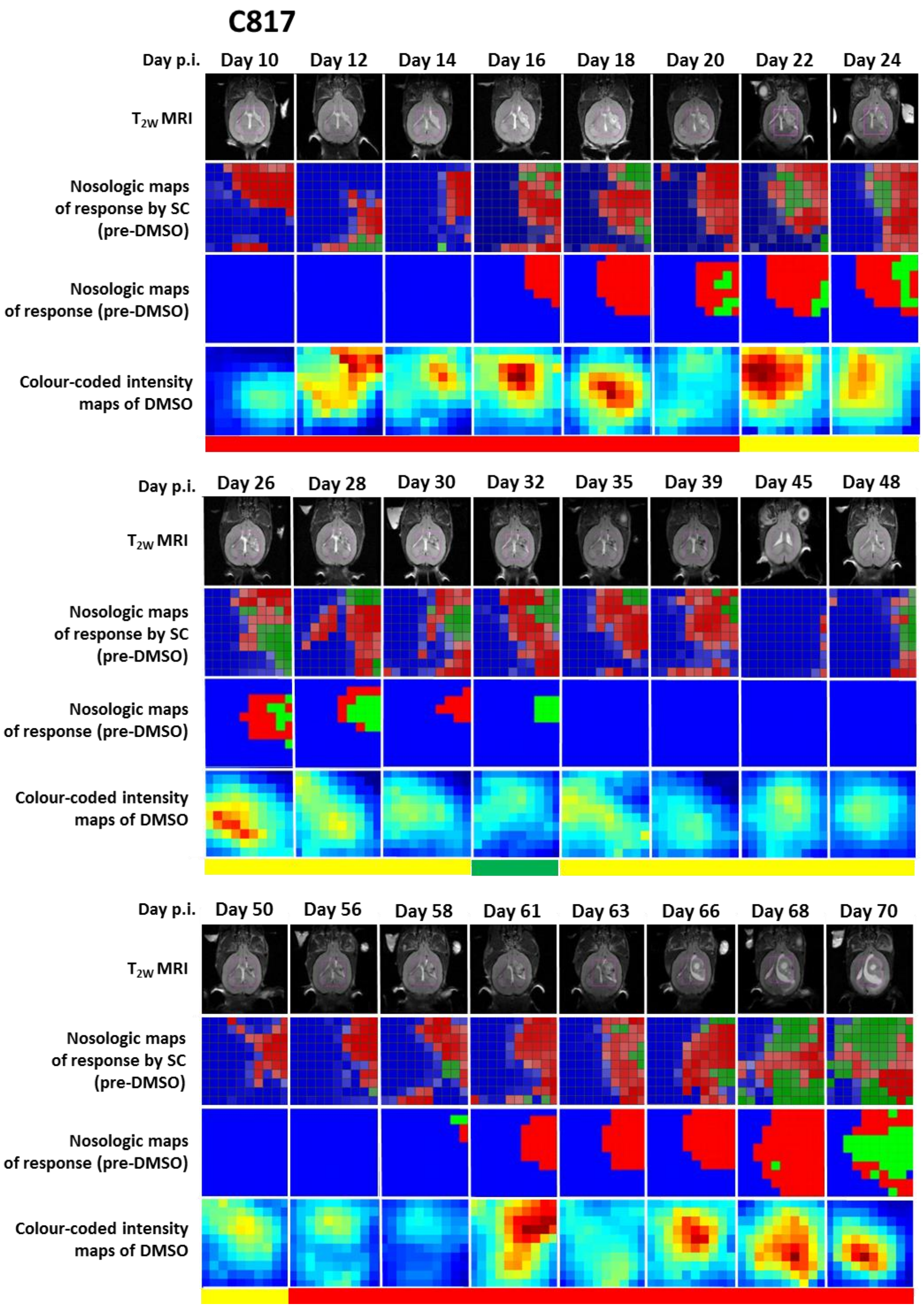
C817
Day p.i.
Day 10
Day 12
Day 14
Day 16
Day 18
Day 20
Day 22
Day 24
$T_{2w}$ MRI
Nosologic maps of response by SC (pre-DMSO)
Nosologic maps of response (pre-DMSO)
Colour-coded intensity maps of DMSO
Day p.i.
Day 26
Day 28
Day 30
Day 32
Day 35
Day 39
Day 45
Day 48
$T_{2w}$ MRI
Nosologic maps of response by SC (pre-DMSO)
Nosologic maps of response (pre-DMSO)
Colour-coded intensity maps of DMSO
Day p.i.
Day 50
Day 56
Day 58
Day 61
Day 63
Day 66
Day 68
Day 70
$T_{2w}$ MRI
Nosologic maps of response by SC (pre-DMSO)
Nosologic maps of response (pre-DMSO)
Colour-coded intensity maps of DMSO

**Figure 7.13.** Nosologic colour-coded maps corresponding to the partially responding case C817 obtained by using Spectra Classifier (SC), developed in [123], in comparison to the source extraction method described in Section 7.3.6 -7.3.7, with corresponding HR $T_{2W}$ images (top). ROI obtained prior to DMSO injection at different time points of the tumour evolution, during and after the course of therapy. The green voxels were predicted as responding tumour, red voxels as untreated/unresponsive tumour, and blue voxels as normal parenchyma. Refer to Figure 7.1 for a comparison with the tumour volume evolution. Bottom row represents the MRSI colour-coded maps of DMSO accumulation (calculated as in [113]) acquired at different time points. Under the maps there is a colour-bar showing the response stage determined by the RECIST criteria along the therapy protocol (red means progressive disease; yellow, stable disease and green partial response).

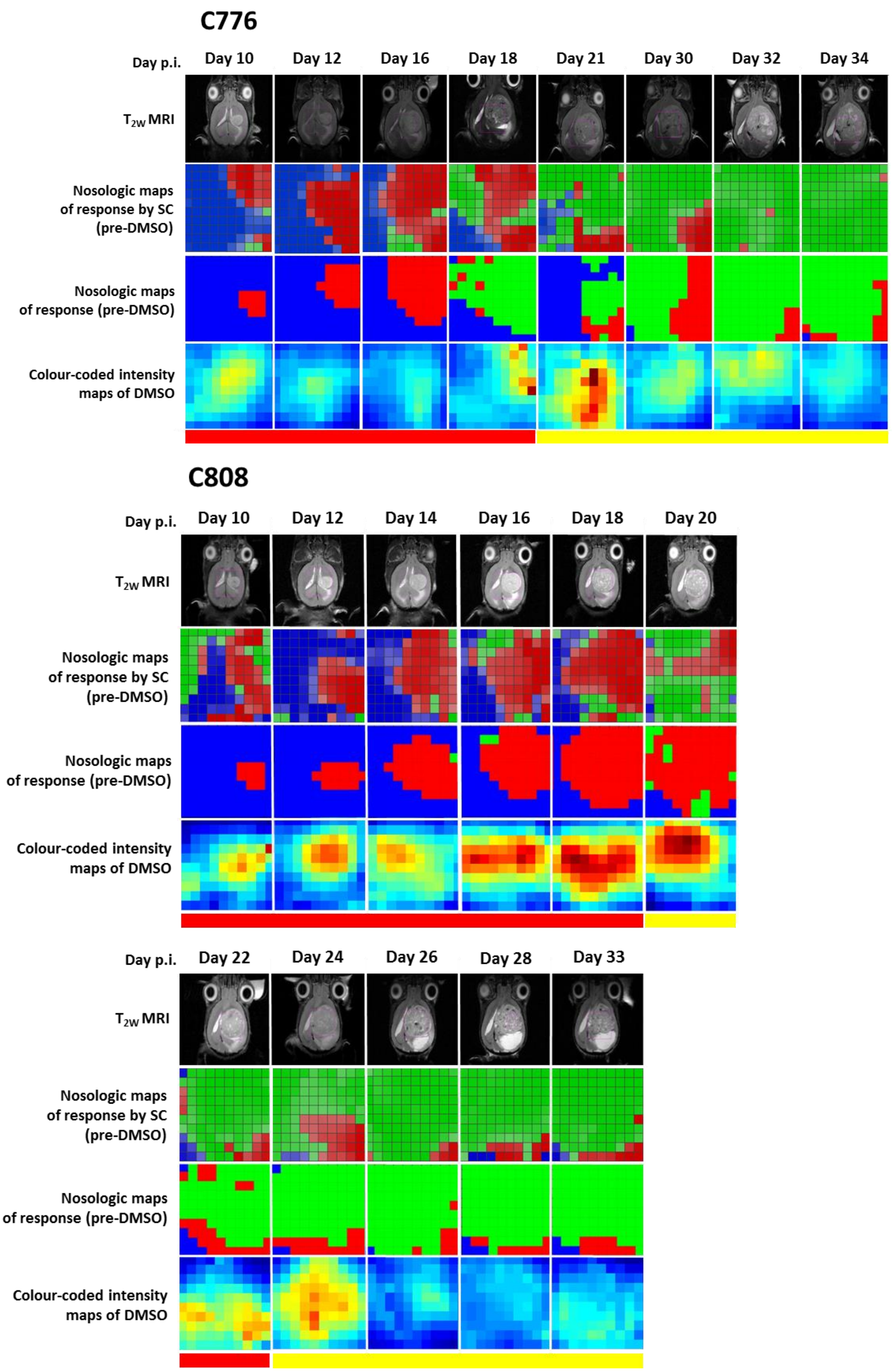
C776
Day p.i.
Day 10
Day 12
Day 16
Day 18
Day 21
Day 30
Day 32
Day 34
T2w MRI
Nosologic maps of response by SC (pre-DMSO)
Nosologic maps of response (pre-DMSO)
Colour-coded intensity maps of DMSO
C808
Day p.i.
Day 10
Day 12
Day 14
Day 16
Day 18
Day 20
T2w MRI
Nosologic maps of response by SC (pre-DMSO)
Nosologic maps of response (pre-DMSO)
Colour-coded intensity maps of DMSO
Day p.i.
Day 22
Day 24
Day 26
Day 28
Day 33
T2w MRI
Nosologic maps of response by SC (pre-DMSO)
Nosologic maps of response (pre-DMSO)
Colour-coded intensity maps of DMSO

**Figure 7.14.** Nosologic colour-coded maps corresponding to stable disease case C776 and C808 obtained by using Spectra Classifier (SC), developed in [123], in comparison to the source extraction method described in Section 7.3.6 -7.3.7, with corresponding HR $T_{2W}$ images (top). ROI obtained prior to DMSO injection at different time points of the tumour evolution, during and after the course of therapy. The green voxels were predicted as responding tumour, red voxels as untreated/unresponsive tumour, and blue voxels as normal parenchyma. Refer to Figure 7.1 for a comparison with the tumour volume evolution. Bottom row represents the MRSI colour-coded maps of DMSO accumulation (calculated as in [113]) acquired at different time points. Under the maps there is a colour-bar showing the response stage determined by the RECIST criteria along the therapy protocol (red means progressive disease; yellow, stable disease and green partial response).

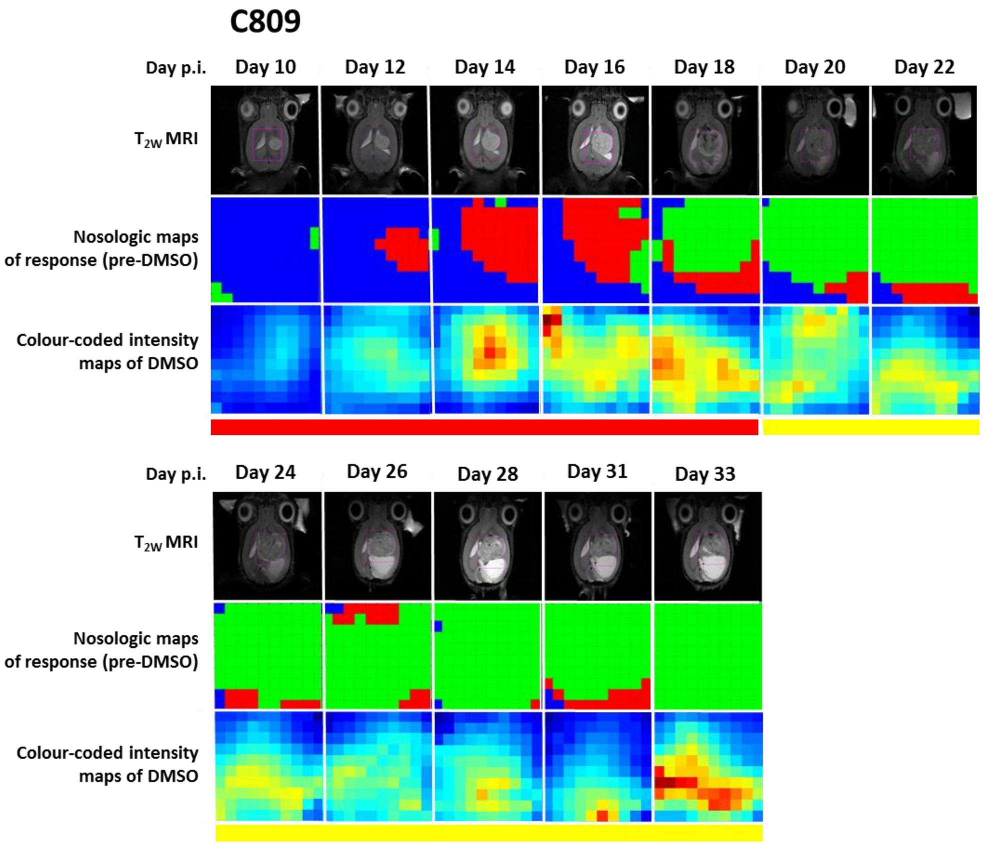
C809
Day p.i.
Day 10
Day 12
Day 14
Day 16
Day 18
Day 20
Day 22
T2W MRI
Nosologic maps of response (pre-DMSO)
Colour-coded intensity maps of DMSO
Day p.i.
Day 24
Day 26
Day 28
Day 31
Day 33
T2W MRI
Nosologic maps of response (pre-DMSO)
Colour-coded intensity maps of DMSO

**Figure 7.15.** Nosologic colour-coded maps corresponding to stable disease case C809 obtained by using the source extraction method described in Section 7.3.6 -7.3.7, with corresponding HR $T_{2W}$ images (top). ROI obtained prior to DMSO injection at different time points of the tumour evolution, during and after the course of therapy. The green voxels were predicted as responding tumour, red voxels as untreated/unresponsive tumour, and blue voxels as normal parenchyma. Refer to Figure 7.1 for a comparison with the tumour volume evolution. Bottom row represents the MRSI colour-coded maps of DMSO accumulation (calculated as in [113]) acquired at different time points. Under the maps there is a colour-bar showing the response stage determined by the RECIST criteria along the therapy protocol (red means progressive disease; yellow, stable disease and green partial response).

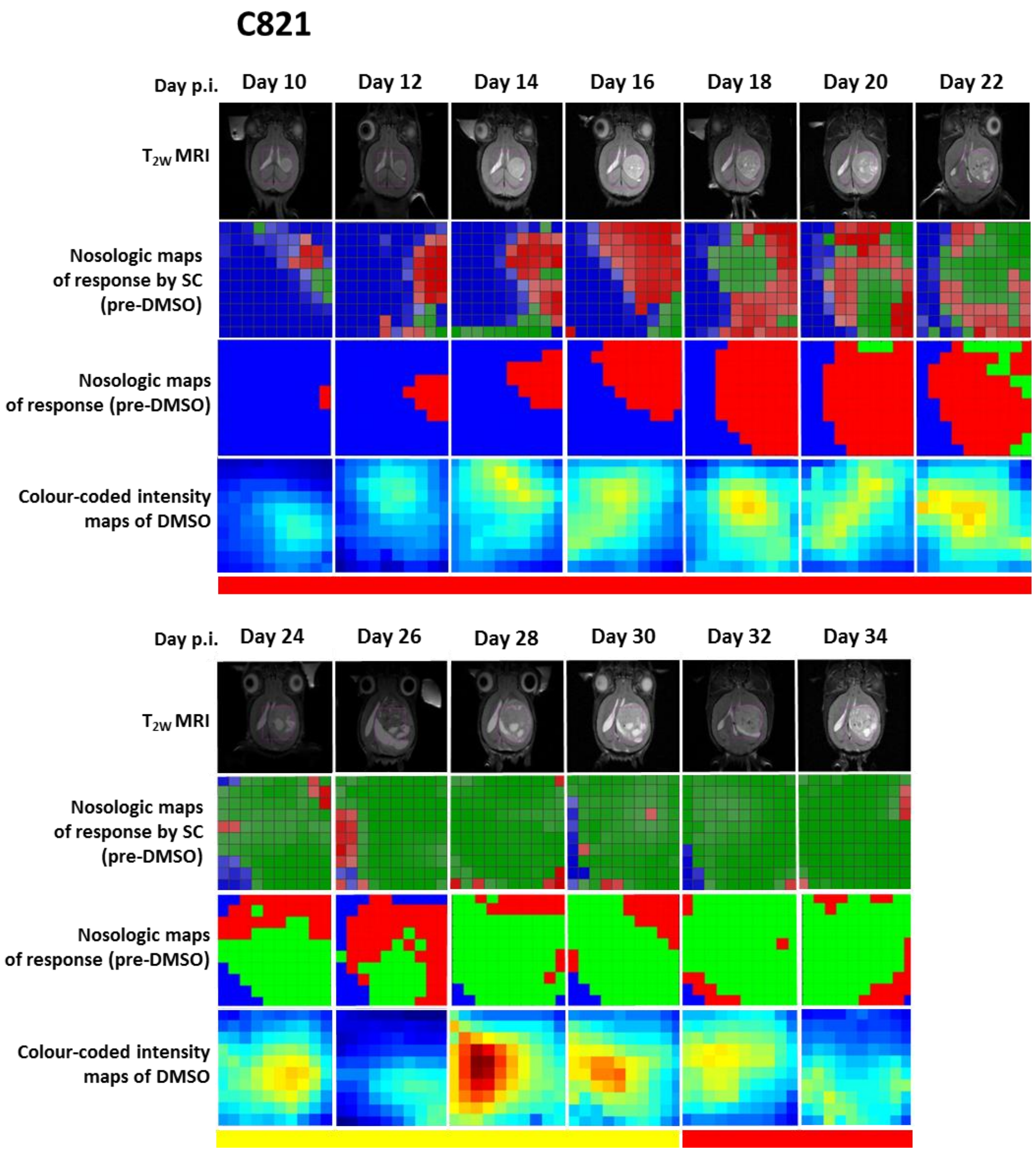
C821
Day p.i.
Day 10
Day 12
Day 14
Day 16
Day 18
Day 20
Day 22
T2W MRI
Nosologic maps of response by SC (pre-DMSO)
Nosologic maps of response (pre-DMSO)
Colour-coded intensity maps of DMSO
Day p.i.
Day 24
Day 26
Day 28
Day 30
Day 32
Day 34
T2W MRI
Nosologic maps of response by SC (pre-DMSO)
Nosologic maps of response (pre-DMSO)
Colour-coded intensity maps of DMSO

**Figure 7.16.** Nosologic colour-coded maps corresponding to stable disease case C821 obtained by using Spectra Classifier (SC), developed in [123], in comparison to the source extraction method described in Section 7.3.6 - 7.3.7, with corresponding HR $T_{2W}$ images (top). ROI obtained prior to DMSO injection at different time points of the tumour evolution, during and after the course of therapy. The green voxels were predicted as responding tumour, red voxels as untreated/unresponsive tumour, and blue voxels as normal parenchyma. Refer to Figure 7.1 for a comparison with the tumour volume evolution. Bottom row represents the MRSI colour-coded maps of DMSO accumulation (calculated as in [113]) acquired at different time points. Under the maps there is a colour-bar showing the response stage determined by the RECIST criteria along the therapy protocol (red means progressive disease; yellow, stable disease and green partial response).

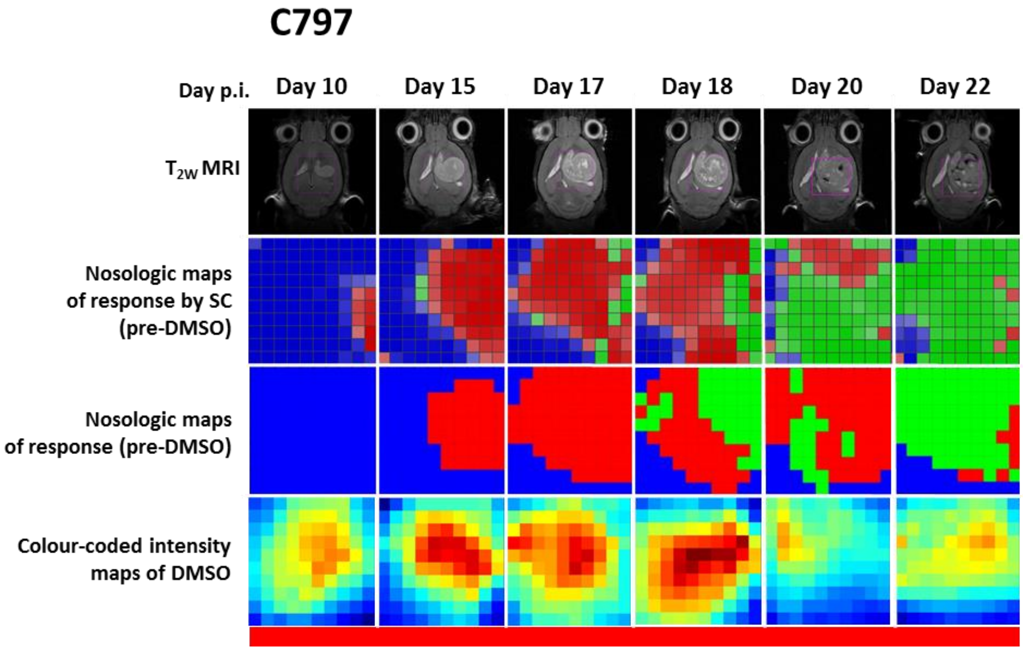
C797
Day p.i.
Day 10
Day 15
Day 17
Day 18
Day 20
Day 22
$T_{2W}$ MRI
Nosologic maps of response by SC (pre-DMSO)
Nosologic maps of response (pre-DMSO)
Colour-coded intensity maps of DMSO

**Figure 7.17.** Nosologic colour-coded maps corresponding to progressive disease case C797 obtained by using Spectra Classifier (SC), developed in [123], in comparison to the source extraction method described in Section 7.3.6 -7.3.7, with corresponding HR $T_{2W}$ images (top). ROI obtained prior to DMSO injection at different time points of the tumour evolution, during and after the course of therapy. The green voxels were predicted as responding tumour, red voxels as untreated/unresponsive tumour, and blue voxels as normal parenchyma. Refer to Figure 7.1 for a comparison with the tumour volume evolution. Bottom row represents the MRSI colour-coded maps of DMSO accumulation (calculated as in [113]) acquired at different time points. Under the maps there is a colour-bar showing the response stage determined by the RECIST criteria along the therapy protocol (red means progressive disease; yellow, stable disease and green partial response).

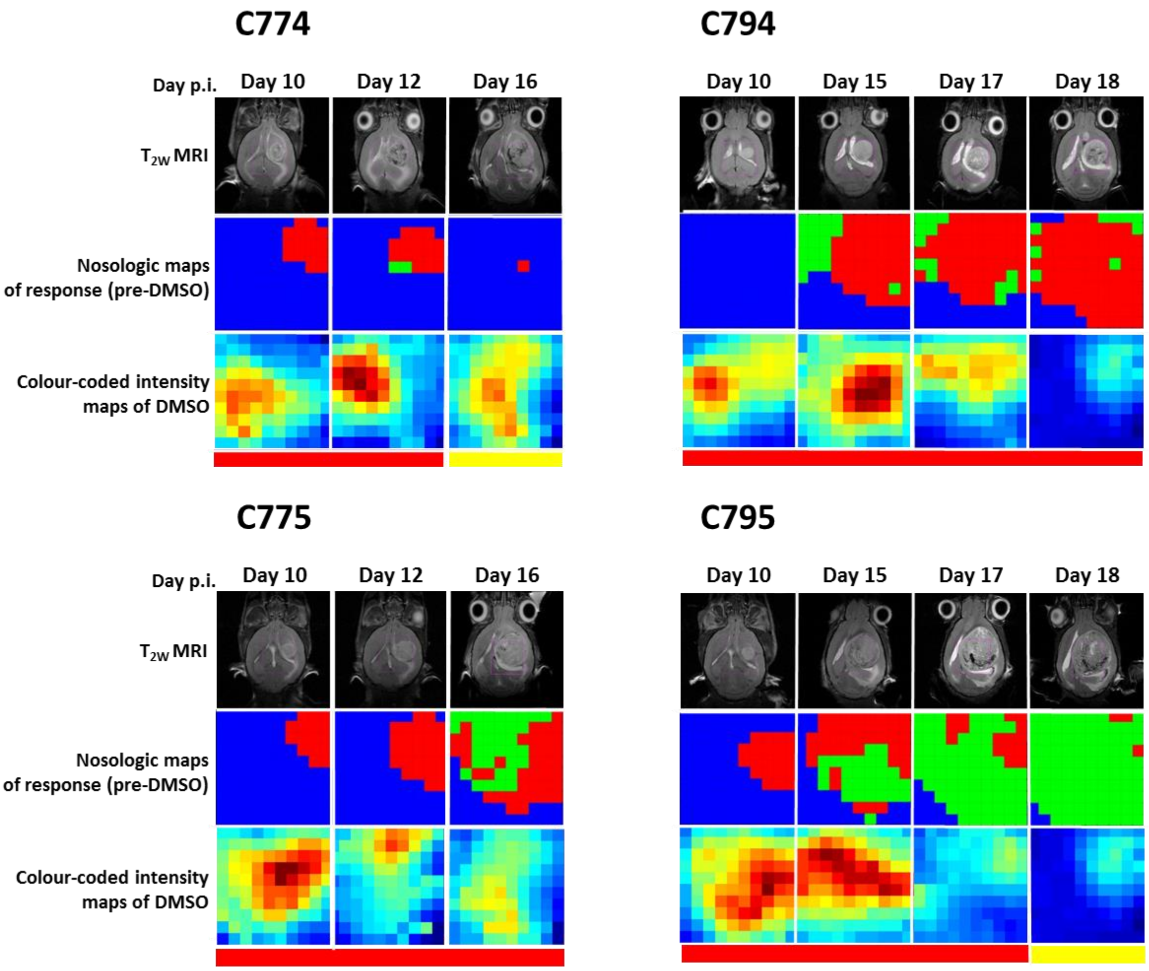
C774
C794
Day p.i.
Day 10
Day 12
Day 16
Day 10
Day 15
Day 17
Day 18
T2W MRI
Nosologic maps of response (pre-DMSO)
Colour-coded intensity maps of DMSO
C775
C795
Day p.i.
Day 10
Day 12
Day 16
Day 10
Day 15
Day 17
Day 18
T2W MRI
Nosologic maps of response (pre-DMSO)
Colour-coded intensity maps of DMSO

**Figure 7.18.** Nosologic colour-coded maps corresponding to the non-evaluable group, considering the overall response, namely cases C774, C775, C794 and C795 obtained by using the source extraction method described in Section 7.3.6 -7.3.7, with corresponding HR $T_{2W}$ images (top). ROI obtained prior to DMSO injection at different time points of the tumour evolution, during and after the course of therapy. The green voxels were predicted as responding tumour, red voxels as untreated/unresponsive tumour, and blue voxels as normal parenchyma. Refer to Figure 7.1 for a comparison with the tumour volume evolution. Bottom row represents the MRSI colour-coded maps of DMSO accumulation (calculated as in [113]) acquired at different time points. Under the maps there is a colour-bar showing the response stage determined by the RECIST criteria along the therapy protocol (red means progressive disease; yellow, stable disease and green partial response).

### 7.3.8. Histopathological studies and correlation between calculated nosologic maps

Histopathology is one of the most applied techniques to assess tumour response to therapy in many types of cancer [186, 187] and, in some cases, this parameter seems to be more effective for response detection than the RECIST criteria [188], except that it requires a tissue biopsy to be made. Ki67 and caspase 3 indexes, evaluating proliferation and apoptosis respectively, have previously been reported by other authors as response biomarkers in preclinical [189-191] and clinical GBM.

Accordingly, we have compared the results using the sources methodology with the corresponding post-sacrifice histopathological evaluation, whenever available. For this, once the MRSI studies were concluded, most of the animals from the training set group (namely 3 controls and 7 treated) from previous GABRMN studies (refer to Section 7.3.6) and animals from different validation groups (5 animals of the longitudinal studies of this thesis, namely C776, C808 and C821, belonging to the stable disease group, and C797 and C795, belonging to the progressive disease and the atypical non-evaluable group, respectively; as well as the retrospective control group of 7 animals from [102] and the treated group of 11 animals) were analysed histopathologically, as described in Section 3.8.1, to correlate the histological preparations with the reference images of the MRSI and validate the semi-supervised source extraction methodology. Each individual case of the longitudinal studies was compared with the average values for control tumours and tumours treated with TMZ in [123], as well as with the average values of the remaining validation groups previously explored by our group, as mentioned above. Corresponding values for proliferation and apoptotic and mitotic rates calculated from immunostaining shown in Table 7.2.

According to the previous, TMZ induces cell proliferation arrest [168], apoptosis [192] and a decrease in the mitotic index [193] of different preclinical GBM models. This has also been reported for the GL261 model in [123], from which some of the mice treated with two or three TMZ cycles were included in the training set of presented source extraction methodology. The study in [123] showed significant differences were detected when comparing the mean proliferation percentage of control tumours (57.8 ± 5.4%), or those treated with one TMZ cycle (61.7 ± 14.2%), against those treated with three TMZ cycles (29.82 ± 10.34%). The apoptotic rate showed a significant 4.6-fold increase after therapy, i.e. 0.6 % apoptotic cells in control tumours with respect to 2.7 % apoptotic cells in treated tumours. Moreover, there were also significant differences in mitotic index between the control group (14.1 ± 4.2 mitoses per field) and treated groups, either with one (5.3 ± 2.8 mitoses per field), two (4.9 ± 2.6 mitoses per field) or three TMZ cycles (3.3 ± 2.9 mitoses per field).

**Table 7.2**. Tumour volume (acquired by MRI) and histopathological parameters (proliferation, apoptotic and mitotic rates) calculated for the test set cases. All the values are compared with the corresponding averages for control and treated GBM (average values for the whole tumour) reported in [123].

| | | **MRSI acquisition (day p.i.)** | **Tumour volume (mm$^3$)$^*$** | **Proliferation rate (%)** | **Apoptotic rate (% cells/mm$^2$)** | **Mitotic index (mitoses/field)** |
|---|---|---|---|---|---|---|
| **Control** | **Average in training set**<br>**n = 3** | 18 | 149 ± 52.3 | 58.6 ± 13.6 | 1.3 ± 1.2 | 13.5 ± 6.2 |
| | **Average in group from [102]**<br>**n = 7** | 17 | 53.7 ± 16.4 | 60 ± 10.7 | N/A | N/A |
| | **Average in [123]**<br>**n = 6** | 18 | 102 ± 1.7 | 57.8 ± 5.4 | 0.6 ± 0.4 | 14.1 ± 4.2 |
| **TMZ treated** | **Average in training set**<br>**n = 7** | 23 | 117.6 ± 29.3 | 45.6 ± 9.3 | 2.3 ± 1.3 | 3.4 ± 2 |
| | **Average** 1 TMZ cycle<br>**n = 10**<br>**(manuscript in preparation)** | 18 | 59.6 ± 32.9 | 61.7 ± 15 | 3.4 ± 1.7 | 5.3 ± 2.8 |
| | **C776 3 TMZ cycles** | **34** | **223.5** | **23.7 ± 5.2** | **0.5 ± 0.4** | **0.9 ± 0.9** |
| | **C795 1 TMZ cycle** | **18** | **152.3** | **12.6 ± 4.7** | **1 ± 0.9** | **1.3 ± 0.9** |
| | **C797 2 TMZ cycles** | **22** | **96.9** | **41.4 ± 8.9** | **0.7 ± 0.7** | **2.3 ± 1.4** |
| | **C808 3 TMZ cycles** | **33** | **142.6** | **20.1 ± 8.6** | **0.5 ± 0.5** | **1.3 ± 2.1** |
| | **C821 3 TMZ cycles** | **34** | **192.5** | **28.9 ± 7.5** | **0.7 ± 0.6** | **2.1 ± 1.1** |
| | **Average in [123]**<br>**n = 12** | 24 | 100.9 ± 41.6 | 29.8 ± 10.3 | 2.7 ± 1.2 | 3.3 ± 2.9 |

The individual cases from the training set of the source extraction methodology (shown in Table 7.2 as average and Annex 9 as individual cases) were compared with the average control and treated tumours described in [123] and several were found to be included within the box plot range described for their reference group (control or treated, Figure 7.19), as well as correctly recognized by the sources methodology (nosological maps are shown in Annex 6). Even cases that were supposed to be responding (C415 and C525), according to the treatment received, were correctly recognized by the sources as non-responders, in agreement with their respective proliferation indexes (Annex 9).

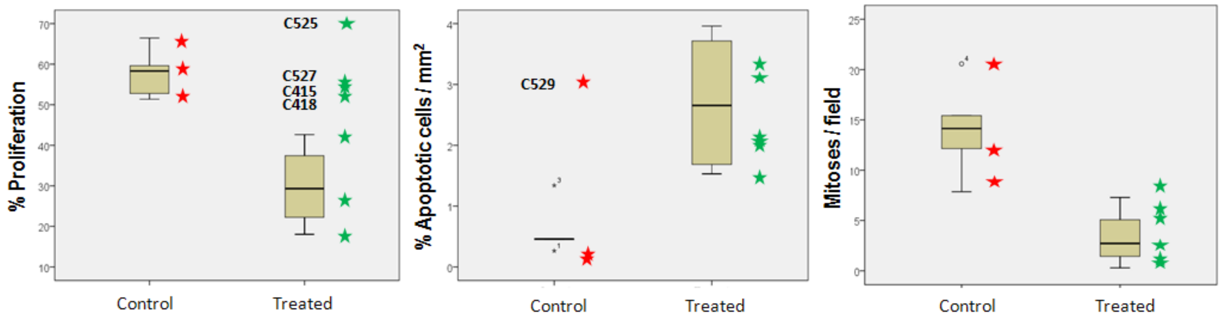

**Figure 7.19.** Box-plots representing the reference ranges for proliferation, apoptosis and mitotic indexes calculated for control and treated tumours in [123]. Cases from the training set are represented with red (control) and green (treated) stars.

The seven retrospective control GL261 cases from [102] had most of their tumour spvs, detected as abnormal tissue by $T_{2W}$ MRI, recognized by the source classifier as actively proliferating tumour (i.e. non-responding, refer to Annex 7) and this classification agreed well with their proliferation index and also with average values for reference GL261 tumours in [123] (Table 7.2). In the prospective group of 10 animals treated with 1 TMZ cycle, as expected from [123], most (8) were recognized as non-responders, while 2 as partially responding (refer to Annex 8) and both patterns were also in agreement with the corresponding proliferation (Table 7.2). However, the response maps calculated with the sources methodology did not correlate with the caspase 3 staining performed and apoptosis rate was in the range or higher than in the animals treated with two or three TMZ cycles reported in [123]. This could be due to the fact that untreated GBM have been reported to inherently express caspase 3 as part of their intrinsic process of cell death [194, 195] or even related to migration and invasiveness [196]. If caspase 3 basal levels, or its upregulation induced by treatment, are not always homogeneous, an increase in the number of cases analyzed may disperse the effect and it could not be possible to differentiate between basal and post-treatment situations. Thus, it would be difficult to correlate caspase 3 levels with the response stage and consequently with the source analysis.

Considering the longitudinal study cases, representative histopathological Ki67 and caspase 3 staining in relation to the nosologic images are presented in Figure 7.20. These animals were evaluated at different time points along the therapy protocol, but the nosologic images are related to the day just prior to death/ethical sacrifice, when tumour proliferation was assessed by histopathology.

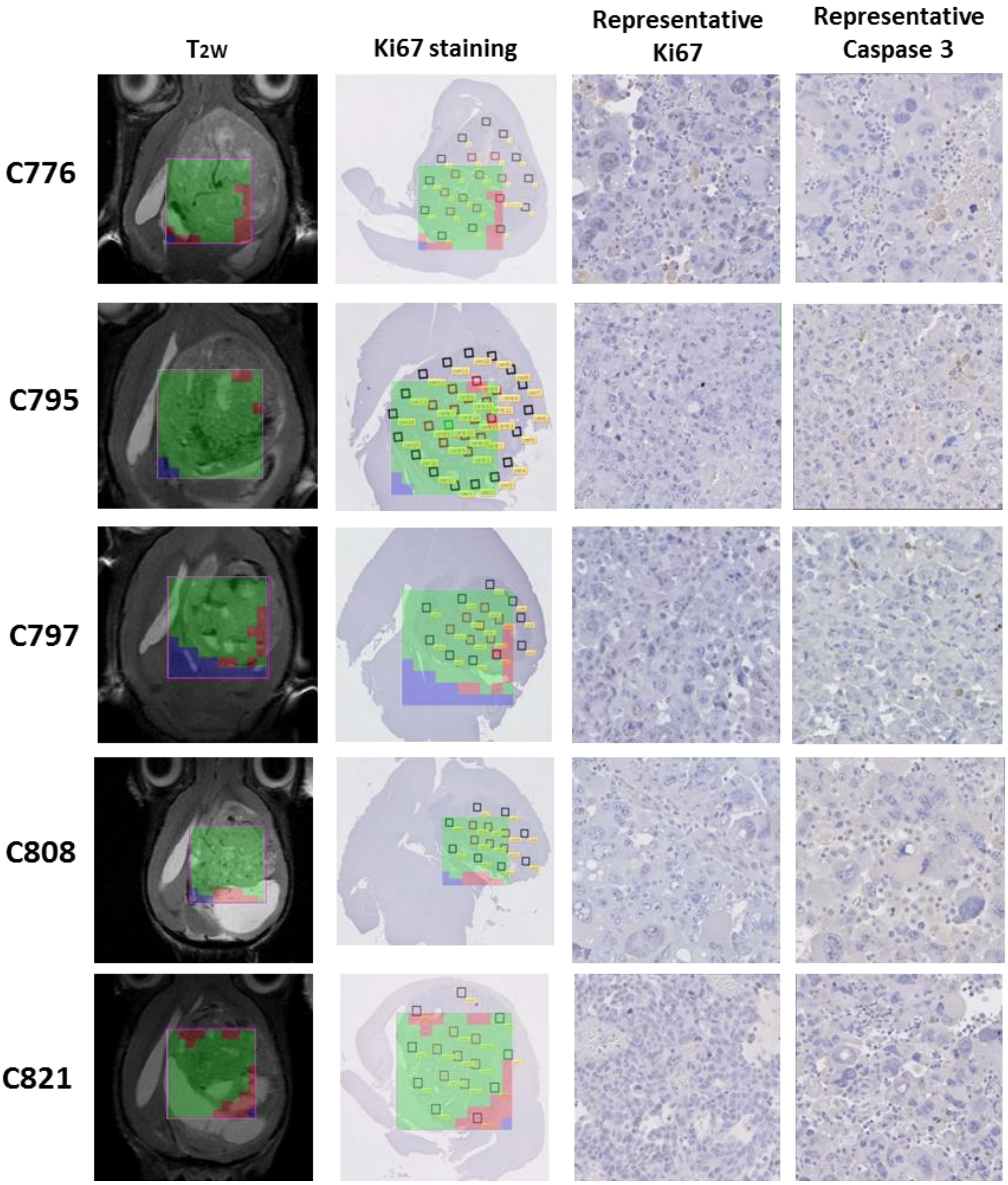

**Figure 7.20.** Nosologic maps and representative histopathological samples stained with Ki67 and caspase 3 of the longitudinal study cases selected for histopathology. First row represents $T_{2W}$ image superimposed with the nosological image corresponding to the explorations on the day just prior to death/ethical sacrifice. The second row represents the histopathological sampling image, with 0.1 $mm^3$ squares in which proliferation was counted, superimposed with the nosological image on the day just prior to death/ethical sacrifice. The third and the fourth row, show representative Ki67 and caspase staining, respectively, obtained from the responding (green) zone of each tumour. Refer to Table 7.2 for the average histopathological parameters calculated.

The proliferation values (Table 7.2) of the longitudinal study cases were included within the range described for their group in [123] and were mostly correctly recognized by the sources methodology as responders (Figure 7.20). The only “abnormal” case was the animal C795, that died at day 18 before starting the second therapy cycle and according to [123] should have not respond to therapy. However, the tumour in the MRSI sampled ROI was recognized as almost fully responding which was in agreement with the histopathology in the core tumour region (average 12.6% proliferation) and with the RECIST criteria and it was stable with respect to the previous measurement. Still, the volume of the tumour (152.3 mm$^3$) was significantly higher than the average for controls (102 ± 1.7 mm$^3$) and caused the death of the animal. Moreover, other cases such as C776 or C808, which underwent 3 therapy cycles and showed nearly full response by nosological imaging in agreement with the relatively low tumour proliferation (23.7% and 20.1%, respectively), died regardless being stable disease according to the RECIST criteria. And as for the case C795, volumes of these tumours at death were significantly higher (223.5 and 142.6 mm$^3$, respectively) than of the control tumours. The explanation to this tumour active growth possibly resides in the restricted ROI being sampled by the MRSI, because the high proliferation region was found to be in the thin layer (~100 µm) of the tumour periphery (black circular region shown in Figure 7.21), which was mostly beyond the nosological image evaluated zone and missed when assessing histopathologically 0.1 mm$^2$ squares regions (as shown in Figure 7.20). And considering for example the case C808, the proliferation rate counted in the periphery was 65.1% and significantly higher than in the core of the tumour (20.1%).

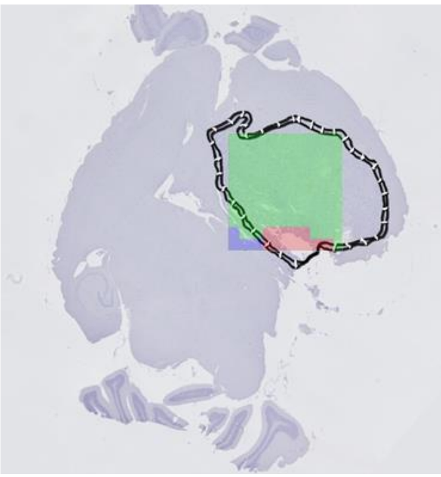

**Figure 7.21.** Digitalized histopathological image of the case C808, in which proliferation was counted in the thin layer (about 100 µm) of the periphery (in black), superimposed with the nosological image at the time of death (day 33 p.i.).

Regarding the longitudinal studies validation cases and apoptotic rates, the latter did not correlate with the response maps calculated with the sources methodology and was significantly lower than GL261 treated tumours in [123]. This could be due to the fact some of these tumours upon the histopathological analysis were already far from the therapy on the growth curve (i.e. C776, C808 and C821, Figure 7.22) and caspase 3 correlates with early stage apoptosis [197], whereas the increase in PUFAs seen in the responding source profile (refer to Section 7.3.6) relates to cumulative apoptosis [180]. Therefore, a different staining may be needed to better correlate cumulative apoptosis with the changes detected in the nosologic maps.

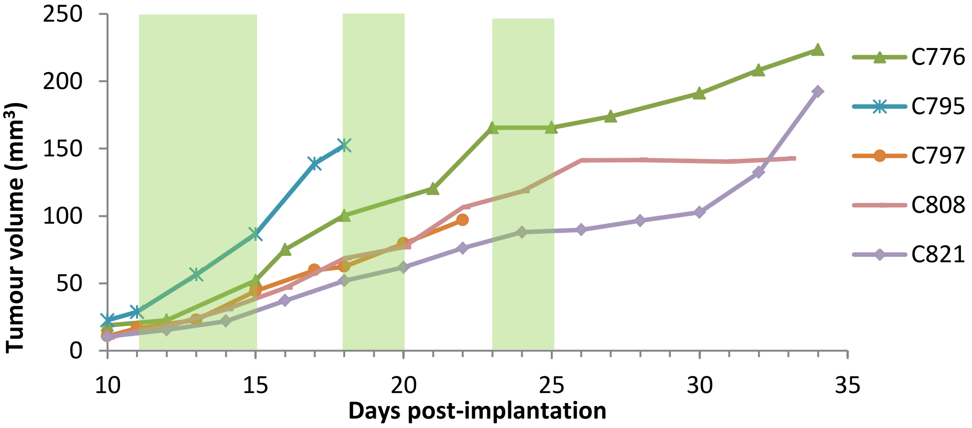

**Figure 7.22.** Volume growth dynamics of GL261 tumours treated with TMZ from the longitudinal studies of this thesis that underwent histopathological analysis. Green sections show each therapy cycle duration.

Finally, a global analysis was performed including all cases from the training and validation groups that had histopathology data available and with apparently homogeneous nosologic maps, in order to detect if there was correlation between both types of response biomarker. The corresponding contingency tables are included in Figure 7.23. The Ki67 proliferation index showed a strong correlation with the response detected using the sources methodology (Phi = -0.85, p<0.001), indicating that higher proliferation rates correlate with a lack of response in the nosologic maps. No relationship was detected between caspase 3 values and the sources results. A further analysis comparing the Ki67 indexes of cases with non-responding nosologic maps with those showing responding maps demonstrated a significantly lower proliferation rate in responding-source cases.

**A**

**Response * Ki67 Crosstabulation**

Count

| | | Ki67 | | Total |
|---|---|---|---|---|
| | | Ki67 <50% | Ki67 >50% | |
| Response | Not responding | 2 | 19 | 21 |
| | Responding | 8 | 0 | 8 |
| Total | | 10 | 19 | 29 |

**Response * Caspase3 Crosstabulation**

Count

| | | Caspase3 | | Total |
|---|---|---|---|---|
| | | Caspase <1% | Caspase >1% | |
| Response | Not responding | 2 | 12 | 14 |
| | Responding | 4 | 4 | 8 |
| Total | | 6 | 16 | 22 |

**B**

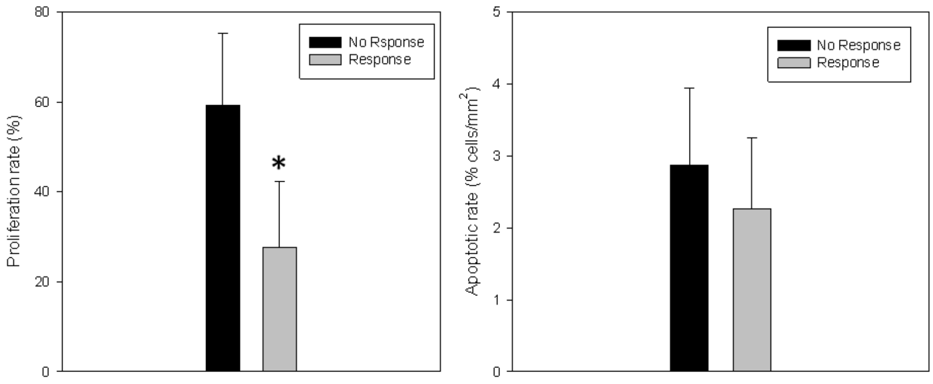

**Figure 7.23. A)** Contingency tables calculated with the cases from the test set considering the response detected by the semi-supervised methodology and the proliferation and apoptotic indexes from the corresponding histopathological slides. Cases with heterogeneous nosologic maps (approximately 50% of responding and non-responding tissue) were excluded. **B)** Proliferation and apoptotic indexes comparison between cases classified as responders or non-responders using the sources analysis.

## 7.4. Conclusions

1. A total of 12 TMZ-treated animals were analysed by MRI/MRS/MRSI/PE-MRSI, tumour growth evolution, histopathology and pattern recognition.

2. Previous results obtained by our group were confirmed, namely, the established TMZ protocol was able to produce a growth arrest in GL261 GBM preclinical tumours and the survival rate of treated animals was significantly longer than the survival of the untreated animals.

3. Overall response was evaluated according to the RECIST criteria and out 12 animals 2 presented partial response, 5 presented stable disease, 1 presented progressive disease and 4 were non-evaluable due to an early death.

4. The methodology described in this work allowed convenient non-invasive monitoring of response to TMZ in preclinical GBM throughout and after the therapy cycles, through source extraction analyses and nosological maps.

5. The sources extracted were not only able to distinguish between the responding and non-responding/control tumours, but also did suggest segmentation ability within the same tumour and made clear the intratumoural heterogeneity of response, hinting the growth arrest and relapse even before changes in tumour volume were observed.

6. The main differences in the sources extracted were mainly, but not only, due to total mobile lipid and polyunsaturated fatty acids mobile lipid resonances, which are accepted biomarkers for apoptosis.

7. The response patterns detected using the sources methodology correlated with the histopathological analysis of Ki67 proliferation index and higher proliferation correlated with a lack of response in the nosologic maps.

8. DMSO “hotspots” showed a tendency to decrease and/or displace outside the tumour mass at the time point corresponding to growth arrest and tumour shrinkage, i.e. when tumours responded to treatment.

9. Presented strategy bears a potential translational application for monitoring patient response to treatment and allowing early decision making with respect to second line therapeutic strategies.

# 8. General Discussion

Brain tumours account for less than 2% of all primary tumours, but are one of the most lethal cancers when “life lost” years are considered. Gliomas are the most prevalent type with a very prognosis and a median survival of less than 15 months for GBM [10], and between 3 years and 7 years for anaplastic astrocytoma or anaplastic oligodendroglial tumors [198-200]. They are extremely resistant to conventional radiation and chemotherapies and, despite current therapeutic advances, the treatment remains essentially palliative. Usually, even patients with a promising radiographic response suffer recurrence and/or progression of their cancers. This is partially due to the cancer stem cells that present capacity to promote tumour invasion, tumour angiogenesis, therapeutic resistance and repopulation after treatment [30, 201-203]. Additionally, due to the lack of the response biomarkers, an early response to treatments remains challenging to assess non-invasively. Therefore, innovative neuroimaging methods are critically needed to provide metabolic or functional information that is indicative of targeted therapeutic action at early time points during the course of treatment. For this reason, we took measures to improve the process of therapy response assessment.

However, to improve studies with patients, extensive studies with preclinical tumours is needed, due to obvious ethical restrictions. In our laboratory we had two murine models available, namely the stereotactic GL261 GBM model with highly reproducible tumour growth kinetics and close to 100% penetrance, however not exactly mimicking the steps of tumour progression seen in spontaneous tumour, and the GEM, recapitulating specific patterns of primary human glioma, but having a very low penetrance and stochastic onset, which made them impractical for use in therapy response studies. Therefore, to combine advantages of both models, the transplantable exogenous and spontaneous endogenous one, we decide intended to generate a transplantable model derived from GEM tumour. Additionally, most preclinical studies focus on high grade models; therefore we screened the GEM colony systematically, searching for a low/intermediate grade tumour candidate in order to attempt to transform it into a transplantable line by disaggregation.

It can be summarized that we successfully established a new transplantable model of GBM with significantly slower growth and higher survival with respect to the standard GL261 model and with significantly higher penetrance than the original GEM colony. The fact that the S912 mass, used for generation of gliospheres, was originally diagnosed as an anaplastic oligoastrocytoma (grade III) and that the combined procedures related to gliospheres generation, freezing and transplantation produced a progression to grade IV GBM, makes the developed model qualify as a potential secondary GBM model in mice, which has a potential interest in future therapeutic protocols.

Although, we fully characterised the new transplantable model, the therapy studies were chosen to be done with the standard GL261model, as to continue the previous group work described in [123]. However, in the future we plan to apply them to our transplantable models.

The semi-supervised source extraction methodology applied in this work was able to monitor the response along time and detect non-invasively an early response and relapse. The differences between the normal tissue, control tumour and tumour responding to treatment sources were based on specific biomarkers, that have already been described: higher ML, low NAA and a higher ratio choline/creatine differentiate control tumour spectra from normal brain parenchyma [106]; ML and ML polyunsaturated fatty acids (PUFA) signals were higher in responsive tumours in comparison to untreated/unresponsive tumours, indicating therapy-related metabolic changes, based on apoptosis induced by treatment [180, 204]. Additionally, our results were validated histopathologically with Ki67 staining, that was reported as a good therapy response biomarker [191], and responding and not responding profiles described by the nosologic maps, strongly correlated with the proliferation stage of the tumours. Therefore, this strategy bears translational potential and could be implemented in the future to improve cancer therapy by allowing treatment to be tailored to the individual.

On the other hand, DMSO seemed to have differential retention along the therapy protocol inside tumoral mass of TMZ-treated GL261 GBM mice, decreasing just before transient response detectable by MRI and increasing again during tumour recurrence, indicating that DMSO could be another potential biomarker for early therapy response in brain tumours. It would be interesting to carry out the therapy protocols and test DMSO-MRSI detection of early response to develop classifiers of response and test the source extraction methodology in low/intermediate preclinical tumour models to potentially be used in the future in patients.

# 9. General Conclusions

1. Two different GEM colonies (namely, S and R) genotyped (n = 269) for the specific genetic modifications in order to select animals for breeding and MRI screening.

2. The tumour incidence rate in GEM (1% for R and 16% for S), nevertheless was found to be much smaller than the one reported by founders (>90%). The evaluation technique used for diagnosis (MRI screening of transgenic mice versus histopathological analysis) could at last partially explain this difference.

3. Variability in tumour growth patterns and in the type of tumours developed by the GEM indicates that they would not be good models for therapy response studies requiring several homogenous diseased mice for comparable evaluation.

4. Despite the low incidence rate and large variability, GEM tumours developed were characterized using MR-based techniques and selected cases considered of interest were used for development and training of tumour type grade classifiers based in MRSI perturbed spectra.

5. The screening of the GEM colonies also helped to select for tumours suitable for disaggregation protocols and generation of transplantable models of potentially low/intermediate grade glioma.

6. Gliospheres from an anaplastic OA (grade III) GEM tumour were successfully generated. However, freezing and cell culture protocols produced a progression to grade IV glioblastoma (GBM). This makes the developed transplantable model qualify as potential secondary GBM model in mice.

7. The newly established model of GBM presented significantly slower growth and higher survival with respect to the standard GL261 model, as well as significantly higher penetrance than the original GEM colony, which makes this model a potential candidate for future therapy protocols.

8. Different samples from our glioma models, namely GL261 tumours, GL261 cells line, S colony tumours and tumours developed during the GEM tumour disaggregation protocol were sequenced and no IDH1, IDH2 and p53 mutations at particular sites reported for human gliomas were detected. This suggests that the driver mutations found in humans do not correspond to the same gene location in the investigated murine tumour genes.

9. A total of 12 TMZ-treated animals were analysed by MRI/MRS/MRSI/PE-MRSI, tumour growth evolution, histopathology and pattern recognition.

10. Previous results obtained by our group were confirmed, namely, the established TMZ protocol was able to produce a growth arrest in GL261 GBM preclinical tumours and the survival rate of treated animals was significantly longer than the survival of the untreated animals.

11. The semi-supervised source extraction methodology was able to characterize the response to TMZ in preclinical GBM both at a defined time-point and along the therapy protocol. The response patterns detected suitably correlated with the histopathological analysis of the tumours at each stage.

12. The semi-supervised source extraction methodology bears a potential translational application for monitoring response to treatment in clinical cases and allowing early decision making with respect to second line personalized therapeutic strategies.

## References

1. *GLOBOCAN 2012: Estimated Cancer Incidence, Mortality and Prevalence Worldwide in 2012*. 2012; Available from: http://globocan.iarc.fr.
2. Louis DN, Ohgaki H, Wiestler OD, Cavenee WK, Burger PC, Jouvet A, Scheithauer BW and Kleihues P. *The 2007 WHO classification of tumours of the central nervous system.* Acta Neuropathol, 2007. **114**(2): p. 97-109.
3. DeAngelis LM, Posner JB and Posner JB. *Neurologic complications of cancer*. 2nd ed. Contemporary neurology series. 2009, Oxford ; New York: Oxford University Press. xv, 634 p.
4. Eichler AF and Loeffler JS. *Multidisciplinary management of brain metastases.* Oncologist, 2007. **12**(7): p. 884-98.
5. Maher EA, Furnari FB, Bachoo RM, Rowitch DH, Louis DN, Cavenee WK and DePinho RA. *Malignant glioma: genetics and biology of a grave matter.* Genes Dev, 2001. **15**(11): p. 1311-33.
6. Ostrom QT, Gittleman H, Farah P, Ondracek A, Chen Y, Wolinsky Y, Stroup NE, Kruchko C and Barnholtz-Sloan JS. *CBTRUS statistical report: Primary brain and central nervous system tumors diagnosed in the United States in 2006-2010.* Neuro Oncol, 2013. **15 Suppl 2**: p. ii1-56.
7. Bernstein MM and Berger MS. *Neuro-oncology : the essentials*. 2nd ed. 2008, New York: Thieme. XVII, 477 p.
8. Stewart BW and Kleihues P. *World cancer report*. 2003, Lyon: IARC Press ; Oxford : Oxford University Press [distributor]. 351 p.
9. Nakada M, Nakada S, Demuth T, Tran NL, Hoelzinger DB and Berens ME. *Molecular targets of glioma invasion.* Cell Mol Life Sci, 2007. **64**(4): p. 458-78.
10. Stupp R, Mason WP, van den Bent MJ, Weller M, Fisher B, Taphoorn MJ, Belanger K, Brandes AA, Marosi C, Bogdahn U, Curschmann J, Janzer RC, Ludwin SK, Gorlia T, Allgeier A, Lacombe D, Cairncross JG, Eisenhauer E and Mirimanoff RO. *Radiotherapy plus concomitant and adjuvant temozolomide for glioblastoma.* N Engl J Med, 2005. **352**(10): p. 987-96.
11. Behin A, Hoang-Xuan K, Carpentier AF and Delattre JY. *Primary brain tumours in adults.* Lancet, 2003. **361**(9354): p. 323-31.
12. Ohgaki H and Kleihues P. *The definition of primary and secondary glioblastoma.* Clin Cancer Res, 2013. **19**(4): p. 764-72.
13. Vogelstein B and Kinzler KW. *The multistep nature of cancer.* Trends Genet, 1993. **9**(4): p. 138-41.
14. Hanahan D and Weinberg RA. *The hallmarks of cancer.* Cell, 2000. **100**(1): p. 57-70.
15. Hainaut P. *The tumor suppressor protein p53: a receptor to genotoxic stress that controls cell growth and survival.* Curr Opin Oncol, 1995. **7**(1): p. 76-82.
16. Kamb A, Shattuck-Eidens D, Eeles R, Liu Q, Gruis NA, Ding W, Hussey C, Tran T, Miki Y, Weaver-Feldhaus J and et al. *Analysis of the p16 gene (CDKN2) as a candidate for the chromosome 9p melanoma susceptibility locus.* Nat Genet, 1994. **8**(1): p. 23-6.
17. Holland EC. *Gliomagenesis: genetic alterations and mouse models.* Nat Rev Genet, 2001. **2**(2): p. 120-9.
18. Reitman ZJ and Yan H. *Isocitrate dehydrogenase 1 and 2 mutations in cancer: alterations at a crossroads of cellular metabolism.* J Natl Cancer Inst, 2010. **102**(13): p. 932-41.
19. Zhao S, Lin Y, Xu W, Jiang W, Zha Z, Wang P, Yu W, Li Z, Gong L, Peng Y, Ding J, Lei Q, Guan KL and Xiong Y. *Glioma-derived mutations in IDH1 dominantly inhibit IDH1 catalytic activity and induce HIF-1alpha.* Science, 2009. **324**(5924): p. 261-5.
20. Ichimura K. *Molecular pathogenesis of IDH mutations in gliomas.* Brain Tumor Pathol, 2012. **29**(3): p. 131-9.
21. Enger PO. *IDH1 and IDH2 mutations in gliomas.* BMC Cancer, 2009. **360**(8): p. 765-73.

22. Ichimura K, Pearson DM, Kocialkowski S, Backlund LM, Chan R, Jones DT and Collins VP. *IDH1 mutations are present in the majority of common adult gliomas but rare in primary glioblastomas.* Neuro Oncol, 2009. **11**(4): p. 341-7.
23. Hanahan D and Weinberg RA. *Hallmarks of cancer: the next generation.* Cell, 2011. **144**(5): p. 646-74.
24. Reya T, Morrison SJ, Clarke MF and Weissman IL. *Stem cells, cancer, and cancer stem cells.* Nature, 2001. **414**(6859): p. 105-11.
25. Cho RW and Clarke MF. *Recent advances in cancer stem cells.* Curr Opin Genet Dev, 2008. **18**(1): p. 48-53.
26. Lobo NA, Shimono Y, Qian D and Clarke MF. *The biology of cancer stem cells.* Annu Rev Cell Dev Biol, 2007. **23**: p. 675-99.
27. Visvader JE and Lindeman GJ. *Cancer stem cells in solid tumours: accumulating evidence and unresolved questions.* Nat Rev Cancer, 2008. **8**(10): p. 755-68.
28. Bonnet D and Dick JE. *Human acute myeloid leukemia is organized as a hierarchy that originates from a primitive hematopoietic cell.* Nat Med, 1997. **3**(7): p. 730-7.
29. Clarke MF, Dick JE, Dirks PB, Eaves CJ, Jamieson CH, Jones DL, Visvader J, Weissman IL and Wahl GM. *Cancer stem cells--perspectives on current status and future directions: AACR Workshop on cancer stem cells.* Cancer Res, 2006. **66**(19): p. 9339-44.
30. Bao S, Wu Q, McLendon RE, Hao Y, Shi Q, Hjelmeland AB, Dewhirst MW, Bigner DD and Rich JN. *Glioma stem cells promote radioresistance by preferential activation of the DNA damage response.* Nature, 2006. **444**(7120): p. 756-60.
31. Liu G, Yuan X, Zeng Z, Tunici P, Ng H, Abdulkadir IR, Lu L, Irvin D, Black KL and Yu JS. *Analysis of gene expression and chemoresistance of CD133+ cancer stem cells in glioblastoma.* Mol Cancer, 2006. **5**: p. 67.
32. Vescovi AL, Galli R and Reynolds BA. *Brain tumour stem cells.* Nat Rev Cancer, 2006. **6**(6): p. 425-36.
33. Chang SM, Parney IF, Huang W, Anderson FA, Jr., Asher AL, Bernstein M, Lillehei KO, Brem H, Berger MS, Laws ER and Glioma Outcomes Project I. *Patterns of care for adults with newly diagnosed malignant glioma.* JAMA, 2005. **293**(5): p. 557-64.
34. Stummer W, Reulen HJ, Meinel T, Pichlmeier U, Schumacher W, Tonn JC, Rohde V, Oppel F, Turowski B, Woiciechowsky C, Franz K, Pietsch T and Group AL-GS. *Extent of resection and survival in glioblastoma multiforme: identification of and adjustment for bias.* Neurosurgery, 2008. **62**(3): p. 564-76; discussion 564-76.
35. Sanai N and Berger MS. *Extent of resection influences outcomes for patients with gliomas.* Rev Neurol (Paris), 2011. **167**(10): p. 648-54.
36. Spetzler RF and Sanai N. *The quiet revolution: retractorless surgery for complex vascular and skull base lesions.* J Neurosurg, 2012. **116**(2): p. 291-300.
37. Sanai N, Mirzadeh Z and Berger MS. *Functional outcome after language mapping for glioma resection.* N Engl J Med, 2008. **358**(1): p. 18-27.
38. Gasser T, Szelenyi A, Senft C, Muragaki Y, Sandalcioglu IE, Sure U, Nimsky C and Seifert V. *Intraoperative MRI and functional mapping.* Acta Neurochir Suppl, 2011. **109**: p. 61-5.
39. Senft C, Bink A, Franz K, Vatter H, Gasser T and Seifert V. *Intraoperative MRI guidance and extent of resection in glioma surgery: a randomised, controlled trial.* Lancet Oncol, 2011. **12**(11): p. 997-1003.
40. Stummer W, Pichlmeier U, Meinel T, Wiestler OD, Zanella F, Reulen HJ and Group AL-GS. *Fluorescence-guided surgery with 5-aminolevulinic acid for resection of malignant glioma: a randomised controlled multicentre phase III trial.* Lancet Oncol, 2006. **7**(5): p. 392-401.
41. Begg AC, Stewart FA and Vens C. *Strategies to improve radiotherapy with targeted drugs.* Nat Rev Cancer, 2011. **11**(4): p. 239-53.
42. Andersen AP. *Postoperative irradiation of glioblastomas. Results in a randomized series.* Acta Radiol Oncol Radiat Phys Biol, 1978. **17**(6): p. 475-84.

43. Walker MD, Green SB, Byar DP, Alexander E, Jr., Batzdorf U, Brooks WH, Hunt WE, MacCarty CS, Mahaley MS, Jr., Mealey J, Jr., Owens G, Ransohoff J, 2nd, Robertson JT, Shapiro WR, Smith KR, Jr., Wilson CB and Strike TA. *Randomized comparisons of radiotherapy and nitrosoureas for the treatment of malignant glioma after surgery.* N Engl J Med, 1980. **303**(23): p. 1323-9.
44. Short S and Tobias J. *Radiosurgery for brain tumours.* BMJ, 2010. **340**: p. c3247.
45. Rodrigues LM, Stubbs M, Robinson SP, Newell B, Mansi J and Griffiths JR. *The C-neu mammary carcinoma in Oncomice; characterization and monitoring response to treatment with herceptin by magnetic resonance methods.* MAGMA, 2004. **17**(3-6): p. 260-70.
46. Ken S, Vieillevigne L, Franceries X, Simon L, Supper C, Lotterie JA, Filleron T, Lubrano V, Berry I, Cassol E, Delannes M, Celsis P, Cohen-Jonathan EM and Laprie A. *Integration method of 3D MR spectroscopy into treatment planning system for glioblastoma IMRT dose painting with integrated simultaneous boost.* Radiat Oncol, 2013. **8**: p. 1.
47. Saraswathy S, Crawford FW, Lamborn KR, Pirzkall A, Chang S, Cha S and Nelson SJ. *Evaluation of MR markers that predict survival in patients with newly diagnosed GBM prior to adjuvant therapy.* J Neurooncol, 2009. **91**(1): p. 69-81.
48. Baumann M, DuBois W, Pu A, Freeman J and Suit HD. *Response of xenografts of human malignant gliomas and squamous cell carcinomas to fractionated irradiation.* Int J Radiat Oncol Biol Phys, 1992. **23**(4): p. 803-9.
49. Baumann M, Krause M, Thames H, Trott K and Zips D. *Cancer stem cells and radiotherapy.* Int J Radiat Biol, 2009. **85**(5): p. 391-402.
50. Villano JL, Seery TE and Bressler LR. *Temozolomide in malignant gliomas: current use and future targets.* Cancer Chemother Pharmacol, 2009. **64**(4): p. 647-55.
51. Yang LJ, Zhou CF and Lin ZX. *Temozolomide and radiotherapy for newly diagnosed glioblastoma multiforme: a systematic review.* Cancer Invest, 2014. **32**(2): p. 31-6.
52. Newlands ES, Foster T and Zaknoen S. *Phase I study of temozolamide (TMZ) combined with procarbazine (PCB) in patients with gliomas.* Br J Cancer, 2003. **89**(2): p. 248-51.
53. Glas M, Happold C, Rieger J, Wiewrodt D, Bahr O, Steinbach JP, Wick W, Kortmann RD, Reifenberger G, Weller M and Herrlinger U. *Long-term survival of patients with glioblastoma treated with radiotherapy and lomustine plus temozolomide.* J Clin Oncol, 2009. **27**(8): p. 1257-61.
54. Tentori L, Leonetti C, Scarsella M, D'Amati G, Vergati M, Portarena I, Xu W, Kalish V, Zupi G, Zhang J and Graziani G. *Systemic administration of GPI 15427, a novel poly(ADP-ribose) polymerase-1 inhibitor, increases the antitumor activity of temozolomide against intracranial melanoma, glioma, lymphoma.* Clin Cancer Res, 2003. **9**(14): p. 5370-9.
55. Yamini B, Yu X, Pytel P, Galanopoulos N, Rawlani V, Veerapong J, Bickenbach K and Weichselbaum RR. *Adenovirally delivered tumor necrosis factor-alpha improves the antiglioma efficacy of concomitant radiation and temozolomide therapy.* Clin Cancer Res, 2007. **13**(20): p. 6217-23.
56. McConville P, Hambardzumyan D, Moody JB, Leopold WR, Kreger AR, Woolliscroft MJ, Rehemtulla A, Ross BD and Holland EC. *Magnetic resonance imaging determination of tumor grade and early response to temozolomide in a genetically engineered mouse model of glioma.* Clin Cancer Res, 2007. **13**(10): p. 2897-904.
57. Sul J and Fine HA. *Malignant gliomas: new translational therapies.* Mt Sinai J Med, 2010. **77**(6): p. 655-66.
58. Gilbert MR, Sulman EP and Mehta MP. *Bevacizumab for newly diagnosed glioblastoma.* N Engl J Med, 2014. **370**(21): p. 2048-9.
59. Gilbert MR, Dignam JJ, Armstrong TS, Wefel JS, Blumenthal DT, Vogelbaum MA, Colman H, Chakravarti A, Pugh S, Won M, Jeraj R, Brown PD, Jaeckle KA, Schiff D, Stieber VW, Brachman DG, Werner-Wasik M, Tremont-Lukats IW, Sulman EP, Aldape KD, Curran WJ, Jr. and Mehta MP. *A randomized trial of bevacizumab for newly diagnosed glioblastoma.* N Engl J Med, 2014. **370**(8): p. 699-708.

60. Szatmari T, Lumniczky K, Desaknai S, Trajcevski S, Hidvegi EJ, Hamada H and Safrany G. *Detailed characterization of the mouse glioma 261 tumor model for experimental glioblastoma therapy.* Cancer Sci, 2006. **97**(6): p. 546-53.
61. Cha S, Johnson G, Wadghiri YZ, Babb J, Zagzag D and Tumbull DH. *Dynamic, contrast-enchanced perfusion MRI in mouse gliomas: correlation with histopathology.* Magn Reson Med, 2003. **49**: p. 848-855.
62. Gutmann DH, Baker SJ, Giovannini M, Garbow J and Weiss W. *Mouse models of human cancer consortium symposium on nervous system tumors.* Cancer Res, 2003. **63**(11): p. 3001-4.
63. Weiss WA, Burns MJ, Hackett C, Aldape K, Hill JR, Kuriyama H, Kuriyama N, Milshteyn N, Roberts T, Wendland MF, DePinho R and Israel MA. *Genetic determinants of malignancy in a mouse model for oligodendroglioma.* Cancer Res, 2003. **63**(7): p. 1589-95.
64. Fomchenko EI and Holland EC. *Mouse models of brain tumors and their applications in preclinical trials.* Clin Cancer Res, 2006. **12**(18): p. 5288-97.
65. Ding H, Roncari L, Shannon P, Wu X, Lau N, Karaskova J, Gutmann DH, Squire JA, Nagy A and Guha A. *Astrocyte-specific expression of activated p21-ras results in malignant astrocytoma formation in a transgenic mouse model of human gliomas.* Cancer Res, 2001. **61**(9): p. 3826-36.
66. Meir EG, Munoz D, Agnihotri S and Guha A. *Transgenic Mouse Models of CNS Tumors: Using Genetically Engineered Murine Models to Study the Role of p21-Ras in Glioblastoma Multiforme*, in *CNS Cancer*. 2009, Humana Press. p. 61-76.
67. Shannon P, Sabha N, Lau N, Kamnasaran D, Gutmann DH and Guha A. *Pathological and Molecular Progression of Astrocytomas in a GFAP:12V-Ha-Ras Mouse Astrocytoma Model.* Am J Pathol, 2005. **167**(3): p. 859-867.
68. Ridgway JP. *Cardiovascular magnetic resonance physics for clinicians: part I.* J Cardiovasc Magn Reson, 2010. **12**: p. 71.
69. Weigle JP and Broome DR. *Nephrogenic systemic fibrosis: chronic imaging findings and review of the medical literature.* Skeletal Radiol, 2008. **37**(5): p. 457-64.
70. Frahm J, Bruhn H, Gyngell ML, Merboldt KD, Hanicke W and Sauter R. *Localized high-resolution proton NMR spectroscopy using stimulated echoes: initial applications to human brain in vivo.* Magn Reson Med, 1989. **9**(1): p. 79-93.
71. Bottomley PA. *Spatial localization in NMR spectroscopy in vivo.* Ann N Y Acad Sci, 1987. **508**: p. 333-48.
72. Howe FA, Barton SJ, Cudlip SA, Stubbs M, Saunders DE, Murphy M, Wilkins P, Opstad KS, Doyle VL, McLean MA, Bell BA and Griffiths JR. *Metabolic profiles of human brain tumors using quantitative in vivo 1H magnetic resonance spectroscopy.* Magn Reson Med, 2003. **49**(2): p. 223-32.
73. Simoes RV, Garcia-Martin ML, Cerdan S and Arus C. *Perturbation of mouse glioma MRS pattern by induced acute hyperglycemia.* NMR Biomed, 2008. **21**(3): p. 251-64.
74. Simmons ML, Frondoza CG and Coyle JT. *Immunocytochemical localization of N-acetyl-aspartate with monoclonal antibodies.* Neuroscience, 1991. **45**(1): p. 37-45.
75. Govindaraju V, Young K and Maudsley AA. *Proton NMR chemical shifts and coupling constants fro brain metabolites.* NMR Biomed, 2000. **13**: p. 129-153.
76. Barker PB. *N-acetyl aspartate--a neuronal marker?* Ann Neurol, 2001. **49**(4): p. 423-4.
77. Tsai G and Coyle JT. *N-acetylaspartate in neuropsychiatric disorders.* Prog Neurobiol, 1995. **46**(5): p. 531-40.
78. Brulatout S, Meric P, Loubinoux I, Borredon J, Correze JL, Roucher P, Gillet B, Berenger G, Beloeil JC, Tiffon B, Mispelter J and Seylaz J. *A one-dimensional (proton and phosphorus) and two-dimensional (proton) in vivo NMR spectroscopic study of reversible global cerebral ischemia.* J Neurochem, 1996. **66**(6): p. 2491-9.
79. De Stefano N, Matthews PM and Arnold DL. *Reversible decreases in N-acetylaspartate after acute brain injury.* Magn Reson Med, 1995. **34**(5): p. 721-7.

80. Wang Z, Sutton LN, Cnaan A, Haselgrove JC, Rorke LB, Zhao H, Bilaniuk LT and Zimmerman RA. *Proton MR spectroscopy of pediatric cerebellar tumors.* AJNR Am J Neuroradiol, 1995. **16**(9): p. 1821-33.
81. Barker PB, Breiter SN, Soher BJ, Chatham JC, Forder JR, Samphilipo MA, Magee CA and Anderson JH. *Quantitative proton spectroscopy of canine brain: in vivo and in vitro correlations.* Magn Reson Med, 1994. **32**(2): p. 157-63.
82. Michaelis T, Merboldt KD, Bruhn H, Hanicke W and Frahm J. *Absolute concentrations of metabolites in the adult human brain in vivo: quantification of localized proton MR spectra.* Radiology, 1993. **187**(1): p. 219-27.
83. Pouwels PJ and Frahm J. *Regional metabolite concentrations in human brain as determined by quantitative localized proton MRS.* Magn Reson Med, 1998. **39**(1): p. 53-60.
84. Davie CA, Hawkins CP, Barker GJ, Brennan A, Tofts PS, Miller DH and McDonald WI. *Detection of myelin breakdown products by proton magnetic resonance spectroscopy.* Lancet, 1993. **341**(8845): p. 630-1.
85. Brenner RE, Munro PM, Williams SC, Bell JD, Barker GJ, Hawkins CP, Landon DN and McDonald WI. *The proton NMR spectrum in acute EAE: the significance of the change in the Cho:Cr ratio.* Magn Reson Med, 1993. **29**(6): p. 737-45.
86. Kreis R, Ross BD, Farrow NA and Ackerman Z. *Metabolic disorders of the brain in chronic hepatic encephalopathy detected with H-1 MR spectroscopy.* Radiology, 1992. **182**(1): p. 19-27.
87. Lowry OH, Berger SJ, Carter JG, Chi MM, Manchester JK, Knor J and Pusateri ME. *Diversity of metabolic patterns in human brain tumors: enzymes of energy metabolism and related metabolites and cofactors.* J Neurochem, 1983. **41**(4): p. 994-1010.
88. Tong Z, Yamaki T, Harada K and Houkin K. *In vivo quantification of the metabolites in normal brain and brain tumors by proton MR spectroscopy using water as an internal standard.* Magn Reson Imaging, 2004. **22**(7): p. 1017-24.
89. Munoz Maniega S, Cvoro V, Armitage PA, Marshall I, Bastin ME and Wardlaw JM. *Choline and creatine are not reliable denominators for calculating metabolite ratios in acute ischemic stroke.* Stroke, 2008. **39**(9): p. 2467-9.
90. Chang L, Ernst T, Osborn D, Seltzer W, Leonido-Yee M and Poland RE. *Proton spectroscopy in myotonic dystrophy: correlations with CTG repeats.* Arch Neurol, 1998. **55**(3): p. 305-11.
91. Ross BD. *Biochemical considerations in 1H spectroscopy. Glutamate and glutamine; myo-inositol and related metabolites.* NMR Biomed, 1991. **4**(2): p. 59-63.
92. Brand A, Richter-Landsberg C and Leibfritz D. *Multinuclear NMR studies on the energy metabolism of glial and neuronal cells.* Dev Neurosci, 1993. **15**(3-5): p. 289-98.
93. Zhu H and Barker PB. *MR spectroscopy and spectroscopic imaging of the brain.* Methods Mol Biol, 2011. **711**: p. 203-26.
94. Peet AC, Lateef S, MacPherson L, Natarajan K, Sgouros S and Grundy RG. *Short echo time 1 H magnetic resonance spectroscopy of childhood brain tumours.* Childs Nerv Syst, 2007. **23**(2): p. 163-9.
95. Candiota AP, Majos C, Julia-Sape M, Cabanas M, Acebes JJ, Moreno-Torres A, Griffiths JR and Arus C. *Non-invasive grading of astrocytic tumours from the relative contents of myo-inositol and glycine measured by in vivo MRS.* JBR-BTR, 2011. **94**(6): p. 319-29.
96. Gruetter R, Weisdorf SA, Rajanayagan V, Terpstra M, Merkle H, Truwit CL, Garwood M, Nyberg SL and Ugurbil K. *Resolution improvements in in vivo 1H NMR spectra with increased magnetic field strength.* J Magn Reson, 1998. **135**(1): p. 260-4.
97. Tkac I, Andersen P, Adriany G, Merkle H, Ugurbil K and Gruetter R. *In vivo 1H NMR spectroscopy of the human brain at 7 T.* Magn Reson Med, 2001. **46**(3): p. 451-6.
98. Chamuleau RA, Bosman DK, Bovee WM, Luyten PR and den Hollander JA. *What the clinician can learn from MR glutamine/glutamate assays.* NMR Biomed, 1991. **4**(2): p. 103-8.

99. Poptani H, Gupta RK, Roy R, Pandey R, Jain VK and Chhabra DK. *Characterization of intracranial mass lesions with in vivo proton MR spectroscopy.* AJNR Am J Neuroradiol, 1995. **16**(8): p. 1593-603.
100. Rudkin TM and Arnold DL. *Proton magnetic resonance spectroscopy for the diagnosis and management of cerebral disorders.* Arch Neurol, 1999. **56**(8): p. 919-26.
101. De Edelenyi FS, Rubin C, Esteve F, Grand S, Decorps M, Lefournier V, Le Bas JF and Remy C. *A new approach for analyzing proton magnetic resonance spectroscopic images of brain tumors: nosologic images.* Nat Med, 2000. **6**(11): p. 1287-9.
102. Ortega-Martorell S, Lisboa PJ, Vellido A, Simoes RV, Pumarola M, Julia-Sape M and Arus C. *Convex non-negative matrix factorization for brain tumor delimitation from MRSI data.* PLoS One, 2012. **7**(10): p. e47824.
103. Howe FA and Opstad KS. *1H MR spectroscopy of brain tumours and masses.* NMR Biomed, 2003. **16**(3): p. 123-31.
104. Tate AR, Underwood J, Acosta DM, Julia-Sape M, Majos C, Moreno-Torres A, Howe FA, van der Graaf M, Lefournier V, Murphy MM, Loosemore A, Ladroue C, Wesseling P, Luc Bosson J, Cabanas ME, Simonetti AW, Gajewicz W, Calvar J, Capdevila A, Wilkins PR, Bell BA, Remy C, Heerschap A, Watson D, Griffiths JR and Arus C. *Development of a decision support system for diagnosis and grading of brain tumours using in vivo magnetic resonance single voxel spectra.* NMR Biomed, 2006. **19**(4): p. 411-34.
105. Nelson SJ. *Multivoxel magnetic resonance spectroscopy of brain tumors.* Mol Cancer Ther, 2003. **2**(5): p. 497-507.
106. Simoes RV, Delgado-Goni T, Lope-Piedrafita S and Arus C. *1H-MRSI pattern perturbation in a mouse glioma: the effects of acute hyperglycemia and moderate hypothermia.* NMR Biomed, 2010. **23**(1): p. 23-33.
107. Simoes RV, Ortega-Martorell S, Delgado-Goni T, Le Fur Y, Pumarola M, Candiota AP, Martin J, Stoyanova R, Cozzone PJ, Julia-Sape M and Arus C. *Improving the classification of brain tumors in mice with perturbation enhanced (PE)-MRSI.* Integr Biol (Camb), 2012. **4**(2): p. 183-91.
108. Siesjo BK. *Brain energy metabolism and catecholaminergic activity in hypoxia, hypercapnia and ischemia.* J Neural Transm Suppl, 1978(14): p. 17-22.
109. Rhodes CG, Wise RJ, Gibbs JM, Frackowiak RS, Hatazawa J, Palmer AJ, Thomas DG and Jones T. *In vivo disturbance of the oxidative metabolism of glucose in human cerebral gliomas.* Ann Neurol, 1983. **14**(6): p. 614-26.
110. Ziegler A, von Kienlin M, Decorps M and Remy C. *High glycolytic activity in rat glioma demonstrated in vivo by correlation peak 1H magnetic resonance imaging.* Cancer Res, 2001. **61**(14): p. 5595-600.
111. Provent P, Benito M, Hiba B, Farion R, Lopez-Larrubia P, Ballesteros P, Remy C, Segebarth C, Cerdan S, Coles JA and Garcia-Martin ML. *Serial in vivo spectroscopic nuclear magnetic resonance imaging of lactate and extracellular pH in rat gliomas shows redistribution of protons away from sites of glycolysis.* Cancer Res, 2007. **67**(16): p. 7638-45.
112. Hamans B, Navis AC, Wright A, Wesseling P, Heerschap A and Leenders W. *Multivoxel (1)H MR spectroscopy is superior to contrast-enhanced MRI for response assessment after anti-angiogenic treatment of orthotopic human glioma xenografts and provides handles for metabolic targeting.* Neuro Oncol, 2013. **15**(12): p. 1615-24.
113. Delgado-Goni T, Martin-Sitjar J, Simoes RV, Acosta M, Lope-Piedrafita S and Arus C. *Dimethyl sulfoxide (DMSO) as a potential contrast agent for brain tumors.* NMR Biomed, 2013. **26**(2): p. 173-84.
114. Lovelock JE and Bishop MW. *Prevention of freezing damage to living cells by dimethyl sulphoxide.* Nature, 1959. **183**(4672): p. 1394-5.
115. Silveira PC, Victor EG, Schefer D, Silva LA, Streck EL, Paula MM and Pinho RA. *Effects of therapeutic pulsed ultrasound and dimethylsulfoxide (DMSO) phonophoresis on parameters of oxidative stress in traumatized muscle.* Ultrasound Med Biol, 2010. **36**(1): p. 44-50.

116. Altman DG, Vergouwe Y, Royston P and Moons KG. *Prognosis and prognostic research: validating a prognostic model.* BMJ, 2009. **338**: p. b605.
117. Duda RO, Hart PE, Stork DG, Duda ROPc and scene a. *Pattern classification*. 2nd ed. / Richard O. Duda, Peter E. Hart, David G. Stork. ed. 2001, New York ; Chichester: Wiley. xx, 654 p.
118. Sajda P, Du S, Brown TR, Stoyanova R, Shungu DC, Mao X and Parra LC. *Nonnegative matrix factorization for rapid recovery of constituent spectra in magnetic resonance chemical shift imaging of the brain.* IEEE Trans Med Imaging, 2004. **23**(12): p. 1453-65.
119. Urbán N, Martín-Ibañez R, Herranz C, Esgleas M, Crespo E, Pardo M, Crespo-Enríquez I, Méndez-Gómez HR, Waclaw R, Chatzi C, Alvarez R, Duester G, Campbell K, de Lera AR, Vicario-Abejón C, Martinez S, Alberch J and Canals JM. *Nolz1 promotes striatal neurogenesis through the regulation of retinoic acid signaling.* Neural Dev, 2010. **5**: p. 21.
120. Goldhoff P, Warrington NM, Limbrick DD, Jr., Hope A, Woerner BM, Jackson E, Perry A, Piwnica-Worms D and Rubin JB. *Targeted inhibition of cyclic AMP phosphodiesterase-4 promotes brain tumor regression.* Clin Cancer Res, 2008. **14**(23): p. 7717-25.
121. Houghton PJ, Stewart CF, Cheshire PJ, Richmond LB, Kirstein MN, Poquette CA, Tan M, Friedman HS and Brent TP. *Antitumor activity of temozolomide combined with irinotecan is partly independent of O6-methylguanine-DNA methyltransferase and mismatch repair phenotypes in xenograft models.* Clin Cancer Res, 2000. **6**(10): p. 4110-8.
122. Kato Y, Okollie B, Raman V, Vesuna F, Zhao M, Baker SD, Bhujwalla ZM and Artemov D. *Contributing factors of temozolomide resistance in MCF-7 tumor xenograft models.* Cancer Biol Ther, 2007. **6**(6): p. 891-7.
123. Delgado-Goni T, Julia-Sape M, Candiota AP, Pumarola M and Arus C. *Molecular imaging coupled to pattern recognition distinguishes response to temozolomide in preclinical glioblastoma.* NMR Biomed, 2014. **27**(11): p. 1333-45.
124. Ortuno JE, Ledesma-Carbayo MJ, Simoes RV, Candiota AP, Arus C and Santos A. *DCE@urLAB: a dynamic contrast-enhanced MRI pharmacokinetic analysis tool for preclinical data.* BMC Bioinformatics, 2013. **14**: p. 316.
125. Ernst T and Hennig J. *Improved water suppression for localized in vivo 1H spectroscopy.* J Magn Reson B, 1995. **106**(2): p. 181-6.
126. Mehrara E, Forssell-Aronsson E, Ahlman H and Bernhardt P. *Specific growth rate versus doubling time for quantitative characterization of tumor growth rate.* Cancer Res, 2007. **67**(8): p. 3970-5.
127. http://gabrmn.uab.es/DMPM.
128. Ortega-Martorell S, Olier I, Julia-Sape M and Arus C. *SpectraClassifier 1.0: a user friendly, automated MRS-based classifier-development system.* BMC Bioinformatics, 2010. **11**.
129. Lee DD and Seung HS. *Learning the parts of objects by non-negative matrix factorization.* Nature, 1999. **401**(6755): p. 788-91.
130. Paatero P and Tapper U. *Positive matrix factorization: A non-negative factor model with optimal utilization of error estimates of data values.* Environmetrics, 1994. **5**(2): p. 111-126.
131. Ding C, Li T and Jordan MI. *Convex and semi-nonnegative matrix factorizations.* IEEE Trans Pattern Anal Mach Intell, 2010. **32**(1): p. 45-55.
132. Ortega-Martorell S, Ruiz H, Vellido A, Olier I, Romero E, Julia-Sape M, Martin JD, Jarman IH, Arus C and Lisboa PJ. *A Novel Semi-Supervised Methodology for Extracting Tumor Type-Specific MRS Sources in Human Brain Data.* PLoS One, 2013. **8**(12): p. e83773.
133. Amari S. *Information geometry on hierarchy of probability distributions. IEEE Trans. Inf. Theory*. 2001. p. 1701-1711.
134. Heiser WJ. *Convergent computation by iterative majorization: Theory and applications in multidimensional data analysis, in: Recent Advances in descriptive Multivariate Analysis, W. J. Krzanowski*. 1995, Oxford: Oxford University Press. p. 157–189.
135. Kiers HAL. *Setting up alternating least squares and iterative majorization algorithms for solving various matrix optimization problems.* Comput. Stat. Data Anal., 2002. **41**(1): p. 157-170.

136. *Breeding Strategies for Maintaining Colonies of Laboratory Mice. A Jackson Laboratory Resource Manual*. Available from: http://ko.cwru.edu/info/breeding_strategies_manual.pdf.
137. Giraldi T, Zorzet S, Perissin L and Rapozzi V. *Stress and chemotherapy. Combined effects on tumor progression and immunity in animal models.* Ann N Y Acad Sci, 2000. **917**: p. 549-59.
138. Weiss WA, Aldape K, Mohapatra G, Feuerstein BG and Bishop JM. *Targeted expression of MYCN causes neuroblastoma in transgenic mice.* EMBO J, 1997. **16**(11): p. 2985-95.
139. Bulik M, Jancalek R, Vanicek J, Skoch A and Mechl M. *Potential of MR spectroscopy for assessment of glioma grading.* Clin Neurol Neurosurg, 2013. **115**(2): p. 146-53.
140. Candiota AP, Acosta M, Simoes RV, Delgado-Goni T, Lope-Piedrafita S, Irure A, Marradi M, Bomati-Miguel O, Miguel-Sancho N, Abasolo I, Schwartz S, Jr., Santamaria J, Penades S and Arus C. *A new ex vivo method to evaluate the performance of candidate MRI contrast agents: a proof-of-concept study.* J Nanobiotechnology, 2014. **12**: p. 12.
141. Simoes RV, Ortuno JE, Bokacheva L, Candiota AP, Ledesma-Carbayo MJ, Delgado-Goni T, Garcia-Martin ML, Santos A and Arus C. *Effect of acute hyperglycemia on moderately hypothermic GL261 mouse glioma monitored by T1-weighted DCE MRI.* MAGMA, 2014.
142. Masters JRW and Palsson B. *Cancer cell lines*. 2002, New York (N.Y.) etc.: Kluwer Academic Publishers.
143. Yi L, Zhou C, Wang B, Chen T, Xu M, Xu L and Feng H. *Implantation of GL261 neurospheres into C57/BL6 mice: a more reliable syngeneic graft model for research on glioma-initiating cells.* Int J Oncol, 2013. **43**(2): p. 477-84.
144. Mullins CS, Schneider B, Stockhammer F, Krohn M, Classen CF and Linnebacher M. *Establishment and characterization of primary glioblastoma cell lines from fresh and frozen material: a detailed comparison.* PLoS One, 2013. **8**(8): p. e71070.
145. Shimada Y, Maeda M, Watanabe G, Yamasaki S, Komoto I, Kaganoi J, Kan T, Hashimoto Y, Imoto I, Inazawa J and Imamura M. *Cell culture in esophageal squamous cell carcinoma and the association with molecular markers.* Clin Cancer Res, 2003. **9**(1): p. 243-9.
146. Barker M, Hoshino T, Gurcay O, Wilson CB, Nielsen SL, Downie R and Eliason J. *Development of an animal brain tumor model and its response to therapy with 1,3-bis(2-chloroethyl)-1-nitrosourea.* Cancer Res, 1973. **33**(5): p. 976-86.
147. Halfter H, Kremerskothen J, Weber J, Hacker-Klom U, Barnekow A, Ringelstein EB and Stogbauer F. *Growth inhibition of newly established human glioma cell lines by leukemia inhibitory factor.* J Neurooncol, 1998. **39**(1): p. 1-18.
148. Onda K, Nagai S, Tanaka R, Morii K, Yoshimura JI, Tsumanuma I and Kumanishi T. *Establishment of two glioma cell lines from two surgical specimens obtained at different times from the same individual.* J Neurooncol, 1999. **41**(3): p. 247-54.
149. Goike HM, Asplund AC, Pettersson EH, Liu L, Ichimura K and Collins VP. *Cryopreservation of viable human glioblastoma xenografts.* Neuropathol Appl Neurobiol, 2000. **26**(2): p. 172-6.
150. Sundlisaeter E, Wang J, Sakariassen PO, Marie M, Mathisen JR, Karlsen BO, Prestegarden L, Skaftnesmo KO, Bjerkvig R and Enger PO. *Primary glioma spheroids maintain tumourogenicity and essential phenotypic traits after cryopreservation.* Neuropathol Appl Neurobiol, 2006. **32**(4): p. 419-27.
151. Chong YK, Toh TB, Zaiden N, Poonepalli A, Leong SH, Ong CE, Yu Y, Tan PB, See SJ, Ng WH, Ng I, Hande MP, Kon OL, Ang BT and Tang C. *Cryopreservation of neurospheres derived from human glioblastoma multiforme.* Stem Cells, 2009. **27**(1): p. 29-39.
152. Cha S. *Perfusion MR imaging: basic principles and clinical applications.* Magn Reson Imaging Clin N Am, 2003. **11**(3): p. 403-13.
153. Law M, Yang S, Wang H, Babb JS, Johnson G, Cha S, Knopp EA and Zagzag D. *Glioma grading: sensitivity, specificity, and predictive values of perfusion MR imaging and proton MR spectroscopic imaging compared with conventional MR imaging.* AJNR Am J Neuroradiol, 2003. **24**(10): p. 1989-98.
154. Price SJ. *The role of advanced MR imaging in understanding brain tumour pathology.* Br J Neurosurg, 2007. **21**(6): p. 562-75.

155. Jenkinson MD, Du Plessis DG, Walker C and Smith TS. *Advanced MRI in the management of adult gliomas.* Br J Neurosurg, 2007. **21**(6): p. 550-61.
156. Cairncross JG, Ueki K, Zlatescu MC, Lisle DK, Finkelstein DM, Hammond RR, Silver JS, Stark PC, Macdonald DR, Ino Y, Ramsay DA and Louis DN. *Specific genetic predictors of chemotherapeutic response and survival in patients with anaplastic oligodendrogliomas.* J Natl Cancer Inst, 1998. **90**(19): p. 1473-9.
157. Bigner SH, Rasheed BK, Wiltshire R and McLendon RE. *Morphologic and molecular genetic aspects of oligodendroglial neoplasms.* Neuro Oncol, 1999. **1**(1): p. 52-60.
158. Jen J, Harper JW, Bigner SH, Bigner DD, Papadopoulos N, Markowitz S, Willson JK, Kinzler KW and Vogelstein B. *Deletion of p16 and p15 genes in brain tumors.* Cancer Res, 1994. **54**(24): p. 6353-8.
159. Schmidt EE, Ichimura K, Reifenberger G and Collins VP. *CDKN2 (p16/MTS1) gene deletion or CDK4 amplification occurs in the majority of glioblastomas.* Cancer Res, 1994. **54**(24): p. 6321-4.
160. Lai A, Kharbanda S, Pope WB, Tran A, Solis OE, Peale F, Forrest WF, Pujara K, Carrillo JA, Pandita A, Ellingson BM, Bowers CW, Soriano RH, Schmidt NO, Mohan S, Yong WH, Seshagiri S, Modrusan Z, Jiang Z, Aldape KD, Mischel PS, Liau LM, Escovedo CJ, Chen W, Nghiemphu PL, James CD, Prados MD, Westphal M, Lamszus K, Cloughesy T and Phillips HS. *Evidence for sequenced molecular evolution of IDH1 mutant glioblastoma from a distinct cell of origin.* J Clin Oncol, 2011. **29**(34): p. 4482-90.
161. Sasaki M, Knobbe CB, Munger JC, Lind EF, Brenner D, Brustle A, Harris IS, Holmes R, Wakeham A, Haight J, You-Ten A, Li WY, Schalm S, Su SM, Virtanen C, Reifenberger G, Ohashi PS, Barber DL, Figueroa ME, Melnick A, Zuniga-Pflucker JC and Mak TW. *IDH1(R132H) mutation increases murine haematopoietic progenitors and alters epigenetics.* Nature, 2012. **488**(7413): p. 656-9.
162. Turcan S, Rohle D, Goenka A, Walsh LA, Fang F, Yilmaz E, Campos C, Fabius AW, Lu C, Ward PS, Thompson CB, Kaufman A, Guryanova O, Levine R, Heguy A, Viale A, Morris LG, Huse JT, Mellinghoff IK and Chan TA. *IDH1 mutation is sufficient to establish the glioma hypermethylator phenotype.* Nature, 2012. **483**(7390): p. 479-83.
163. Yan H, Parsons DW, Jin G, McLendon R, Rasheed BA, Yuan W, Kos I, Batinic-Haberle I, Jones S, Riggins GJ, Friedman H, Friedman A, Reardon D, Herndon J, Kinzler KW, Velculescu VE, Vogelstein B and Bigner DD. *IDH1 and IDH2 mutations in gliomas.* N Engl J Med, 2009. **360**(8): p. 765-73.
164. Lu C, Ward PS, Kapoor GS, Rohle D, Turcan S, Abdel-Wahab O, Edwards CR, Khanin R, Figueroa ME, Melnick A, Wellen KE, O'Rourke DM, Berger SL, Chan TA, Levine RL, Mellinghoff IK and Thompson CB. *IDH mutation impairs histone demethylation and results in a block to cell differentiation.* Nature, 2012. **483**(7390): p. 474-8.
165. Bogler O, Huang HJ, Kleihues P and Cavenee WK. *The p53 gene and its role in human brain tumors.* Glia, 1995. **15**(3): p. 308-27.
166. Zupanska A and Kaminska B. *The diversity of p53 mutations among human brain tumors and their functional consequences.* Neurochem Int, 2002. **40**(7): p. 637-45.
167. Eisenhauer EA, Therasse P, Bogaerts J, Schwartz LH, Sargent D, Ford R, Dancey J, Arbuck S, Gwyther S, Mooney M, Rubinstein L, Shankar L, Dodd L, Kaplan R, Lacombe D and Verweij J. *New response evaluation criteria in solid tumours: revised RECIST guideline (version 1.1).* Eur J Cancer, 2009. **45**(2): p. 228-47.
168. Park SD, Kim CH, Kim CK, Park JA, Sohn HJ, Hong YK and Kim TG. *Cross-priming by temozolomide enhances antitumor immunity of dendritic cell vaccination in murine brain tumor model.* Vaccine, 2007. **25**(17): p. 3485-91.
169. Kitange GJ, Carlson BL, Schroeder MA, Grogan PT, Lamont JD, Decker PA, Wu W, James CD and Sarkaria JN. *Induction of MGMT expression is associated with temozolomide resistance in glioblastoma xenografts.* Neuro Oncol, 2009. **11**(3): p. 281-91.

170. Breton E, Goetz C, Kintz J, Accart N, Aubertin G, Grellier B, Erbs P, Rooke R, Constantinesco A and Choquet P. *In vivo preclinical low-field MRI monitoring of tumor growth following a suicide-gene therapy in an orthotopic mice model of human glioblastoma.* C R Biol, 2010. **333**(3): p. 220-5.
171. Jost SC, Collins L, Travers S, Piwnica-Worms D and Garbow JR. *Measuring brain tumor growth: combined bioluminescence imaging-magnetic resonance imaging strategy.* Mol Imaging, 2009. **8**(5): p. 245-53.
172. Boudreau EA, Chen G, Li X and Kroenke CD. *Magnetic resonance imaging approaches for studying alcoholism using mouse models.* Alcohol Res Health, 2008. **31**(3): p. 247-8.
173. Therasse P, Arbuck SG, Eisenhauer EA, Wanders J, Kaplan RS, Rubinstein L, Verweij J, Van Glabbeke M, van Oosterom AT, Christian MC and Gwyther SG. *New guidelines to evaluate the response to treatment in solid tumors. European Organization for Research and Treatment of Cancer, National Cancer Institute of the United States, National Cancer Institute of Canada.* J Natl Cancer Inst, 2000. **92**(3): p. 205-16.
174. Delgado-Goñi T. *Aproximación a la caracterización morfológica y molecular por IRM y ERM de la respuesta a la terapia en modelos pre-clinicos de glioma.* 2011, Universitat Autònoma de Barcelona: Available from: http://hdl.handle.net/10803/83967.
175. Nelson SJ and Cha S. *Imaging glioblastoma multiforme.* Cancer J, 2003. **9**(2): p. 134-45.
176. Balmaceda C, Critchell D, Mao X, Cheung K, Pannullo S, DeLaPaz RL and Shungu DC. *Multisection 1H magnetic resonance spectroscopic imaging assessment of glioma response to chemotherapy.* J Neurooncol, 2006. **76**(2): p. 185-91.
177. Pirzkall A, McGue C, Saraswathy S, Cha S, Liu R, Vandenberg S, Lamborn KR, Berger MS, Chang SM and Nelson SJ. *Tumor regrowth between surgery and initiation of adjuvant therapy in patients with newly diagnosed glioblastoma.* Neuro Oncol, 2009.
178. Li Y, Lupo JM, Parvataneni R, Lamborn KR, Cha S, Chang SM and Nelson SJ. *Survival analysis in patients with newly diagnosed glioblastoma using pre- and postradiotherapy MR spectroscopic imaging.* Neuro Oncol, 2013. **15**(5): p. 607-17.
179. Sankar T, Caramanos Z, Assina R, Villemure JG, Leblanc R, Langleben A, Arnold DL and Preul MC. *Prospective serial proton MR spectroscopic assessment of response to tamoxifen for recurrent malignant glioma.* J Neurooncol, 2008. **90**(1): p. 63-76.
180. Hakumaki JM, Poptani H, Sandmair AM, Yla-Herttuala S and Kauppinen RA. *1H MRS detects polyunsaturated fatty acid accumulation during gene therapy of glioma: implications for the in vivo detection of apoptosis.* Nat Med, 1999. **5**(11): p. 1323-7.
181. Jimenez-Xarrie E, Davila M, Gil-Perotin S, Jurado-Rodriguez A, Candiota AP, Delgado-Mederos R, Lope-Piedrafita S, Garcia-Verdugo JM, Arus C and Marti-Fabregas J. *In vivo and ex vivo magnetic resonance spectroscopy of the infarct and the subventricular zone in experimental stroke.* J Cereb Blood Flow Metab, 2015.
182. Li Y, Sima DM, Van Cauter S, Himmelreich U, Croitor Sava AR, Pi Y, Liu Y and Van Huffel S. *Unsupervised nosologic imaging for glioma diagnosis.* IEEE Trans Biomed Eng, 2013. **60**(6): p. 1760-3.
183. Luts J, Laudadio T, Idema AJ, Simonetti AW, Heerschap A, Vandermeulen D, Suykens JA and Van Huffel S. *Nosologic imaging of the brain: segmentation and classification using MRI and MRSI.* NMR Biomed, 2009. **22**(4): p. 374-90.
184. Day SE, Kettunen MI, Gallagher FA, Hu DE, Lerche M, Wolber J, Golman K, Ardenkjaer-Larsen JH and Brindle KM. *Detecting tumor response to treatment using hyperpolarized 13C magnetic resonance imaging and spectroscopy.* Nat Med, 2007. **13**(11): p. 1382-7.
185. Chaumeil MM, Ozawa T, Park I, Scott K, James CD, Nelson SJ and Ronen SM. *Hyperpolarized 13C MR spectroscopic imaging can be used to monitor Everolimus treatment in vivo in an orthotopic rodent model of glioblastoma.* Neuroimage, 2012. **59**(1): p. 193-201.
186. Fang F. *Evaluation and Reporting of Breast Cancer after Neoadjuvant Chemotherapy.* The Open Pathology Journal, 2009. **3**: p. 58-63.

187. Le T, Williams K, Senterman M, Hopkins L, Faught W and Fung-Kee-Fung M. *Histopathologic assessment of chemotherapy effects in epithelial ovarian cancer patients treated with neoadjuvant chemotherapy and delayed primary surgical debulking.* Gynecol Oncol, 2007. **106**(1): p. 160-3.
188. Kurokawa Y, Shibata T, Ando N, Seki S, Mukaida H and Fukuda H. *Which is the optimal response criteria for evaluating preoperative treatment in esophageal cancer: RECIST or histology?* Ann Surg Oncol, 2013. **20**(9): p. 3009-14.
189. Assadian S, Aliaga A, Del Maestro RF, Evans AC and Bedell BJ. *FDG-PET imaging for the evaluation of antiglioma agents in a rat model.* Neuro Oncol, 2008. **10**(3): p. 292-9.
190. Hadaczek P, Ozawa T, Soroceanu L, Yoshida Y, Matlaf L, Singer E, Fiallos E, James CD and Cobbs CS. *Cidofovir: a novel antitumor agent for glioblastoma.* Clin Cancer Res, 2013. **19**(23): p. 6473-83.
191. Marrero L, Wyczechowska D, Musto AE, Wilk A, Vashistha H, Zapata A, Walker C, Velasco-Gonzalez C, Parsons C, Wieland S, Levitt D, Reiss K and Prakash O. *Therapeutic efficacy of aldoxorubicin in an intracranial xenograft mouse model of human glioblastoma.* Neoplasia, 2014. **16**(10): p. 874-82.
192. Park I, Bok R, Ozawa T, Phillips JJ, James CD, Vigneron DB, Ronen SM and Nelson SJ. *Detection of early response to temozolomide treatment in brain tumors using hyperpolarized 13C MR metabolic imaging.* J Magn Reson Imaging, 2011. **33**(6): p. 1284-90.
193. Bai RY, Staedtke V, Aprhys CM, Gallia GL and Riggins GJ. *Antiparasitic mebendazole shows survival benefit in 2 preclinical models of glioblastoma multiforme.* Neuro Oncol, 2011. **13**(9): p. 974-82.
194. Ray SK, Patel SJ, Welsh CT, Wilford GG, Hogan EL and Banik NL. *Molecular evidence of apoptotic death in malignant brain tumors including glioblastoma multiforme: upregulation of calpain and caspase-3.* J Neurosci Res, 2002. **69**(2): p. 197-206.
195. Saggioro FP, Neder L, Stavale JN, Paixao-Becker AN, Malheiros SM, Soares FA, Pittella JE, Matias CC, Colli BO, Carlotti CG, Jr. and Franco M. *Fas, FasL, and cleaved caspases 8 and 3 in glioblastomas: a tissue microarray-based study.* Pathol Res Pract, 2014. **210**(5): p. 267-73.
196. Gdynia G, Grund K, Eckert A, Bock BC, Funke B, Macher-Goeppinger S, Sieber S, Herold-Mende C, Wiestler B, Wiestler OD and Roth W. *Basal caspase activity promotes migration and invasiveness in glioblastoma cells.* Mol Cancer Res, 2007. **5**(12): p. 1232-40.
197. Scabini M, Stellari F, Cappella P, Rizzitano S, Texido G and Pesenti E. *In vivo imaging of early stage apoptosis by measuring real-time caspase-3/7 activation.* Apoptosis, 2011. **16**(2): p. 198-207.
198. Nieder C, Grosu AL, Mehta MP, Andratschke N and Molls M. *Treatment of malignant gliomas: radiotherapy, chemotherapy and integration of new targeted agents.* Expert Rev Neurother, 2004. **4**(4): p. 691-703.
199. Prados MD, Seiferheld W, Sandler HM, Buckner JC, Phillips T, Schultz C, Urtasun R, Davis R, Gutin P, Cascino TL, Greenberg HS and Curran WJ, Jr. *Phase III randomized study of radiotherapy plus procarbazine, lomustine, and vincristine with or without BUdR for treatment of anaplastic astrocytoma: final report of RTOG 9404.* Int J Radiat Oncol Biol Phys, 2004. **58**(4): p. 1147-52.
200. van den Bent MJ, Carpentier AF, Brandes AA, Sanson M, Taphoorn MJ, Bernsen HJ, Frenay M, Tijssen CC, Grisold W, Sipos L, Haaxma-Reiche H, Kros JM, van Kouwenhoven MC, Vecht CJ, Allgeier A, Lacombe D and Gorlia T. *Adjuvant procarbazine, lomustine, and vincristine improves progression-free survival but not overall survival in newly diagnosed anaplastic oligodendrogliomas and oligoastrocytomas: a randomized European Organisation for Research and Treatment of Cancer phase III trial.* J Clin Oncol, 2006. **24**(18): p. 2715-22.
201. Bao S, Wu Q, Sathornsumetee S, Hao Y, Li Z, Hjelmeland AB, Shi Q, McLendon RE, Bigner DD and Rich JN. *Stem cell-like glioma cells promote tumor angiogenesis through vascular endothelial growth factor.* Cancer Res, 2006. **66**(16): p. 7843-8.

202. Bleau AM, Hambardzumyan D, Ozawa T, Fomchenko EI, Huse JT, Brennan CW and Holland EC. *PTEN/PI3K/Akt pathway regulates the side population phenotype and ABCG2 activity in glioma tumor stem-like cells.* Cell Stem Cell, 2009. **4**(3): p. 226-35.
203. Huang Z, Cheng L, Guryanova OA, Wu Q and Bao S. *Cancer stem cells in glioblastoma--molecular signaling and therapeutic targeting.* Protein Cell, 2010. **1**(7): p. 638-55.
204. Mirbahai L, Wilson M, Shaw CS, McConville C, Malcomson RD, Kauppinen RA and Peet AC. *Lipid biomarkers of glioma cell growth arrest and cell death detected by 1 H magic angle spinning MRS.* NMR Biomed, 2012. **25**(11): p. 1253-62.
205. Li Y, Sima DM, Cauter SV, Croitor Sava AR, Himmelreich U, Pi Y and Van Huffel S. *Hierarchical non-negative matrix factorization (hNMF): a tissue pattern differentiation method for glioblastoma multiforme diagnosis using MRSI.* NMR Biomed, 2013. **26**(3): p. 307-19.

# ANNEXES

## ANNEX 1: DESCRIPTION AND COMPOSITION OF MICE NUTRITION

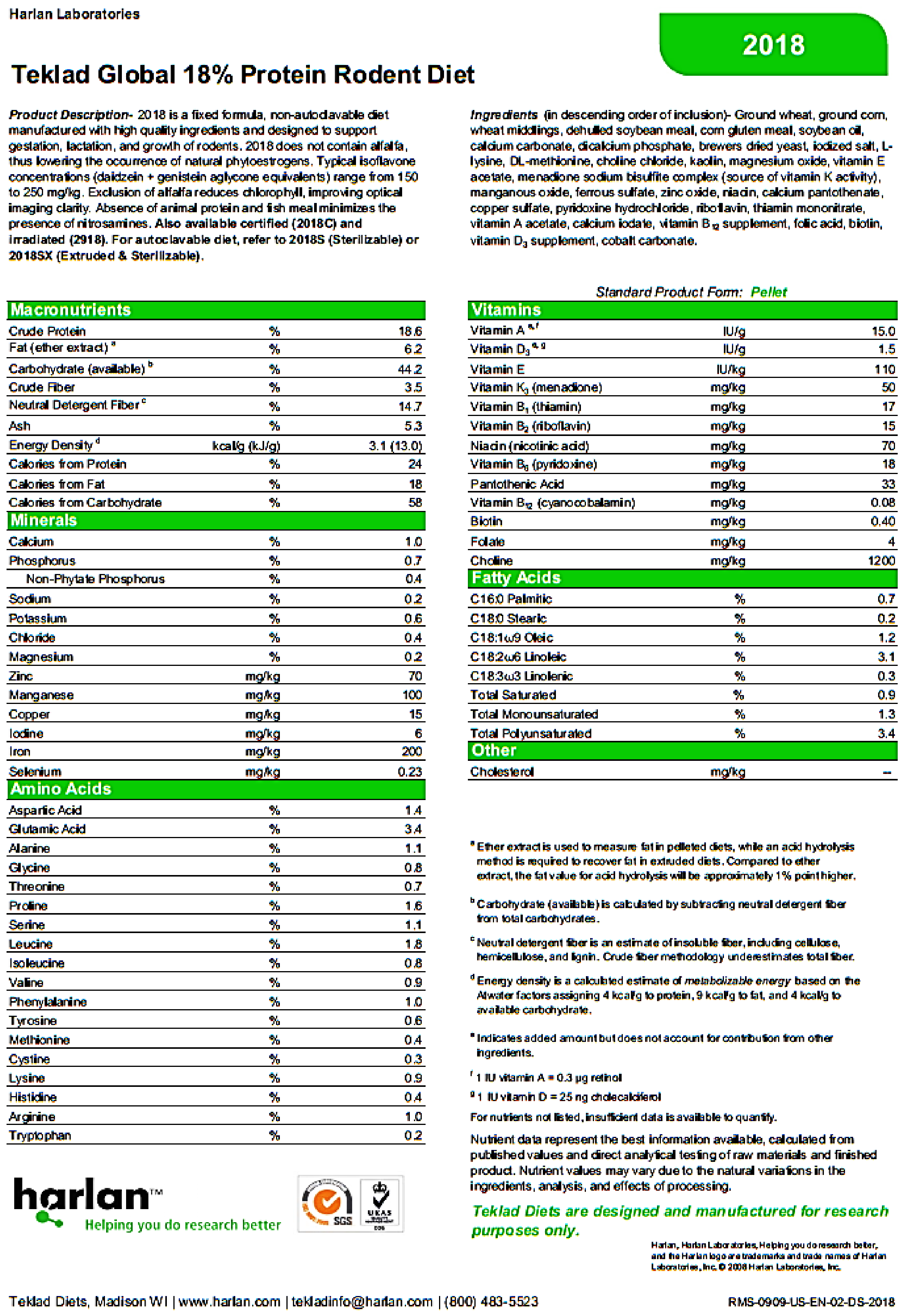

Harlan Laboratories

2018

### Teklad Global 18% Protein Rodent Diet

*Product Description*- 2018 is a fixed formula, non-autoclavable diet manufactured with high quality ingredients and designed to support gestation, lactation, and growth of rodents. 2018 does not contain alfalfa, thus lowering the occurrence of natural phytoestrogens. Typical isoflavone concentrations (daidzein + genistein aglycone equivalents) range from 150 to 250 mg/kg. Exclusion of alfalfa reduces chlorophyll, improving optical imaging clarity. Absence of animal protein and fish meal minimizes the presence of nitrosamines. **Also available certified (2018C) and irradiated (2918). For autoclavable diet, refer to 2018S (Sterilizable) or 2018SX (Extruded & Sterilizable).**

*Ingredients* (in descending order of inclusion)- Ground wheat, ground corn, wheat middlings, dehulled soybean meal, corn gluten meal, soybean oil, calcium carbonate, dicalcium phosphate, brewers dried yeast, iodized salt, L-lysine, DL-methionine, choline chloride, kaolin, magnesium oxide, vitamin E acetate, menadione sodium bisulfite complex (source of vitamin K activity), manganous oxide, ferrous sulfate, zinc oxide, niacin, calcium pantothenate, copper sulfate, pyridoxine hydrochloride, riboflavin, thiamin mononitrate, vitamin A acetate, calcium iodate, vitamin $B_{12}$ supplement, folic acid, biotin, vitamin $D_3$ supplement, cobalt carbonate.

*Standard Product Form:* *Pellet*

| **Macronutrients** | | |
|---|---|---|
| Crude Protein | % | 18.6 |
| Fat (ether extract) [a] | % | 6.2 |
| Carbohydrate (available) [b] | % | 44.2 |
| Crude Fiber | % | 3.5 |
| Neutral Detergent Fiber [c] | % | 14.7 |
| Ash | % | 5.3 |
| Energy Density [d] | kcal/g (kJ/g) | 3.1 (13.0) |
| Calories from Protein | % | 24 |
| Calories from Fat | % | 18 |
| Calories from Carbohydrate | % | 58 |
| **Minerals** | | |
| Calcium | % | 1.0 |
| Phosphorus | % | 0.7 |
| Non-Phytate Phosphorus | % | 0.4 |
| Sodium | % | 0.2 |
| Potassium | % | 0.6 |
| Chloride | % | 0.4 |
| Magnesium | % | 0.2 |
| Zinc | mg/kg | 70 |
| Manganese | mg/kg | 100 |
| Copper | mg/kg | 15 |
| Iodine | mg/kg | 6 |
| Iron | mg/kg | 200 |
| Selenium | mg/kg | 0.23 |
| **Amino Acids** | | |
| Aspartic Acid | % | 1.4 |
| Glutamic Acid | % | 3.4 |
| Alanine | % | 1.1 |
| Glycine | % | 0.8 |
| Threonine | % | 0.7 |
| Proline | % | 1.6 |
| Serine | % | 1.1 |
| Leucine | % | 1.8 |
| Isoleucine | % | 0.8 |
| Valine | % | 0.9 |
| Phenylalanine | % | 1.0 |
| Tyrosine | % | 0.6 |
| Methionine | % | 0.4 |
| Cystine | % | 0.3 |
| Lysine | % | 0.9 |
| Histidine | % | 0.4 |
| Arginine | % | 1.0 |
| Tryptophan | % | 0.2 |

| **Vitamins** | | |
|---|---|---|
| Vitamin A [e, f] | IU/g | 15.0 |
| Vitamin $D_3$ [e, g] | IU/g | 1.5 |
| Vitamin E | IU/kg | 110 |
| Vitamin $K_3$ (menadione) | mg/kg | 50 |
| Vitamin $B_1$ (thiamin) | mg/kg | 17 |
| Vitamin $B_2$ (riboflavin) | mg/kg | 15 |
| Niacin (nicotinic acid) | mg/kg | 70 |
| Vitamin $B_6$ (pyridoxine) | mg/kg | 18 |
| Pantothenic Acid | mg/kg | 33 |
| Vitamin $B_{12}$ (cyanocobalamin) | mg/kg | 0.08 |
| Biotin | mg/kg | 0.40 |
| Folate | mg/kg | 4 |
| Choline | mg/kg | 1200 |
| **Fatty Acids** | | |
| C16:0 Palmitic | % | 0.7 |
| C18:0 Stearic | % | 0.2 |
| C18:1ω9 Oleic | % | 1.2 |
| C18:2ω6 Linoleic | % | 3.1 |
| C18:3ω3 Linolenic | % | 0.3 |
| Total Saturated | % | 0.9 |
| Total Monounsaturated | % | 1.3 |
| Total Polyunsaturated | % | 3.4 |
| **Other** | | |
| Cholesterol | mg/kg | -- |

[a] Ether extract is used to measure fat in pelleted diets, while an acid hydrolysis method is required to recover fat in extruded diets. Compared to ether extract, the fat value for acid hydrolysis will be approximately 1% point higher.

[b] Carbohydrate (available) is calculated by subtracting neutral detergent fiber from total carbohydrates.

[c] Neutral detergent fiber is an estimate of insoluble fiber, including cellulose, hemicellulose, and lignin. Crude fiber methodology underestimates total fiber.

[d] Energy density is a calculated estimate of *metabolizable energy* based on the Atwater factors assigning 4 kcal/g to protein, 9 kcal/g to fat, and 4 kcal/g to available carbohydrate.

[e] Indicates added amount but does not account for contribution from other ingredients.

[f] 1 IU vitamin A = 0.3 μg retinol

[g] 1 IU vitamin D = 25 ng cholecalciferol

For nutrients not listed, insufficient data is available to quantify.

Nutrient data represent the best information available, calculated from published values and direct analytical testing of raw materials and finished product. Nutrient values may vary due to the natural variations in the ingredients, analysis, and effects of processing.

*Teklad Diets are designed and manufactured for research purposes only.*

harlan™
Helping you do research better

Harlan, Harlan Laboratories, Helping you do research better, and the Harlan logo are trademarks and trade names of Harlan Laboratories, Inc. © 2008 Harlan Laboratories, Inc.

Teklad Diets, Madison WI | www.harlan.com | tekladinfo@harlan.com | (800) 483-5523

RMS-0909-US-EN-02-DS-2018

## ANNEX 2: SUPERVISION OF LABORATORY ANIMALS

Procedure: 530-CEEAH, 2449-DMA

**MONITORING PARAMETERS (scale: 0-3 points)**:

Weight Loss

0) Normal Weight

1) Less than 10% loss

2) Between 10 and 15% loss

3) Consistent or rapid, exceeding 20% loss maintained for 72h

Physical appearance

0) Normal

1) More than 10% dehydration, body condition 2 (BC2; see further for details), skin tenting

2) Erected hair. Cyanosis

3) Hunched back. Loss of muscle mass

Clinical signs

0) None

1) Circular motion of the animal

2) Mucous secretions and/or bleeding from any orifice. Detectable hypertrophy of organs (lymph nodes, spleen, liver)

3) Shortness of breath (particularly if accompanied by nasal discharge and / or cyanosis). Cachexia.

Changes in behaviour

0) No

1) Inability to move normally

2) Inability to get to the food / drink. Isolation from the rest of the animals in the cage

3) Unconsciousness or comatose. Lack of response (Dying)

Wounds

0) No

1) Scratches

2) Nonhealing wounds. Infection at the surgical site

3) Ulcerating, festering wounds. Ulcerating or necrotic tumours

**The animal condition according to the parameters and overall score:**

a) 0 points: Healthy animal

b) 1-2 points: Minor signs, follow established protocol

c) 3-11 points: Daily supervision of the animal. Analgesics* or sacrifice of the animal **

d) 12-30 points: sacrifice **

* Analgesic: Meloxicam (subcutaneously: 1 mg /kg)

** The *Servei d'Estabulari* veterinary staff informed a group member as soon as possible to consider halting of the protocol / experiment.

**NOTE:** As the tumour grows, it affects in the motor function of the brain. Animals may suffer from: paresis, decreased strength, plegia, paralysis. In these cases, food and water (i.e. hydrogel or water-soaked food) should be placed inside the cage to facilitate access by the animal.

**Body condition (BC):**

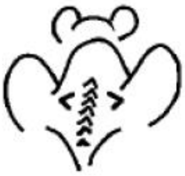

**BC 1**

Mouse is emaciated.
- *Skeletal structure extremely prominent; little or no flesh cover.*
- *Vertebrae distinctly segmented.*

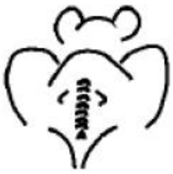

**BC 2**

Mouse is underconditioned.
- *Segmentation of vertebral column evident.*
- *Dorsal pelvic bones are readily palpable.*

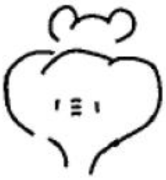

**BC 3**

Mouse is well-conditioned.
- *Vertebrae and dorsal pelvis not prominent; palpable with slight pressure.*

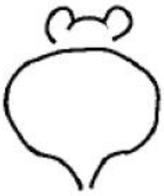

**BC 4**

Mouse is overconditioned.
- *Spine is a continuous column.*
- *Vertebrae palpable only with firm pressure.*

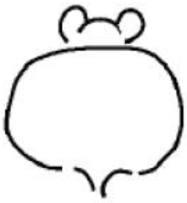

**BC 5**

Mouse is obese.
- *Mouse is smooth and bulky.*
- *Bone structure disappears under flesh and subcutaneous fat.*

## ANNEX 3: EXAMPLE OF A WEEKLY ANIMAL INSPECTION DOCUMENT FOR S COLONY

***Servei d'Estabulari, UAB*** **Número: GABRMN __ __ __ - 09**

# Protocolo de Inspección Semanal de Animales

| | |
|---|---|
| **IP:** | **Ratones:** |
| C. Arús | Colonia S, más de 8 semanas de edad |

| | | | |
|---|---|---|---|
| **Fecha:** | **Animal:** | **Sala:** | **Colab. SE:** |
| ___ / ___ / ______ | S ______ | _____ | __________ |
| (dd/mm/aaaa) | | | |

## Observaciones:

| | SI |
|---|---|
| Comportamiento anormal | ☐ |
| Movilidad anormal | ☐ |
| Paresia: ____________________________________ | ☐ |
| Parálisis: ____________________________________ | ☐ |
| Anomalías oculares | ☐ |
| Crisis epiléptica | ☐ |
| Tumoraciones: _______________________________ | ☐ |

Otras observaciones:

_________________________________________________

________________________________________________

***Número Full Estabulari:*** _____________

## ANNEX 4: HOMOGENIZATION OF TISSUES

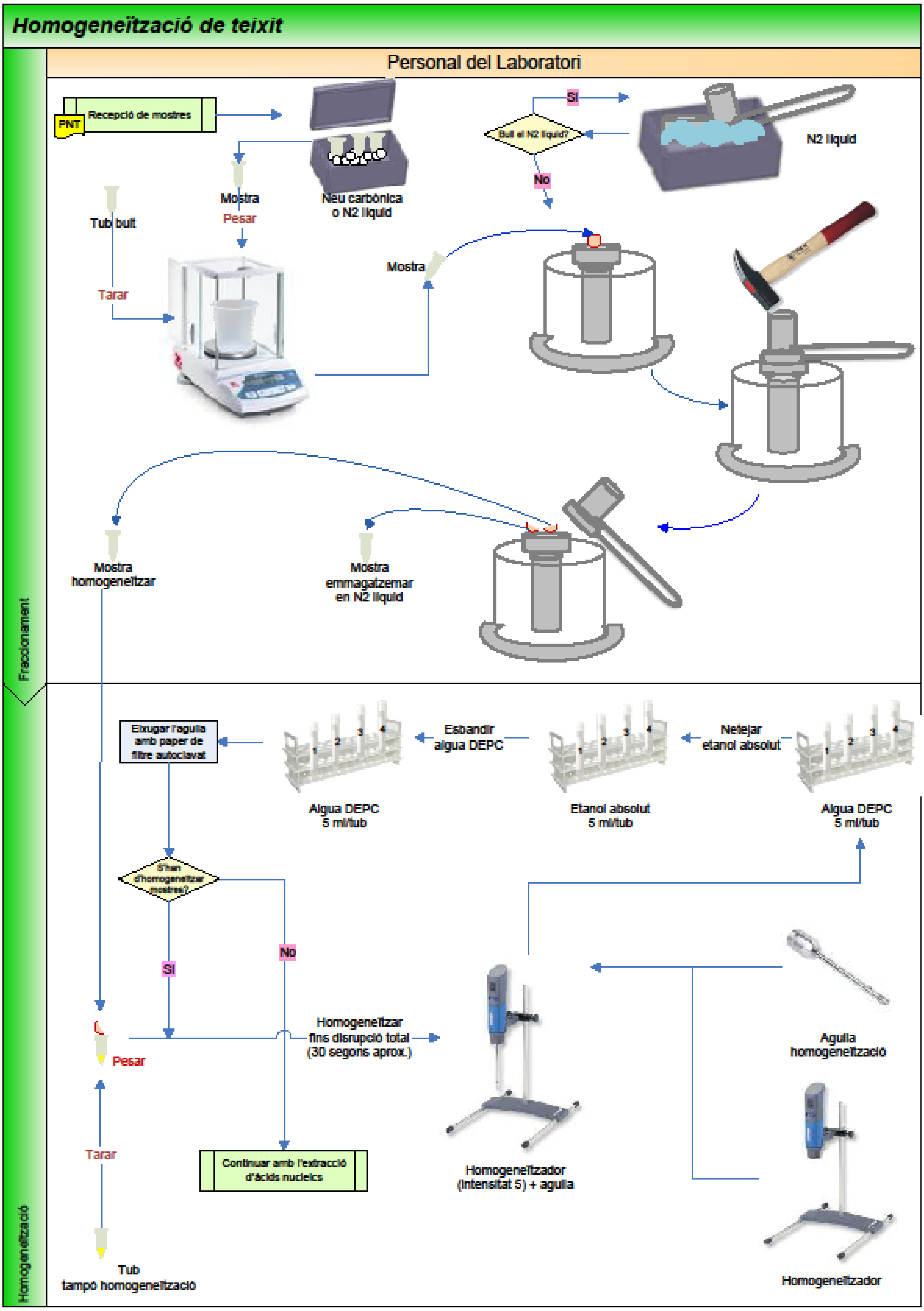
Homogeneïtzació de teixit
Personal del Laboratori
PNT
Recepció de mostres
Mostra
Pesar
Neu carbònica
o N2 líquid
Bull el N2 líquid?
Sí
No
N2 líquid
Tub buit
Tarar
Mostra
Mostra
homogeneïtzar
Mostra
emmagatzemar
en N2 líquid
Fraccionament
Eixugar l'agulla
amb paper de
filtre autoclavat
Esbandir
aigua DEPC
Netejar
etanol absolut
1
2
3
4
Aigua DEPC
5 ml/tub
Etanol absolut
5 ml/tub
Aigua DEPC
5 ml/tub
S'han
d'homogeneïtzar
mostres?
Sí
No
Pesar
Tarar
Tub
tampó homogeneïtzació
Homogeneïtzar
fins disrupció total
(30 segons aprox.)
Continuar amb l'extracció
d'àcids nucleics
Homogeneïtzador
(intensitat 5) + agulla
Agulla
homogeneïtzació
Homogeneïtzador
Homogeneïtzació

## ANNEX 5: PCR CONDITIONS FOR AMPLIFICATION OF MURINE IDH1, IDH2 and p53

PCR Cocktail:

| *Reagents* (Bioline) | *Volume (for IDH1 & IDH2*) | *Volume (for p53*) |
|---|---|---|
| MiliQ $H_2O$ | 16.2 µl | 15.5 µl |
| 10x PCR NH4 buffer w/o $MgCl_2$ | 2.5 µl | 2.5 µl |
| $MgCl_2$ | 2 µl | 1.5 µl |
| dNTPs mix (100 mM) | 1 µl | 1 µl |
| primers mix (100 µM) | 1 µl | 2 µl (diluted 1:10) |
| DNA (50 ng /µl) | 2 µl | 2 µl |
| *Taq* DNA polymerase | 0.3 µl | 0.5 µl |
| Total volume | 25 µl | 25 µl |

Thermocycler program:

| | | | |
|---|---|---|---|
| Initial denaturation: | | 94.0°C | 10 mins |
| 39 cycles: | - denaturation: | 94.0°C | 1 min |
| | - annealing: | 58.7°C | 1 min |
| | - extension: | 72.0°C | 45 sec |
| Final extension: | | 72.0°C | 5 min |
| Storage: | | 4.0°C | |

## ANNEX 6: CONTROL AND TREATED CASES INCLUDED IN THE TRAINING SET

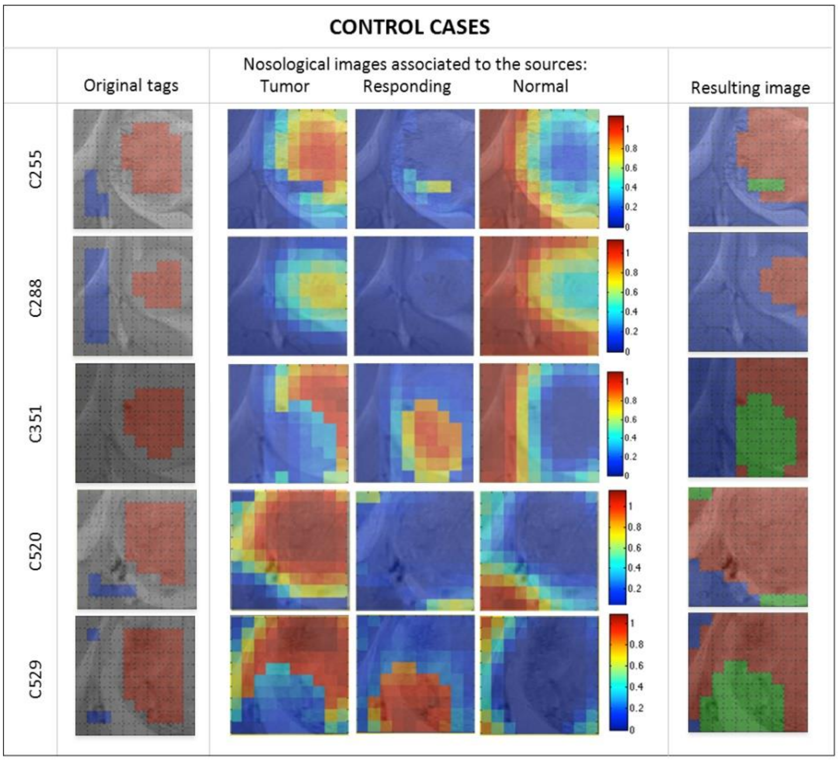
CONTROL CASES
Original tags
Nosological images associated to the sources:
Tumor
Responding
Normal
Resulting image
C255
C288
C351
C520
C529
1
0.8
0.6
0.4
0.2
0

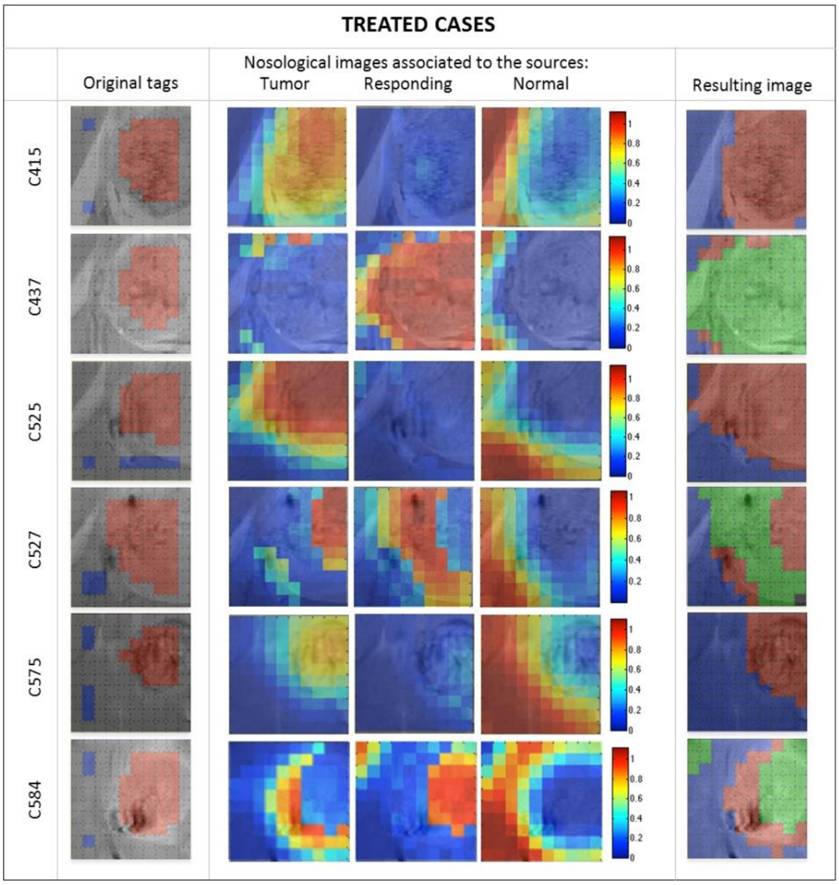
TREATED CASES
Original tags
Nosological images associated to the sources:
Tumor
Responding
Normal
Resulting image
C415
C437
C525
C527
C575
C584
1
0.8
0.6
0.4
0.2
0

## ANNEX 7: CONTROL CASES OF THE INDIVIDUAL TEST SET

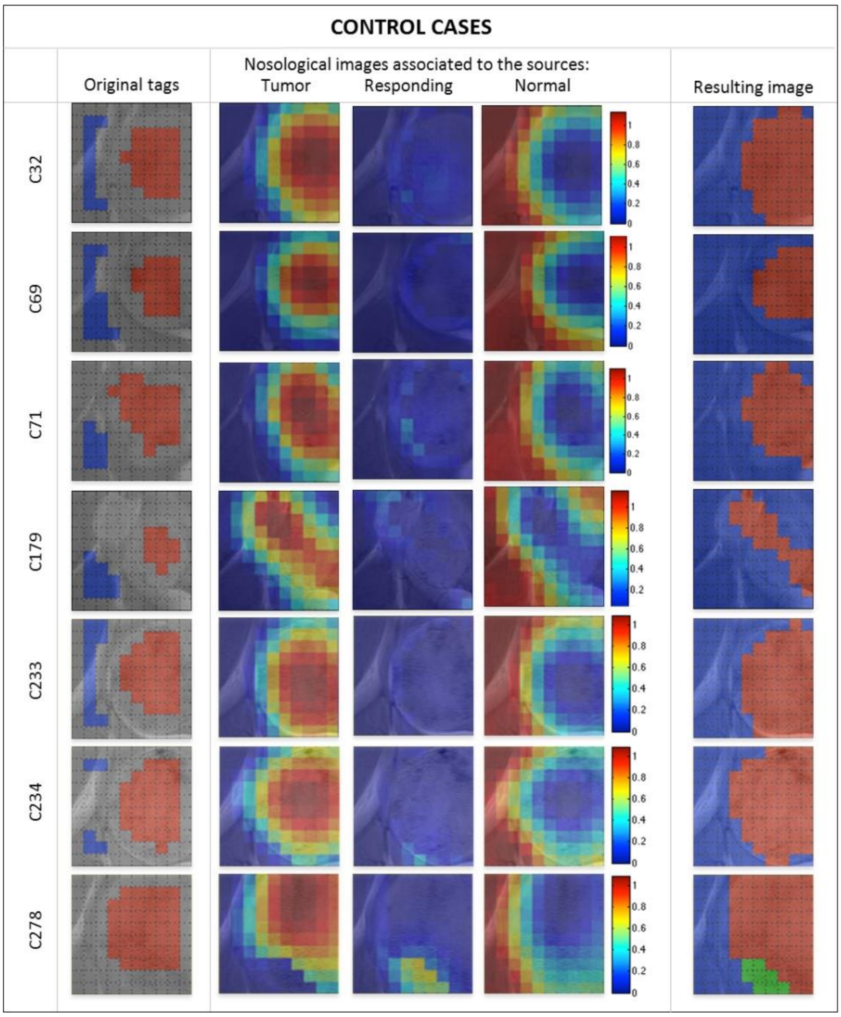
CONTROL CASES
Original tags
Nosological images associated to the sources:
Tumor
Responding
Normal
Resulting image
C32
C69
C71
C179
C233
C234
C278
1
0.8
0.6
0.4
0.2
0

## ANNEX 8: CASES TREATED WITH 1 TMZ OF THE INDIVIDUAL TEST SET

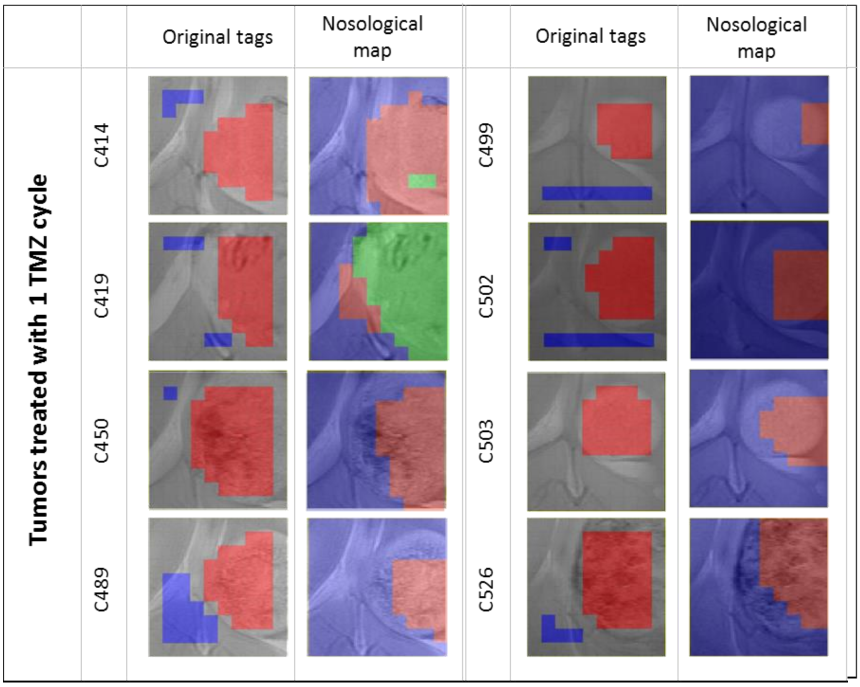
Original tags
Nosological map
Original tags
Nosological map
Tumors treated with 1 TMZ cycle
C414
C419
C450
C489
C499
C502
C503
C526

## ANNEX 9: VALUES CALCULATED IN SOME OF THE TRAINING SET CASES FOR TUMOUR VOLUME (ACQUIRED FROM $T_{2W}$ MRI) AND HISTOPATHOLOGICAL PARAMETERS: PROLIFERATION, APOPTOTIC AND MITOTIC RATES

| | | | MRSI acquisition (day p.i.) | Tumour volume (mm$^3$) | Proliferation rate (%) | Apoptotic rate (% cells/mm$^2$) | Mitotic index (mitoses/field) |
|---|---|---|---|---|---|---|---|
| **Control** | **C520** | | 18 | 187.5 | 51.4 ± 12.2 | 0.46 ± 0.4 | 20.6 ± 7.9 |
| | **C529** | | 18 | 170 | 66.5 ± 15.5 | 2.8 ± 2.8 | 7.9 ± 7.2 |
| | **C583** | | 18 | 89.4 | 57.9 ± 13.1 | 0.5 ± 0.3 | 12.1 ± 3.6 |
| **Average in [123] n = 6** | | | **18** | **102 ± 1.7** | **57.8 ± 5.4** | **0.6 ± 0.4** | **14.1 ± 4.2** |
| **Treated** | **C415** | 2 TMZ cycles | 22 | 115.4 | 53.6 ± 12.7 | 1.9 ± 0.9 | 4.9 ± 1.8 |
| | **C418** | 2 TMZ cycles | 22 | 156.2 | 51.7 ± 12.9 | 2.1 ± 1 | 5.6 ± 1.9 |
| | **C525** | 2 TMZ cycles | 22 | 100 | 69.9 ± 6.5 | 1.8 ± 0.9 | 0.8 ± 0.5 |
| | **C527** | 2 TMZ cycles | 22 | 128.9 | 55.7 ± 13.7 | 2.2 ± 1.4 | 7.7 ± 4.3 |
| | **C575** | 3 TMZ cycles | 26 | 71.7 | 18 ± 5.7 | 1.5 ± 0.8 | 0.3 ± 2.3 |
| | **C584** | 3 TMZ cycles | 26 | | 26.4 ± 10.2 | 3.5 ± 1.4 | 2.9 ± 2.3 |
| | **C586** | 2 TMZ cycles | 22 | 133.3 | 43.8 ± 14.1 | 3.3 ± 2.5 | 1.6 ± 0.9 |
| **Average in [123] n = 12** | | | **24** | **100.9 ± 41.6** | **29.8 ± 10.3** | **2.7 ± 1.2** | **3.3 ± 2.9** |